Modelling Degradation in Adhesive Joints Subjected to Fluctuating Service Conditions

by

Aamir Mubashar

A doctoral thesis submitted in partial fulfilment of the requirements for the award of Doctor of Philosophy of Loughborough University

Wolfson School of Mechanical and Manufacturing Engineering

January 2010

Certificate of Originality

Dedicated to my parents and my wife

Abstract

Adhesive joining is an attractive alternative to conventional joining methods, such as welding and mechanical fastening. The benefits of adhesive bonding include: the ability to form lightweight, high stiffness structures; joining of different types of materials; better fatigue performance, and reduction in the stress concentrations or the effects of the heat associated with welding. However, concerns about the durability of adhesive joints still hinder their widespread use in structural applications. Moisture has been identified as one of the major factors affecting joint durability. This is especially important in applications where joints are exposed to varying moisture conditions throughout their useful life.

The aim of this research is to develop models to predict degradation in adhesive joints under varying moisture conditions. This was achieved by a combination of experimental and numerical methods. Experiments were carried out to characterise the moisture uptake and mechanical properties of the single part epoxide adhesive, FM73-M. Single lap joints were manufactured from aluminium alloy 2024 in heat treated (T3) and non heat treated (O) states using the FM73-M, BR127 adhesive-primer system. Tensile testing of the single lap joints was carried out after the joints had been exposed to hot-wet conditioning environments.

Models were developed for predicting moisture concentration in the adhesive under cyclic moisture absorption and desorption conditions. A finite element based methodology incorporating moisture history was developed to predict the cyclic moisture concentration. In the next step, a novel finite element based methodology, which was based on moisture history effects, was developed to determine stresses in bonded joints after curing, conditioning and tensile testing. In the final step, a moisture history dependent cohesive zone element based damage and failure criterion was introduced to predict damage initiation, crack growth and failure under variable moisture and temperature conditions. The methodology proposed in this work and its implementation by finite element method provides a systematic approach for determining the degradation in adhesive joints under varying environmental conditions and accomplishes the aim of this research.

Contents

List of Figures

List of Tables

Symbols

Al2024 O	Aluminium alloy 2024, O type in non heat treated form.
Al2024 T3	Aluminium alloy 2024 with T3 type heat treatment.
a, b, d	Power law constants in dual Fickian with damage model
C	Concentration
C_∞	Saturated moisture concentration
C_1, C_2	Fractions of saturated moisture concentration in a dual Fickian model
C_{crit}	Critical moisture concentration
C_t	Moisture concentration at time t
c	Specific heat
D	Diffusion coefficient
D_1	Diffusion coefficient of first stage in a dual Fickian model
D_2	Diffusion coefficient of second stage in a dual Fickian model
D_c	Damage variable
D_d	Diffusion coefficient during desorption
D_o	Diffusion coefficient of first absorption/desorption cycle
D_{po}, D_{pr}	Prony series diffusion coefficient
E	Elastic modulus
F	Flux
F_y	Yield function
FV	Flag variable used in ABAQUS subroutine UMAT
$FV1, FV2$	Field variables used in ABAQUS
f	Void volume fraction in modified Gurson model
f^*	Modified void volume fraction in modified Gurson model
f_c	Critical void volume fraction in modified Gurson model
f_F	Void volume fraction at failure in modified Gurson model
f_u^*	$1/q_1$
G	Strain energy release rate
G_c	Critical strain energy release rate
G_{coh}	Cohesive energy used in cohesive zone model
J_2	Second stress invariant
K	Stiffness
K_c	Critical stress intensity factor
K^*	Flow stress ratio
k	Thermal conductivity

l	Length of the diffusion path
M_∞	Saturated moisture content
$M_{\infty o}$	Saturated moisture content of the first absorption cycle
$M_{1\infty}, M_{2\infty}$	Fractions of saturated moisture content in a dual Fickian model
M_d	Short term mass uptake
$M_{d\infty}$	Saturated moisture content due to secondary rapid uptake
$M_{R\infty}$	Long term mass uptake
M_t	Moisture content at time t
N	Number of diffusion cycles
n	Number of terms in a series
p^*	Hydrostatic stress
Q	Activation energy
q_1, q_2	Yield surface multipliers
R	Universal gas constant
r	Relaxation constant
r^*	Third stress invariant
S_N	Strength of joint after N number of absorption or desorption cycles
S_R	Percentage reduction in joint strength
SV	State variable used in ABAQUS
T	Temperature
t	Time
t_1	Start time of secondary uptake in dual Fickian with damage model
t_n	Stress in normal direction at any time t
$\overline{t}_n$	Stress in normal direction without damage at time t
t_n^o	Maximum stress in normal direction
t_s, t_t	Stresses in shear directions at any time t
$\overline{t}_s, \overline{t}_t$	Stresses in shear directions without damage at any time t
t_s^o, t_t^o	Maximum stresses in shear directions
u, v, w, p, q	Curve fitting parameters
V	Volume
x, y, z	Spatial coordinates
α	Parameter to determine K
β	Material angle of friction
δ	Displacement
δ_m^o	Displacement at damage initiation
δ_m^f	Displacement at failure
$\delta_m^{\max}$	Maximum displacement during loading history
σ	Stress
$\overline{\sigma}$	Von Mises equivalent stress
σ_c	Compressive yield stress
σ_{ult}	Ultimate tensile strength
σ_y	Yield stress

ε	Strain
ε^{pl}	Plastic strain
τ	Traction
τ_c	Tripping traction
τ_r	Retardation time
Φ	Heaviside step function
ρ	Density
Ω	Relaxation rate constant
$\langle\ \rangle$	Macaulay bracket

Acronyms

2D	Two Dimensional
3D	Three Dimensional
ACDC	Alternating Current Direct Current Anodising
CAA	Chromic Acid Anodising
CTE	Coefficient of Thermal Expansion
CZM	Cohesive Zone Model
DFD	Dual Fickian with Damage Model
GUI	Graphical User Interface
MMF	Mixed Mode Flexure
RH	Relative Humidity
SEM	Scanning Electron Microscopy
XPS	X-Ray Photoelectron Spectroscopy

Acknowledgement

I am deeply in debt to my supervisors Dr. I. A. Ashcroft and Dr. G. W. Critchlow for their guidance, suggestions, constructive criticism and encouragement. Their patience and understanding helped me sail through the hard times. I would also like to thank Prof. A. D. Crocombe for his inputs at various stages of the research.

Special thanks are due to Dr. Keith Yendall for his help in the experimentation, especially in ACDC anodising and spectroscopic analysis.

Thanks are also due to the staff of the Wolfson School of Mechanical and Manufacturing Engineering for their support and help. I appreciate the guidance provided by Mr. Richard Price and Mr. Andy Sandaver during the experimentation and characterisation phases of the research.

I would also like to extend my gratitude to my fellow researchers; Dr. Juan Pablo Casas Rodriguez, Dr. Furo Jumbo, Dr. Vikram Shenoy and Mr. Zahid R. Khokhar for their help and friendship throughout the research.

Publications

1. Mubashar, A., I.A. Ashcroft, G.W. Critchlow, and A.D. Crocombe, *Modelling cyclic moisture uptake in an epoxy adhesive.* J. Adhesion, 2009. **85**: p. 711-735.

2. Mubashar, A., I.A. Ashcroft, G.W. Critchlow, and A.D. Crocombe, *Moisture absorption-desorption effects in adhesive joints.* International Journal of Adhesion and Adhesives, 2009. **29**(8): p. 751-760.

3. Mubashar, A., I.A. Ashcroft, G.W. Critchlow, and A.D. Crocombe, *A method of predicting the strength of adhesive joints after cyclic moisture conditioning*. being submitted to International Journal of Adhesion and Adhesives.

4. Mubashar, A., I.A. Ashcroft, G.W. Critchlow, and A.D. Crocombe, *Damage and failure* p*rediction of adhesive joints after cyclic moisture conditioning*. draft being finalised.

5. Mubashar, A., I.A. Ashcroft, G.W. Critchlow, and A.D. Crocomb, *Strength recovery in epoxy adhesive joints under cyclic moisture conditioning environment*. in *Abstract book of 3rd International Conference on Advanced Computational Engineering and Experimenting, ACE-X*. 2009: Rome.

Chapter 1
Introduction

1.1 Background

In this age of rapidly diminishing fossil fuels and cutting edge competition, each company is striving to make its products more and more efficient. The demand for low weight and high performance structures is continuing to increase. This is particularly true in the aerospace and automobile sectors. A vital enabling technology in product design and manufacture is material joining where designers have the options of welding, fastening, riveting, adhesive joining, etc.

Adhesive joints offer several advantages over other methods: the stress is distributed over a wider area in comparison to bolted or riveted joints; different materials can be joined; better fatigue performance; high stiffness; no heat effects on adherends as observed in welding, and; there are special applications where traditional joining methods may not be applicable such as in joining thin and delicate materials. The cost of adhesive joints is also comparable to the traditional joining methods [1-3]. However, adhesive joining is not without its disadvantages. Separation of adhesively joined surfaces is difficult and thus adhesive joints are not preferred for components that need to be regularly changed or serviced. Monitoring of the health of adhesive joints is difficult and field repairs of adhesive joints may require specialised equipment. Adhesives are sensitive to environmental changes and their performance may degrade over time as they are subjected to varying moisture and temperature conditions. However, the advantages of adhesive joining make it an attractive choice and adhesive joints are being increasingly used in structural applications [4-6].

An important aspect in the use of adhesive joints in structural applications is the ability to predict their performance at the design stage. It is extremely important to include environmental factors, such as moisture and temperature in any predictions, as they may significantly decrease the joint strength over time [7]. It is difficult to measure strength degradation of bonded joints during their service life in a structure. Thus, for successful industrial application of adhesive joints, reliable and easy to use methods of predicting service life are required. Such methods would not only provide confidence in the use of adhesives, but would also enable improved joint designs. Presently, the most commonly used method of joint performance determination, under moisture and temperature effects, is physical testing. Physical testing is costly and time consuming, especially when adhesive performance over a long period of time is to be determined. This contradicts the two main drivers of today's industrial environment, namely minimisation of cost and short lead times. The absence of reliable and easily applicable performance prediction methods also discourages optimisation and design improvement studies. Thus a need exists for the development of solutions that can simulate field conditions over a long period of time and predict the performance of adhesive joints over that period. The development of reliable and industrially applicable predictive models will satisfy the need for low cost and time efficient testing methods whilst reducing the amount of physical testing. The predictive model would also provide the opportunity to explore different scenarios which may contribute towards design optimisation.

In recent years, research has been carried out to predict the durability of adhesive joints under different moisture and temperature conditions [8-10]. Most of the present research is based on the use of fixed environmental conditions and considers single moisture uptake. However, in real applications, adhesive joints are likely to be exposed to changing environmental conditions where temperature and moisture will vary with the ambient and operational conditions. The variable conditions make reversibility an important factor that needs to be incorporated in the models to make them useful industrial tools. The reversibility effects are not limited to a single moisture absorption-desorption cycle but take place repeatedly during the life cycle of a joint. This makes the moisture history of the joint a vital

component of the reversibility studies and modelling. A mechanism of incorporating the moisture history and predicting the history dependent moisture characteristics is also required in order to lay the foundation of reliable durability predictions.

The research presented in this thesis aims to develop methodologies and models to predict the moisture diffusion and strength of joints under variable moisture conditions. The complex multi-physics modelling of adhesive joints has only become possible during recent years due to the advent of multi-physics commercial software packages. Material models which can accurately represent the damage initiation and failure in adhesion, such as Cohesive Zone Elements, are now implemented in the most recent versions of many commercial finite element codes. These technological advances lay down a framework for successfully tackling the challenging issues of environmental fatigue. The proposed research is timely and industrially applicable in the context of modern developments in modelling techniques and methods. This is of significance for all industrial sectors including aerospace, defence, automobile, marine and electronics. The research provides methods and models that may be adopted to develop tools for designers and engineers for use during the design process. This would reduce the time to manufacture, improve the reliability and durability of products and give manufacturers more confidence in use of adhesive joints, which would also open new avenues for the application of adhesive joining. The study, analysis and modelling of the effects of cyclic environmental fatigue is a novel approach to an area which is, at present, largely ignored.

1.2 Aim and Objectives

The aim of this research is to develop a modelling methodology for the prediction of degradation in adhesive joints subjected to fluctuating environmental service conditions. The following objectives were identified to achieve the overall aim of the research.

- Characterisation of a structural adhesive to determine the moisture dependent diffusion and mechanical properties for use in numerical models.

- Experimental determination of joint durability under cyclic moisture conditions at different temperatures.
- Development and implementation of a cyclic environmental strength prediction methodology for predicting moisture diffusion and joint strength under variable moisture conditions
- Investigation of the failure surfaces, using different techniques, to determine any changes in the failure mode of the joints after moisture conditioning.
- Analysis of moisture diffusion in adhesive joints under cyclic moisture conditions at different temperatures.
- Investigation of the residual stresses generated in single lap joints due to curing, cyclic moisture diffusion and mechanical loading.
- Investigation of damage and failure in joints when conditioned under cyclic moisture conditions.

1.3 Research Methodology

A schematic of the overall research methodology is given in Figure 1.1. The research is comprised of an experimental and a finite element modelling part. Experimentation was carried out to characterise the history dependent diffusion and mechanical properties of the adhesive and to observe the effects of moisture diffusion on adhesive joint durability. Bulk adhesive samples were conditioned for multiple cycles of absorption and desorption at 50 and 70°C in water. Tensile testing of bulk adhesive samples was carried out to determine the effect of moisture on adhesive strength. Adhesive joints were prepared with two types of pretreatment; ACDC anodising and chromic acid anodising. The joints were conditioned at 50 and 70°C in water for single and multiple absorption and desorption cycles. Tensile testing of the joints was carried out for various time intervals. The failure surfaces of the joints were examined using scanning electron microscopy (SEM) and X-ray photoelectron spectroscopy (XPS) to determine the mode of failure. The experimental results were used in the development of the predictive models and in their validation.

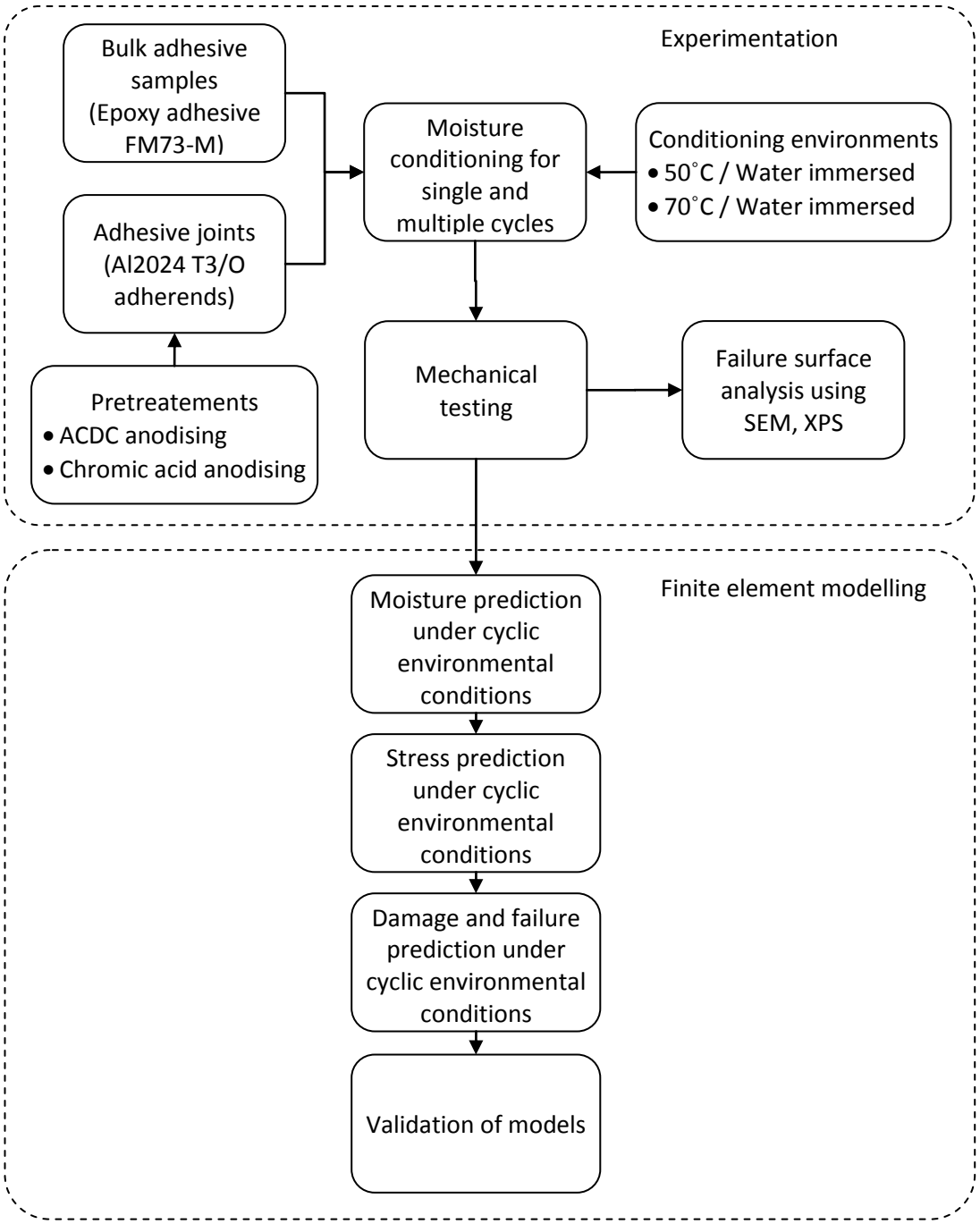

Figure 1.1: Overall research methodology.

For the predictive modelling of joint durability, a novel methodology for predicting cyclic moisture diffusion has been developed, that is applicable under variable environmental conditions. This methodology provides understanding and estimates of moisture concentration in an adhesive joint at any time during its service life. The cyclic moisture diffusion methodology was coupled with stress based methods

to determine stress development in adhesive joints under cyclic environmental conditions. In order to predict damage and failure of the joints, a cohesive zone model (CZM) was coupled with the cyclic moisture diffusion and stress based models and strength of joints, as a function of ageing was predicted. The modelling results were validated by comparison with experimental data.

1.4 Thesis structure

A brief description of the contents of the remaining chapters of the thesis is given below.

Chapter 2 Literature Reveiw. This chapter provides a review of the literature to identify the relevant previous research. The chapter is divided into two main parts. Mechanisms of moisture diffusion, its effects on adhesives and adhesives joints and testing methods for adhesive joints are summarised in the first part. The second part deals with the modelling of moisture diffusion.

Chapter 3 Experimental Methods. Details of the materials, joints types, experimental plan and experimental methods are provided in this chapter. The chapter also details the methods used for failure surface characterisation.

Chapter 4 Experimental Results. Results from the experimental programme are provided in this chapter. A comparison of analytical moisture diffusion models and experimental moisture uptake data is carried out in order to select suitable analytical model for later use in the finite element analysis.

Chapter 5 Finite Element Modelling Methods. This chapter provides details of the finite element modelling methods used in the project. The geometry, boundary conditions, meshing methodology, element choice, mesh convergence and thermal and diffusion analysis details are provided.

Chapter 6 Moisture Diffusion in Cyclic Environmental Conditions. A methodology for the prediction of moisture diffusion under cyclic moisture conditions is presented in this chapter. Model development and its verification procedures are discussed. A case study to investigate the difference between the proposed methodology and commonly used modelling methods ignoring history effects is also

included. The proposed methodology is than used to determine moisture diffusion in single lap joints, conditioned under cyclic environmental conditions.

Chapter 7 Stress Prediction in Cyclic Environmental Conditions. The cyclic moisture prediction methodology is coupled with mechanical analysis and stresses in single lap joints are investigated in this chapter. Hygrothermal residual stresses, due to curing and moisture induced swelling were considered, in addition to load induced stresses in the mechanical analysis.

Chapter 8 Damage and Failure Predictions in Adhesive Joints. Damage and failure of single lap joints is investigated in this chapter by combining the cyclic moisture prediction method with cohesive zone modelling. The behaviour of joints conditioned under different environments is discussed.

Chapter 9 Discussion. This chapter presents a discussion of the experimental results and the modelling methodologies presented in previous chapters.

Chapter 10 Conclusions and Future Work. The conclusions of the research along with proposals for future work are presented in this chapter.

Chapter 2
Literature Review

2.1 Introduction

Durability of adhesive joints is a primary consideration due to their known sensitivity to environmental conditions, particularly combinations of high temperature, humidity and stress [4, 11-21]. An adhesively bonded joint may be manufactured using a variety of adherends, including; metals, composites and polymers, where each material has its own unique response to environmental factors. Various environmental factors affect the durability of polymers, such as; temperature, moisture and ultra-violet radiation. The two major factors influencing the strength of adhesive joints are temperature and moisture. The effect of temperature may be observed in the form of variations in the mechanical properties of an adhesive [22]. Temperature variations may also affect the moisture diffusion rate through an adhesive. Moisture diffusion in an adhesive affects the strength of the adhesive, where the degradation in adhesive strength may be reversible or irreversible. Examples of degradation in joint strength after moisture diffusion are shown in Figure 2.1. In an adhesive joint, the adhesive-adherend interface may also degrade in strength, in addition to the adhesive strength degradation. Interface strength degradation may occur owing to debonding by moisture ingress, corrosion or weakening of material in the interphase. Characterisation of the long term response of adhesives and adhesive joints to moisture diffusion and an understanding of the underlying failure mechanisms, such as; plasticisation, swelling, micro-cracking and modification of the chemical structure are important to develop methods for predicting joint durability.

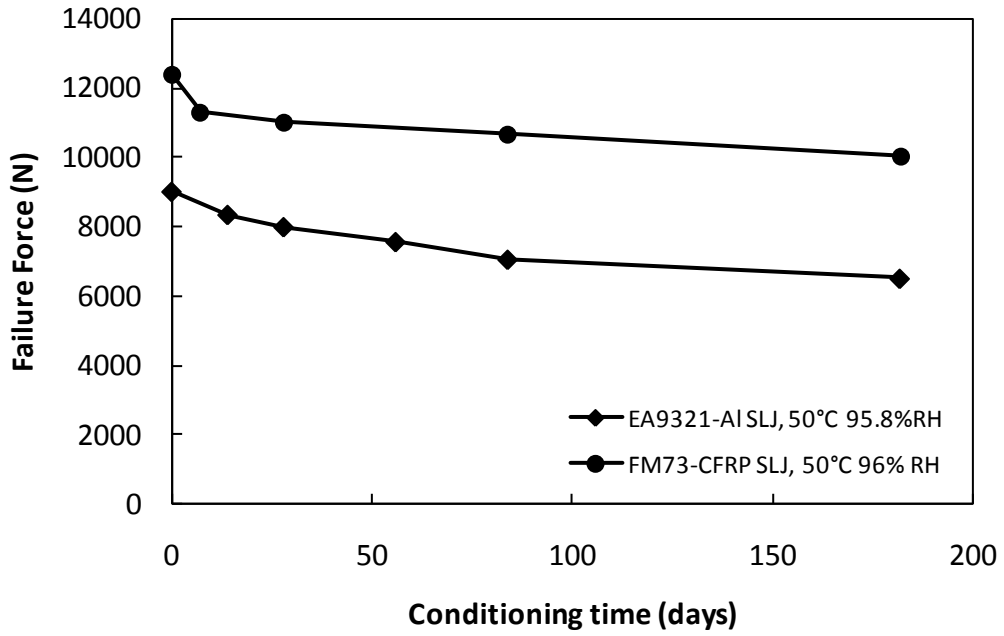

Figure 2.1: Examples of degradation in joint strength after moisture absorption (♦) aluminium-epoxy joints [7] (•) composite-epoxy joints [23].

This chapter presents a literature review of the effects of moisture on adhesives and adhesive joints along with methods used for modelling adhesive joint durability. The chapter starts with a discussion of moisture diffusion and its effects on epoxide adhesives. Moisture diffusion under cyclic environmental conditions is discussed as joints may experience environmental variations during their service life. The testing methods used for determining joint strength and the effect of moisture diffusion on adhesive joint durability are reviewed. The later part of the chapter reviews the modelling of moisture diffusion and presents a comparison of different moisture diffusion models. This is followed by a discussion of joint durability modelling methodologies and their use in modelling the environmental degradation of adhesive joints.

2.2 Moisture Diffusion in Adhesive Joints

Structural epoxy adhesives have a natural tendency to absorb water as the epoxy based adhesives have hydroxyl (OH) groups in their molecular structure, which attract water molecules and form hydrogen bonds [12, 24]. The ingress of moisture

in adhesive occurs by diffusion, which is the transportation of matter by random molecular motion. Diffusion is a concentration gradient based process and removes the chemical potential differences in an adhesive by progressing towards a state of equilibrium.

A polymer resin consists of occupied volume and free volume [24]. Free volume may be defined as the difference between the volume at a given temperature and volume at 0 K. The free volume exists in a polymer due to gaps between the polymer chains and depends on the density and physical state of the polymer. The diffusion of water in a polymer depends on the available free volume within the polymer as a higher free volume results in a higher capacity for the absorption of water. It allows for higher moisture ingress in polymers by diffusion as it provides more passages for diffusing particles [25, 26]. It has also been suggested that during initial moisture uptake, the moisture enters the free volume of the polymer, which does not cause swelling of the polymer [24]. During later stages, when most of the free volume is filled, the absorbed moisture distorts the polymer network and causes swelling. As the polymer swells, additional free volume may become available for diffused water.

Carter and Kibler [27] suggested that water in a polymer can exist in free or bound states. If there are chemical reactions between the polymer and the water, the water becomes attached to the polymer and is not free to move, whereas, the water present in the free volume of the polymer is free to move. A Langmuir type model was suggested by Carter and Kibler to predict moisture concentration based on the probability that bound water may be released and the probability that free water may become bound. This mechanism has been used to explain moisture diffusion by several researchers [28-31].

Water ingress in a joint may occur by diffusion through the bulk adhesive or through the interface region. Cracks in the adhesive may also absorb water by capillary action and permeable adherends, such as polymer matrix composites, also provide diffusion paths in the joint. It has been reported that the rate of diffusion, when measured in the bulk adhesive, is much less than the diffusion rate of the same adhesive in bonded joints [15, 32-34], which may be attributed to higher

diffusion through the interface region. However, by using high quality surface preparation methods such as anodising, interfacial diffusion can be minimised and its effects become negligible [4].

Moisture diffusion in adhesives is generally described by Fick's law, which is based on the assumption that the rate of transfer of diffusion substance through a unit area of a section is proportional to the concentration gradient, as given in Equation (2.1).

$$F = -D\frac{\partial C}{\partial x} \tag{2.1}$$

where F is the diffusion flux, D is the diffusion coefficient, C is the concentration of diffusing substance and x is the spatial coordinate. The equation has a negative sign as diffusion occurs in the opposite direction to increasing concentration. Typical diffusion coefficient values for epoxy adhesive are of the order of 1 x 10^{-13} m^2/s [14, 35, 36]. The maximum amount of moisture that can be absorbed by a volume is known as the saturated moisture content, M_∞. The diffusion coefficient and saturated moisture content are commonly used to define the moisture diffusion characteristics of polymers.

Moisture uptake in adhesives has been measured using several methods. The most commonly used methods are based on gravimetric measurements in which the changes in mass of samples subjected to moist conditions at a given temperature are measured [37]. Other methods, such as spectroscopy and dielectric measurements, have also been used for measuring moisture uptake [38-48].

2.3 Factors Affecting Moisture Diffusion

Moisture diffusion in polymers is affected by a number of factors, such as; conditioning temperature, environmental humidity and additives in polymers. The effect of these factors may be characterised in terms of changes in the diffusion coefficient and saturated moisture content.

An increase in diffusion coefficient has been observed with increase in temperature [49-51], as diffusion is a thermally activated process. This has been used to

accelerate the ageing of adhesives under laboratory conditions, where samples are subjected to humid environments at high temperatures. The temperature dependence of water uptake in an epoxy adhesive, at different temperatures, was studied by Gledhill et al [50]. Cast sheets of adhesive of 0.7-1.3 mm thickness were conditioned in water at 20, 40, 60 and 90°C and moisture uptake was measured by a gravimetric method. The diffusion coefficients measured from the experimental data showed an increase from 2.43 x 10^{-11} m^2/s to 60.7 x 10^{-11} m^2/s when the conditioning temperature increased from 20°C to 90°C, thus showing an increase in diffusion coefficient with increasing conditioning temperature. Duncan et al [52] obtained the diffusion coefficient of an epoxy adhesive by measuring the moisture uptake of 1 mm thick samples conditioned at 4, 23, 44 and 64°C in deionised water. It was seen that the diffusion coefficient increased from 1.26 x 10^{-14} m^2/s at 4°C to 3.23 x 10^{-12} at 64°C. Similar results were reported by Wright [49] after observing the effects of conditioning temperature on the diffusion coefficients of three epoxy adhesives. It has been suggested [53, 54] that dependence of diffusion coefficient on temperature often follows Arrhenius relationship given by:

$$D = D_o \exp(-\frac{Q}{RT}) \tag{2.2}$$

where Q is the activation energy for diffusion, R is the universal gas constant and T is temperature.

Saturated moisture content has also been shown to increase with increase in conditioning temperature. The mobility of molecular chains increases with an increase in temperature, resulting in reduced density owing to thermal expansion. This increases the free volume of the polymer, thus increasing the saturated moisture content [55].

Relative humidity (RH) of the conditioning environment is another major factor affecting moisture diffusion [49, 56]. The nature of an adhesive is important in considering the effect of environmental humidity. Hydrophobic polymers absorb relatively low amounts of water and the diffusion coefficient is generally independent of moisture concentration while hydrophilic polymers mostly have moisture concentration dependent diffusion coefficients. Moisture uptake of an

epoxy based adhesive was measured by Brewis et al [14] using thin films of adhesive. The results of the moisture uptake at 50°C showed a progressive increase in the diffusion coefficient with increase in relative humidity as diffusion coefficient changed from 7.2 x 10^{-13} m^2/s at 23% RH to 14 x 10^{-13} m^2/s at 100% RH. Increase in the saturated moisture content with increase in environmental humidity was also reported as saturated moisture content increased from 0.54 wt% to 2.1 wt% with change in conditioning environment from 23% RH to 100% RH. Increase in saturated moisture content with increase in conditioning environment humidity has also been reported in [49, 57]. In some cases, increase in saturated moisture content with increase in relative humidity follows Henry's law, which states that solubility is directly proportional to external gas pressure [55].

Structural adhesives may be considered as composite materials since they include various additives to improve their characteristics. The amount of hardener in an epoxide adhesive affects the saturated moisture concentration. Brewis et al [56] studied the effect of hardener rich and depleted adhesive films of DGEBA and observed an increase in the hardener resulted in an increase in the saturated moisture content of the adhesive. This was attributed to the introduction of more hydrophilic groups by the hardener in the matrix. Another factor affecting the moisture diffusion in an adhesive may be the presence of a carrier as the carrier may increase the moisture diffusion by capillary action. However, deleterious effects on durability, owing to the presence of carrier, are not always observed. Brewis et al [58] studied the effect of nylon and polyester carriers on durability of metal adhesive joints using a modified epoxy adhesive and reported that a slight decrease in the strength of unconditioned joints was observed while the strength of the conditioned joints remained unaffected.

2.4 Effects of Moisture Diffusion

Water may cause several changes in the structure of an adhesive including; plasticisation, increased free volume due to swelling [59], micro-cracking or crazing [60], chain scission [61], leaching of material [40] and chemical reaction of water with the polymer. It has been suggested [13, 14, 50, 62] that a critical concentration

of water exists and adhesive properties are only affected once the critical moisture concentration has been achieved, however, this has not been observed for all adherend/adhesive systems [4, 63]. The effects of moisture, on the adhesive, may be reversible, such as those brought about by plasticisation, or irreversible [64].

The effect of moisture diffusion in an adhesive may be observed in the form of changes in the mechanical properties. The elastic modulus and yield strength of an adhesive decrease with an increase in absorbed moisture [14, 20]. The failure stress of the adhesive also decreases with increasing amount of moisture. Loh et al [65] determined the moisture dependent mechanical properties of a one part rubber toughened epoxy adhesive when conditioned at three different environments; 81.2% RH, 95.8% RH and water immersion. Bulk adhesive specimens of 0.4 and 0.8 mm thickness were environmentally conditioned. Stress strain curves from tensile testing of the bulk adhesive specimens showed a decrease of 38% in elastic modulus and 52.3% in ultimate tensile stress with increase of 7.6 wt% in moisture content. A progressive loss of strength in an aluminium filled epoxy adhesive, with increasing exposure to moisture, was reported by Bowditch [13] and a combination of plasticisation and hydration at the interface of the filler particles and epoxy was considered responsible for the decrease in failure stress of the adhesive.

Decrease in fracture toughness of an adhesive, with increasing conditioning time, has also been reported [63, 66]. The change in the fracture energy of an epoxy based adhesive, due to moisture ingress, was studied by Liljedahl et al [23] using mixed mode flexure (MMF) specimens. The specimens were conditioned to saturation at 80% RH and 96% RH. A progressive decrease in the fracture energy of the adhesive was observed with increasing moisture content. Hand et al [66] also observed a decrease in the fracture toughness of an epoxy adhesive after conditioning. The decrease in fracture toughness may be attributed to the plasticisation effect of the moisture.

In addition to degradation in mechanical properties, moisture has also been observed to lower the glass transition temperature [20, 56] of an adhesive. The plasticising effect of water makes it easier for molecular conformation to occur and thus lowers the glass transition temperature of the adhesive [67]. It has been

suggested that for a 1% increase in water content, there may be a drop of up to 20°C in the glass transition temperature [49].

The absorption of moisture in an adhesive joint affects the adhesion and durability of the joint, which is discussed in Section 2.7.

2.5 Cyclic Moisture Diffusion

Adhesives may be exposed to varying humidity conditions during their service life. When an adhesive is subjected to cyclic moisture uptake, a change in diffusion properties may occur during the absorption-desorption cycles, which may cause reversible and irreversible changes in the structure of the adhesive. The mechanisms of moisture interaction with an adhesive were discussed in Section 2.4 and typical moisture cycling profiles are shown in Figure 2.2. The effects of cyclic moisture diffusion may be observed in the form of changes in diffusion coefficient and saturated moisture content, occurring over absorption and desorption cycles.

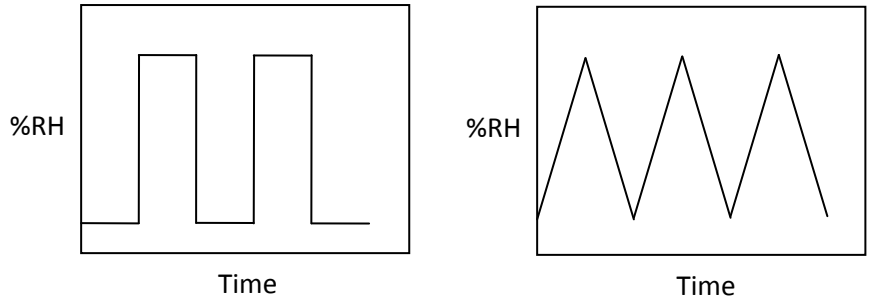

Figure 2.2: Typical moisture cycling profiles.

The diffusion coefficient of an adhesive has been observed to increase progressively after each moisture absorption cycle when subjected to multiple cycles of moisture absorption. The changes in the diffusion coefficient of a DGEBA/DDA epoxy system were studied by Lin and Chen [59]. The epoxy was conditioned for absorption, desorption and absorption cycles at 85°C and 85% RH. The moisture diffusion during the second absorption cycle was faster than the first absorption cycle. Bao et al [68] conditioned a bismaleimide resin for three absorption cycles at 70°C in water. The rate of diffusion increased consistently after each absorption cycle and it was

concluded that the moisture diffusion properties were moisture history dependent. It has also been reported that the moisture diffusion coefficient during moisture desorption is faster than the preceding moisture absorption [59]. A change in diffusion coefficient over multiple moisture diffusion cycles indicates a change in the polymer network with hygrothermal ageing. The increase in diffusion coefficient may be owing to the increase in the polymer free volume by hygroscopic swelling. The increased free volume decreases the restrictions to free molecular movement. The re-absorption cycles may be considered the continuation of the first absorption cycle, with the structural relaxation resuming when the water is reintroduced in the re-absorption cycles [68, 69].

The saturated moisture content of a polymer has also been shown to be moisture history dependent. A progressive increase in saturated moisture content, with each absorption cycle, has been reported in a number of studies [49, 56, 59]. Lin and Chen [59] reported an increase of 1.7% in saturated moisture content after an absorption, desorption and re-absorption cycle and Brewis et al [15] observed an increase of 9.9% over five absorption and desorption cycles in an epoxy adhesive. Any increase in moisture content on cycling may be owing to the increased free volume by swelling and new sorption sites produced by micro-cracking. In polymers having non-Fickian moisture absorption, the moisture absorption cycles have been reported to show increasingly Fickian absorption behaviour with increasing number of moisture absorption cycles. This indicates the replacement of a slow relaxation controlled moisture diffusion process with a rapid Fickian diffusion process [69].

When an adhesive is subjected to multiple cycles of absorption and desorption, a moisture history dependence in its mechanical properties is also observed [56, 59]. The moisture history dependence of a DGEBA/DDA epoxy polymer was investigated by Lin and Chen [59] who subjected the polymer to cycles of absorption, desorption and absorption. The tensile strength and the elastic modulus of the polymer decreased by 29.5% and 29.1% respectively, after the first moisture absorption cycle. When the samples were dried, the strength and the elastic modulus recovered to at least 90% of the unconditioned values. After the second moisture absorption cycle, the reduction in the tensile strength and the elastic modulus, as

compared to unconditioned samples, was 42.6% and 54% respectively, which was significantly greater than the reduction after the first moisture absorption cycle. Plasticisation of the adhesive was proposed as the main reason for the observed degradation in the mechanical properties of the adhesive. As plasticisation is considered, potentially reversible [64], a large recovery in the elastic modulus and the tensile strength was observed after drying. However, after the desorption cycle, elastic modulus and tensile strength did not return to the levels measured in the unconditioned state. This suggested that irreversible mechanisms were present, in addition to reversible mechanisms, during the moisture absorption. Moisture can affect adhesives in an irreversible manner by causing chemical degradation, chain scission and micro-cracking [64].

2.6 Testing Methods for Adhesive Joints

Testing methods for adhesively bonded joints may be classified according to the end requirements, which include; prediction of adhesive strength, investigation of the effect of different pretreatments or determination of the shelf-life of material. Test methods for determining joint strength and durability are discussed in this section. These test methods may be further classified as strength of materials methods, which may be used to measure stress and fracture mechanics tests for the determination of fracture energy.

For the determination of joint durability, lap joints are commonly used to study the effect of environmental ageing on joint strength owing to their ease of manufacture and testing [70-72]. They also provide a good representation of industrial joints. A number of lap joint configurations have been used [73], the most common being the single lap and double lap joints, as shown in Figure 2.3. Recommendations for manufacturing single lap joints are provided in BS ISO 4587:2003 [74].

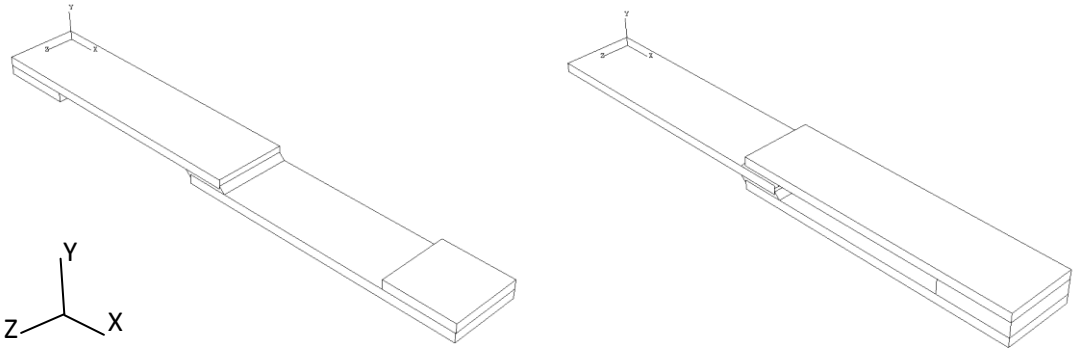

(a) (b)

Figure 2.3: Configuration of (a) single lap and (b) double lap joint.

Non-collinear forces act on a single lap joint under tensile loading and the resultant moments causes the adherends to bend, as can be seen in Figure 2.4 [75]. The lap joints develop a complex state of stress when loaded in tension. Peel forces at the end of the overlap ends result in peel stresses in Y direction. In plane shear forces give rise to shear stresses in XY plane and out of plane shear force in Z direction results in shear stresses, which are found due to lateral shrinking of the adherends. Several geometric and material factors govern the strength of a lap joint including; adherend and bondline thickness, joint width, adherend surface treatment and curing time.

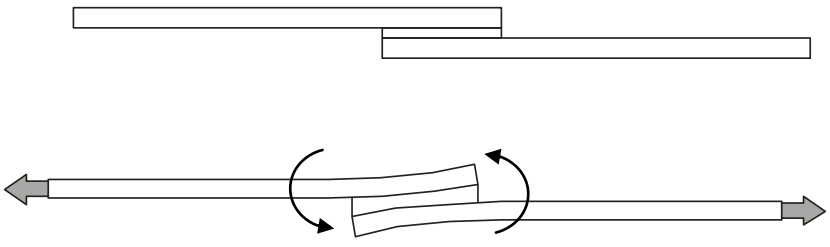

Figure 2.4: Bending moment after application of load in a single lap joint.

Peel joint tests are used to obtain a measure of adhesive peel strength. A number of standards are available for the peel testing of adhesives including; BS5350-C13:1990

[76], BS EN 1464:1995 [77], BS EN 28510-1:1993 [78] and BS EN 28510-2:1993 [79]. The tests differ in regards to testing requirements and peel angles.

The climbing drum peel test, given in BS5350-C13:1990, uses one rigid and one flexible adherend. The flexible adherend is wrapped around a drum as it peels away from the rigid adherend due to the movement of the drum. The roller peel test described in BS EN 1464:1995 uses a rigid and a relatively flexible adherend. The flexible adherend is bent over a roller and pulled away from the rigid adherend using a constant force. A constant peel angle is maintained during the test. BS EN 28510-1:1993 also describes a peel test for a flexible and rigid adherend, however, in this case the flexible adherend is pulled at 90° to the rigid adherend.

The stress state in a peel joint is complex and difficult to solve. Kaelble [80] provided a solution that gives the stress state of a strip peeled away from a joint. Kaelble assumed that the strip is pivoted about the point where the strip is being peeled off. The equation represents a sine wave decreasing in magnitude with increasing distance in the joint. It shows that the adhesive experiences tensile as well as compressive forces.

The double cantilever beam (DCB) test is used to measure the fracture toughness of adhesive joints. BS 7991:2001 [81] describes the specifications for the DCB specimen and test. An initial crack is introduced at one edge of the DCB specimen, which is comprised of two rigid adherends joined together with adhesive as shown in Figure 2.5. Load is applied to the end with the initial crack by pulling the adherends apart at a constant rate. Data regarding the load, the crack length and the deflection should be recorded during the test. This is then used to calculate critical strain energy release rate as a function of crack length.

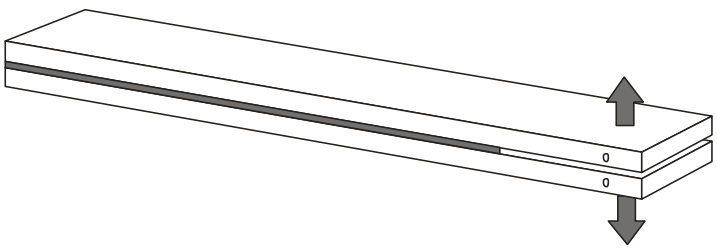

Figure 2.5: Double Cantilever Beam (DCB) configuration

The Boeing wedge test can also be used to measure the fracture strength of an adhesive. The test has been standardised as ASTM D3762. The specimen is prepared in a manner similar to DCB specimen, where two rigid adherends are bonded, leaving an un-bonded area at one end. A wedge is then used to initiate a crack at the un-bonded end as shown in Figure 2.6. The separation of bonded surfaces occurs as the crack releases elastic energy which is denoted by U_E. The strain energy release rate is given by $G = \partial U_E/\partial A$. If the energy required to separate the two surfaces is denoted by U_S then energy required to create a unit surface is give by $W_S = \partial U_S/\partial A$. The crack will stop propagating when $G=W_S$. The test employs mode I fracture conditions, as in the DCB, however, in this case the applied load is not known and beam theory must be used to determine fracture energy based on the applied displacement.

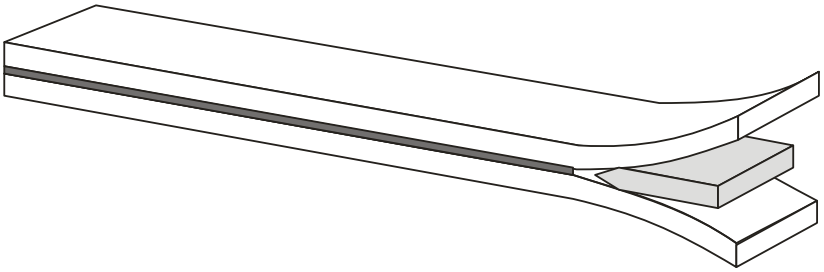

Figure 2.6: Boeing Wedge Test specimen

The wedge test is based on the assumption that the adherends only deform elastically, which is satisfied when thick and stiff adherends are used. It may be difficult to measure the cracks produced during the test and cracks may propagate in an uneven manner resulting in errors in the determination of fracture energy. The test can provide information regarding cohesive or interfacial failure based on the position of the crack. A wedge is forced in the joint to initiate a crack and the joint is then exposed to moisture. Change in crack length is measured and may be used to compare joint durability under different pretreatments.

2.7 Durability of Adhesive Joints

Durability studies of adhesive joints are commonly carried out by accelerated conditioning under extreme environmental conditions. The joints are conditioned at an elevated temperature, chosen to increase the moisture diffusion rate whilst, hopefully, not introducing non-representative behaviour. The joints are tested at selected time intervals to determine their strength. Many of these durability studies show a decrease in adhesive joint strength with increasing moisture absorption. The change in the strength of aluminium-epoxy adhesive joints subjected to deionised and salt water at 65°C was reported by Doyle and Pethrick [28]. A progressive decrease in the shear strength of the joints with ageing time was observed. The initial fracture of the adhesive was cohesive. This changed to a mixed failure mode after 300 days of conditioning. A decrease in joint strength with increasing exposure time was also reported by Hua et al [7] when aluminium single lap joints manufactured using a two-part epoxy adhesive were conditioned at 50°C, 95.8% RH. The failure surface was primarily cohesive, in the adhesive layer and close to the interface. The decrease in joint strength may be owing to a combination of adhesive layer and interface strength degradation mechanisms. Adhesive degradation mechanisms were discussed in Section 2.4 and interface degradation is discussed later in this section.

In contradiction to the results cited above, increases in the joint strength after moisture conditioning have also been reported by some researchers [4, 82]. In some cases, the joint strength has been observed to increase with moisture absorption and pass through a maximum value before it starts to fall off [4]. It has been suggested that this was owing to a competition between stress relief and strength degradation mechanisms. The two processes occur simultaneously but during the initial phase, the stress relief process dominates the overall behaviour of the joint and strength improvement is observed owing to a decrease in curing stresses or more favourable stress distribution. At later stages, plasticisation degrades the strength of the adhesives sufficiently that the benefits of stress relief are lost and the strength of the joint starts to degrade [13].

Recovery of strength has been observed after drying adhesive joints that had previously undergone strength degradation after moisture conditioning. The recovery of joint strength depends on the nature of the damage mechanisms. Orman and Kerr [83] conditioned aluminium epoxy joints at 5% RH and 100% RH. When the joints were dried after conditioning, most of the original strength was recovered. The large recovery may be due to the reversible effects of plasticisation of the adhesive. The irreversible mechanisms of disruption of the bonds at the interface and micro-cracking in the adhesive layer may be responsible for irrecoverable joint strength.

Durability studies of adhesive joints show that the adherend-adhesive interface is important for good joint durability. With metallic adherends, adhesive joints have a complex adhesive-adherend interphase, which is composed of thin layers of oxide and primer, surrounded by the adhesive and the metal. One commonly observed effect of moisture ingress is a change in the failure locus for adhesive joints. Failure in high strength, unconditioned joints generally occurs in the adhesive layer and is known as cohesive failure [28]. However, as moisture is absorbed by the adhesive layer, the failure locus moves from adhesive layer to the adhesive-adherend interface and apparent interfacial failure is observed [84]. The failure surface in an apparent interfacial failure may pass through layers of adhesive, primer, oxide and metal. A typical interface of anodised aluminium adherends and epoxy adhesive is schematically shown in Figure 2.7 along with cohesive and interfacial failures.

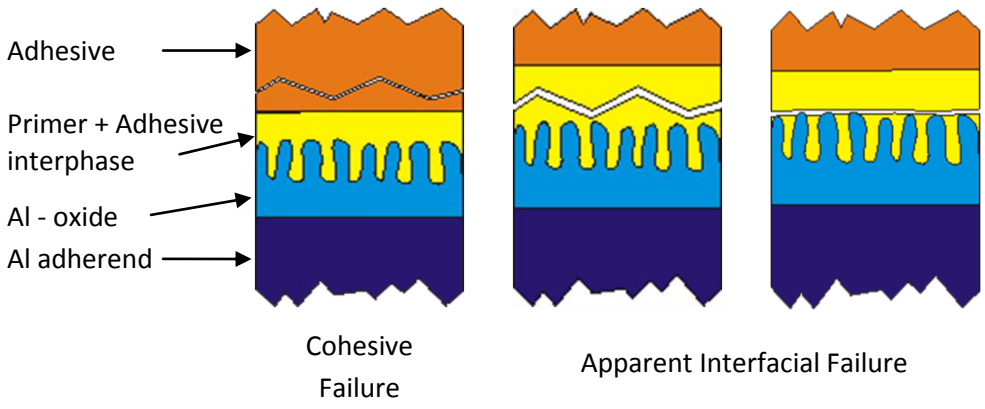

Figure 2.7: A representation of anodised aluminium adherend and epoxy adhesive interface and failure modes.

For metal adherends, an important consideration is the stability of the oxide layer and the adhesive-adherend interface in the presence of moisture. Hydration of the oxide layer may be caused by moisture ingress and resultant weakening of the oxide layer may occur. Electro-chemical corrosion of the adherends may also occur that would result in corrosion oxide products that have little or no cohesive strength and may cause failure in the interfacial region. Another mechanism of attack on the oxide layer is cathodic delamination where hydroxyl ions generated as a result of the electro-chemical corrosion may increase the hydrolysis of the bonds at the interface or attack the primer-adhesive interphase [4].

The surfaces of metallic adherends are generally pretreated to achieve a stable interface that will resist moisture ingress. The effect of different pretreatments on the joint durability was explored by Comrie et al [85]. The strength of the joints decreased with ageing time and differences in the retained strength were observed with different pretreatments. Wahab et al [33] studied the durability of single lap and butt joints after exposing them to water at 60°C. The joints were pretreated using grit blasting and grit blasting + silane pretreatments. The strength of the butt joints decreased with conditioning time. The grit blasted single lap joints showed an initial decrease in the strength before the strength started to recover. This was followed by another reduction in the strength. On the other hand, the grit blast + silane treated single lap joints showed an initial increase in joint strength, which was followed by a reduction in the strength. However, the strength never decreased below the unconditioned strength. The rate of degradation in butt joints was faster than in the single lap joints.

Kinloch and co-workers [50, 86] used the thermodynamic work of adhesion to assess the stability of an interface; where the work of adhesion is the energy required to separate unit areas of two phases forming an interface. For an adhesive-adherend interface, the work of adhesion is positive under dry conditions, inferring that the interface is stable. The presence of moisture at the interface can make the work of adhesion negative and, hence, provides a driving force for debonding by the rupture of secondary forces, e.g. van der Waals forces, by displacing the adhesive on the oxide layer by the diffused water or by hydrolysis of interfacial covalent

bonds [50]. However, this theory does not account for mechanical interlocking and the effect of primary and secondary interfacial forces. Also complete displacement of the adhesive at an interface by water is difficult in metallic adherends with anodised pretreatment, which produces a highly porous surface. The flow of primer in the surface pores creates a material interphase with a high degree of mechanical interlocking.

2.8 Summary of Moisture Diffusion in Adhesive Joints

Structural adhesives absorb moisture when exposed to humidity. The structure of an epoxy adhesive consists of filled and free volume. The moisture in an adhesive may exist in free and bound states and the diffusion of moisture in an adhesive may be described by Fick's law of diffusion. The diffusion coefficient and saturated moisture content of an adhesive may be regarded as characteristics of the adhesive. Gravimetric moisture uptake is commonly used to measure the moisture diffusion in an adhesive.

The diffusion coefficient and saturated moisture content are affected by the conditioning temperature and environmental humidity. The absorbed moisture may affect the adhesive in a number of ways such as; plasticisation, swelling, micro-cracking, crazing and chain scission. The mechanisms may be reversible or irreversible. The diffusion properties may also exhibit moisture history dependence when the adhesive is subjected to cyclic moisture conditioning. The history dependence is observed in the form of increases in the diffusion coefficient and saturated moisture content with each absorption cycle. The durability of conditioned adhesive joints may be determined by a number of testing methods including; lap joints, peel joints, double cantilever joints and the Boeing wedge test. Durability studies of adhesive joints have shown changes in strength with ageing where both increases and decreases in joint strength have been observed with increasing moisture content. In joints with strength degradation after the moisture conditioning, drying of the joint was seen to recover most of the joint strength. Adhesive-adherend interface stability is important in the durability study of a joint

and different pretreatments provide different level of protection against moisture ingress.

2.9 Modelling Moisture Diffusion

The prediction of moisture diffusion provides the moisture concentration distribution in an adhesive, which is required for determining the joint strength after conditioning. The mathematical description of diffusion was presented by Fick by adopting the mathematical equation of heat diffusion and is generally referred to as Fickian diffusion. However, some polymers also exhibit non-Fickian diffusion behaviour. Thus the moisture diffusion in an adhesive may be classified on the basis of observed diffusion behaviour as follows [87].

Fickian Diffusion - Case I: The diffusion behaviour of a polymer is Fickian if the diffusion rate is much less than the relaxation rate.

Non-Fickian Diffusion - Case II: This occurs when the diffusion rate is much higher than the relaxation rate.

Anomalous Diffusion – Case III: Anomalous diffusion takes place when the diffusion rate and relaxation rate are close to each other.

Several models for predicting moisture diffusion in a polymer have been presented in the literature. These may be classified based on the type of moisture diffusion or the mechanism governing moisture diffusion. The models also differ in the number of required parameters and ease of application. A discussion of moisture diffusion models based on diffusion type and diffusion processes is provided in the following sections.

2.9.1 Fickian Diffusion

Fick's law of diffusion was introduced in Section 2.2. Fick's first law relates the diffusion flux through a unit area to concentration gradient through a diffusion coefficient and is given by Equation (2.1). Fick's second law of diffusion describes

diffusion in a non-steady state and for diffusion in three dimensional space, it is given by Equation (2.3).

$$\frac{\partial C}{\partial t} = D\left(\frac{\partial^2 C}{\partial x^2} + \frac{\partial^2 C}{\partial y^2} + \frac{\partial^2 C}{\partial z^2}\right) \tag{2.3}$$

where t is time and x, y and z are spatial coordinates. Fickian diffusion results in a large gradient of moisture and hence, rapid diffusion, in the polymer during the initial stages of diffusion with moisture concentration decreasing exponentially from the area of high concentration to the centre of the polymer. The diffusion distance is proportional to the square root of diffusion time [25].

The solution of Fick's law for a plane sheet of thickness $2l$ was provided by Crank [87] and can be used to find the concentration in the sheet in temporal and spatial coordinates. The solution, as given in Equation (2.4), is based on the assumption that the region is initially at a uniform concentration and the surfaces of the region are assumed to be exposed to a constant moisture concentration.

$$C_t = \left(1 - \frac{4}{\pi}\sum_{n=0}^{\infty}\frac{(-1)^n}{2n+1} e^{\frac{-D(2n+1)^2\pi^2 t}{4l^2}} \cos\frac{(2n+1)\pi x}{2l}\right) \times C_\infty \tag{2.4}$$

where C_t is the moisture concentration at any time interval t and C_∞ is the saturated moisture concentration. The mass of diffused substance at any time, t, can be determined by Equation (2.5).

$$M_t = \left(1 - \frac{8}{\pi^2}\sum_{n=0}^{\infty}\frac{1}{(2n+1)^2} e^{\frac{-D(2n+1)^2\pi^2 t}{4l^2}}\right) \times M_\infty \tag{2.5}$$

where M_t is the mass uptake at any time interval t and M_∞ is the saturated mass uptake. Fickian diffusion is generally observed when the conditioning temperature is above the glass transition temperature of a polymer. The soft state of the polymer allows for easier diffusion of the absorbing substance. However, Fickian diffusion has also been observed after the addition of plasticizers to a polymer when conditioning below the glass transition temperature [25].

2.9.2 Dual Sorption Models

Dual sorption models can be used to predict non-Fickian moisture diffusion and are based on the mechanisms of free moisture absorption and chemical interaction between moisture and polymer matrix [88-90]. A two phase theory is used to define the non-Fickian diffusion mechanisms where water is assumed to be present in free and bound states. Free water molecules are free to move and may readily diffuse in the polymer. On the other hand, bound water molecules are attached to the polymer matrix and are not able to more freely unless they break free. Diffusion models based on this two phase theory have been presented by Carter and Kibler [27] and Gurtin and Yatomi [89]. The Carter and Kibler model, as given in Equation (2.6), includes parameters γ and β to define the probabilities of a free water molecule becoming bound or a bound molecule becoming free, respectively.

$$\frac{M_t}{M_\infty} = 1 - \frac{\gamma}{\gamma+\beta} e^{-\beta t} - \frac{8\beta}{\pi^2(\gamma+\beta)} \sum_0^\infty \frac{1}{(2n+1)^2} e^{-K(2n+1)^2 t} \tag{2.6}$$

where $K = \pi^2 D / l^2$. A constant diffusion coefficient is assumed and good prediction of non-Fickian diffusion in epoxy adhesives, as well as composites, has been reported [30, 91].

2.9.3 Dual Fickian Model

The dual Fickian model is based on the observation that in some polymers, the diffusion rate changes after an initial diffusion period and is able to predict non-Fickian moisture uptake [10, 65, 92]. The dual Fickian model consists of two stages of Fickian diffusion. The two Fickian diffusion processes are considered to be working in parallel, where the concentration at any point in the polymer may be determined by:

$$C_t = \left(1 - \frac{4}{\pi}\sum_{n=0}^{\infty} \frac{(-1)^n}{2n+1} e^{\frac{-D_1(2n+1)^2\pi^2 t}{4l^2}} \cos\frac{(2n+1)\pi x}{2l}\right) \times C_{1\infty} + \left(1 - \frac{4}{\pi}\sum_{n=0}^{\infty} \frac{(-1)^n}{2n+1} e^{\frac{-D_2(2n+1)^2\pi^2 t}{4l^2}} \cos\frac{(2n+1)\pi x}{2l}\right) \times C_{2\infty} \tag{2.7}$$

where $C_{1\infty}$ and $C_{2\infty}$ are fractions of saturated concentration C_∞, D_1 and D_2 are the diffusion coefficients and $2l$ is the length of the diffusion path. The mass uptake for the dual Fickian model at any time, t, is given by:

$$M_t = \left(1 - \frac{8}{\pi^2}\sum_{n=0}^{\infty}\frac{1}{(2n+1)^2}e^{\frac{-D_1(2n+1)^2\pi^2 t}{4l^2}}\right)\times M_{1\infty} + \left(1 - \frac{8}{\pi^2}\sum_{n=0}^{\infty}\frac{1}{(2n+1)^2}e^{\frac{-D_2(2n+1)^2\pi^2 t}{4l^2}}\right)\times M_{2\infty} \quad (2.8)$$

where $M_{1\infty}$ and $M_{2\infty}$ are fractions of saturated mass uptake M_∞. The dual Fickian model parameters may be determined by curve fitting to experimental moisture uptake data.

2.9.4 Diffusion Relaxation Models

These models may be used for the prediction of non-Fickian and anomalous moisture uptake [93-96]. A model based on the assumption that moisture uptake is governed by both diffusion and relaxation processes was presented by Berens and Hopfenberg [97]. The initial phase of diffusion in a polymer was considered to be controlled by a rapid Fickian type diffusion process while the relaxation was responsible for the later phase of diffusion. The relaxation process in a polymer was related to the slow distribution of free volume in the polymer by the motion of polymer chains in the network. The relaxation process was modelled by using relaxation terms where one or two such terms were considered sufficient to predict the non-Fickian moisture uptake of a polymer. The diffusion and relaxation were combined in a single model by adding the relaxation terms to a Fickian diffusion model, as given below.

$$M_t = \left(1 - \frac{8}{\pi^2}\sum_{n=0}^{\infty}\frac{1}{(2n+1)^2}e^{\frac{-D(2n+1)^2\pi^2 t}{4l^2}}\right)\times M_\infty + \sum_i M_{R\infty,i}[1 - e^{-\Omega_i t}] \quad (2.9)$$

where $M_{R\infty,i}$ is the saturated moisture content owing to the relaxation process and Ω_i is the relaxation rate constant.

Wilde and Shopov [98] also presented a model based on the assumption that the non-Fickian diffusion in an epoxy polymer is based on both diffusion and relaxation processes. The two diffusion processes were assumed to be independent of each other. The mass uptake at any time interval, t, may be obtained from the following equation.

$$M_t = M_d(t) + M_{R\infty}(1 - e^{-rt}) \tag{2.10}$$

where r is the relaxation constant. M_d is the short term mass uptake and $M_{R\infty}$ is the saturated moisture content due to relaxation. The model incorporates the effect of delay in achieving equilibrim by the surface concentration of the polymer.

Another model for predicting anomalous moisture uptake in polymers was presented by Roy et al [99]. Since the diffusion and relaxation rates are comparable in anomalous moisture uptake, time dependent behaviour of the polymer, in the form of varying diffusion coefficient and surface concentration, was included in the model. A Prony series representation was used to define time dependent diffusion coefficient, as given in Equation (2.11).

$$M_t = 1 - \frac{8}{\pi^2}\sum_{n=0}^{\infty}\frac{1}{(2n+1)^2} e^{\frac{-(2n+1)^2}{h^2}\left[D_{po}t + \sum_{i=1}^{\infty} D_{pr,i}\left[t + \tau_{r,i}(e^{-t/\tau_{r,i}} - 1)\right]\right]} \tag{2.11}$$

where D_{po} and D_{pr} are Prony series diffusion coefficients and τ_r is the corresponding retardation time. The Prony series parameters can be obtained by fitting the model to experimental data obtained from gravimetric experiments.

2.9.5 Other Models

In addition to the moisture prediction models discussed above, several other models are available, which can predict moisture with varying degrees of success. A moisture prediction model incorporating the effects of swelling, temperature, surface effects and surface texture was presented by Gupta and Pawar [100] for glass fibre epoxy composite. A secondary diffusion phenomenon was observed during absorption, as seen in the case of two stage diffusion. This was attributed to the capillary diffusion occurring in the composite matrix.

Tsai et al [101] presented a model that was able to predict the dynamic penetrant front of a diffusing substance and the closed form solution for an infinite two dimensional plate of finite thickness. It was assumed that hygroscopic expansion was proportional to the moisture concentration. The results were validated by gravimetric experiments using T700 carbon / epoxy composite laminates. However, the model showed no significant improvement over the results obtained by the Fickian Diffusion Model.

2.10 Modelling the Durability of Adhesive Joints

The ability to predict the effect of moisture diffusion on adhesive joint strength is of key importance in determining the long term behaviour of adhesive joints. The finite element method (FEM) has been successfully employed, in recent years, to determine the stresses in adhesive joints and to predict joint strength [6, 102-104]. A number of modelling methodologies may be found in the literature for determining adhesive joint strength. The models may be classified on the basis of the underlying mechanics and are discussed in the following sections.

2.10.1 Strength of Materials Based Methods

These methods are based on the study of stresses and strains in an adhesive joint and the application of a suitable stress or strain based failure criterion. Bulk tensile testing of rubber toughened structural adhesives has shown that they exhibit plasticity and elasto-plastic material models may be used to predict their behaviour under load [105-107]. Various failure criteria have been used, in combination with elasto-plastic material models, to predict adhesive joint strength. These include; maximum stress [72, 108], maximum strain [109, 110], plastic yielding, maximum principal stress or strain, and plastic energy density [111-115].

The definition of the yield surface is important when using elasto-plastic material models. The yield behaviour of polymers has been shown to exhibit hydrostatic stress dependence and thus a yield criterion which includes hydrostatic stress effects should be used to determine the yield surface [103, 116, 117]. Modifications

to the von Mises yield criterion have been suggested to include hydrostatic stress sensitivity, but with limited success [118]. A detailed study of the yield surface for a rubber toughened epoxy adhesive was carried out by Wang and Chalkley [119] under multi-axial loading conditions. Several yield criteria with hydrostatic stress dependence were used to predict the experimental stress strain results. The modified Drucker-Prager/cap plasticity model provided the best predictions of the experimentally observed yield behaviour of the adhesive [119].

Maximum stress and strain based failure criteria were used by Harris and Adams [72] to predict the failure of single lap joints. A non-linear finite element analysis with an elasto-plastic material model for the adhesive and adherends was carried out. The selection of stress or strain based failure criterion was based on the results of the uniaxial tensile test results. For an un-toughened adhesive, a brittle failure was observed and a maximum stress criterion was used while for a toughened adhesive, failure was ductile and a maximum strain based criteria was used. However, these criteria are difficult to implement when highly localised stress concentrations or stress singularities exist in an adhesive joint.

To avoid the localised stress effects in an adhesive joint during the strength prediction, Crocombe [120] used a global yielding criteria. Failure of the joint was defined when a path of adhesive along the overlap region started deforming plastically and no further increase in applied load was observed. This criterion was used to study failure in single lap, double lap and shear test joints and a good correlation between experimental and numerical results was reported. A similar approach was applied to the failure prediction of composite single lap joints by Kim et al [121], where an elastic-perfectly plastic material model for the adhesive layer was used. Failure in the adhesive layer was defined when the overall region of the adhesive layer became plastic and was not able to support any load. However, this type of failure criterion may not be applicable in joints where localised failure may occur. Dorn and Liu [122] used an accumulative plastic strain based criterion for single lap joint strength prediction. A critical region was identified and the maximum accumulative effective plastic strain in the critical region was used as a parameter for strength prediction.

The concept of a failure envelope based on the relationship between the bending moment at the edge of the overlap at failure and the tensile failure load was proposed by Grant et al [6]. Failure of single lap joints was studied in tensile loading, three-point bending and four-point bending and a two dimensional finite element model was used. A relationship between the bending moment at the edge of the overlap and the tensile failure load was observed and a failure envelope was developed where failure of the joint may occur if a combination of bending moment and failure load is outside the failure envelope.

The strength based failure methods are relatively simple to use compared with the criteria discussed in the following sections, however, they are sensitive to mesh refinement and an overall mesh convergence study should be carried out to obtain reliable results. In the case of stress singularities, the selection of failure criteria, based on localised values, becomes difficult. Although the concept of selection of a failure parameter at a characteristic length from the singularity has been used [6, 123]; the selection of an appropriate characteristic length becomes important in this case. Strength based methods do not cater for the mechanisms specific to toughened adhesives such as cavitation of rubber particles and the growth of voids.

2.10.2 Fracture Mechanics based Methods

Fracture mechanics methods assume that all materials have flaws or cracks and that crack growth will occur when a selected fracture criterion is satisfied. The fracture criterion may be energy based, such as the critical strain energy release rate, G_c, proposed by Griffith [124], or stress based, such as the stress intensity factor, K, given by Irwin [125]. In recent years the J-Integral approach has been used to determine the strain energy release rate through the use of a path independent integral around the crack tip. In linear elastic materials, J is equal to G; in nonlinear elastic materials, J represents the strain energy release rate.

The energy based fracture mechanics failure criteria have been used to predict failure in adhesives [126-131]. This criterion dictates that failure will occur when the strain energy release rate equals the critical strain energy release rate. The

suitability of strain energy release rate as a failure criterion for adhesive joints was investigated by Hamoush and Ahmad [132] by using compact tension and shear joints to closely resemble mode I and mode II failure. Experimentally obtained failure loads were applied in a finite element model to calculate the strain energy release rates and it was concluded that strain energy release rate was independent of initial crack length, adhesive layer thickness and loading mode and thus may be considered a material parameter. Akisanya and Meng [133] determined the suitability of a fracture mechanics based initiation criterion at the interface using butt joints. Layer thicknesses from 0.5 to 3 mm were used in aluminium joints made using a two-pack araldite adhesive. It was concluded that the critical intensity factor may be used to predict the fracture initiation at the interface corner of the joints.

Analytical solutions have been developed to determine the strain energy release rate for different sample geometries and these may be used to predict failure. Marannano et al [134] developed a solution for the strain energy release rate in the mixed mode end loaded split (MMELS) test. The model was based on a modified beam theory for the MMELS test. The results were compared with strain energy release rate determined from finite element analysis using the virtual crack closure technique. A difference of less than 10% was reported between the analytical and numerical results. An analytical model to determine the strain energy release rate in single lap joints and double cantilever beam was presented by Shahin and Taheri [135], which was based on the analysis of adhesive layer stresses and a crack closure integral method. The results were compared with classical beam theory results for the double cantilever beam and end-notch flexure specimens and a good correlation was reported.

Another fracture mechanics based approach for joint strength prediction is based on Irwin's crack closure integral method. It is based on the assumption that the energy absorbed upon crack growth is equal to the work required to close the crack. The method was used by Wahab and De Roeck [136] to calculate strain energy release rate from a three-dimensional finite element analysis and good correlation with literature values was reported. Wahab [137] also used the same approach for designing lap joints.

One of the limitations of the fracture mechanics methods is that they require the existence of a pre-crack to determine the strain energy release rate. Fracture mechanics approaches may require several finite element analyses to determine fracture energies at different crack lengths.

2.10.3 Cohesive Zone Model (CZM)

The cohesive zone model has been used increasingly in recent years to simulate crack initiation, propagation and failure [138-142]. The cohesive zone model allows multiples cracks to be modelled and the direction of crack propagation need not be known in advance. A review of the advantages, limitations and challenges in the use of cohesive zone models has been presented in [143].

Cohesive zone models follow a traction-separation constitutive law to predict failure initiation, damage and failure. Several shapes for the traction-separation law have been presented in the literature, with the bilinear, linear-parabolic, exponential and trapezoidal shapes being the most commonly used for strength prediction [144-147]. The shape of the traction-separation law is difficult to determine from experimental methods and is often assumed or simplified. The actual shape of the traction-separation law is dependent on the nature of the problem and on the ratio of the toughness of the interface and stiffness of the bulk material [148]. The shape of the traction-separation law also influences the numerical performance of the solution and more convergence difficulties have been observed when using trapezoidal than bilinear traction-separation laws in a finite element analysis [148]. The bilinear law provides a good balance between computational cost and approximation of the problem [148]. The influence of shape of the traction-separation law, on the predicted strength, has been reported by some authors [147, 149, 150], however, others have observed no effect of the shape of traction-separation law [151]. In a bilinear traction-separation law, the initial response of the cohesive zone is elastic until reaching a critical traction. Once the critical traction is reached, stiffness degradation starts and continues until it reaches zero and failure occurs. The area under the traction-separation curve is

equal to the fracture toughness of the material and known as the cohesive energy, G_{coh}.

The parameters input into the cohesive zone model may be determined by a combination of experimental and numerical methods [152, 153]. An experimental method to determine the cohesive zone parameters has been proposed by Li and Ward [154] and was used by Sorensen and Jacobsen [155]. It was based on the measurement of J-integral and the end opening displacement of the cohesive zone in a specimen. Sorensen and Jacobsen [155] used a double cantilever beam specimen, which was loaded in pure bending. The opening displacement of the cohesive zone was measured and a closed form solution for determination of the J-integral was provided. The cohesive law parameters were then used to predict the failure strength of adhesive joints.

Another experimental approach for the determination of cohesive zone parameters was presented by Ferracin et al [156]. It was suggested that the cohesive zone parameters may be obtained experimentally by measuring the radius of curvature and the crack length in a wedge peel test where the adherends deform plastically. An alternative option was to measure the radius of curvature from two different test specimens, having adherends of different thicknesses.

Turon [157] presented a methodology to determine the constitutive parameters of the cohesive zone model based on the properties of the surrounding material. A closed form solution was provided for the stiffness of the cohesive zone. In addition, an analytical solution to find the length of the cohesive zone was provided. The cohesive zone is the softening region ahead of the crack tip, which should contain a sufficient number of finite elements to accurately predict the damage propagation. A study was carried out by Harper and Hallett [158] to determine the accuracy of the available methods of determining the cohesive zone length. The cohesive zone length was found to be affected by specimen depth and the longitudinal and shear moduli, especially in orthotropic materials. Based on this, improvements to the existing methods were suggested and a minimum of two to three elements were deemed necessary, within the cohesive zone for accurate numerical representation.

One of the main limitations of the cohesive zone model is that cohesive elements should be present on the crack path. Although several layers of cohesive elements may be introduced in a structure, it is not feasible to introduce cohesive elements between every field element, even in a moderate size mesh. The method is suitable for interfacial failure or crack representation when the bulk material failure, based on micro-mechanics, does not affect fracture. Although several methods have been suggested for calibration of the traction-separation laws, a generally accepted method is still required.

2.10.4 Continuum Damage Models

Continuum damage models are able to predict damage and failure in a ductile material. A specimen is said to be damaged when a large number of microcracks are randomly scattered over a large part of the volume such that the volume partially looses the ability to transfer momentum and fracture strength [159]. A damage variable is used in continuum damage models to determine the degradation in material stiffness. The damage variables used are of two types; the first type of variable can predict the value of damage but does not characterise the damage itself, such as damage equivalent stress. The second type of damage variable is linked to some physical definition of damage such as porosity or relative area of micro-cavities [160]. The second type of variable is based on macroscopic material properties and its evolution is governed by a state equation. If several damage mechanisms are occurring in a material, each of them may be represented by an independent damage variable.

A general framework for damage models was provided by Lemaitre and Desmorat [161]. It consists of the definition of variables that define the state of corresponding material mechanisms, known as state variables. The damage model framework also includes the definition of state laws and definition of the laws of evolution of the state variables. A detailed review of continuum damage mechanics based methods was carried out by Lemaitre [162]. The Gurson model is one of the models based upon a continuum damage framework that has been used to determine the strength of polymers [127, 163].

A modified Gurson model was presented by Gurson [164] that was further modified by Tvergaard [165] and Needleman [166]. It is a phenomenological micromechanical model, based on the observation of damage and failure mechanisms in a ductile material. The mechanisms involve the nucleation, growth and coalescence of micro voids, as shown in Figure 2.8. The voids nucleate by decohesion of second phase particles or by fracture and grow by plastic deformation of the surrounding material. Void coalescence occurs by necking down of material between adjacent voids or by localised shearing between voids. The material stiffness is degraded by this progressive cavitation and eventually this results in failure [167].

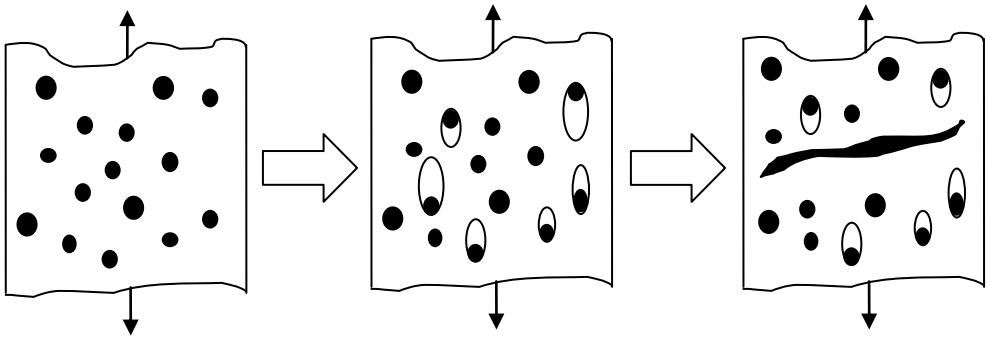

Figure 2.8: Ductile failure by nucleation, growth and coalescence of voids.

The effect of including damage and failure prediction in a material model may be observed with the help of a typical stress-strain curve for a ductile material, as shown in Figure 2.9. Point 'a' is the start of the loading, 'b' is the yield point, 'c' is the failure initiation point and 'd' represents complete failure. An elasto-plastic material model would follow the curve abcd' after application of a tensile load while the modified Gurson model would follow the curve abcd. A damage evolution law controls the damage in material, represented by curve cd.

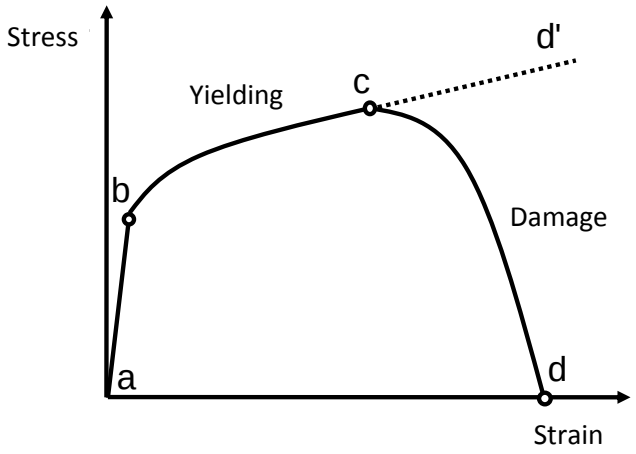

Figure 2.9: Typical uniaxial stress-strain response of a ductile material.

The yield function for the modified Gurson model is given by:

$$F_y = \left(\frac{\bar{\sigma}}{\sigma_y}\right)^2 + 2q_1 f^* \cosh\left(\frac{q_2 p^*}{2\sigma_y}\right) - \left[1 + \left(q_1 f^*\right)^2\right] = 0 \qquad (2.12)$$

where $\bar{\sigma}$ is the von Mises equivalent stress, σ_y is the yield stress of fully dense matrix material, p^* is the hydrostatic stress, q_1 and q_2 are the yield surface multipliers and f^* is the modified void volume fraction. The two yield function multipliers, q_1 and q_2 were added to the modified Gurson model for better response under small values of void volume fraction. The damage parameter in the yield function is the modified void volume fraction, f^*. The modified void volume fraction is dependent on a single scalar damage parameter, the void volume fraction f.

$$f^* = f \qquad \text{if } f \le f_c \qquad (2.13)$$

$$f^* = f_c + \left(\frac{f_u^* - f_c}{f_F - f_c}\right)\left(f - f_c\right) \qquad \text{if } f > f_c \qquad (2.14)$$

where f_c is the critical void volume fraction, f_F is the void volume fraction at failure and $f_u^* = 1/q_1$. The change in void volume fraction may be owing to the growth of the existing voids and/or nucleation of new voids. The modified Gurson model may be used with or without void nucleation.

The modified Gurson model parameters can be obtained by using optimisation algorithms [168], which would require at least some programming effort or by curve fitting of stress-strain material response [127, 167, 169]. The curve fitting method is relatively straightforward, as simulation results can be directly compared with the experimental material curves. However, it may prove cumbersome to determine a good fit for all parameters. Different methodologies to measure the damage by experimental methods were presented by Lemaitre and Dufailly [170] including; measurement of the surface density of micro-cracks and cavities by observations of micrographs, measurement of variations in elastic modulus and measurement of variation of micro-hardness.

The modified Gurson model provides good predictions under stress triaxiality conditions and the damage parameters are independent of specimen geometry. However, any effects of void shape change due to deformation and shear failure mechanisms are not included in the modified Gurson model. Modifications have been proposed to include the void shearing mechanism [171]. The large number of parameters required as input for the model makes the model calibration a relatively difficult job.

2.10.5 Modelling Environmental Degradation

The methods available for modelling joint durability, as discussed in Sections 2.10.1 to 2.10.4, have been implemented with various degrees of success to model the environmental degradation of adhesive joints [172, 173]. A framework, to assess the environmental degradation of adhesive joints, was presented by Crocombe [174]. The framework was implemented by a coupled hygro-mechanical analysis using the finite element method. The experimentally determined moisture diffusion and moisture dependent mechanical properties of the adhesive were used in the modelling. The residual strength of a single lap joint was determined based on the adhesive failure strains and good correlation with experimental results was observed.

A strength of materials based approach was used by Wahab et al [33] to predict the joint durability of single lap and butt joints. The joints were conditioned in water at

60°C for up to 60 weeks. The moisture diffusion in the adhesive layer was determined by transient finite element analysis. A coupled hygro-mechanical analysis was used to determine the swelling strains. Changes in peel and shear stresses with increasing moisture absorption were observed. The increased moisture diffusion resulted in increased plasticity, which was considered responsible for the joint failure after conditioning. Similar results were reported by Broughton and Hinopoulos [175] when lap joints, conditioned in water, were analysed by non-linear finite element analysis.

A methodology for the determination of cohesive zone model parameters and its application to different joint configurations has been successfully implemented by Crocombe and his co-workers [23, 172, 173, 176]. Cohesive energy of the adhesive and substrate system was determined using a mixed mode flexure joint (MMF) in three point bend configuration. The failure loads of unconditioned and conditioned MMF specimens were used to determine the cohesive zone model parameters. These were then used to model the joint durability of single lap, double lap and L-joints. Good correlation was found in the predicted and experimental strengths of the joints. Use of different joint configurations for the determination of the cohesive zone parameters provided geometry independent cohesive zone model parameters.

A critical equivalent plastic strain based progressive failure model for the prediction of joint durability, was proposed by Hua et al [35]. The model was used to predict damage growth and cohesive failure in the adhesive layer. The strength predictions for aluminium and composite single lap joints were in good agreement with experimental results. The critical equivalent plastic strain, used as failure index in the model, was sensitive to mesh size.

2.11 Conclusions

The strength of structural adhesives is affected by their working environment. Moisture and temperature have been identified as two of the major factors affecting the strength of an adhesive, in addition to applied stress. The moisture

diffusion in an adhesive may result in micro-cracking, swelling, chain scission, leaching of material and plasticisation. A combination of these mechanisms acts to degrade the strength of the adhesive. The degradation in the adhesive strength may be reversible or irreversible, based on the degradation mechanism. The diffusion properties of a structural adhesive may exhibit moisture history dependence and the diffusion coefficient and saturated moisture content change with absorption and desorption cycles. In adhesive joints, a degradation of strength may occur with increasing moisture uptake. The mechanisms of degradation may involve the adhesive and interface degradation. The durability of the adhesive joints may be determined by using various test specimens. However, the testing of adhesive properties and adhesive joint durability resulting from diffusion of moisture is generally carried out for a single cycle of moisture uptake. In-service adhesive joints will usually be exposed to varying moisture conditions, which makes the effects of moisture history important in a life prediction study of a joint. The changing diffusion properties may result in a different moisture concentration in an adhesive joint than predicted without including moisture history dependence.

Durability predictions of adhesive joints may be carried out by a combination of moisture diffusion and mechanical strength modelling. Several moisture diffusion models are available for Fickian and non-Fickian types of moisture uptake and the selection of a particular model depends on the type of adhesive. Durability modelling may be based on strength of materials, fracture mechanics or continuum damage mechanics failure criteria. A number of studies of joint strength prediction, based on various methods of modelling, have been presented in the literature; however, the effects of moisture history have not been included in any of them. There is thus a requirement for a durability predictive methodology that incorporates the effects of varying moisture conditions and moisture history. This is the aim of the present work.

Chapter 3
Experimental Methods

3.1 Introduction

This chapter describes the methods, equipment and procedures used during the experimental programme carried out in this research. The experimental programme had two major parts. The first part was to obtain the diffusion and mechanical properties of the adhesive FM73-M, under cyclic moisture conditions. These material properties were not available from the literature and were required for use in the analytical and numerical models. Bulk adhesive samples were prepared and conditioned in water at different temperatures, for multiple cycles, and the moisture uptake properties were determined. The mechanical properties under cyclic conditions were also determined, using bulk samples that were conditioned at different temperatures.

The second part consisted of testing adhesively bonded single lap joints to determine the effects of moisture history on joint durability. The experimental results were used to validate the results of the numerical models. Batches of single lap joints were conditioned in water at two different temperatures and the failure load was determined by tensile testing. Since single lap joints were the only type of joint used in this work, thus the terms 'joint' and 'single lap joint' are used interchangeably from hereon.

The failure surfaces of the tested joints were analysed using a variety of techniques, which included digital image processing, scanning electron microscopy (SEM) and X-ray photoelectron spectroscopy (XPS). These provided an insight to changes in the fracture path and the failure mechanisms in response to the environmental effects.

3.2 Material Characterisation

The structural adhesive FM73-M, available from Cytec Engineered Materials Ltd, was used to manufacture the bulk adhesive samples and aluminium alloy 2024 (Al2024) and the adhesive were used to manufacture the adhesive joints. FM73-M was chosen based on its high strength, good resistance to moisture, broad applicable temperature range and wide use in the aerospace industry. It is a single part, heat curing, rubber toughened epoxy, which has a manufacturer recommended curing temperature of 120°C. The adhesive comes in film form and has a polyester knit carrier for support and handling. This also ensures good uniformity in layer thickness when applied in a bonded joint. The nominal thickness of the adhesive film is 0.12 mm and it has a weight of 150 g/m^2. The adhesive has a shelf life of twelve months when stored at -18°C or below and a life of 30 days at room temperature [177]. Typical properties of the adhesive are given in Table 3.1. The adhesive was used with BR127 modified epoxy primer. The primer provides protection from corrosion and protects prepared adherend surfaces from oxidation. It has an operating range of -55°C to 150°C and may be cured for 30 minutes at 120°C [178].

Table 3.1: Typical properties of the adhesive FM73-M.

Property	Value
Elastic modulus (E)	2260 MPa
Poisson's ratio (ν)	0.33
Ultimate tensile strength (σ_{ult})	49.89 MPa
Glass transition temperature (T_g)	99.7°C [36]
Fracture energy (G_c)	2.9 KJ/mm2 [23]

Adherends for the single lap joints were manufactured from Al2024. The alloy includes 4.4% Cu, 1.5% Mg and 0.6% Mn. It has high strength, especially at elevated temperatures, and good toughness. The alloy is generally heat treated to improve its strength. These characteristics make it a good choice for high strength to weight ratio structures such as those required in the aerospace industry where it has been

used in wing and fuselage construction for many years. It has excellent machinability and fair workability and corrosion resistance and is also used in machined products and orthopaedic equipment. The Al2024 is available in unclad and clad forms where in the later, the surface is coated with a layer of aluminium. Unclad aluminium in both heat treated (T3) and soft (O) states was used in this research in order to observe the effects of adherend strength.

Details of the characterisation of diffusion and mechanical properties of the adhesive and adherend materials are described in the following sections.

3.2.1 Bulk Adhesive Sample Preparation

Bulk adhesive samples were prepared to determine the moisture diffusion characteristics and mechanical properties. The adhesive was stored at -24°C and brought to room temperature in a desiccator before further processing. A lay-up method was used for preparation of the bulk samples. Six layers of the adhesive film, each of 0.12 mm thickness, were stacked together and pressed using a heavy stainless steel roller to ensure that air did not remain trapped between the layers. This helped in minimising the formation of voids during curing.

Keeping voids to a minimum was the major challenge faced during the preparation and curing of the bulk samples. Several techniques were investigated and it was found that practically void free samples could be obtained when the adhesive lay-up was cured in a hot press. In this method, a rectangular mould of 100 x 100 x 1 mm, with top and bottom plates, was used, as shown in Figure 3.1. The surface of the mould was degreased with laboratory grade acetone and sprayed with a PTFE based mould release spray. This ensured that any adhesive overflowing during the curing did not stick to the surface of the mould. A PTFE film was place between the mould and the top and bottom plates to avoid sticking of the adhesive to the plates.

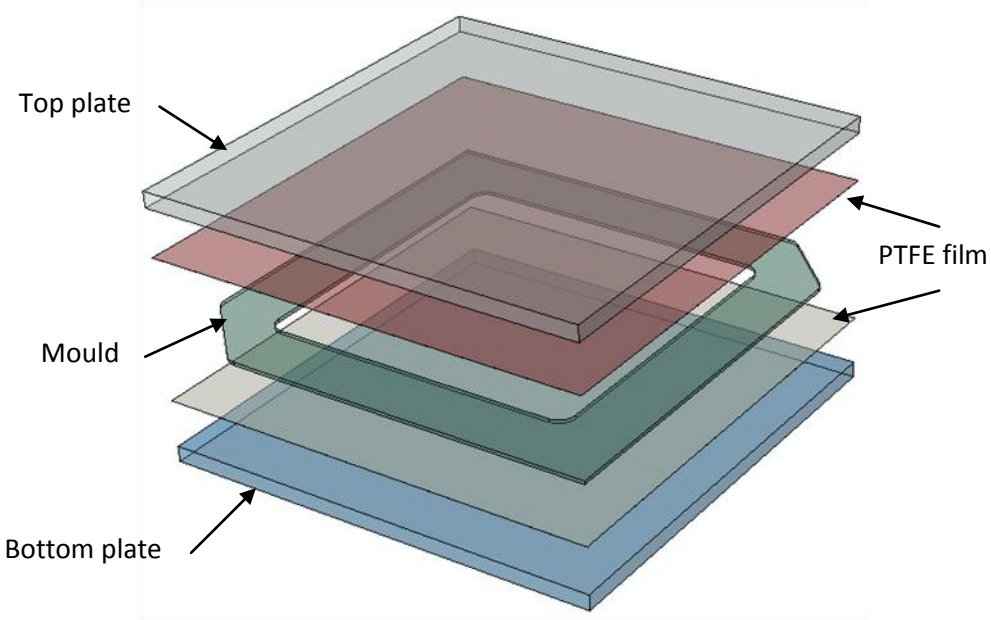

Figure 3.1: Mould setup used for curing the bulk adhesive sheets.

The mould assembly, with the adhesive lay-up, was placed in a hot press and pressure of 0.28 MPa was applied. The press was brought to 120°C from room temperature in 30 minutes and held at this temperature for one hour [177]. The adhesive expands during the curing process and fills the mould cavity. The expansion may be owing to the coefficient of thermal expansion of the adhesive and that the curing is an exothermic reaction where heat is generated during the reaction. Thus the inner sections of the adhesive may be at much higher temperatures than the applied temperature of 120°C and result in expansion of adhesive. The mould was removed from the press and the cured lay-up was allowed to cool down to room temperature in a desiccator. The lay-ups cured in this manner had a negligible amount of porosity. The gravimetric and tensile testing samples were cut from the cured sheets of bulk adhesive.

3.2.2 Cyclic Moisture Diffusion

The cyclic moisture diffusion properties of the adhesive were determined by a gravimetric method. The size of the gravimetric samples and their conditioning environments are given in Table 3.2.

Table 3.2: Sizes and conditioning environments of the bulk adhesive samples.

Thickness of sample (mm)	Dimensions (mm)	Conditioning environment	
		Temperature	Moisture
1	60 x 40	50°C	Immersed in water
1	60 x 40	70°C	

Samples of thickness 1 mm were cut from the cured bulk adhesive sheet, as described in Section 3.2.1. Two batches of 1 mm thickness, containing five samples each, were conditioned at 50°C and 70°C, immersed in water. The two conditioning temperatures provide accelerated conditions for moisture absorption, however, they remain significantly below the glass transition temperature of the adhesive, which has been reported to be 99.7°C when the adhesive is cured at 120°C for one hour [36]. Water is used in many standard tests for adhesion and provides an extreme humidity condition that may be faced by an adhesive during its service life in certain applications. The combination of selected temperature and humidity conditions provide a harsh environment for the study of moisture dependent behaviour in the adhesive joints. The diffusion coefficient of the adhesive was measured by considering the adhesive a homogenous material where effects of rubber particles and polyester carrier were not separately considered as the modelling of the adhesive is carried out as macro scale.

The samples were conditioned for multiple moisture absorption-desorption cycles in order to observe the effects of cyclic moisture conditions. The procedures and guidelines for gravimetric moisture uptake measurements in bulk sample in British Standard BS EN ISO 62:1999 [37] were followed. The bulk samples were dried in an oven at 50°C, until they achieved a constant weight, before starting the environmental conditioning. For conditioning, the bulk samples were suspended by a wire mesh in plastic containers filled with deionised water. These were placed inside temperature controlled ovens for the duration of conditioning. At prescribed time intervals, the samples were removed from the container and the surface was wiped of excess water with a paper tissue. A Mettler Toledo AL204 electronic balance with 0.1 mg accuracy was used to weigh the samples. Care was taken to

complete the weighing process within a couple of minutes to minimise the time that a sample was out of the conditioning environment.

Desorption of the conditioned samples was carried out at the same temperature as that used for absorption. The conditioned samples were weighed prior to the start of the desorption cycle and then placed in a temperature controlled oven. At prescribed time intervals, the samples were removed and weighed, until they achieved a constant weight. The percentage moisture content in the bulk adhesive, M_t, was calculated using the following equation:

$$M_t = \frac{M_2 - M_1}{M_1} \times 100 \tag{3.1}$$

where M_1 is the mass of the specimen after initial drying and before immersion and M_2 is the mass of the specimen at a specified time interval.

3.2.3 Mechanical Properties of the Adhesive

The moisture dependant mechanical properties of the adhesive were determined by tensile testing bulk adhesive samples, which were cut from cured sheets of the bulk adhesive according to BS EN ISO 527-2:1996 [179]. The tensile test samples were conditioned at 50°C and 70°C, immersed in water, for an absorption-desorption-absorption cycle. At preselected time intervals, the tensile samples were withdrawn from the conditioning environment and tensile testing was carried out using an Instron 3366 dual column testing machine, with a displacement rate of 1 mm/min. At least three tensile samples were tested at each selected time interval. The strain was measured using a strain gauge based contact extensometer. The specimens were wrapped with cling film to minimise any changes in moisture concentration during the transportation to the test machine and tensile testing.

3.2.4 Mechanical Properties of the adherend Al2024

Owing to the low yield strength of Al2024 O, the adherends exhibited yielding during the tensile testing of the single lap joints, however, no yielding was observed in the joints manufactured with Al2024 T3 adherends. Tensile testing of Al2024 O

was performed to characterise the elasto-plastic behaviour of the material, which was later used in numerical models. Three tensile test samples were prepared according to BS EN 10002-1:2001 [180] and the tensile testing was carried out using an Instron 3366 dual column testing machine. The strain was measured using a contact type extensometer.

3.3 Single Lap Joints

Single lap joints were used to study the durability and strength recovery under cyclic moisture conditions. A single lap joint configuration was used as this closely represents many joints found in industry and is economical to manufacture and test.

3.3.1 Geometry and Configuration

Al2024 T3 and O adherends were used, along with adhesive FM73-M and primer BR127, to manufacture the single lap joints. The guidelines for preparation of the single lap joints are provided in BS ISO 4587:2003 [74]. The configuration and geometry of the single lap joint are shown in Figure 3.2. The adherends were cut from sheets of Al2024 and pretreated to obtain a high quality surface. Two types of pretreatments; namely ACDC anodising and Chromic Acid Anodising (CAA), were used to prepare the surfaces of the adherends. ACDC anodising is a proprietary pretreatment, developed at the Institute of Polymer Technology and Materials Engineering (IPTME), Loughborough University, UK. CAA was carried out by courtesy of Bombardier Inc., UK. Details of each pretreatment are provided in the following sections.

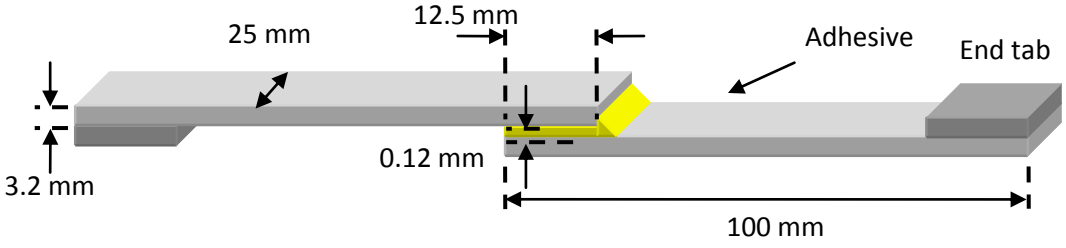

Figure 3.2: Geometry of single lap joint (not to scale).

3.3.2 ACDC Anodising

The ACDC pretreatment is a simple, fast and robust process resulting in durable adhesion and good corrosion performance. The electrolyte is free from the harmful hexavalent chromium found in the CAA pretreatment, which is presently considered the industry standard for aluminium. The ACDC pretreatment combines the advantages of AC (alternating current) and DC (direct current) anodising in a single process. The AC anodising is rapid, requires only surface degreasing as surface preparation and provides an open porous surface structure. On the other hand, the DC anodising provides a thick layer of oxide film with good corrosion resistance. These advantages make the ACDC pretreatment a good replacement of CAA. The pretreatment has been patented [181].

Prior to ACDC anodising, degreasing of the adherends was carried out using laboratory grade acetone. The adherends were placed in a beaker full of acetone and were passed through two five minutes cycles in an ultrasonic bath. The adherends were air dried before ACDC anodising.

For ACDC anodising, the adherends were suspended in an anodising bath containing a combined electrolyte solution of 5% phosphoric and sulphuric acids (2.5% each), as shown in Figure 3.3. The temperature of the bath was maintained at 35°C. An alternating current was applied for 2 minutes by ramping the voltage to 15V in one minute. This was followed by the application of direct current for 10 minutes at 20V where the voltage was increased from zero to 20V in one minute. The process developed a porous oxide surface on the adherends and they were removed from the anodising bath. The adherend surfaces were rinsed with water and dried in air. The ACDC anodising process was followed by application of BR127 corrosion inhibiting primer in the overlap regions. The primer was applied by using a cotton swab, in order to obtain a uniform, thin layer of the primer. The average thickness of the primer layer was 1-2 μm. The primer was air dried for 30 minutes before curing for one hour at 120°C in an oven.

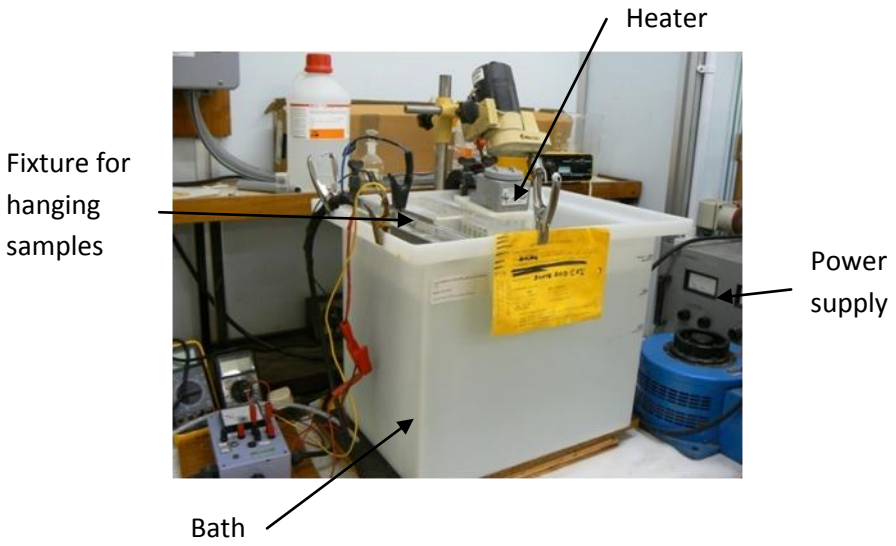

Figure 3.3: ACDC anodising bath with phosphoric and sulphuric acid electrolyte solution.

3.3.3 Chromic Acid Anodising

In order to compare the durability of ACDC and CAA pretreatments, a batch of single lap joints was manufactured with adherends pretreated by CAA. The adherends were degreased by vapour degreasing using trichloroethylene. In the next step, alkaline cleaning was performed by submersion in Isoprep 44 for 10 minutes, which is a proprietary material from Lea Manufacturing. It is a non-caustic cleaner with a pH of 9.3 – 10.45 and is designed to form stable emulsions with both mineral and fatty acid types of oils. The solution consisted of 60g/l of Isoprep 44 dissolved in deionised water at a temperature of 60°C. After this process, the adherends were rinsed in deionised water with air agitation for 3 minutes. Next, de-oxidising was carried out for 30 minutes using the Forest Products Laboratory (FPL) acid etch. The bath was operating at 60°C and the solution was stirred using an electromagnetic stirrer. After etching, the adherends were rinsed in deionised water for 3 minutes.

The CAA pretreatment was carried out by applying a DC voltage, which was ramped to 40V in 10 minutes and then kept constant for 10 minutes. Then the voltage was increased to 50V and maintained a further 10 minutes. After anodising, the adherends were rinsed in deionised water for 5 minutes and dried in warm air.

3.3.4 Joint Preparation and Curing

The pretreated adherends were joined using a single layer of the adhesive. Excessive adhesive, which was outside the overlap area, was removed and the adherends were held together by clips for the duration of curing. Curing was carried out by heating the joints at 120°C for one hour, in an oven. The joints were brought to room temperature in a desiccator, after removal from the oven. The thickness of the bondline was maintained by the knit carrier present in the adhesive and the average thickness was $0.12 \pm 15\%$ mm. Fillets were formed at the ends of the overlap owing to overflow of the adhesive. The joints were stored in a desiccator until conditioning or testing was carried out.

3.3.5 Environmental Conditioning

Single lap joints were conditioned at 50°C and 70°C, immersed in water. The choice of the conditioning environment has been discussed in Section 3.2.2 and the conditioning programme is given in Table 3.3. A set of joints was dried to constant weight in an oven at 50°C and tensile tested to obtain the unconditioned strength of the joints.

The joints in batches I-V in Table 3.3 were subjected to the specified conditioning environment by placing them in plastic containers filled with deionised water. The joints were held in place using meshed baskets, ensuring that the exposed adhesive surfaces were not in contact with the container surfaces. At pre-determined time intervals, two sets, containing three joints each, were withdrawn from the container. One set of joints was immediately subjected to tensile testing. The other set was dried in an oven at the same temperature as the conditioning temperature for that set and then subjected to tensile testing.

Moisture conditioning was also carried out to observe the effects of multiple cycles of moisture absorption-desorption on joint strength. Batch VI of the joints was conditioned for five cycles of 15 days of absorption and desorption each. At the end of each cycle, a set of three joints was removed from the conditioning environment and tensile testing was performed.

Table 3.3: Conditioning programme of single lap joints.

Batch No	Adherend Material	Pretreatment	Conditioning Environment	Conditioning Time Interval
I	Al2024 O	ACDC	50°C / Water immersed	7, 14, 28, 56 and 182 days
II	Al2024 O	ACDC	70°C / Water immersed	
III	Al2024 T3 unclad	ACDC	50°C / Water immersed	
IV	Al2024 T3 unclad	ACDC	70°C / Water immersed	
V	Al2024 T3 unclad	CAA	70°C / Water immersed	
VI	Al2024 T3 unclad	ACDC	70°C / Water immersed	Five absorption and desorption cycles of 15 days each.

3.3.6 Tensile Testing

Tensile testing of the single lap joints was performed using a Hounsfield H20K-W tensometer. The overlap region of the joints was wrapped in cling film to avoid any changes in moisture concentration during transportation to the tensile testing machine and tensile testing. End tabs were used to hold the joints in grips, during tensile testing. A displacement rate of 1.5 mm/min was used and the joints were tested to failure.

3.4 Failure Surface Characterisation

The surfaces of the tensile tested joint adherends were analysed to determine the failure type and the locus of failure. Various techniques, including; digital image processing, SEM and XPS were used for the failure surface analysis. The details of each method are presented in the following sections.

3.4.1 Digital Image Processing

Two types of failure in the adhesive joints could be identified by optical analysis. The first was failure within the adhesive layer, which will be referred to as “cohesive” failure. The second appeared at the interface between the adhesive and aluminium adherend and this will be referred to as “apparent interfacial failure”.

Digital image analysis was used to quantify the proportions of cohesive and apparent interfacial failure and the step by step process is shown in Figure 3.4. The failure surface was digitised using a Reichert MEF-3 Microscope with a macro arm attachment, shown in Figure 3.5, and the image was converted to a grey scale image to obtain high contrast between different image areas. The grey scale image was further converted to a two bit image using the mathematical software Matlab. A Matlab subroutine was then used to determine the percentage of overlap area covered by the adhesive and "metal". The same procedure was carried out on both adherends of a failed joint. The amount of adhesive on the adherends was used in the failure mode quantification, with a cohesive failure represented by unity. Mixed failure was thus quantified as a fraction of the amount of the adhesive left on the adherend to the amount of adhesive on a cohesively failed surface.

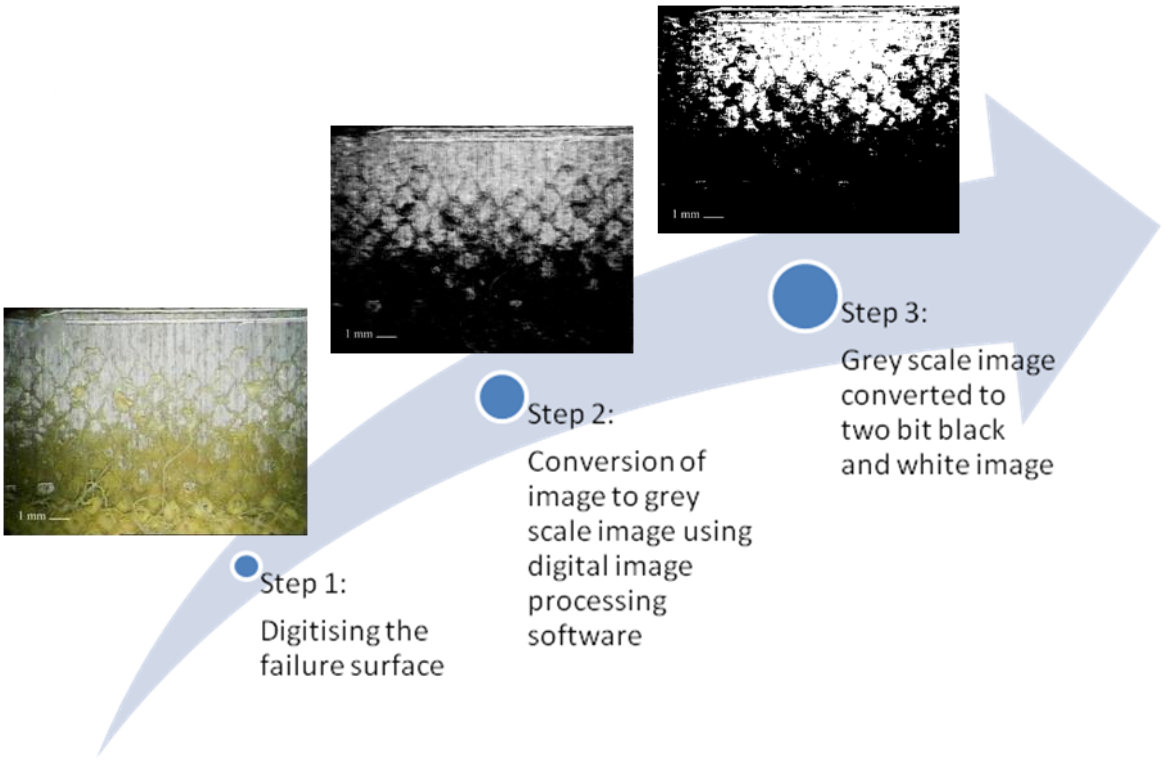

Figure 3.4: Workflow of digital image analysis showing conversion of a failure surface image to two bit black and white image.

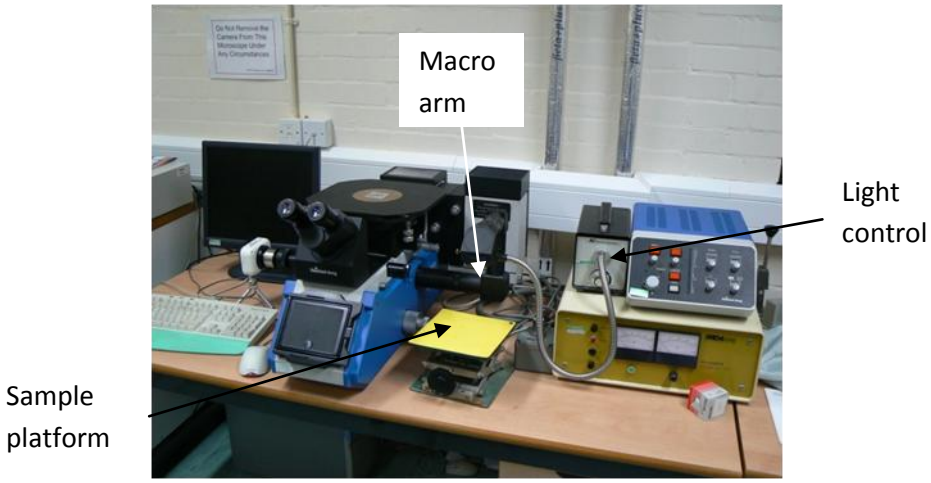

Figure 3.5: Reichert MEF-3 Microscope with macro arm attachment.

3.4.2 X-Ray Photoelectron Spectroscopy (XPS)

The interface between adhesive and adherend is composed of several layers of oxide, primer and adhesive. XPS provides material composition from a depth of a few nanometres (about 5 nm) of the exposed surface and thus has been successfully used in the past for the analysis of fracture surfaces in adhesive joints [17, 21, 182]. The oxide layer, developed on the adherends, had a highly porous structure, as illustrated in Figure 3.6. This enables penetration by the primer, which provided strong mechanical interlocking. The apparent interfacial failure may be originating in any of the interface layers and may travel through multiple layers. XPS analysis of Al2024 T3 and O joints conditioned at 50°C was carried out to investigate the locus of failure where apparent interfacial failure was observed. These samples were selected for analysis as they provided failure surfaces, which were representatives of the failure surfaces obtained in testing all the batches.

The surfaces of adherends were examined using an ESCALAB MK II surface analysis system, with an Al Kα X-ray source operating at a power of 160 W. XPS data was obtained from an area of approximately 2 mm diameter, full width, half maximum (FWHM). Quantification was achieved using theoretically derived relative sensitivity factors based upon ionisation cross-sections and known instrument parameters and

verified using standards of known composition. Peak areas were measured following the removal of a Shirley-type background [183].

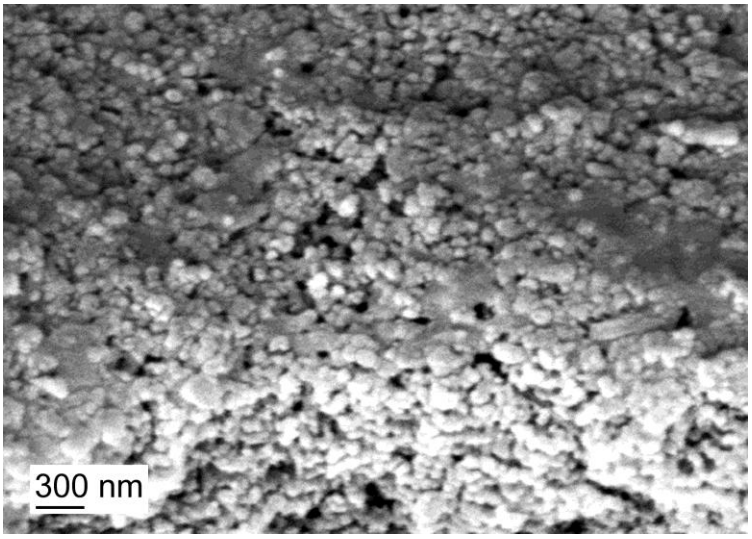

Figure 3.6: Scanning electron microscope image of porous oxide surface generated by ACDC pretreatment on Al2024 T3.

3.5 Summary

The moisture diffusion and mechanical properties of the materials used in this research, were experimentally determined for use in analytical and numerical models. The moisture diffusion behaviour of the adhesive under cyclic conditioning environments was studied using a gravimetric method. The bulk adhesive samples were prepared and conditioned at 50°C and 70°C in water for multiple absorption and desorption cycles. Tensile samples were also prepared from the cured bulk adhesive sheets and were subjected to environmental conditioning cycles at 50° and 70°C. Tensile testing of these samples was carried out by removing them from the conditioning environment at pre-determined time intervals and testing to failure to obtain the moisture dependent mechanical properties of the adhesive.

The durability and strength recovery of the adhesive joints under cyclic environmental conditions were studied by conditioning single lap joints at 50°C and 70°, in water. The adherends were pretreated using ACDC and CAA pretreatments to obtain high quality bonding surfaces. The single lap joints were conditioned for single and multiple absorption-desorption cycles. Tensile testing of the joints was

carried out at various stages during conditioning where the joints were tested to failure. The failure loads of the joints were used for validation of the numerical models. The failure surfaces of the single lap joints were examined using digital image processing, SEM and XPS techniques. This analysis served as a basis for the classification of the joint failure into cohesive and apparent interfacial failure. The change in failure mode with moisture history was also examined.

Chapter 4
Experimental Results

4.1 Introduction

The results of the experimentation carried out for this research are presented in this chapter. The overall experimental programme was described in Chapter 3 and consisted of bulk adhesive and single lap joint testing. The results of the moisture uptake experiments are discussed in the first section, together with the analytical models used to characterise the diffusion of moisture in the adhesive. The selected analytical model was incorporated in a finite element based numerical model for moisture prediction in adhesive joints. The moisture dependent mechanical behaviour of the bulk adhesive was also analysed in order to determine the effect of moisture on the elastic modulus and ultimate tensile strength of the adhesive.

The results of tensile testing single lap joints subjected to hot-wet conditioning and subsequent drying are discussed. These results show the effects of moisture absorption and desorption in the form of strength degradation and recovery in the joints. The failure surfaces of the single lap joints were analysed using digital image analysis, scanning electron microscopy (SEM) and X-ray photoelectron spectroscopy (XPS). The failure surface analysis provided an insight into the failure type and locus of failure.

4.2 Bulk Adhesive Testing

"Bulk" adhesive samples were tested to determine cyclic diffusion and mechanical properties. The results of the gravimetric moisture diffusion experiments and tensile testing of the conditioned adhesive samples are discussed in the following sections.

4.2.1 Cyclic Moisture Diffusion Behaviour

The diffusion of moisture in a substance is often mathematically represented by Fick's law of diffusion, which was described in Section 2.9.1. According to Fickian diffusion, the amount of the diffusing substance entering a medium through a unit area of its surface varies linearly with the square root of time in the initial stage of uptake. Thus the diffusion coefficient (D) may be determined from the slope of an M_t vs $\sqrt{t}/l$ graph and hence it is useful to plot experimental results from moisture diffusion experiments in this form. In this work, at least three samples were conditioned at each selected environmental condition and Figure 4.1 demonstrates that the repeatability of the moisture diffusion experiments was good. The standard deviation was calculated at each data point and no clear trend in the standard deviation with changing conditioning time was observed. The average value of the standard deviation was ± 0.03 wt%. Only the mean values of mass uptake are plotted in the gravimetric experimental plots from hereon in order to enable a clear presentation of the results.

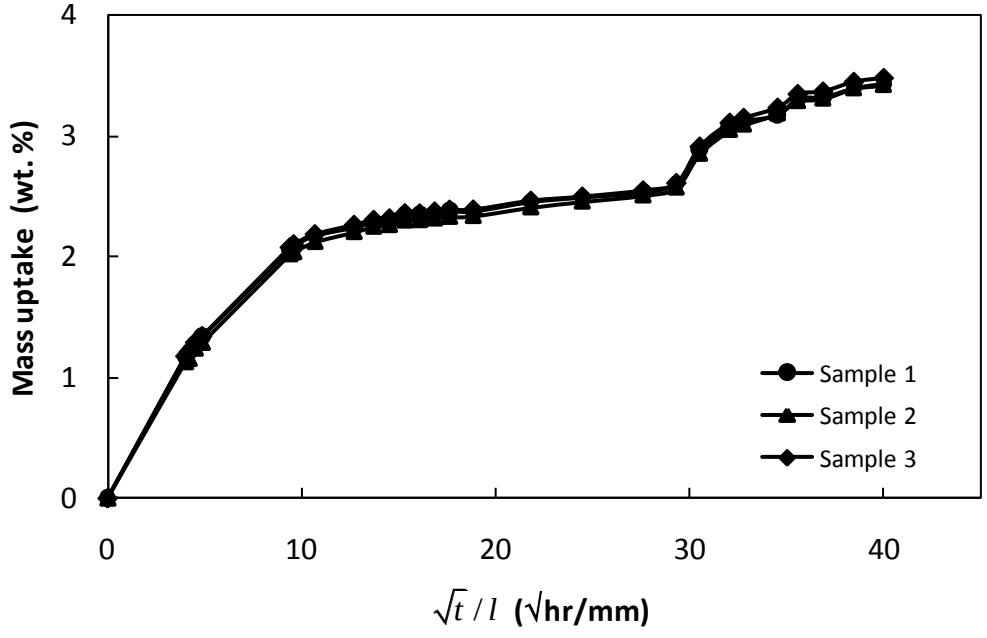

Figure 4.1: First moisture absorption for 1 mm thick bulk adhesive samples when conditioned at 50°C in deionised water.

The percentage mass uptake of moisture as a function of $\sqrt{t}/l$ is shown in Figure 4.2 for 1 mm thick bulk adhesive samples conditioned at 50°C in deionised water. The first absorption curve may be divided into three regions. It can be seen that the rate of absorption was faster in Region I than Region II. At the end of the Region II, there was a sudden increase in mass uptake at $\sqrt{t}/l$ of approximately 28 √hr/mm. This section of the mass uptake curve is denoted by Region III in Figure 4.2. It can be seen in the Figure 4.2 that in the second and third absorption cycles, the moisture uptake was faster than in the first absorption cycle and that only Regions I and II were present.

Desorption plots can also be seen in Figure 4.2. In the first desorption, diffusion takes place until a constant weight was achieved. The desorption process was clearly not the reverse of the absorption process. The initial region of the desorption curves showed a linear relationship between the mass uptake and $\sqrt{t}/l$. The initial linear portion was followed by a rapid slow down in moisture uptake and finally reached equilibrium.

The change in diffusion rate over different moisture absorption and desorption cycles indicates a physical change in the polymer structure [59]. It was also noted that the bulk adhesive samples achieved their original weight after desorption and that the desorption process was faster than absorption, which is a further indication of change in the adhesive structure due to moisture ingress. During the moisture absorption, water enters the free volume of the adhesive and also potentially reacts chemically with the adhesive. A number of mechanisms such as chemical binding of water, swelling, micro cracking may take place during moisture absorption while the desorption mostly entails the desorption of free water and is therefore faster than absorption. The secondary rapid moisture uptake (Region III) observed during first moisture absorption, has been reported previously [20] and may be due to swelling and micro cracking of the adhesive, which increased the amount of free volume, allowing for rapid moisture uptake. These mechanisms would be irreversible and thus no substantial effect was observed in further absorption cycles.

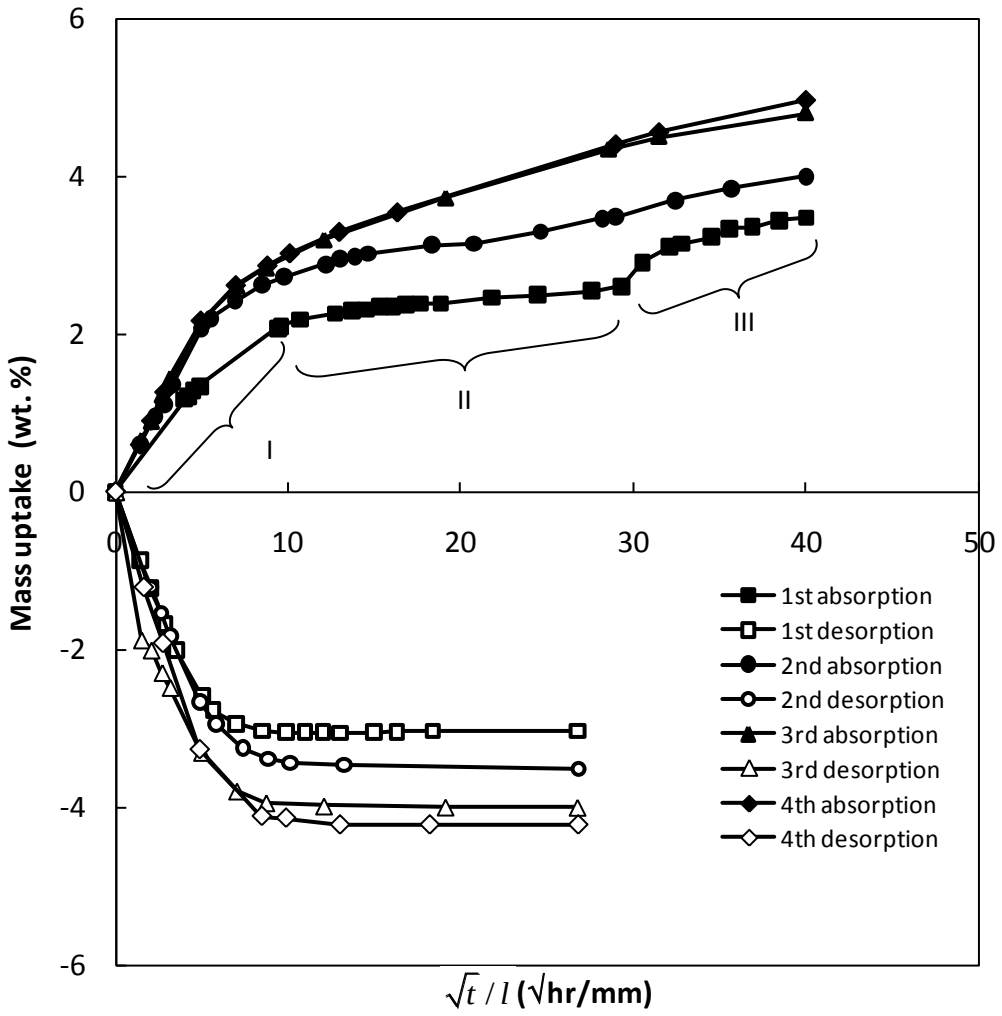

Figure 4.2: Moisture absorption and desorption curves for 1 mm thick bulk adhesive samples when conditioned at 50°C.

Figure 4.3 shows the percentage mass uptake as a function of $\sqrt{t}/l$ as obtained from the absorption and desorption gravimetric measurements at 70°C for 1 mm thick bulk adhesive samples. During absorption, a change in rate of mass uptake occurred with increasing conditioning time. In contrast to the results at 50°C, a second stage of rapid moisture absorption was not observed at 70°C. The moisture diffusion rate increased in each subsequent cycle of moisture absorption. The moisture desorption plots, as shown in Figure 4.3, showed a nearly linear relationship between the mass uptake and $\sqrt{t}/l$ before rapidly reaching equilibrium. The moisture desorption rate was faster than the corresponding moisture absorption rate.

A comparison of moisture absorption at 50°C and 70°C showed that the moisture diffusion rate was higher at 70°C than 50°C. This may be attributed to diffusion being a thermally activated process where high energy molecules of water diffuse in the polymer more rapidly. The moisture diffusion at 50°C and 70°C was similar in respect that the moisture desorption was faster than moisture absorption.

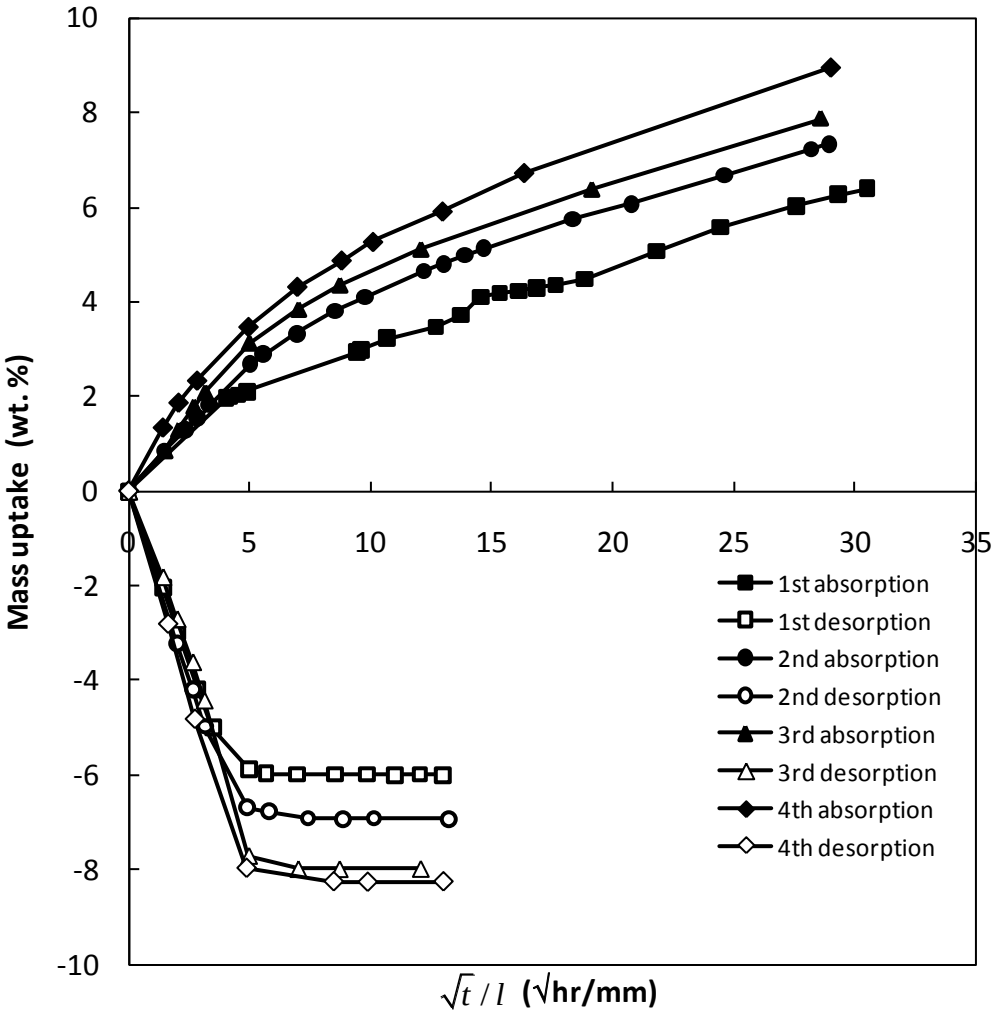

Figure 4.3: Moisture absorption and desorption curves for 1 mm thick bulk adhesive samples when conditioned at 70°C.

Various analytical moisture diffusion models were used to predict the experimental moisture absorption and desorption data in order to obtain the most suitable analytical model. The selected analytical moisture diffusion model was later used in the finite element simulations for moisture diffusion predictions. The analytical modelling process is described in the following section.

4.2.2 Modelling of Moisture Diffusion

Different types of moisture diffusion analytical models were discussed in Section 2.9. In this section, the analytical moisture diffusion models were applied to predict the experimental moisture diffusion data and the most suitable diffusion model was selected. The parameters of the analytical moisture diffusion models were determined by curve fitting the diffusion model to the experimental data. Figures 4.2 and 4.3 showed that saturation was not achieved during the moisture absorption experiments. This was owing to the conditioning of bulk adhesive samples for a predetermined time to perform cyclic moisture diffusion. The M_∞ and D used in the analytical moisture diffusion models were estimated by least square fitting of analytical models to the experimental data. The curve fitting was carried out in MathCAD using the genfit function, which employs an optimised Levenberg-Marquardt method [184].

The curve fitting of a Fickian diffusion model to the experimental results of 1 mm thick samples was carried out initially. In the case of bulk adhesive samples conditioned at 50°C, the Fickian diffusion model did not provide a good prediction of the moisture absorption cycles, as shown in Figure 4.4. The secondary rapid uptake, observed during the first moisture uptake was not considered in the curve fitting. In contrast to the absorption results, a good prediction of the moisture desorption cycles was obtained using the Fickian model, as shown in Figure 4.5. The curve fitting of the Fickian to the experimental absorption and desorption cycles at 70°C, is shown in Figures 4.6 and 4.7, respectively. As was observed in the case of the bulk adhesive samples conditioned at 50°C, the prediction of moisture uptake during the absorption cycles was poor, whilst the moisture desorption cycles were well predicted.

The good correlation between Fickian diffusion model predictions and the desorption experimental data showed that the moisture desorption was governed by a Fickian diffusion process at both 50°C and 70°C. The Fickian diffusion model uses a constant value of D and is not suitable in situations where the moisture diffusion rate is dependent on concentration as was observed during moisture

absorption in the bulk adhesive. Thus a model that allows for the change in diffusion rate during absorption may provide better predictions of the moisture absorption in the adhesive.

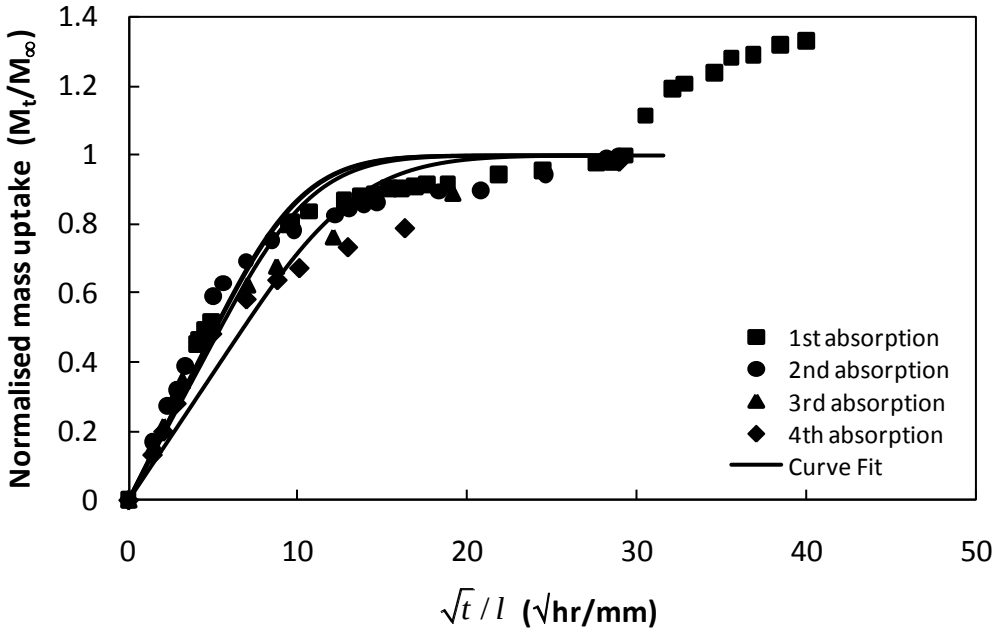

Figure 4.4: Fickian curve fit to moisture absorption for 1 mm thick samples when conditioned at 50°C.

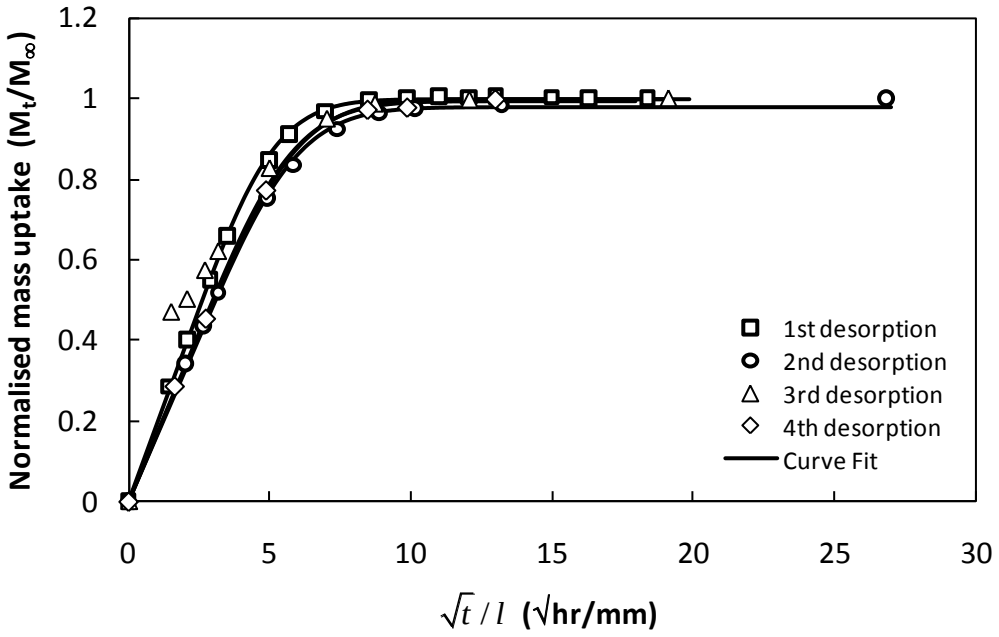

Figure 4.5: Fickian curve fit to moisture desorption for 1 mm thick samples when conditioned at 50°C.

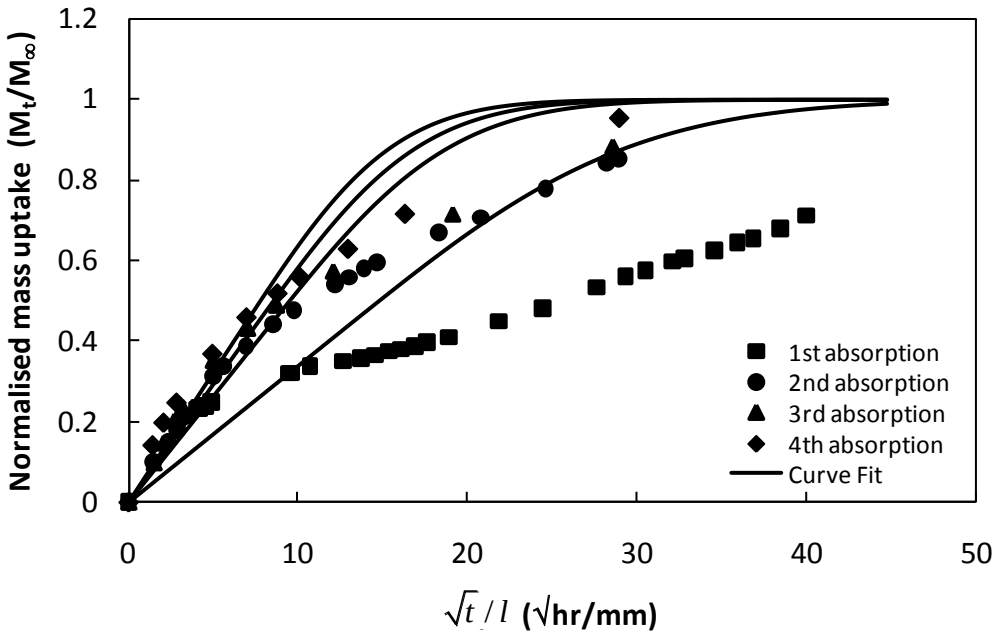

Figure 4.6: Fickian curve fit to moisture absorption for 1 mm thick samples when conditioned at 70°C.

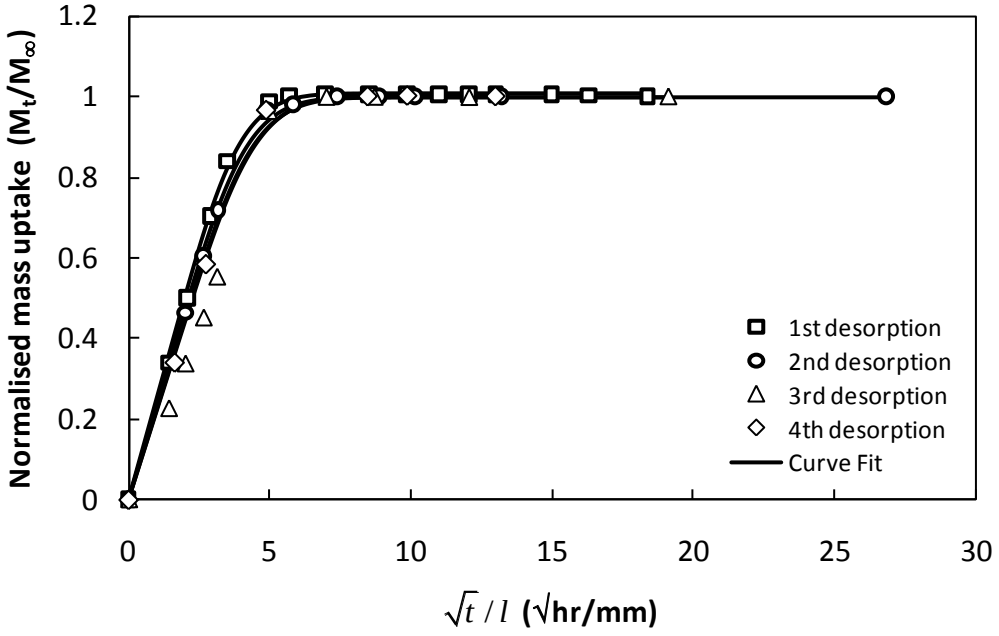

Figure 4.7: Fickian curve fit to moisture desorption for 1 mm thick samples when conditioned at 70°C.

In order to obtain better prediction of the experimental moisture absorption results, the moisture absorption in bulk adhesive samples, conditioned at 50°C and

70°C, was modelled using the dual Fickian model, which was discussed in Section 2.9.3. Comparison of the experimental moisture absorption results and the dual Fickian model predictions at 50°C and 70°C are shown in Figures 4.8 and 4.9, respectively. At both conditioning temperatures, the dual Fickian model predictions of moisture uptake were in good agreement with the experimental moisture uptake results. The secondary rapid uptake, observed during the first moisture uptake at 50°C was not considered in the curve fitting as this model does not account for such discontinuities. The moisture diffusion parameters for absorption, as determined from the dual Fickian model, are given in Table 4.1 and the diffusion parameters for moisture desorption, as determined from the Fickian diffusion model, are given in Table 4.2. The value of D_1 after the first absorption at 50°C is in good agreement with the D_1 value of 0.52 x 10^{-12} m^2/s [176] reported in the literature.

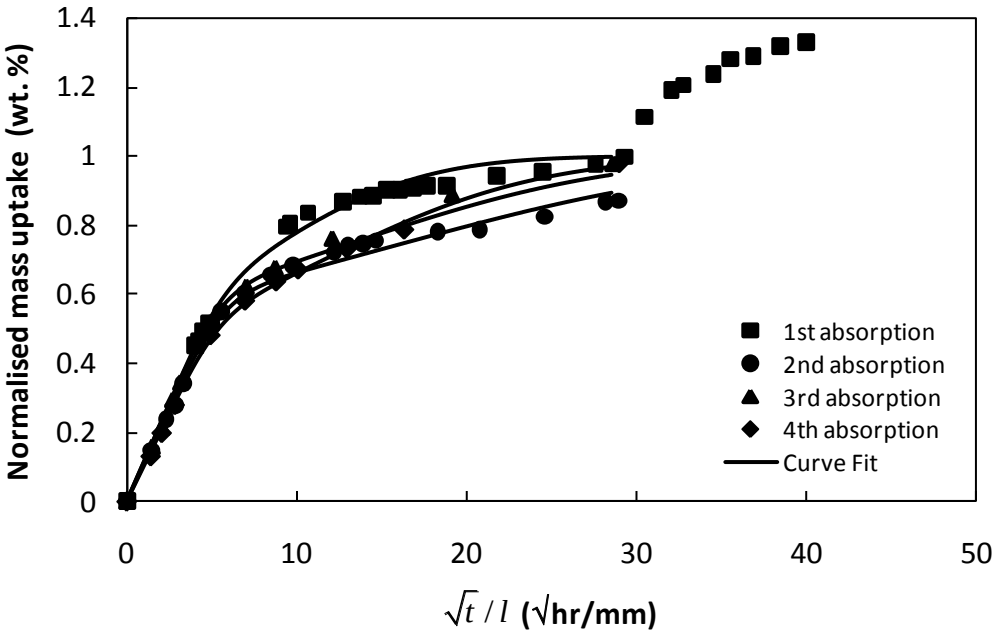

Figure 4.8: Dual Fickian model curve fit to experimental moisture uptake for 1 mm thick samples when conditioned at 50°C.

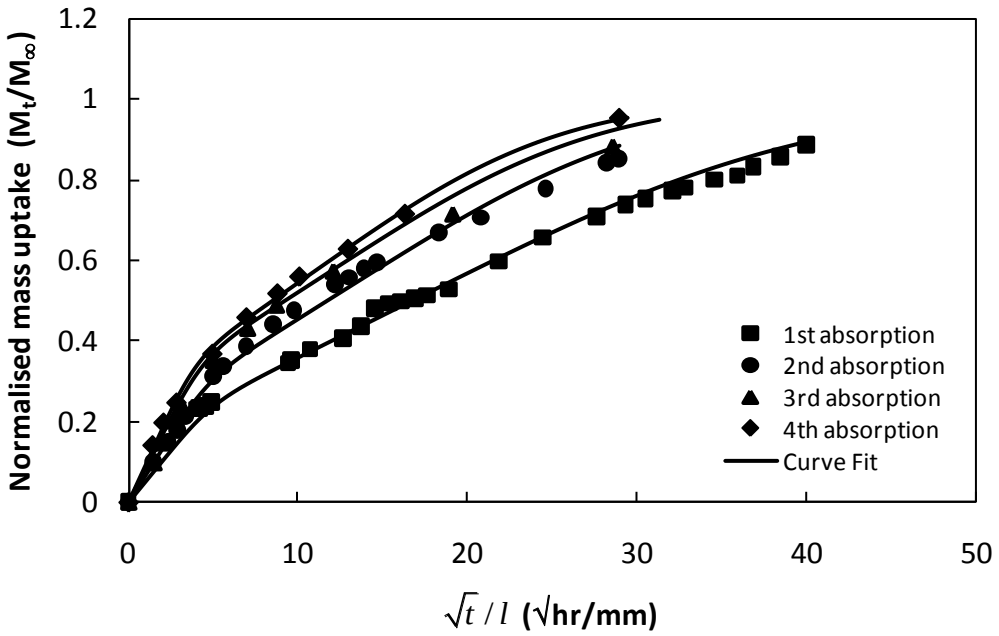

Figure 4.9: Dual Fickian model curve fit to experimental moisture uptake for 1 mm thick samples when conditioned at 70°C.

Table 4.1: Dual Fickian diffusion model parameters for moisture absorption of 1 mm thick adhesive samples.

Absorption cycle	Diffusion coefficient D_1 (m²/s)	Diffusion coefficient D_2 (m²/s)	Saturated moisture content M_∞ (wt%)
	50°C, immersed in water		
First	0.97 x 10^{-12}	31.1 x 10^{-15}	3.7
Second	1.68 x 10^{-12}	44.9 x 10^{-15}	4.0
Third	1.76 x 10^{-12}	66.4 x 10^{-15}	4.2
Fourth	1.82 x 10^{-12}	95.0 x 10^{-15}	4.5
	70°C, immersed in water		
First	2.22 x 10^{-12}	33.3 x 10^{-15}	8.5
Second	2.38 x 10^{-12}	58.1 x 10^{-15}	8.6
Third	2.77 x 10^{-12}	71.4 x 10^{-15}	8.9
Fourth	3.33 x 10^{-12}	84.7 x 10^{-15}	9.4

Table 4.2: Fickian diffusion model parameters for moisture desorption of 1 mm thick samples.

Desorption cycle	Diffusion coefficient D_d (m²/s)
50°C, immersed in water	
First	1.17 x 10^{-12}
Second	1.49 x 10^{-12}
Third	1.51 x 10^{-12}
Fourth	1.82 x 10^{-12}
70°C, immersed in water	
First	3.33 x 10^{-12}
Second	3.05 x 10^{-12}
Third	2.73 x 10^{-12}
Fourth	2.64 x 10^{-12}

The dual Fickian model curve fit to the first moisture uptake at 50°C may be considered adequate for short cycles as it successfully predicts the moisture absorption without the secondary uptake. However, to incorporate the secondary uptake in the analytical model, a phenomenological model based on the moisture contributions of a dual Fickian model and a secondary rapid uptake was considered. A similar methodology has been used by Berens and Hopfenberg [97] to model non-Fickian diffusion based on Fickian and relaxation diffusion components. The saturated moisture content in the adhesive is given by:

$$M_\infty = M_{1\infty} + M_{2\infty} + M_{d\infty} \tag{4.1}$$

where $M_{d\infty}$ is the saturated moisture content due to the secondary moisture uptake. A dual Fickian model with a Heaviside step function was used to model the moisture uptake. A Heaviside step function returns zero for negative values and one for positive values. The secondary moisture uptake was modelled by a power law as this provided the best curve fit to the experimental data from the Fickian, exponential, quadratic polynomial and power law models investigated, as shown in Figure 4.10. This model is termed the dual Fickian with damage (DFD) model as it is

considered that the secondary uptake is likely to be associated with irreversible damage of the polymer. The mass uptake by the DFD model is, hence, given by:

$$M_t = \left(1-\frac{8}{\pi^2}\sum_{n=0}^{\infty}\frac{1}{(2n+1)^2}e^{\frac{-D_1(2n+1)^2\pi^2 t}{4l^2}}\right)\times M_{1\infty} + \left(1-\frac{8}{\pi^2}\sum_{n=0}^{\infty}\frac{1}{(2n+1)^2}e^{\frac{-D_2(2n+1)^2\pi^2 t}{4l^2}}\right)\times M_{2\infty} + \Phi(t-t_1)(at^b+d)\times M_{d\infty} \quad (4.2)$$

where Φ is the Heaviside step function, t_1 is the start time of secondary uptake as determined experimentally and a,b and d are the power law constants determined by curve fitting. It may be seen in Figure 4.10 that the DFD model provides an excellent fit to the first moisture absorption at 50°C.

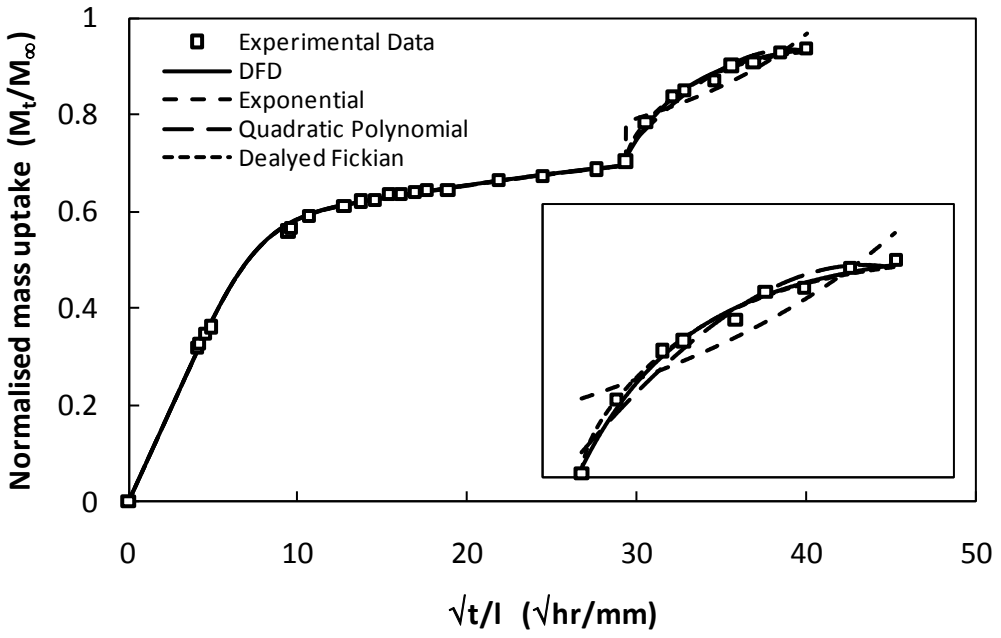

Figure 4.10: Curve fit to first absorption curve using various diffusion models, conditioned at 50°C. The inset shows a close-up of the curve fit to the secondary moisture uptake.

The model parameters obtained from curve fitting the DFD model are given in Table 4.3.

Table 4.3: DFD model curve fit parameters for first moisture absorption curve for 1 mm thick samples conditioned at 50°C.

Diffusion coefficient D_1 (m²/s)	Diffusion coefficient D_2 (m²/s)	t1 (s)	a	b	d
0.93×10^{-12}	47.5×10^{-15}	3.09×10^{6}	-2.56×10^{12}	-4.26	0.85

To summarise, the experimental moisture uptake data for 1 mm thick bulk adhesive samples was fitted to various analytical models. Initially, Fickian diffusion was fitted to the moisture absorption and desorption curves. In all cases, Fickian diffusion was not able to predict the moisture absorption, however, moisture desorption was predicted successfully. The non-Fickian moisture absorption was then fitted by a dual Fickian model, which provided good predictions when no secondary uptake was present. Thus a combination of dual Fickian and Fickian diffusion models may be used to predict the absorption and desorption cycles in the adhesive under cyclic moisture conditions as long as the secondary uptake point is not reached. This selected model combination is used in Chapter 5 where a methodology for prediction of moisture diffusion under cyclic conditions is developed.

4.2.3 Moisture Dependent Mechanical Properties

The stress vs strain curves of bulk adhesive samples, tensile tested at different moisture concentrations at 50°C, are shown in Figure 4.11. The plots are an average of results obtained after testing three specimens at each moisture condition and the standard deviation of the stress results was ±2.6 MPa in all samples. The moisture content in each bulk adhesive specimen is given as the ratio of moisture content at any time, M_t, measured by gravimetric means, to the saturated moisture content, M_∞, i.e. M_t / M_∞. During the first absorption cycle, an increase in strain to failure, over unconditioned specimens, was observed for all moisture concentrations except for M_t / M_∞ = 0.12. The increased strain to failure may be due to the increased plasticisation of the adhesive by moisture. In dried bulk adhesive samples, the strain to failure decreased to a value less than the unconditioned samples, which represents a brittle failure compared to the

unconditioned and conditioned specimens. An increase in strain to failure also occurred after the second moisture absorption cycle, which is consistent with the plasticisation effects of moisture.

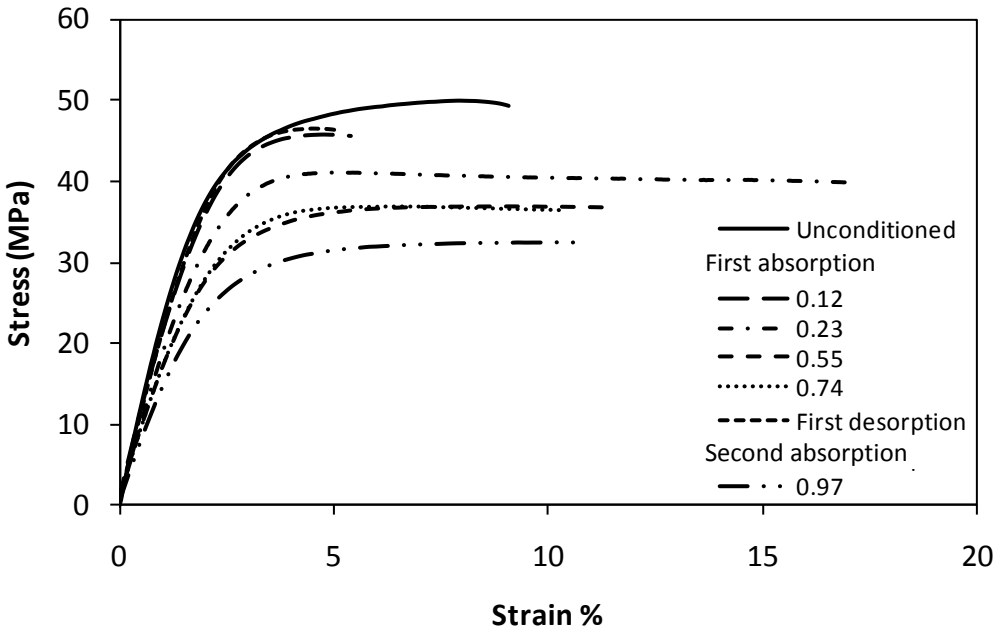

Figure 4.11: Moisture dependant stress vs. strain curves for the adhesive at different values of M_t / M_∞ when conditioned at 50°C.

The effect of moisture cycling on the elastic modulus (E) and ultimate tensile strength (σ_{ult}), as determined from the experimental stress-strain curves, can be seen in Figures 4.12 and 4.13, respectively. The lines joining the experimental data points are to show trends only and join the average values at each data point. A decrease in E with increasing moisture concentration was observed during the first absorption cycle. At relatively high moisture concentrations, above 2 wt%, the change in E reduced. A similar trend was observed in σ_{ult}, where an increase in moisture content decreased the σ_{uts}. There was again a progressive decrease observed from unconditioned state to samples with 2 wt% moisture, however, no change in σ_{ult} was observed above 2 wt% moisture. The minimal change in E and σ_{uts} above 2 wt% moisture indicates that most of the degradation in the mechanical properties took place earlier in the absorption cycle. The E and σ_{ult} for dried bulk adhesive samples regained 95% and 93% of their unconditioned values,

respectively. This shows that a large portion of the degradation of the adhesive was reversible and may be due to plasticisation of the adhesive, which is considered a reversible mechanism [64]. However, a small percentage of irrecoverable damage also occurred in the adhesive, which may be attributed to chemical degradation or mechanical effects, such as micro cracking. Following a second absorption cycle, with a 3.7 wt% moisture uptake, E and σ_{ult} decreased more than in the first absorption cycle. This may be as a consequence of the irreversible damage present in the adhesive after the first absorption.

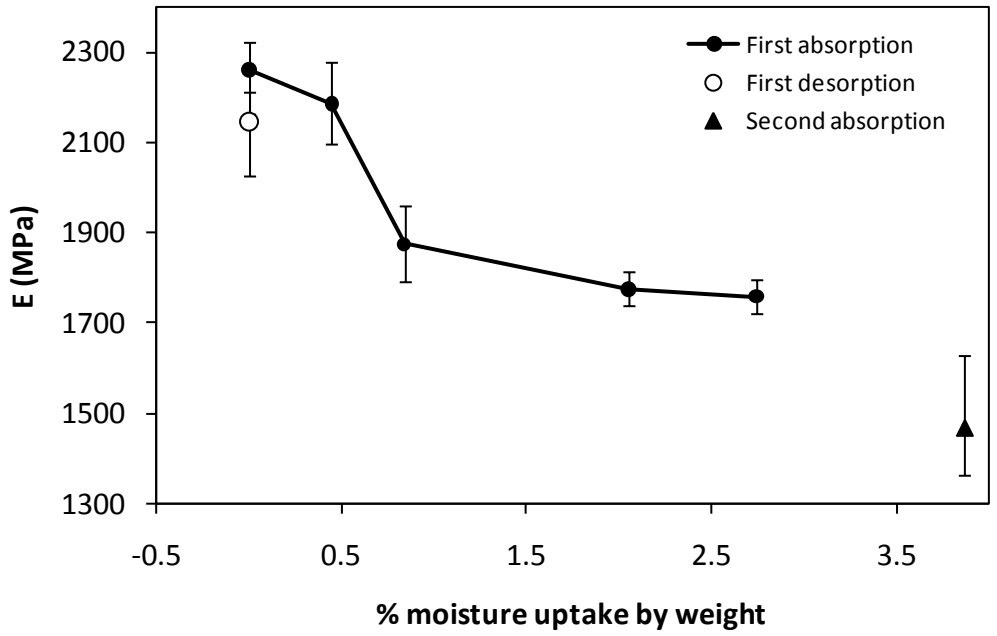

Figure 4.12: Elastic modulus as a function of moisture diffusion when conditioned at 50°C.

The stress vs strain curves of bulk adhesive samples, tensile tested at different moisture concentrations at 70°C, are shown in Figure 4.14. A consistent change in the strain to failure was not observed with increasing moisture content. However, the dried bulk tensile samples exhibited brittle failure compared to the unconditioned and conditioned bulk samples. This was also observed in dried bulk samples conditioned at 50°C and is further evidence of chemical and/or mechanical damage after the first absorption. A ductile failure, with a large amount of plastic strain was observed after the second absorption cycle.

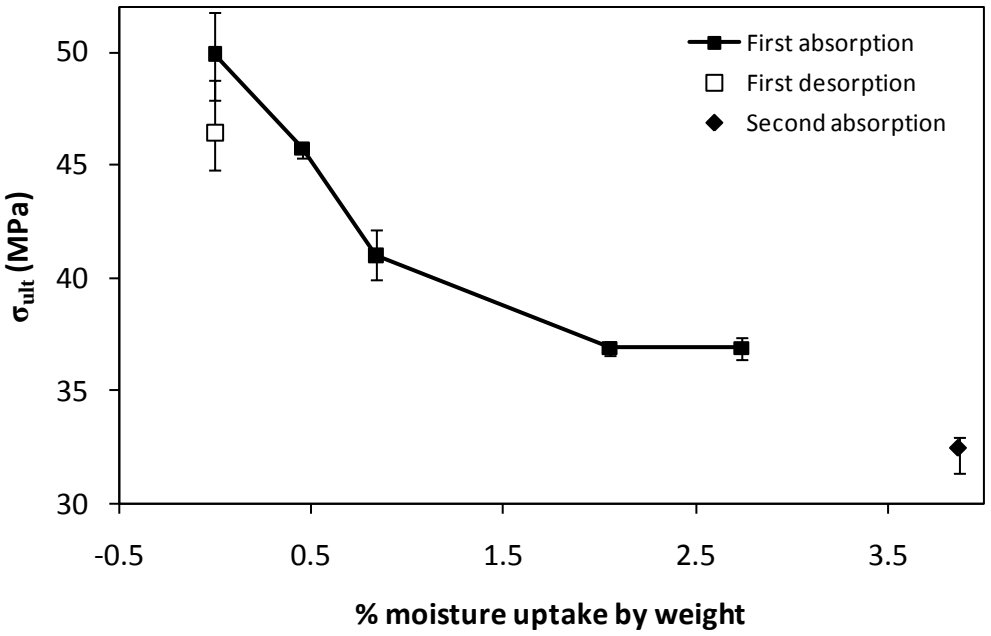

Figure 4.13: Ultimate tensile strength as a function of moisture diffusion when conditioned at 50°C.

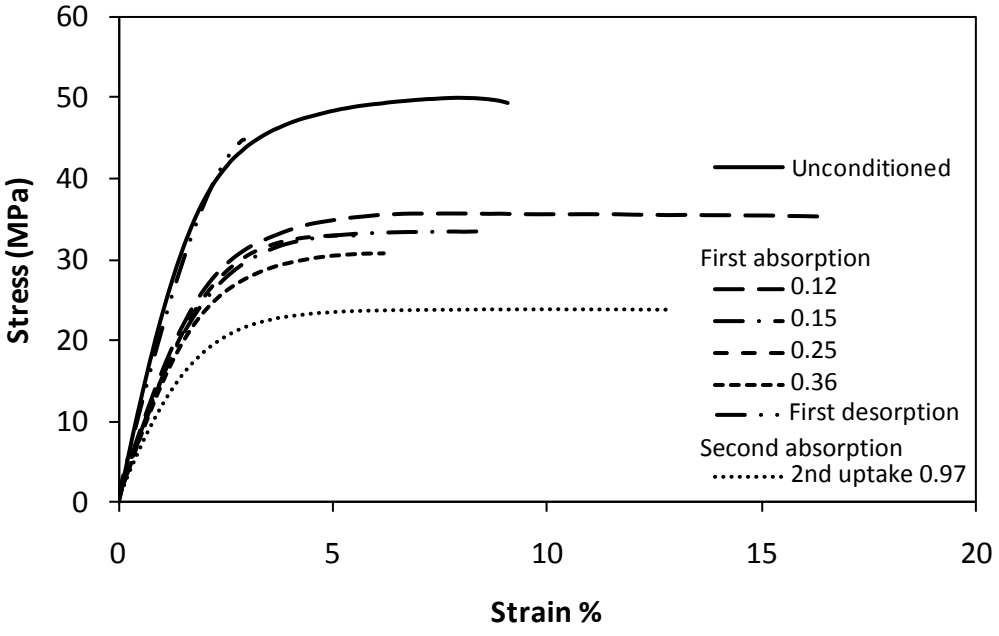

Figure 4.14: Moisture dependant stress vs. strain curves for the adhesive at different values of M_t / M_∞ when conditioned at 70°C.

Both E and σ_{ult} showed a progressive decrease with increasing amount of moisture during the first absorption cycle, as can be seen in Figures 4.15 and 4.16. Upon drying, E and σ_{ult} recovered to 94% and 90% of the unconditioned values, respectively, thus exhibiting a large degree of reversibility. The second moisture absorption cycle similarly showed a decrease in E and σ_{ult} with increasing moisture content.

A comparison of change in E and σ_{ult} with moisture diffusion at 50°C and 70°C was carried out by normalising the moisture uptake to the saturated moisture uptake of the adhesive at each temperature. The change in E and σ_{ult} was compared at 70% normalised moisture uptake during the first absorption, which was the highest moisture concentration available from the experimental data. The value of E decreased by 22% and 37% from the unconditioned values at 50°C and 70°C, respectively. At the same moisture condition, σ_{ult} decreased by 26% and 39% of the unconditioned value at 50°C and 70°C, respectively. The higher degradation of mechanical properties at 70°C than 50°C may be owing to the increased amount of moisture absorption at 70°C. Despite the greater decrease in E and σ_{ult} at 70°C than 50°C, the percentage recovery of E and σ_{ult} was of a similar magnitude at both conditioning temperatures i.e. more than 90% of the unconditioned values. This suggests that the increased amount of moisture at 70°C mostly contributed to the reversible mechanism of plasticisation.

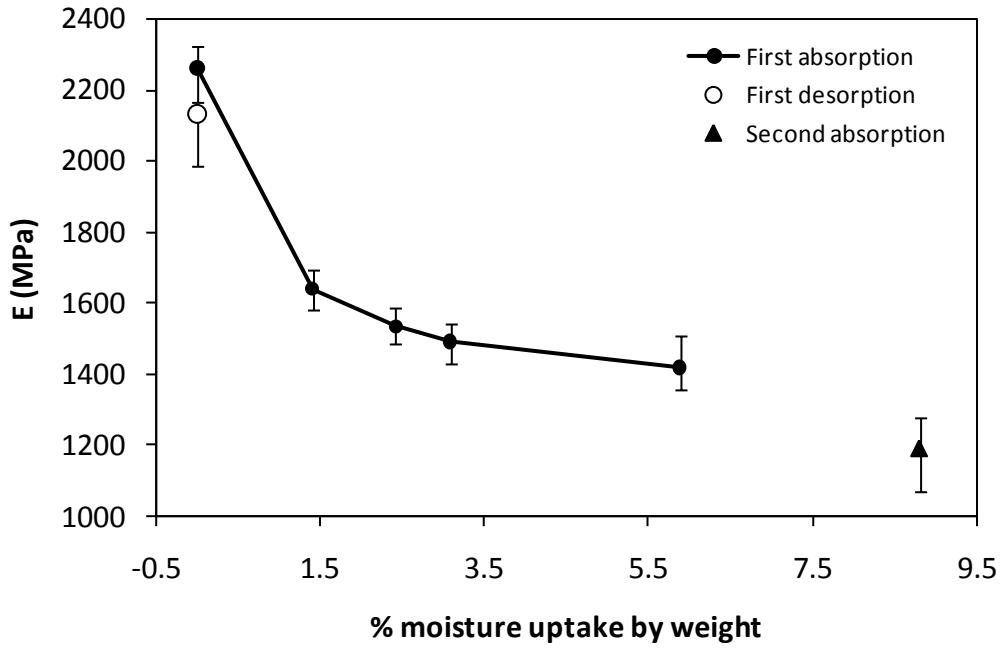

Figure 4.15: Elastic modulus as a function of moisture uptake when conditioned at 70°C.

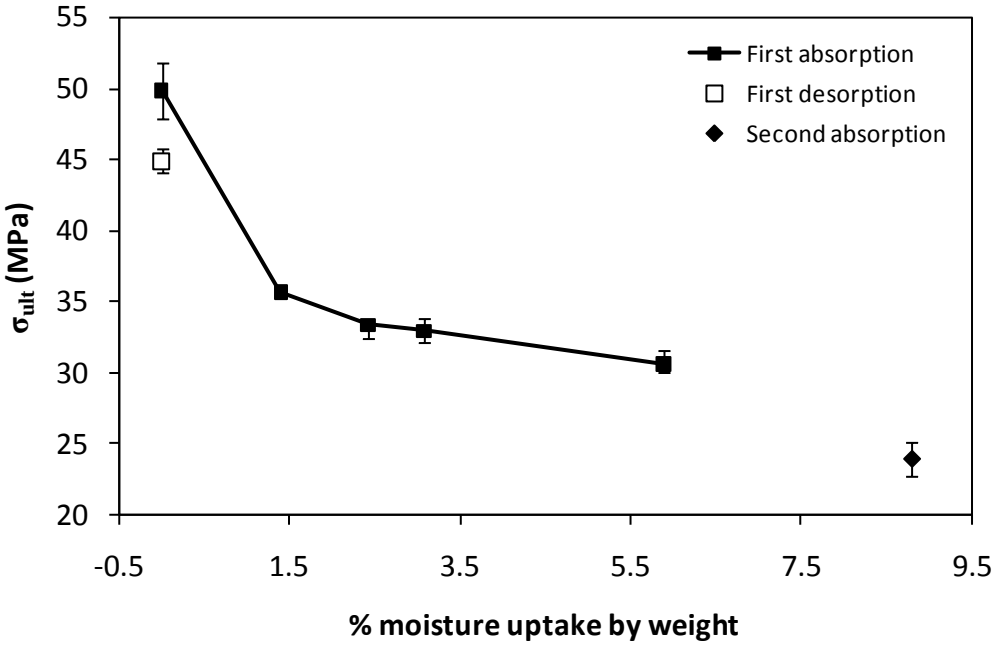

Figure 4.16: Ultimate tensile strength as a function of moisture uptake when conditioned at 70°C.

In summary, the mechanical properties of the bulk adhesive degraded with increased moisture concentration in the adhesive. The dried bulk samples showed a large degree of recovery in E and σ_{ult} at both 50°C and 70°C. The degradation in E and σ_{ult} was higher at 70°C than 50°C, however, the percentage recovery of E and σ_{ult} was of a similar magnitude. More brittle failure was observed in dried bulk samples than either the unconditioned or conditioned bulk samples at both conditioning temperatures, indicating irreversible damage in the first cycle.

4.3 Mechanical Properties of the adherend Al2024

It was explained in Chapter 3 that two types of the aluminium alloy adherend Al2024, were used in the single lap joint adherends i.e. Al2024 T3 and O. An elastic material definition of Al2024 T3 was used in the numerical models as this method exhibited no yielding during the tensile testing of the single lap joints. The elastic properties of Al2024 T3 are available in literature and are shown in Table 4.4. Elasto-plastic material definition was used in the numerical models for Al2024 O owing to the observed plastic deformation during tensile testing of the joints. A representative stress-strain curve obtained from tensile testing an Al2024 O sample is given Figure 4.17.

Table 4.4: Mechanical properties of aluminium alloy 2024 T3 [185] and O.

Mechanical Property	Value
Elastic modulus (GPa)	73
Poisson's ratio	0.33
Yield Strength (MPa)	
T3	345
O	75.8

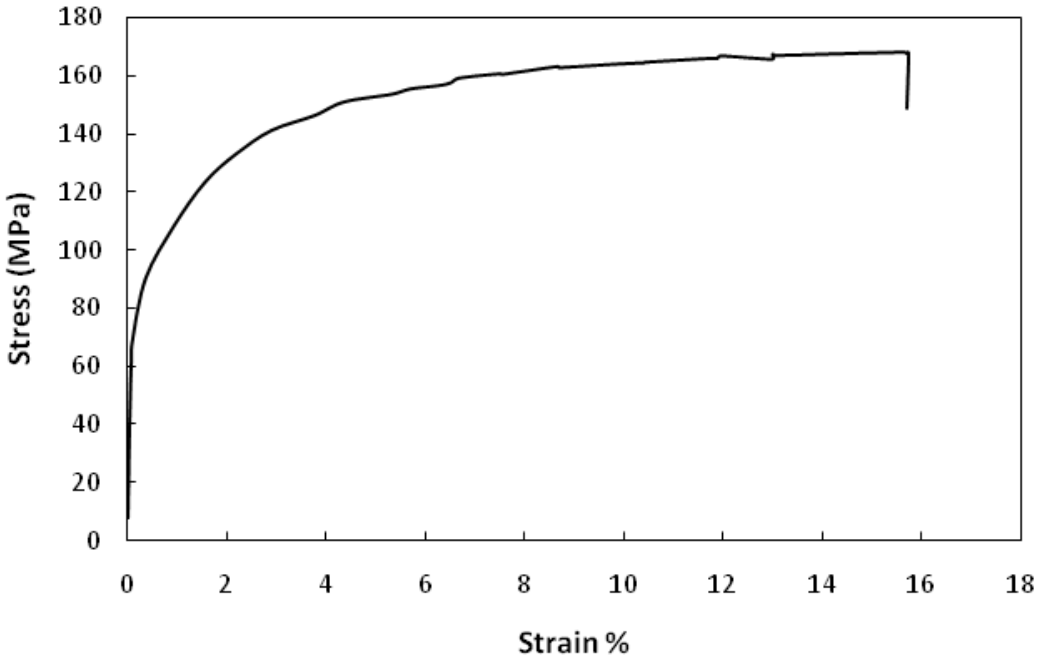

Figure 4.17: Tensile stress vs strain response of Al2024 O.

4.4 Single Lap Joints

The tensile testing of single lap joints conditioned at 50°C and 70°C was carried out to determine joint durability. The results of these tensile tests are discussed in this section.

Figure 4.18 plots the failure load as a function of conditioning time for the single lap joints conditioned at 50°C. It can be seen that the strength of unconditioned Al2024 O joints is significantly less than that of Al2024 T3 joints. This is because of the plastic deformation of the Al2024 O adherends during tensile testing, which occurred because of the lower yield stress of Al2024 O (75.8 MPa) compared to Al2024 T3 (345 MPa). The Al2024 T3 joints exhibited a progressive decrease in strength with conditioning time. When Al2024 T3 joints were dried after conditioning for 7 days and tensile tested, they achieved at least 98% of the original strength. The recovered percentage of the original strength was similar for all moisture absorption time intervals. The Al2024 O joints showed a more rapid decrease in strength than the Al2024 T3 joints in the initial conditioning period of 14 days. However, a strength increase was then observed after tensile testing for 28

days of conditioning. After moisture absorption for 56 days, the strength of the joint recovered to about 86% of its original strength and remained at a similar value after conditioning of 182 days. The Al2024 O joints were also tested after drying and the strength recovered to 88% or more of the unconditioned joint strength.

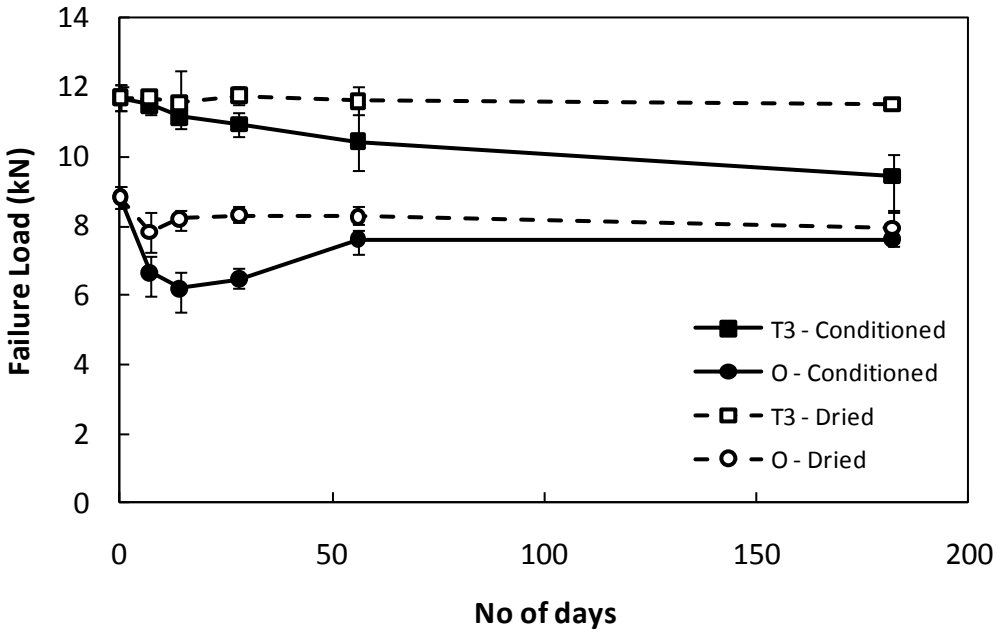

Figure 4.18: Failure load of the single lap joints after conditioning at 50°C.

The failure load as a function of conditioning time for single lap joints, conditioned at 70°C, is plotted in Figure 4.19. As was seen at 50°C, the overall strength of the conditioned Al2024 O type joints was significantly lower than the Al2024 T3 joints. A progressive degradation in joint strength, with increasing conditioning time, was observed for both Al2024 T3 and O joints. Al2024 O joints did not exhibit strength recovery at any stage of moisture conditioning, which was in contrast to their response observed at 50°C. This may be owing to the relatively large amount of moisture in the adhesive layer at 70°C compared with 50°C, resulting in increased plasticisation that would offset the stress relaxation effects.

When the joints were dried, strength recovery was observed in both Al2024 T3 and O joints. The T3 joints showed better overall strength recovery as they achieved 91.7% of their original strength after 182 days of conditioning while Al2024 O joints achieved 76.6% of their original strength after the same conditioning time. A

comparison of strength degradation of Al2024 T3 and O joints at 50°C and 70°C reveals that a greater reduction in failure load occurred at 70°C than at 50°C.

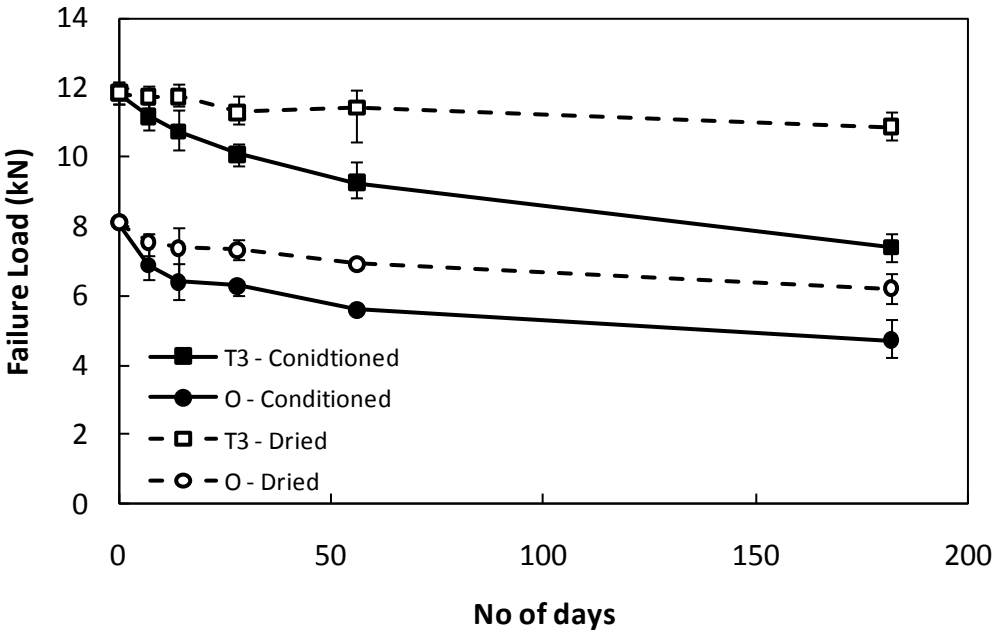

Figure 4.19: Failure load of the single lap joints after conditioning at 70°C.

The failure load of Al2024 T3 single lap joints manufactured with adherends prepared using a CAA pretreatment, at different conditioning times, is shown in Figure 4.20. This batch of joints provided a comparison of joint durability and strength recovery between the ACDC and CAA pretreated joints as CAA pretreatment is considered the present industry standard for aluminium adhesive joints. The unconditioned strength of ACDC and CAA pretreated Al2024 T3 joints was of similar magnitude as can be seen from Figure 4.19 and Figure 4.20. The strength of CAA pretreated Al2024 T3 joints decreased with increasing moisture content and after 182 days of conditioning this had reduced to 58.8% of the unconditioned strength. In comparison, the ACDC pretreated Al2024 T3 had reduced to 62.4% of their unconditioned strength after 182 days of conditioning. Thus the strength degradation in ACDC and CAA pretreated joints was of similar magnitude after the same conditioning time. The CAA pretreated joints showed a large amount of strength recovery, where joints recovered to at least 92.6% of their unconditioned strength after drying. The minimum strength recovery in ACDC

pretreated joints was 91.7% of the unconditioned strength, which again was of similar magnitude to CAA pretreated joints. Thus the durability performance of the two types of pretreated joints was similar under the considered conditioning environment.

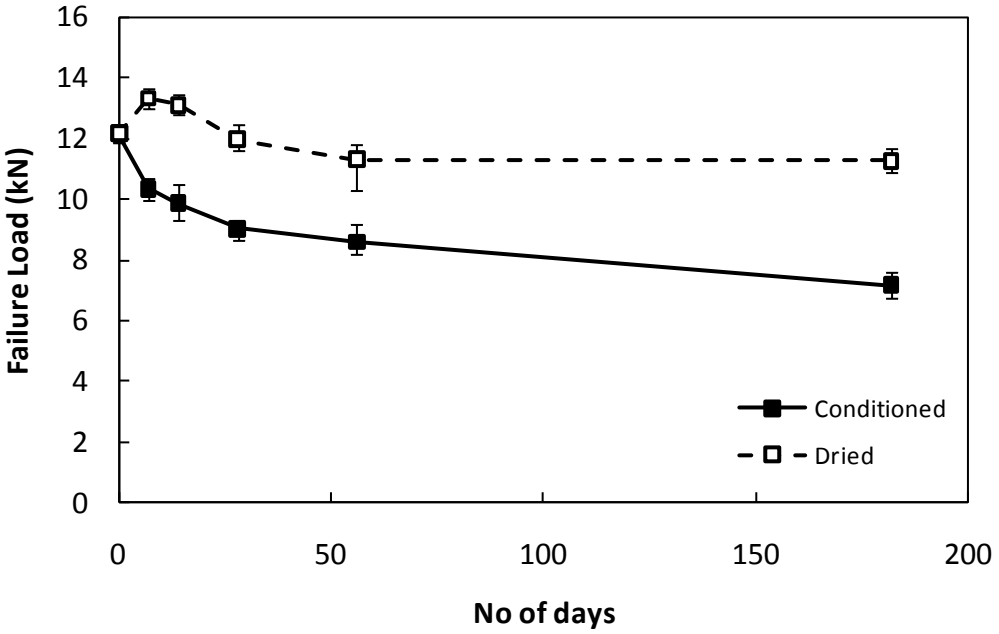

Figure 4.20: Failure load of the single lap joints with CAA pretreatment, after conditioning at 70°C.

The failure loads of Al2024 T3 single lap joints conditioned at 70°C for multiple 15 days absorption and desorption cycles each are given in Figure 4.21. The joint strength showed a fairly steady decrease with number of absorption and desorption cycles and the joint strength had reduced to 75% of the unconditioned strength after the fifth absorption. This showed that the adhesive structure was changing over the multiple absorption and desorption cycles and as a result, the strength of the joint decreased over absorption cycles even when the absorption cycles were of similar duration.

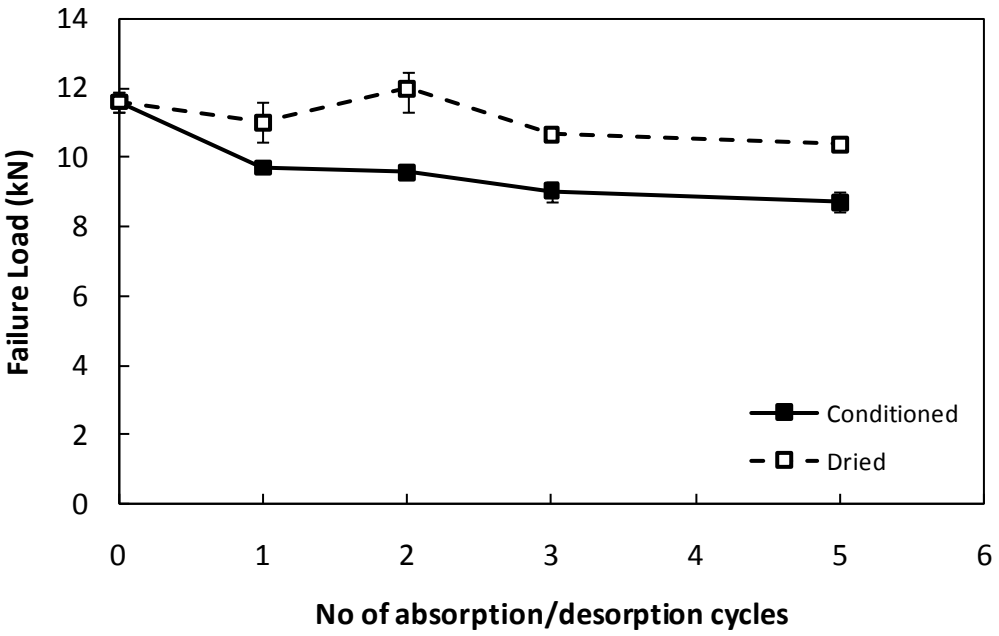

Figure 4.21: Failure load of the single lap joints after conditioning at 70°C for 15 days absorption and desorption cycles each.

The percentage reduction in joint strength, S_R, in each diffusion cycle may be determined by:

$$S_R = \frac{S_{N-1} - S_N}{S_{N-1}} \times 100 \tag{4.3}$$

where S_N is the strength of the joint after N number of absorption or desorption cycles. The strength reduction in each diffusion cycle is given in Figure 4.22. The strength reduction in each diffusion cycle was of similar magnitude except the third cycle where a 24.7% reduction was observed. This may be owing to the higher dried strength achieved in the previous desorption.

The recovery in the strength of the joints on drying was high and a minimum of 89% of the unconditioned strength was observed after the fifth desorption.

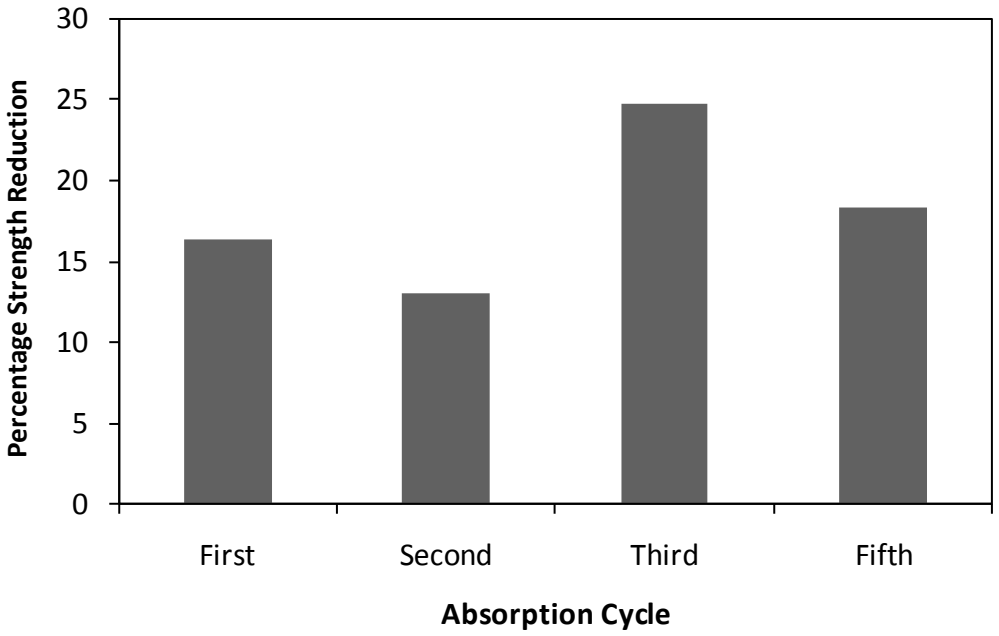

Figure 4.22: Percentage strength reduction in Al2024 T3 joint strength when conditioned at 70°C.

In summary, the moisture conditioning of the Al2024 T3 and O single lap joints caused a progressive decrease in the joint strength, except in Al2024 O joints, conditioned at 50°C. In Al2024 O joints, a strength recovery was observed in the later stages of conditioning. The ACDC and CAA pretreated Al2024 T3 joints showed similar durability performance after conditioning. All the single lap joints showed a large amount of strength recovery after drying.

4.5 Failure Surface Characterisation

The failure surfaces of the single lap joints were analysed to determine the failure type and failure locus. The results of the failure surface investigations are given in the following sections.

4.5.1 Digital Image Processing

Digital image processing provided a method of quantifying the failure type. The results from Al2024 T3 and O joints, conditioned at 50°C are discussed first,

followed by the results from Al2024 T3 and O joints conditioned at 70°C. The failure surfaces of the Al2024 T3 joints pretreated using CAA were similar to the ACDC pretreated Al2024 T3 joint failure surfaces and, hence, are not discussed. The Al2024 T3 joints conditioned at 70°C for multiple cycles also had failure surfaces similar to Al2024 T3 joints conditioned at 70°C and are, similarly, not discussed.

Figure 4.23 shows a comparison of failure load and fractional adhesive area at different moisture absorption time intervals for Al2024 T3 joints, conditioned at 50°C. The fraction of cohesive failure decreased i.e. the amount of apparent interfacial failure increased with the decrease in failure load at 7 and 14 days of moisture absorption. However, the fraction of cohesive failure increased after 28 and 56 days of moisture absorption, finally decreasing to a minimum of 59% after 182 days of moisture absorption.

The analysis of dried Al2024 T3 joints, conditioned at 50°C, also showed mixed failure at all conditioning time intervals. The digital image analysis results are shown in Figure 4.24. The fraction of adhesive area, i.e. cohesive failure, decreased after 7 days of moisture absorption. Then an increase in fractional cohesive failure was seen for 14 and 28 days of moisture absorption and finally the fraction of cohesive failure decreased again after 56 days of moisture absorption. Although the fraction of cohesive failure area does not exactly follow the trend of failure load, the failure remained mainly cohesive. The mixed cohesive and apparent interfacial failure of joints means that the fracture path travels both through the adhesive as well as within the interfacial regions. This may be attributed to the degradation in the adhesive and primer properties. As already mentioned, plasticisation of the adhesive caused by moisture ingress causes degradation of the elastic modulus and lower failure strength would be expected, as observed. Residual adhesive was not observed on apparent interfacial surfaces as was observed in cohesive failure and it was not possible to identify the locus of failure form the visual inspection of the apparent interfacial failure surfaces. A combination of X-Ray Photoelectron Spectroscopy (XPS) and Scanning Electron Microscopy (SEM) was used to determine if the failure was in primer or the oxide layer and is discussed in Sections 4.5.2 and 4.5.3, respectively.

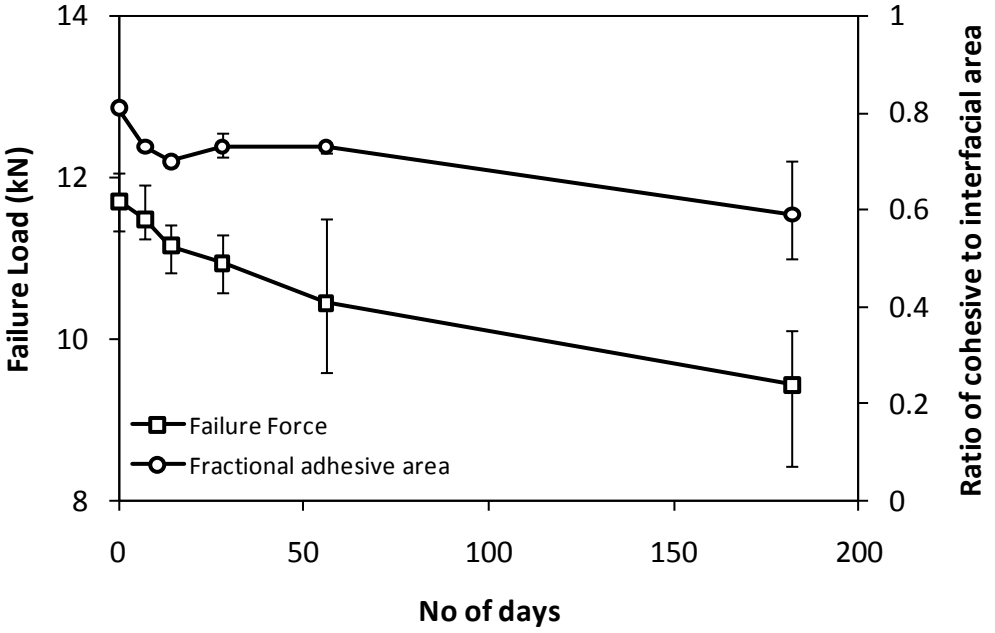

Figure 4.23: Comparison of failure load and failure type in Al2024 T3 joints after conditioning at 50°C.

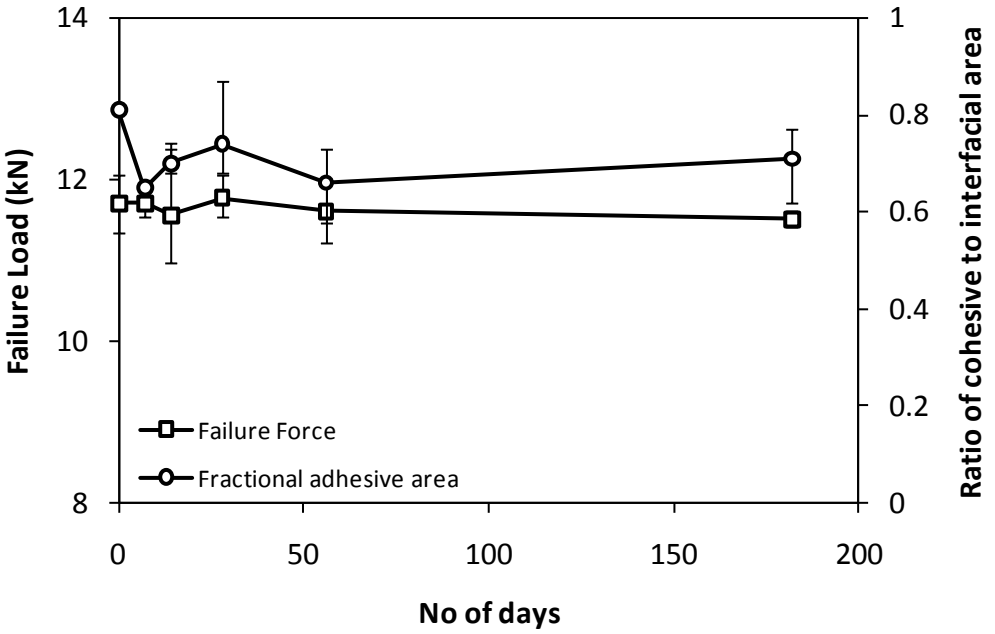

Figure 4.24: Comparison of failure load and failure type in Al2024 T3 joints after conditioning at 50°C and drying.

A comparison of failure load and failure type for Al2024 O joints, conditioned at 50°C, is shown in Figure 4.25. The ratio of cohesive to interfacial failure changed

with the failure load of joints. As the failure load of the joint decreased after 7 and 14 days of moisture absorption, the failure surfaces showed more apparent interfacial failure. The strength of the joint started to recover after 28 days of moisture absorption and recovery continued for 56 and 182 days of moisture absorption. The ratio of cohesive to interfacial failure followed a trend similar to the failure load of the joints. In Al2024 O joints dried after conditioning, an increase in the interfacial failure was observed in joints conditioned for 7 and 14 days and then dried, as shown in Figure 4.26. As the recovered joint strength increased after 28 days of conditioning, increased cohesive failure was also observed. Similar behaviour was observed after 56 and 182 days of conditioning, where mostly cohesive failure was observed.

In Al2024 T3 joints, conditioned at 70°C, the failure load progressively decreased with the increased conditioning time, as shown in Figure 4.27. The amount of apparent interfacial failure increased with the decrease in the failure load of the joints. When the Al2024 T3 joints were dried after conditioning, a recovery in the failure load was observed. The amount of cohesive failure also improved compared to the conditioned joints and the joints failed more cohesively, which may be seen in Figure 4.28. The least amount of strength recovery was observed in joints conditioned for 182 days and dried. These joints also showed the least amount of increase in cohesive failure compared to the conditioned joints.

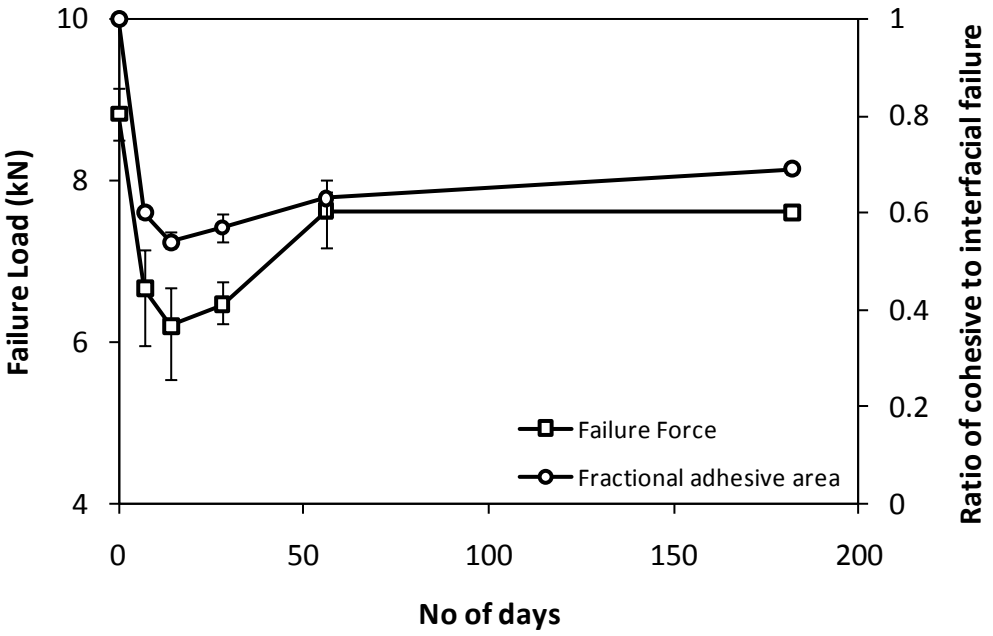

Figure 4.25: Comparison of failure load and failure type in Al2024 O joints after conditioning at 50°C.

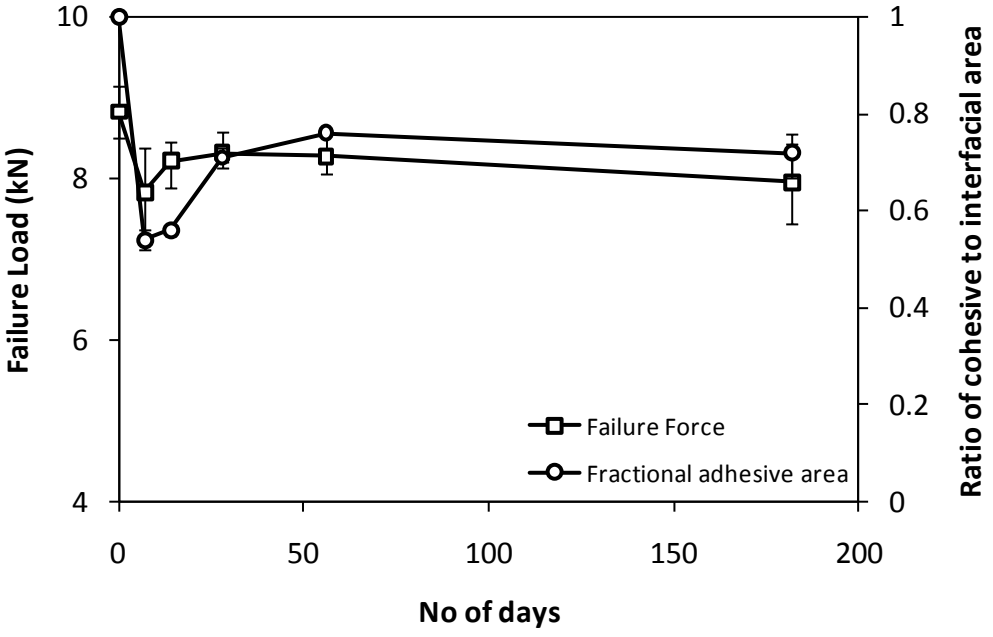

Figure 4.26: Comparison of failure load and failure type in Al2024 O joints after conditioning at 50°C and drying.

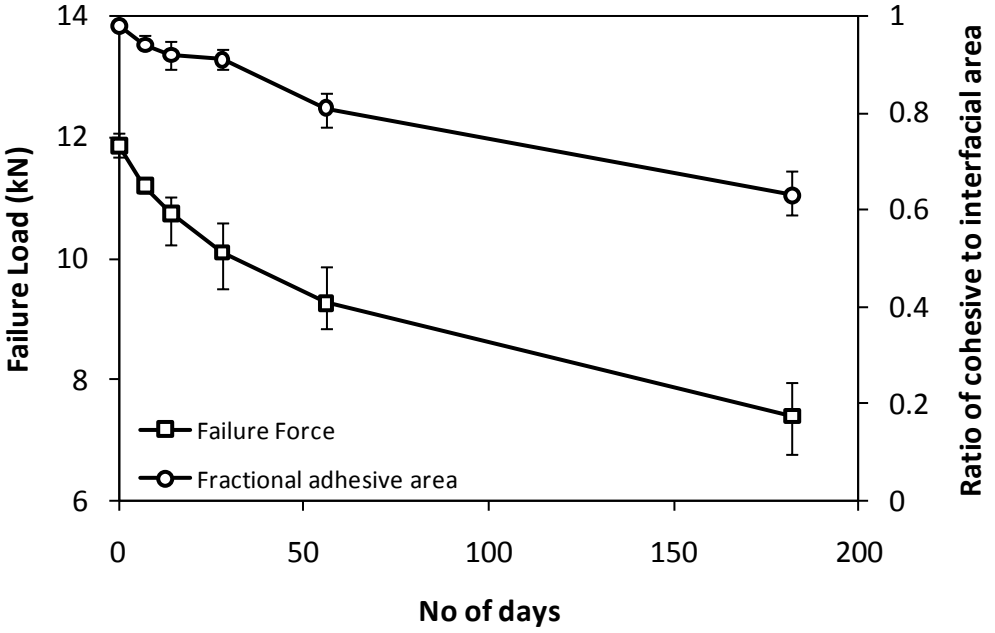

Figure 4.27: Comparison of failure load and failure type in Al2024 T3 joints after conditioning at 70°C.

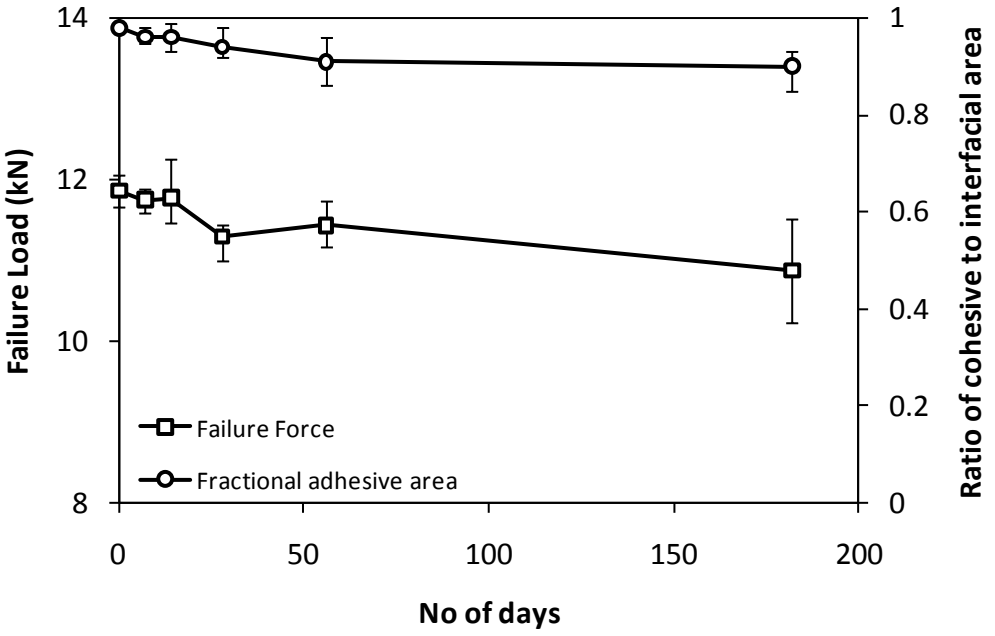

Figure 4.28: Comparison of failure load and failure type in Al2024 T3 joints after conditioning at 70°C and drying.

The failure load of Al2024 O joints, conditioned at 70°C, decreased with moisture conditioning, however, the failure surface did not show a clear trend based on

moisture content, as is shown in Figure 4.29. The amount of interfacial failure increased after 7 days of moisture absorption and similar results were observed after 14 and 28 days of conditioning. The failure surfaces became more cohesive after 56 and 182 days of conditioning. In Al2024 O joints dried after conditioning at 70°C, the failure surfaces did not show a consistent change with increasing conditioning time as shown in Figure 4.30. The failure surfaces became predominantly cohesive after 28 and 56 days of conditioning and drying while apparent interfacial failure increased after 182 days of conditioning and drying. The failure surfaces in conditioned and dried joints had more than 80% cohesive failure.

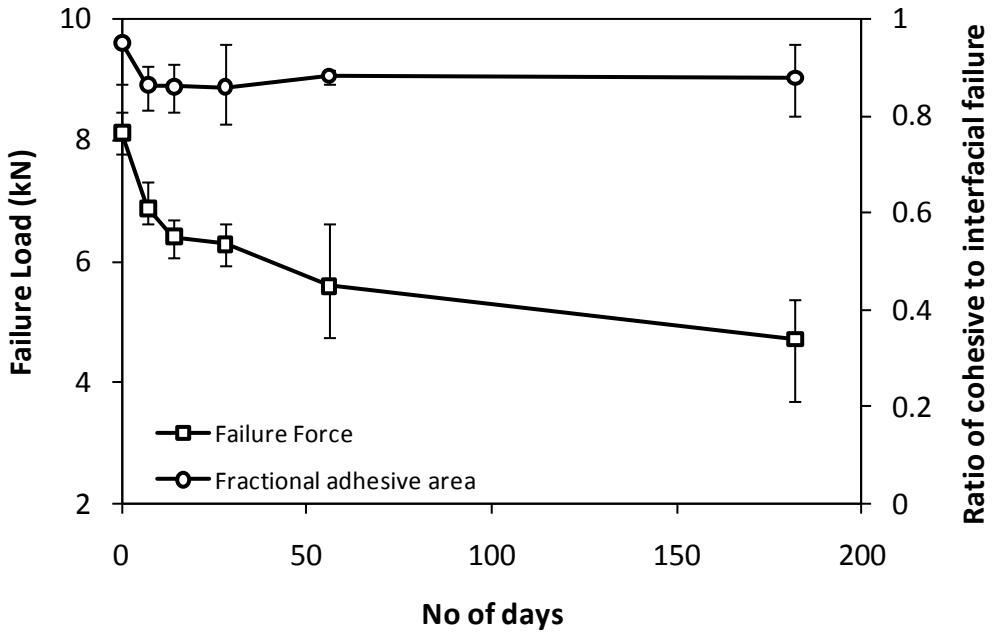

Figure 4.29: Comparison of failure load and failure type in Al2024 O joints after conditioning at 70°C.

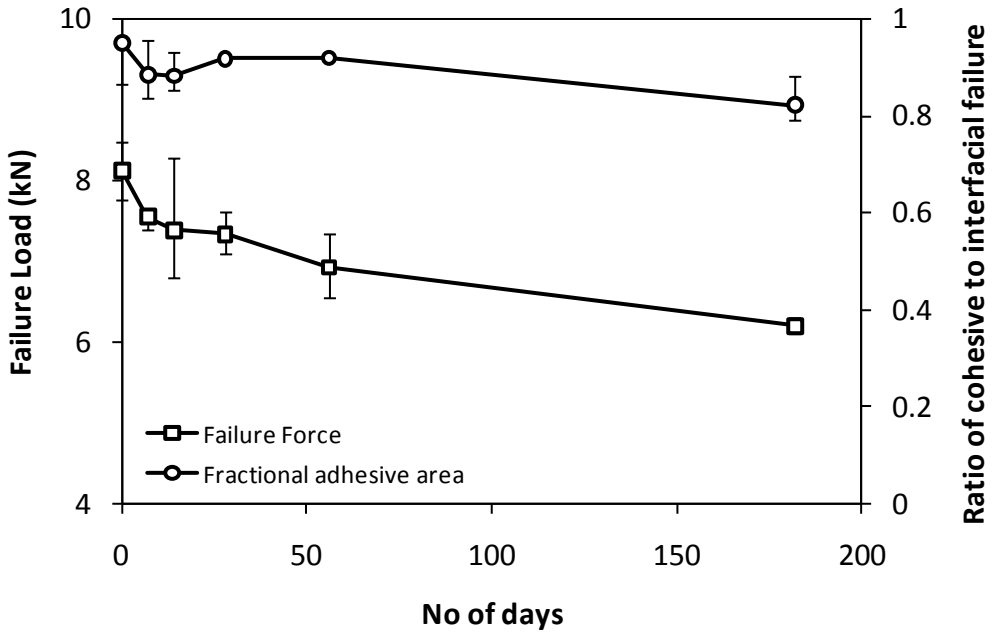

Figure 4.30: Comparison of failure load and failure type in Al2024 O joints after conditioning at 70°C and drying.

Consideration of Figure 4.23 to Figure 4.30 indicates that there is a relationship between joint strength and failure type, with lower joint strength corresponding to increased apparent interfacial failure. Another common trend in most of these figures is a decrease and recovery in proportion of cohesive failure between zero and 56 days exposure. This is more pronounced in the joints with Al2024 O adherends and corresponds to a similar drop and recovery in joint strength.

4.5.2 X-Ray Photoelectron Spectroscopy (XPS) Analysis

The failure of the unconditioned joints was predominately cohesive failure of the adhesive layer. The results of the XPS analysis of the Al2024 T3 and O joints are shown in Table 4.5. Beginning with the Al2024 T3 joints, the unconditioned joints were initially analysed in order to establish a baseline, indicative of cohesive failure. Surfaces of the opposing adherends of a joint were covered with the adhesive when cohesive failure was observed. However, in case of apparent interfacial failure, one of the adherends was covered with the adhesive while the opposing adherend had patches of the adhesive with metal.

In Table 4.5, the adherends of a failed joint are referred to as "metal" and "adhesive" side irrespective of the type of failure. Thus, in case of cohesive failure, one adherend is arbitrarily referred to as metal. For the unconditioned Al2024 T3 joint, both failure surfaces showed large amounts of carbon, which is characteristic of the failure of epoxies. Nitrogen was also detected, which is also indicative of failure in the adhesive layer. A small amount of aluminium was detected on the metal side, which may be the result of signal detection from the edge of the sample or due to surface contamination during the sample preparation process. Aluminium was not detected on the adhesive side.

Table 4.5: Element compositions on the failure surface as obtained by XPS.

Joint type	Moisture conditioning at 50°C	Failure surface	Failure surface composition				Percent of overlap
			Al	O	C	N	
T3	Unconditioned	Metal	1.2	15.1	81	1.3	19
		Adhesive	-	16.3	82.5	Trace	81
	56 days in water	Metal	1.9	14.6	82.4	1.1	27
		Adhesive	1.4	13.3	84.2	1.2	73
O	Unconditioned	Metal	0.5	14.2	83.6	0.8	-
		Adhesive	-	13.6	85.8	Trace	100
	14 days in water	Metal	13.9	27.6	56.1	0.4	46
		Adhesive	2.6	17.3	80	1	54
	Dried after 7 days in water	Metal	18	27.8	49.9	-	46
		Adhesive	-	16.8	82.9	Trace	54

Al2024 T3 joints conditioned for 56 days were also analysed with XPS. These joints had more apparent interfacial failure than the unconditioned joints. A small amount of aluminium was detected on the adhesive side, which was similar to the earlier observation of aluminium in the cohesive failure and may not be an indication of oxide layer failure. A failure through the oxide layer would have shown large amount of aluminium on both the metal and adhesive sides. The metal side also had only a small amount of aluminium present. The amount of carbon on both the metal and adhesive sides was high, indicating failure was either through the adhesive layer or through the interphasial polymer. Nitrogen was also detected on

both sides of the failure surface. This suggests that even though some patches of apparent interfacial failure were present; the failure predominately occurred within or between the adhesive and primer layers, remaining largely cohesive.

In the case of the Al2024 O joints, the surfaces of unconditioned joints with predominately cohesive failure had similar composition to the unconditioned Al2024 T3 joints. The adhesive side had no aluminium while a very small amount of aluminium was detected on the metal side. A large amount of carbon and presence of nitrogen, as found in a cohesive failure, were also present.

The Al2024 O joints conditioned for 7, 14 and 28 days exhibited large areas of apparent interfacial failure. The maximum reduction in joint strength was observed after 14 days of conditioning, with 46% of apparent interfacial area. When analysed using XPS, it was seen that a small amount of aluminium was present on the adhesive face of an Al2024 O joint conditioned for 14 days. The carbon percentage was about 80%, which is typical of an epoxy adhesive. The metal face of the joint, however, showed a significantly higher concentration of the aluminium but also showed presence of nitrogen on the surface. The nitrogen indicates that there might be a very thin layer of primer present on the metal oxide surface. The percentage of carbon on the metal side is also slightly higher than the expected percentage resulting from an oxide failure surface. Another reason for the high amount of aluminium on the metal side may be that the analysis depth of XPS exceeds the thickness of a very thin residual primer layer left on the adherend. The presence of primer was further investigated by scanning electron microscopy and is discussed later.

The highest amount of interfacial failure in dried Al2024 O joints was observed after conditioning for 7 days and then drying. XPS analysis revealed that the adhesive side did not have any aluminium and a high percentage of carbon was present. The metal side had a large percentage of aluminium, indicating that the failure had occurred close to the oxide layer. The failure surface composition was similar to the apparent interfacial failure surfaces observed in conditioned Al2024 O joints, discussed earlier.

4.5.3 Scanning Electron Microscopy (SEM)

As mentioned above, the XPS analysis of the surfaces, which had undergone apparent interfacial failure, pointed towards the possibility that a very thin layer of primer may be present on the metal side of failed joints and failure had not been through the oxide layer. The surfaces of adherends were further examined using a LEO 1530 VP ultra-high-resolution scanning electron microscope (SEM) operating with a primary electron beam of 5 kV and a current of approximately 200 pA. This allowed for high magnification (x50000) images of the apparent interfacial area. Upon close inspection, tiny particles were observed spread throughout the failure surface. These particles may serve as a fingerprint to identify the presence of the thin layer of primer.

A comparative failure surface of the primer was obtained by preparing a joint with the same surface preparation as the conditioned joints i.e. degreasing followed by ACDC anodising. However, the adherends were joined together using only primer BR127, i.e. without adhesive. The joint was subjected to tensile testing and the failure surfaces were observed using SEM, as shown in Figure 4.31. Primer BR127 is an epoxy phenolic system, which contains strontium chromate for corrosion inhibition [186]. This was observed in the form of tiny particles in the failed primer joint. Similar particles were also observed in the failure surfaces of conditioned joints. By comparison of the two surfaces and using these primer particles as a fingerprint, it may be deduced that a thin layer of primer may be present even in the case of an apparent interfacial failure. It is likely, therefore, that the failure occurred in the primer layer close to the oxide layer but did not travel into the oxide layer.

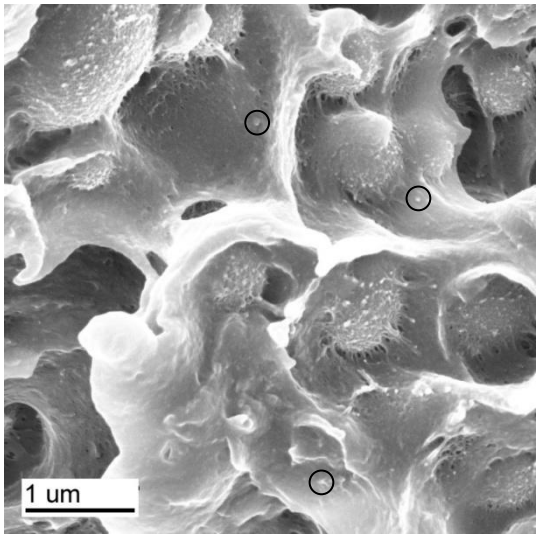

Figure 4.31: Failure surface of a joint made from primer BR127 only (no adhesive was used) when seen by SEM. The circles show the tiny strontium chromate particles.

4.6 Summary

The results of the experimental programme were presented in this chapter. The moisture uptake behaviour of the bulk adhesive under multiple absorption-desorption cycles was observed and it showed that the D and M_∞ had a moisture history dependence. Fickian and non-Fickian analytical moisture diffusion models were used to determine the best fit to the experimental data and to determine D and M_∞. The dual Fickian model gave good predictions for moisture uptake due to the non-Fickian nature of the moisture absorption. The moisture desorption was successfully predicted by Fickian diffusion model. The tensile testing results of the bulk adhesive, conducted at different moisture concentrations, showed that E and σ_{ult} decreased with increasing moisture content. A large recovery in E and σ_{ult} was observed after drying.

The single lap joints showed a decrease in strength with increasing moisture, except for the Al2024 O joints, which showed a strength improvement in the later stages of conditioning. All types of joints showed a large amount of strength recovery after drying, which showed that the strength degradation was mostly due to the reversible mechanism of plasticisation of the adhesive. A comparison of two types

of pretreatment i.e. ACDC and CAA, showed similar joint durability after moisture conditioning.

Failure surface analysis by digital image processing indicated a change in failure type based on the amount of absorbed moisture. Increased apparent interfacial failure was observed with increased conditioning time. When the joints were dried after conditioning, the amount of apparent interfacial failure decreased compared to conditioned joints. This behaviour was observed in most of the joint batches. The investigation of the failure locus by XPS, in joints with apparent interfacial failure, showed that the crack propagation occurred in the primer layer, close to the interface, which allowed for the large amount of strength recovery observed in the joints.

Chapter 5
Finite Element Modelling Methods

5.1 Introduction

Numerical modelling of the adhesive joints was carried out using the finite element method. The effectiveness of the finite element method for modelling adhesive joints has been demonstrated in recent years [6, 71, 121, 187-190]. This chapter provides details of several aspects of the numerical modelling, which were common in most of the models. The commercially available finite element code ABAQUS was used for the numerical analysis. The geometric model development, problem setup and meshing of two (2D) and three dimensional (3D) models was carried out using Abaqus/CAE, the pre and post-processor for ABAQUS. A consistent system of units based on N, mm and hrs was used. A nomenclature for the single lap joint, used to refer to different geometric locations, is introduced at the beginning of the chapter. The model geometry was discretised into finite elements and the selection of element types and meshing methods is discussed. Thermal and diffusion analysis procedures, in addition to structural analysis, were used in the analysis because of the multiphysics nature of the problem and these are described in the chapter. Finally, a number of software specific issues are discussed, which have a significant effect on the analysis results. Specific analysis details, which are only related to a particular model, are further explained in relevant chapters.

5.2 Geometry and Boundary Conditions

The geometry and configuration of the single lap joints used in this research were shown in Figure 3.2 and the nomenclature used to refer to single lap joint geometry is given in Figure 5.1.

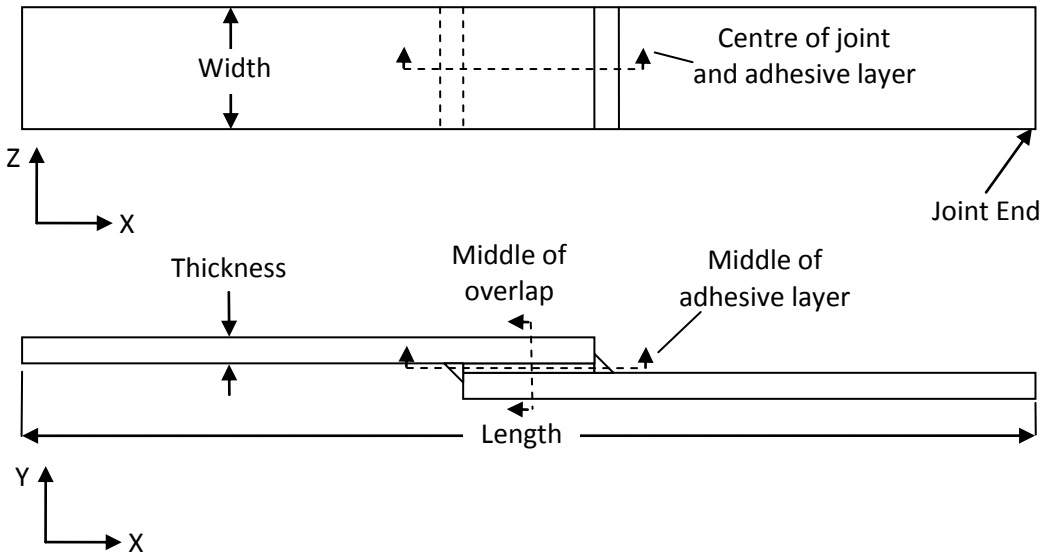

Figure 5.1: Nomenclature for different joint dimensions and geometric locations and global coordinate system used.

In order to minimise the computational cost of the analysis, symmetry in the joint geometry and loading was employed. The joint has planar symmetric geometry in the XZ plane. The geometry and loading may also be considered to be rotationally symmetric about a point situated at the middle of the overlap in 2D or about a line in 3D, as shown in Figure 5.2. This type of symmetry is known as rotational symmetry. The geometric and loading symmetries allowed for modelling of only half of the joint in 2D and a quarter of the joint in 3D, which decreased the analysis time substantially. The results of an analysis can be mapped to full geometry for visualisation during post processing in Abaqus/CAE, although, there are restrictions on the type of results that may be mapped on rotationally symmetric models.

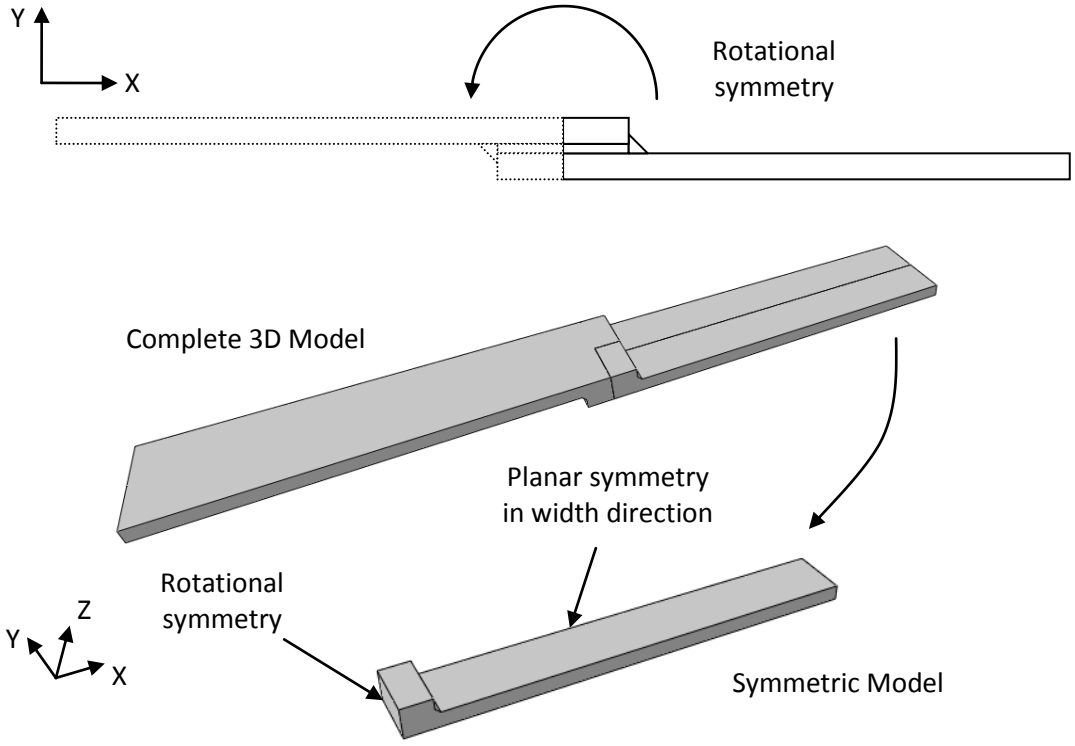

Figure 5.2: Symmetry boundary conditions in a single lap joint model.

For tensile loading, the boundary conditions were applied in the form of fixed displacements at the adherend edge while it was free to move only in the X direction. This was in addition to the planar symmetry and rotational symmetry boundary conditions. The planar symmetry boundary condition was only required in 3D models. Load was applied by displacement control and ramped over the simulation time. The loading and boundary conditions are shown in Figure 5.3.

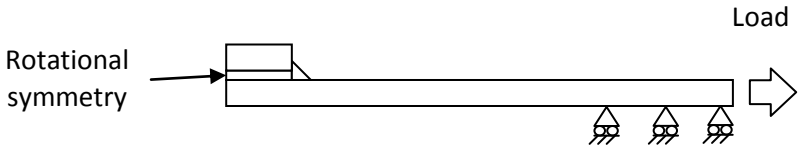

Figure 5.3: Loading and boundary conditions of joints.

End tabs were not included in the single lap joint models as they had no effect on the analysis results. This was verified by analysing a two dimensional joint with and

without end tabs. A comparison of stresses in the middle of the adhesive layer showed the same levels of stress for both types of model, as plotted in Figure 5.4.

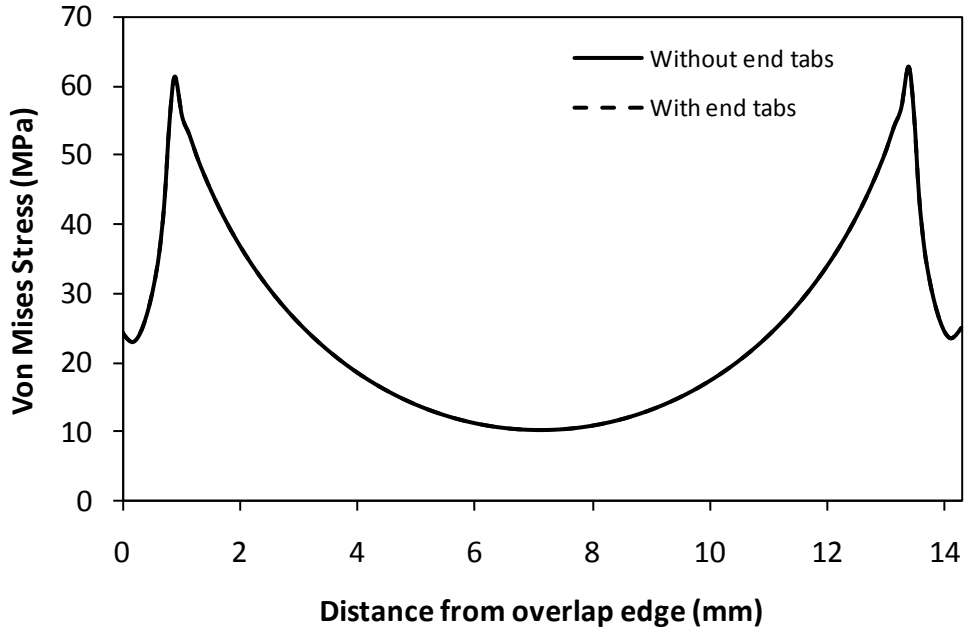

Figure 5.4: Von Mises stresses in the middle of the adhesive layer when analysed with and without end tabs.

5.3 Meshing Methodology

Meshing of a single lap adhesive joint is challenging owing to the presence of the very thin adhesive layer compared to the overall dimensions of the joint. The addition of fillets at the ends of the overlap further complicates the meshing requirements. There are numerical singularities in the single lap joint geometry owing to the rectangular adherends and fillet corners. The meshing strategy was adopted after considering the geometric factors. The rotation / bending of the adherends is another important factor while considering the mesh. The selected mesh should be able to adequately represent the deformed as well as undeformed shape of the joint.

Two methodologies were considered to mesh the single lap joint. The first method was to use a continuous mesh, which may transition from fine mesh to course mesh while maintaining the mesh continuity by sharing nodes between elements. This method required partitioning of the single lap joint geometry in multiple geometric

regions and seeding of each geometric region based on the required mesh density. Seeding is the process of assigning divisions to edges of geometric regions to specify mesh density. The second method was to use dissimilar meshes in the adhesive layer and the adherends and to join them using tie constraints. Tie constraints make the translational and rotational motion, as well as all other active degrees of freedom, equal for nodes on the two sides of the tie constraint. Thus a coarse mesh may be used in the adherends and a fine mesh may be used in the adhesive layer. The first method required more pre-processing time than the second method. However, the use of the tie constraint increased the computational time and resource requirement for an analysis as it required the enforcement of additional constraints. The additional computational cost may offset the advantages obtained by the decrease in number of elements. Thus after the initial study, the first method was used to develop all the meshes used in this research.

A number of meshing methods are available in ABAQUS and each geometric region was meshed based on its geometric shape as shown in Figure 5.5. The adhesive layer and the adherend Region I were meshed with “structured mesh”, which provided a mesh of rectangular shaped elements in the 2D models. Transition meshes between the coarse adherend meshes and fine adhesive meshes were generated by free meshing using the advancing front method. In the three dimensional analyses, the transition sections were meshed using sweep meshing as free meshing is not available for three dimensional meshes. The transition mesh in a 3D model is shown in Region II of Figure 5.5b. The minimum element size was in the highly stressed region of the adhesive layer and the maximum element size was at the adherend ends. The coarse mesh was far from the overlap region that was the area of interest during the analysis. The adherends were meshed with multiple elements through thickness to capture their bending behaviour accurately.

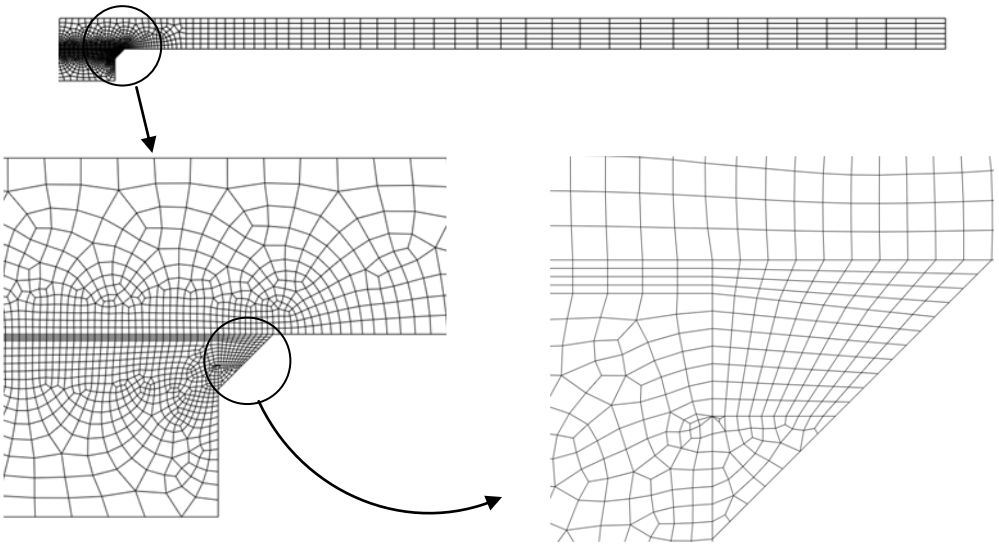

(a)

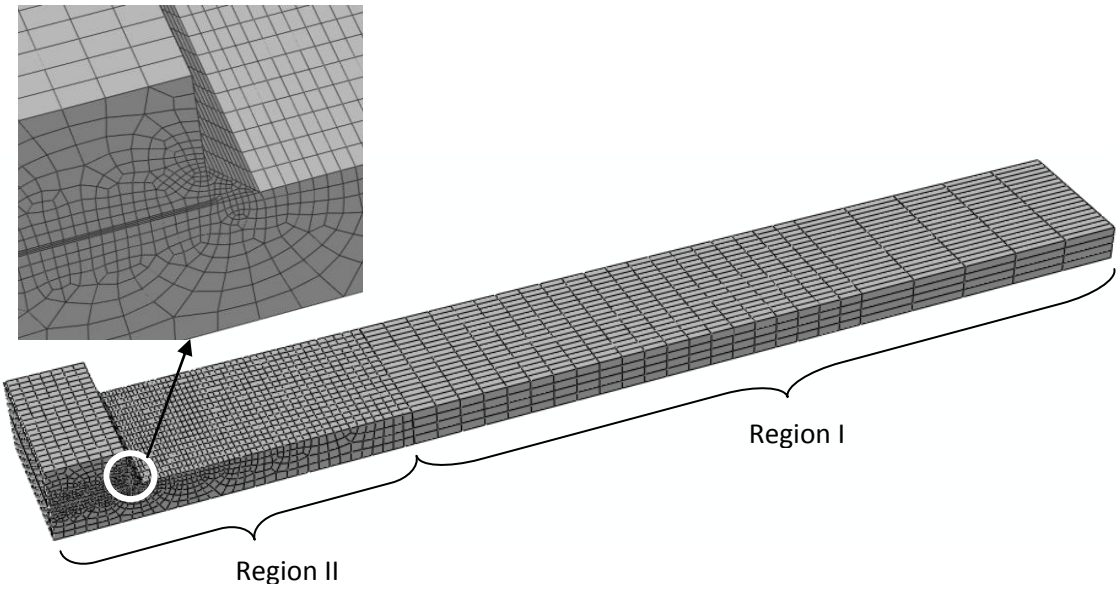

(b)

Figure 5.5: Overall and detailed mesh of a single lap joint for (a) two dimensional (b) three dimensional analysis.

5.4 Choice of Elements

The selection of element type was based on the consideration of single lap joint response under tensile loading. The adherends of single lap joints experience

bending during tensile loading and plastic deformation may be observed in the adherends and the adhesive layer.

Continuum quadrilateral elements in 2D and hexahedral elements in 3D analysis were used for meshing. The accuracy of these elements is generally better than triangular and tetrahedral elements. The quadrilateral and hexahedral elements also have a better convergence rate than triangular and tetrahedral elements [191]. Four node, first order elements were used in 2D analysis while eight node, first order elements were used in 3D analysis, as shown in Figure 5.6.

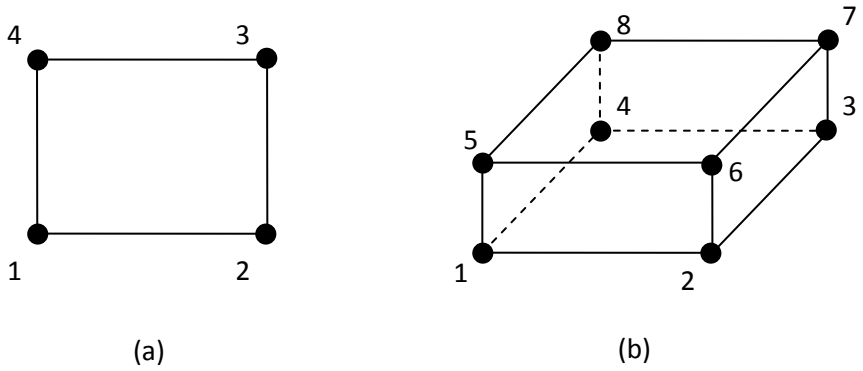

Figure 5.6: Continuum first order elements (a) 4 node quadrilateral (b) 8 node hexahedral

Owing to the bending of the joint, conventional linear elements may suffer from shear locking that generates parasitic shear stress in elements, resulting in a stiffer response under bending conditions than the actual stiffness of the structure. Incompatible mode elements were used to avoid the shear locking in linear elements. In addition to the standard displacement degrees of freedom, incompatible mode elements have incompatible deformation modes added internally to the elements. These elements are computationally more expensive than the continuum first-order elements; however, they are significantly more economical than second-order elements. The incompatible mode elements use full integration and, thus, have no hourglass modes [191].

As mentioned earlier, plastic deformation was observed during tensile testing and was incorporated in simulations by using elastic-plastic material models. During

plastic deformation, second-order, fully integrated elements may develop volumetric locking when the plastic strains are of the order of the elastic strains. This may be avoided by using first-order, fully integrated quadrilateral and hexahedral elements. Thus the first order, incompatible mode elements were the best choice among the library of available elements in ABAQUS and were used for both the 2D and 3D analyses. Based on the above discussion, linear continuum, incompatible mode, four node elements (CPE4I) for 2D and eight node elements (C3D8I) for 3D were selected.

In 3D single lap joint models, continuum shell elements were also used, in addition to continuum elements. Continuum shell elements are similar to continuum elements in geometric representation; however, their kinematic and constitutive behaviour is similar to shell elements. The difference of a shell and continuum shell element is shown in Figure 5.7. The continuum shell elements were used in the adherend area marked as Region I in Figure 5.5b, which was away from the adhesive layer. The advantage of using the continuum shell elements was the reduced computational requirement of these elements when compared to continuum elements. The continuum shell elements have a stacking direction, which should be considered when placing multiple continuum shell elements in a region. The continuum shell elements have only displacement degrees of freedom and thus their kinematic coupling with continuum elements did not require additional constraints. SC8R eight node quadrilateral continuum shell, reduced integration with hourglass control elements were used from the ABAQUS element library.

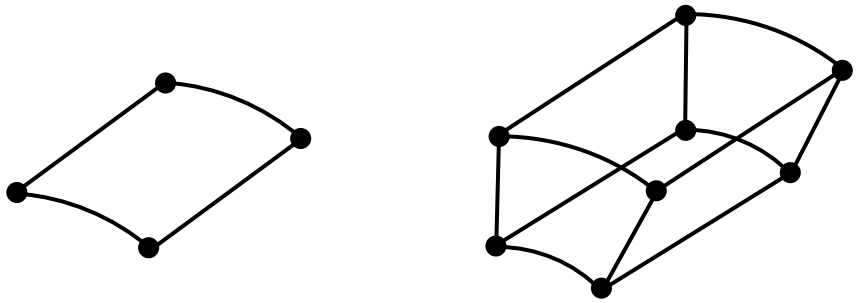

Figure 5.7: Comparison of (a) shell and (b) continuum shell element.

5.5 Formulation of 2D Models

For 2D analysis, plane stress, plane strain and generalised plane strain element formulations were available. A study was carried out to compare the different 2D element formulation results with the 3D element results to select the most suitable element formulation. A single lap joint was modelled in 2D and 3D and the stresses at the middle of the adhesive layer are plotted in Figure 5.8 and Figure 5.9 for a load of 5 kN applied in tension. The stresses for the 3D model were plotted in the centre of the joint to avoid any edge effects.

It can be seen from Figure 5.8 that the von Mises stresses predicted using plane stress elements were higher at the overlap edges than the von Mises stresses predicted by the 3D model. Conversely, lower von Mises stresses than 3D model were predicted using the plane strain and generalised plane strain elements. The plane strain and generalised plane strain elements predicted similar stresses under these loading conditions. Figure 5.9 shows that lower principal stresses were predicted by the 2D models than the 3D model, at the edges of the overlap. However, a comparison of stresses in Figure 5.8 and Figure 5.9 shows that the plane strain element and 3D model predictions were generally in good agreement and hence the plane strain formulation was used for the 2D models.

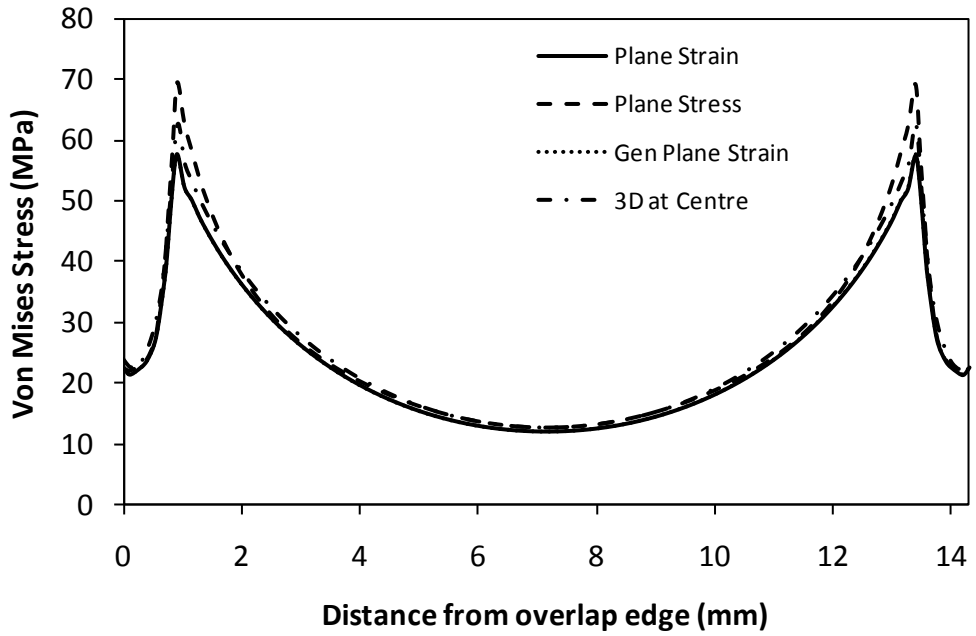

Figure 5.8: Von Mises stress in the middle of the adhesive layer for different element formulations.

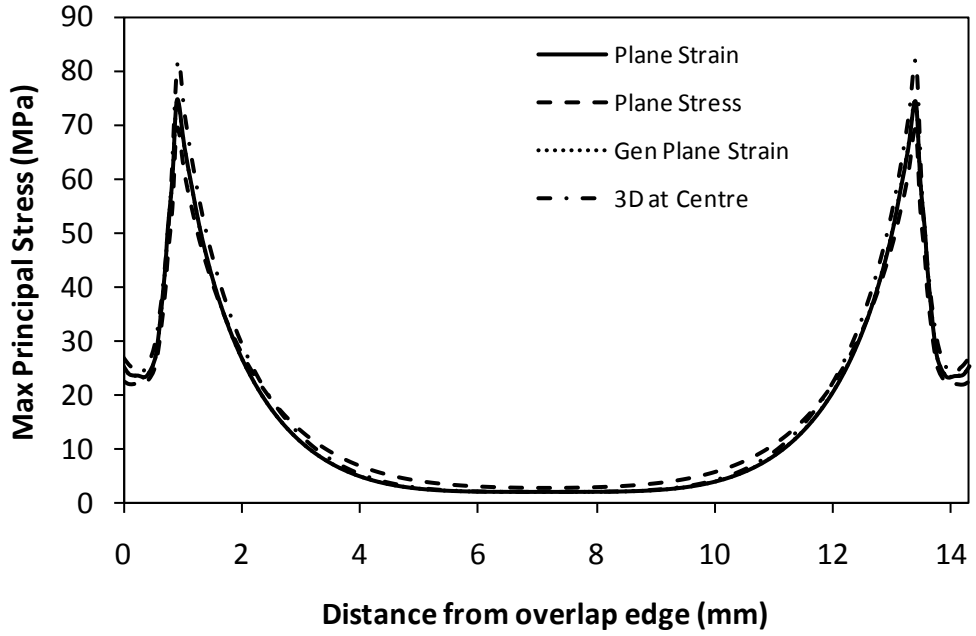

Figure 5.9: Principal stress in the middle of the adhesive layer for different element formulations.

5.6 Mesh Convergence

A mesh convergence study was carried out with three different mesh sizes for 2D and 3D models, where the stresses in the adhesive layer were compared. Details of element size and number of elements in each mesh are given in Table 5.1.

Table 5.1: Details of the different meshes used in the mesh convergence analysis.

Mesh Designation	Dimensionality	Smallest element size (mm)	Total no of elements
Mesh 1	2D	0.25 x 0.06	2,038
Mesh 2	2D	0.125 x 0.03	3,925
Mesh 3	2D	0.063 x 0.015	11,292
Mesh 4	3D	0.24 x 0.06 x 0.5	35,046
Mesh 5	3D	0.12 x 0.06 x 0.5	47,750
Mesh 6	3D	0.06 x 0.06 x 0.5	132,990

The single lap joints were modelled and subjected to a tensile load of 5 kN. The von Mises and principal stresses at the middle of the adhesive layer, for 2D meshes, are plotted in Figure 5.10 and Figure 5.11. The Von Mises stresses predicted by the three meshes were very similar in the middle of the overlap with greatest differences seen in the region of the overlap edges. The results of Mesh 2 and Mesh 3 were in good agreement and Mesh 2 was selected for use in further analyses as it was computationally less expensive.

In the case of the 3D models, Meshes 5 and 6 predicted similar von Mises and principal stresses in the centre of the adhesive layer, as shown in Figure 5.12 and Figure 5.13. Mesh 4 predicted slightly lower maximum stresses in the fillet region. Mesh 5 was selected for further analysis as the results of Mesh 5 and 6 were similar and Mesh 5 was computationally less expensive.

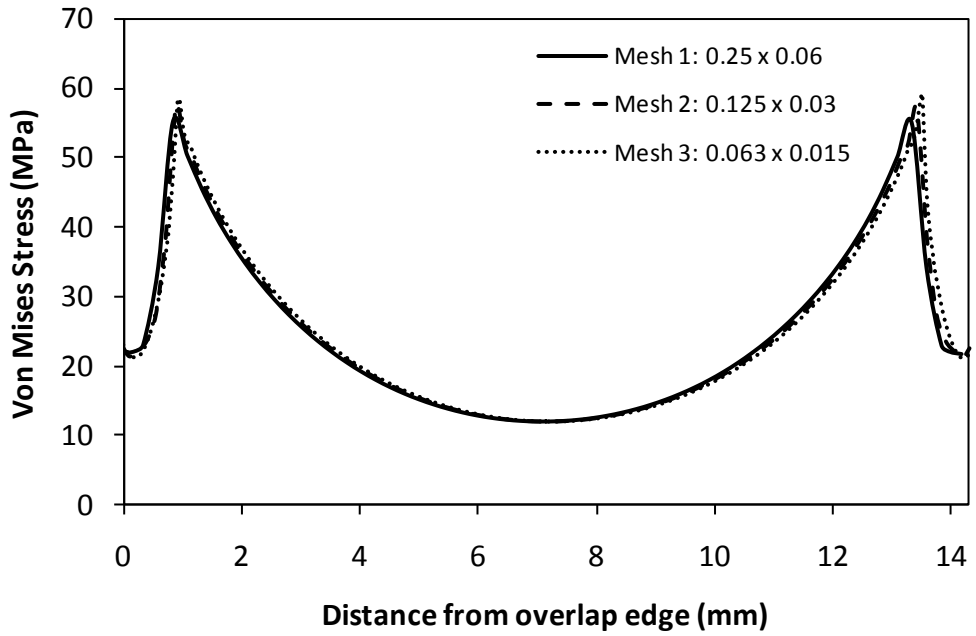

Figure 5.10: Von Mises stresses in the middle of adhesive layer for different mesh densities in two dimensional models.

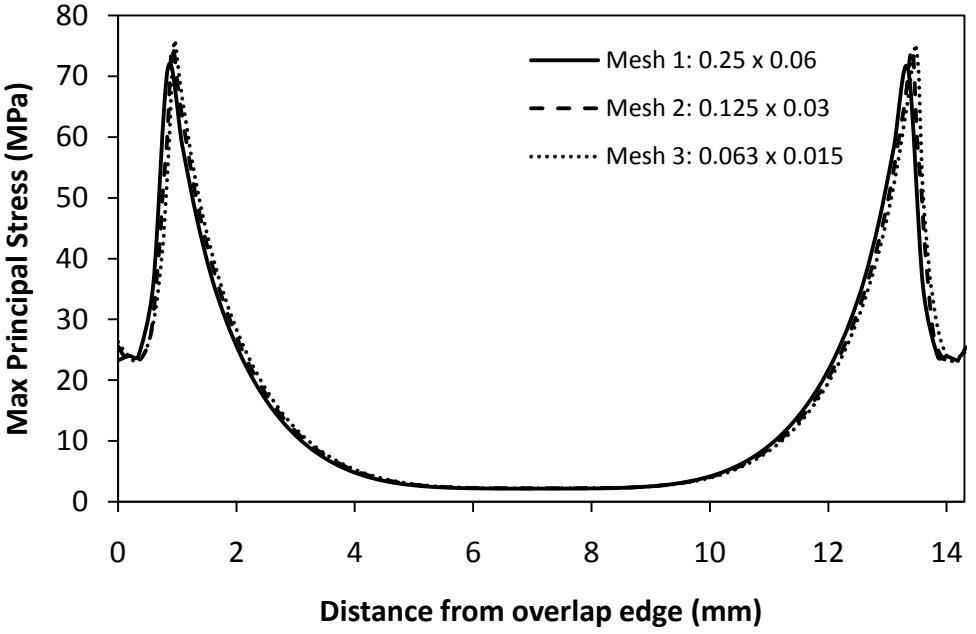

Figure 5.11: Principal stresses in the middle of adhesive layer for different mesh densities in two dimensional models.

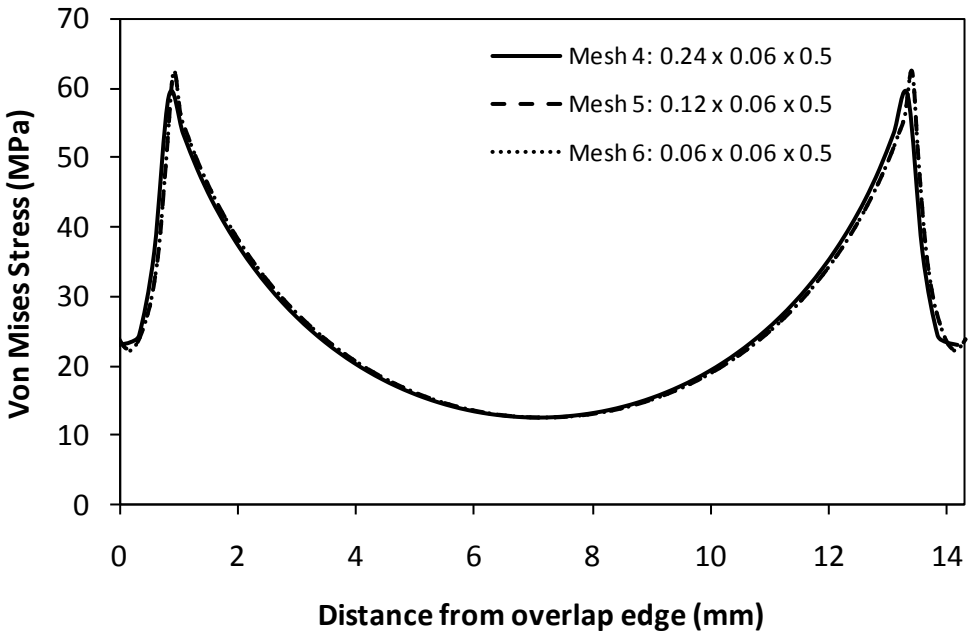

Figure 5.12: Von Mises stresses in the middle of adhesive layer, at centre of joint for different mesh densities in three dimensional models.

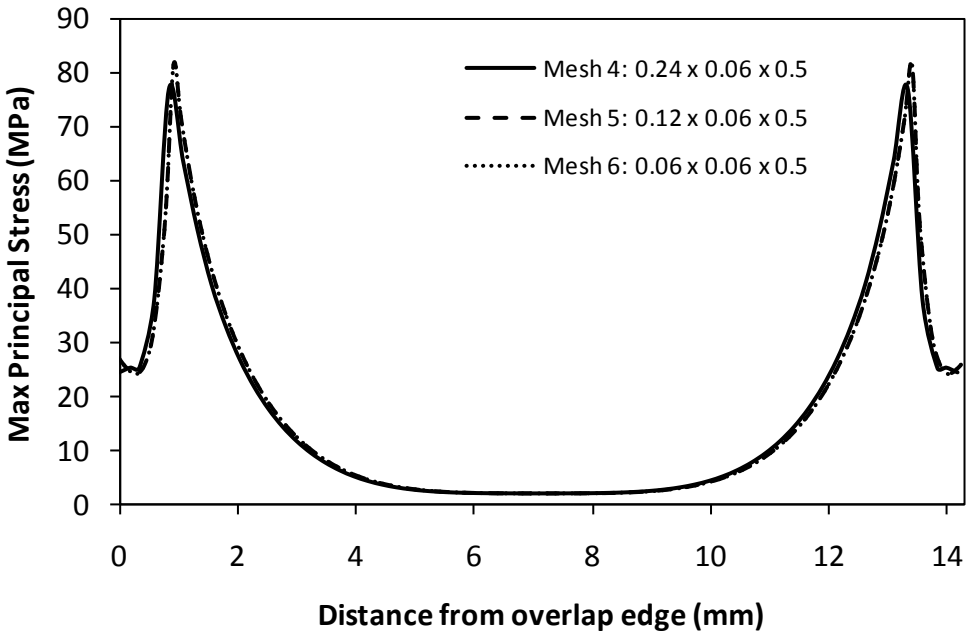

Figure 5.13: Principal stresses in the middle of adhesive layer, at centre of joint for different mesh densities in three dimensional models.

5.7 Thermo-Mechanical and Diffusion Analyses

Thermo-mechanical analysis of the single lap joint was carried out to determine thermal stresses generated as a result of temperature changes during curing and moisture conditioning. Temperature was applied in the form of a state variable in the structural analysis, thus enabling direct solution for thermal stresses. This approach is significantly more computationally efficient than performing a fully coupled thermo-mechanical analysis.

Moisture diffusion analysis was carried out by using the analogy between heat transfer and diffusion equations. This is explained in detail in Section 6.2. Diffusion elements, where diffusion may be governed either by Fick's law or a generalised chemical potential, are available in ABAQUS, however, the use of heat transfer analogy allowed the development of a more generalised approach that may be used in any finite element code with heat transfer capabilities. Also the implementation of heat transfer elements in ABAQUS is more flexible than that of the diffusion elements. The downside to using heat transfer analogy was that a single solution variable was available for storing temperature and moisture concentrations. Thus during a multiphysics analysis involving thermal and hygroscopic analysis, the solution variables had to be initialised when moving from one physics to the other.

Determination of hygroscopic stresses due to the moisture diffusion and subsequent hygroscopic expansion of the adhesive was carried out by sequentially coupled hygro-mechanical analysis. In the sequentially coupled analysis, an uncoupled transient hygroscopic analysis was carried out to determine the nodal moisture concentrations which were then used to calculate hygroscopic expansion and resulting hygroscopic stresses. A fully coupled hygro-mechanical analysis requires significantly more computational resources than a sequentially coupled analysis. The same meshes, as shown in Figure 5.5, were used for the thermo-mechanical and diffusion analyses in order to maintain mesh compatibility for the transfer of results between analyses.

5.8 Analysis Specific Techniques

This section describes various analysis techniques used in different analysis procedures. In nonlinear analysis, the solution convergence was based on the force residual tolerance. ABAQUS uses a default residual force tolerance of 0.5%, which is very strict and provided good solution control. However, in the case of models with temperature or concentration dependent properties, there may be sharp gradients in temperature or concentration fields and convergence may become extremely difficult. In such cases, force residual tolerance of 1% was used, which was still very strict and provided good results.

The 3D models had several hundred thousand degrees of freedom and were computationally expensive and time consuming to solve. ABAQUS provides the facility of parallel computing, where a single machine with multiple nodes / processors may be used for computing the solution. Thread or MPI (message passing interface) based parallel processing options were available. The model was divided in computing domains for solution according to the number of nodes /processors. Thread based parallel processing was used on a dual core shared memory machine to solve the 3D models.

Result transfer between analyses was performed using the analysis continuation facility. When results of one analysis had to be transferred to a subsequent analysis e.g. in a sequentially coupled hygro-mechanical analysis, a restart file was generated during the analysis that allowed for transfer of the mesh and material state. Material properties were redefined in the new analysis based on requirements. Result transfer is possible between similar and dissimilar meshes; however, similar meshes were used to avoid interpolation of results between nodes.

Additional functionality, in the form of material models and results post processing, was added by using user subroutines written in Fortran 9.1 and Python 2.5 scripting language. Python scripts were used for post processing and the transfer of results between analyses where it was not possible by analysis continuation techniques.

Detailed description of user subroutine implementation and functioning and Python scripts is given in Chapter 6 and Chapter 7.

5.9 Summary

The methods employed in the development of the finite element models were discussed in this chapter. The model geometry for 2D and 3D models was selected based on the symmetry in joint geometry and loading. The boundary conditions were based on tensile loading of the joints. A continuous mesh was used to discretise the geometry, where smaller elements were used in the adhesive layer and relatively larger elements used in the adherends. The elements were selected based on suitability for bending and plastic deformation and both continuum and continuum shell elements were used in the 3D models. 2D models were based on a plane strain formulation, which provided good results when compared to the results of a 3D analysis. The sizes of 2D and 3D meshes were finalised after a mesh convergence study and the mesh with the least number of elements was selected after the convergence in stresses was achieved. Thermo-mechanical and hygro-mechanical analyses were carried out by thermal loading and sequentially coupled analysis respectively, which were less computationally expensive than fully coupled analyses. Specific techniques including results transfer between analyses, parallel processing, Python scripting and user subroutines were used, based on analyses requirements.

Chapter 6
Moisture Diffusion in Cyclic Environmental Conditions

6.1 Introduction

The experimental results of moisture diffusion under cyclic moisture conditions, as given in Chapter 4, showed that moisture diffusion in the adhesive had history dependence. In this chapter, a finite element method (FEM) based approach is used to introduce a methodology for the prediction of moisture concentration under cyclic moisture conditions, based upon moisture diffusion history. The moisture diffusion methodology was implemented in the commercial finite element code ABAQUS by using an analogy between conduction heat transfer and moisture diffusion. The implementation was verified by comparing the results from analytical and the finite element models. The experimental data from Chapter 4 was used to determine the input parameters for the cyclic moisture diffusion model. In order to study the effect of moisture history dependence on moisture predictions in a single lap joint, the moisture concentration predictions using the proposed methodology were compared with predictions from an analysis where moisture history effects were not included. The proposed methodology was then used to predict the moisture concentration in single lap joints conditioned for absorption and desorption cycles at 50°C and 70°C, as discussed in Chapter 3.

6.2 Model Development and Verification

FEM provides a means of predicting moisture concentration in complex geometries with multiple boundary conditions and allows for multiphysics coupling; in this case

thermal, hygroscopic and structural. The structural analysis may be used for strength prediction when used with an appropriate failure criterion [23, 35, 172]. FEM is capable of modelling transient moisture diffusion but many of the available commercial software packages lack a built-in capability for modelling moisture diffusion or have limited implementation. The alternative is to use a direct analogy between conduction heat transfer and moisture diffusion. Solutions to the heat conduction equation are given in [192] and correspondence between the equations of heat transfer and moisture diffusion are explained in [87]. Moisture diffusion is often governed by Fick's first and second laws, which are given in Equations (6.1) and (6.2).

$$F = -D\frac{\partial C}{\partial x} \tag{6.1}$$

$$\frac{\partial C}{\partial t} = D\frac{\partial^2 C}{\partial x^2} \tag{6.2}$$

where F is the flux, D is diffusion coefficient, C is concentration and t is time. The corresponding heat transfer equations are given in Equation (6.3) and (6.4).

$$F = -k\frac{\partial T}{\partial x} \tag{6.3}$$

$$\frac{\partial T}{\partial t} = \left(\frac{k}{c\rho}\right)\frac{\partial^2 T}{\partial x^2} \tag{6.4}$$

where T is temperature, k is thermal conductivity, ρ is density, and c is the specific heat. By comparing the above equations, diffusion may be modelled by equating D with k and C with T. The values of ρ and c may be taken as unity for a model with a single permeable material.

To verify the implementation of moisture diffusion in FEM models, a plane sheet of unit thickness was modelled using 2D, plane strain, 4 node elements. The geometry of the sheet is shown in Figure 6.1. A transient analysis was carried out to predict the moisture concentration when conditioned at 100% RH for 1000 hrs. A diffusion coefficient of 3.89 x 10^{-12} m^2/s was used and the diffusion behaviour was assumed Fickian. The material and geometric parameters were selected to obtain gradients

of moisture concentrations in the plane sheet which would allow comparison with an analytical solution. The analytical solution was obtained in MathCAD by using Equation (2.5). For FEM model, one dimensional moisture diffusion was assumed, which occurred through the major flat faces of the sheet. The diffusion boundary conditions were applied in the form of normalised concentration and the edges of the sheet were considered to achieve saturation instantaneously.

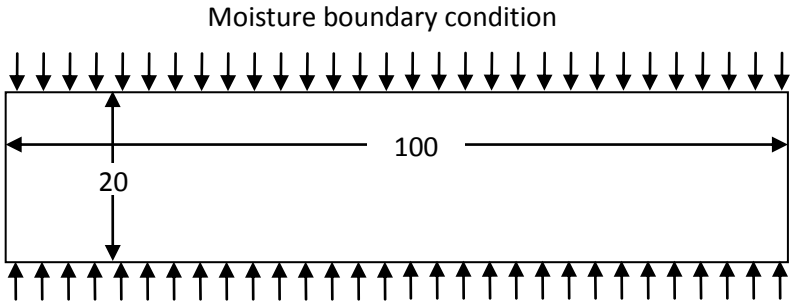

Figure 6.1: Plane sheet with one dimensional moisture diffusion.

The predicted normalised moisture concentration in the plane sheet was compared with the results of the analytical solution of Fick's law, as shown in Figure 6.2. The predictions of moisture distribution using the FEM and analytical model are in excellent agreement, providing confidence in the use of the FEM models.

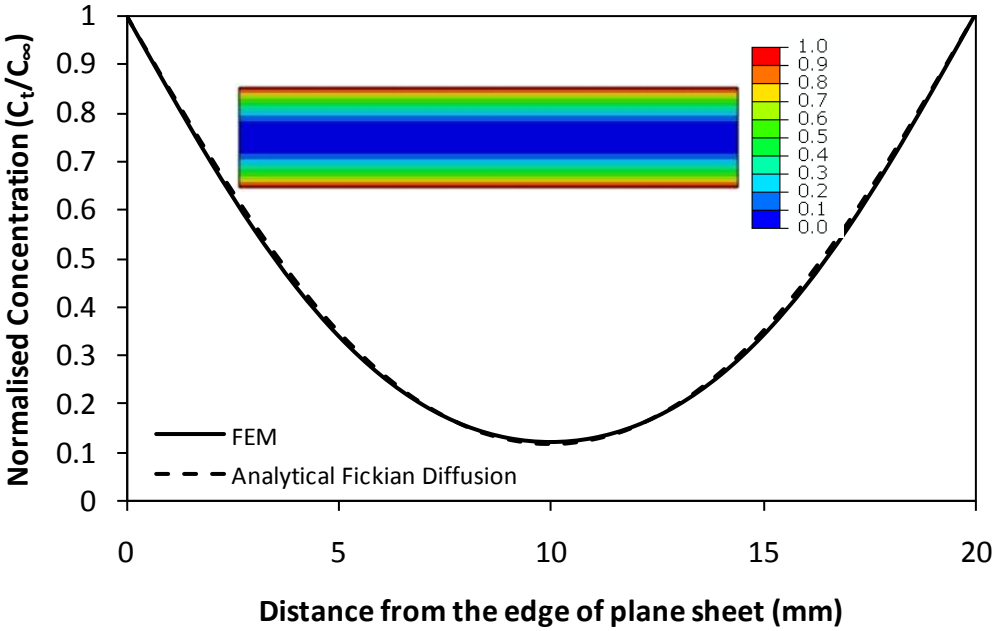

Figure 6.2: Comparison of moisture concentration predicted by analytical Fickian diffusion model and FEM when conditioned for 1000 hrs.

The Fickian moisture diffusion model was also compared with the experimental data. Since the moisture desorption in the adhesive was Fickian, as seen from Figure 4.2, the normalised mass change during the first moisture desorption was compared with the mass uptake predicted by the finite element model of the adhesive film of 60 x 40 x 1 mm. The size of the finite element model and experimental bulk adhesive samples was same. Comparison of the experimental and finite element model predicted normalised moisture uptake is shown in Figure 6.3 and a good correlation between the two was found.

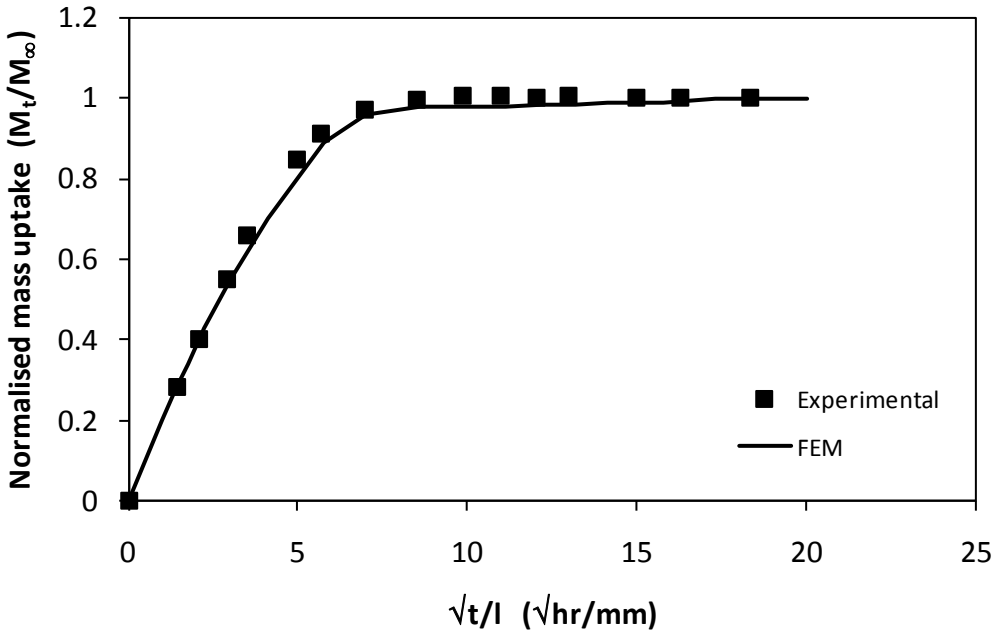

Figure 6.3: Comparison of experimental and finite element predicted moisture uptake in bulk adhesive sample.

The experimental measurements of moisture uptake in the adhesive used in this research showed a non-Fickian moisture uptake that was successfully modelled using a dual Fickian model as shown in Section 4.2.2. The dual Fickian model was implemented in FEM by carrying out two separate Fickian diffusion analyses, with different diffusion coefficient D_1 and D_2 and boundary conditions, C_1 and C_2, from the two stages of the dual Fickian model. The plane sheet model, described above, was used to verify the dual Fickian model implementation in FEM by comparison with an analytical solution. The value of D_1 was 3.89 x 10^{-12} m^2/s and

D_2 was 1.24 x 10^{-12} m^2/s and boundary conditions of C_1 / C_∞ = 0.6 and C_2 / C_∞ =0.4 were used. The results of the two moisture diffusion analyses were combined in the post-processing phase using a Python script. Python is a scripting language that may be used to process the results of an ABAQUS results database. The Python script was implemented in the form of a plug-in in Abaqus/CAE and the graphical user interface (GUI) of the plug-in is shown in Figure 6.4.

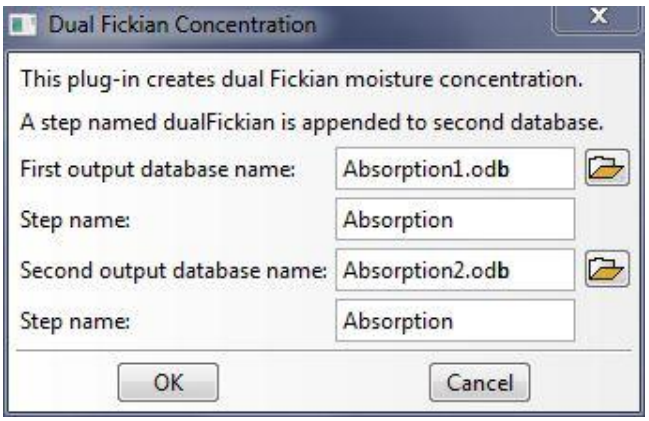

Figure 6.4: The graphical user interface (GUI) for the dual Fickian concentration plug-in.

It can be seen from Figure 6.5 that the normalised moisture concentration predicted by the analytical dual Fickian model and FEM are in good agreement.

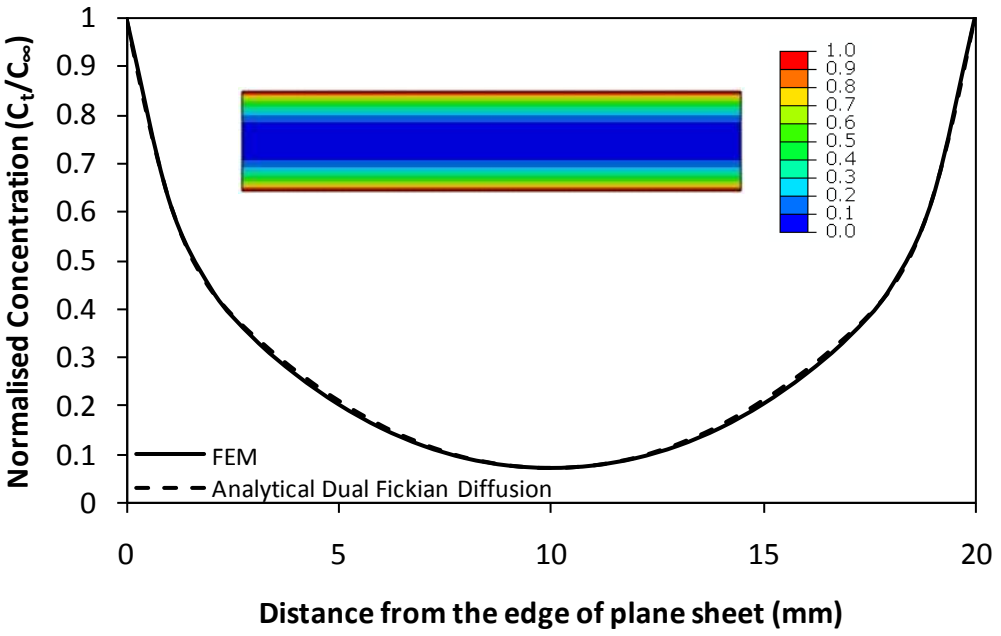

Figure 6.5: Comparison of moisture concentration predicted by analytical dual Fickian method and FEM when conditioned for 1000 hrs.

6.3 Determination of Diffusion Parameters

In order to incorporate the moisture history dependency in a moisture prediction model, the empirical relationships of D and M_∞ with the number of diffusion cycles, N, were determined by least squares curve fitting of experimental data. The curve fitting was carried out in MathCAD for bulk adhesive samples conditioned at 50°C and 70°C. The moisture absorption cycles were curve fitted using dual Fickian model parameters while the moisture desorption cycles were curve fitted with Fickian diffusion parameters since these models provided good predictions of the experimental data, as discussed in Section 4.2.2. The results of the curve fitting for bulk adhesive samples, conditioned at 50°C, are shown in Figure 6.6. The form of the functions used for the curve fitting of D_1, D_d, M_∞ is given in Equation (6.5) and that for D_2 is given in Equation (6.6).

$$D_1, D_d, M_\infty = uN^v + w \tag{6.5}$$

$$D_2 = pe^{qN} \tag{6.6}$$

where u, v, w, p and q are constants obtained by curve fitting and are given in

Table 6.1.

Figure 6.7 shows the results of curve fitting for bulk adhesive samples conditioned at 70°C. In this case, Equation (6.5) was used for curve fitting the experimental data for all diffusion parameters and the constants are given in Table 6.2.

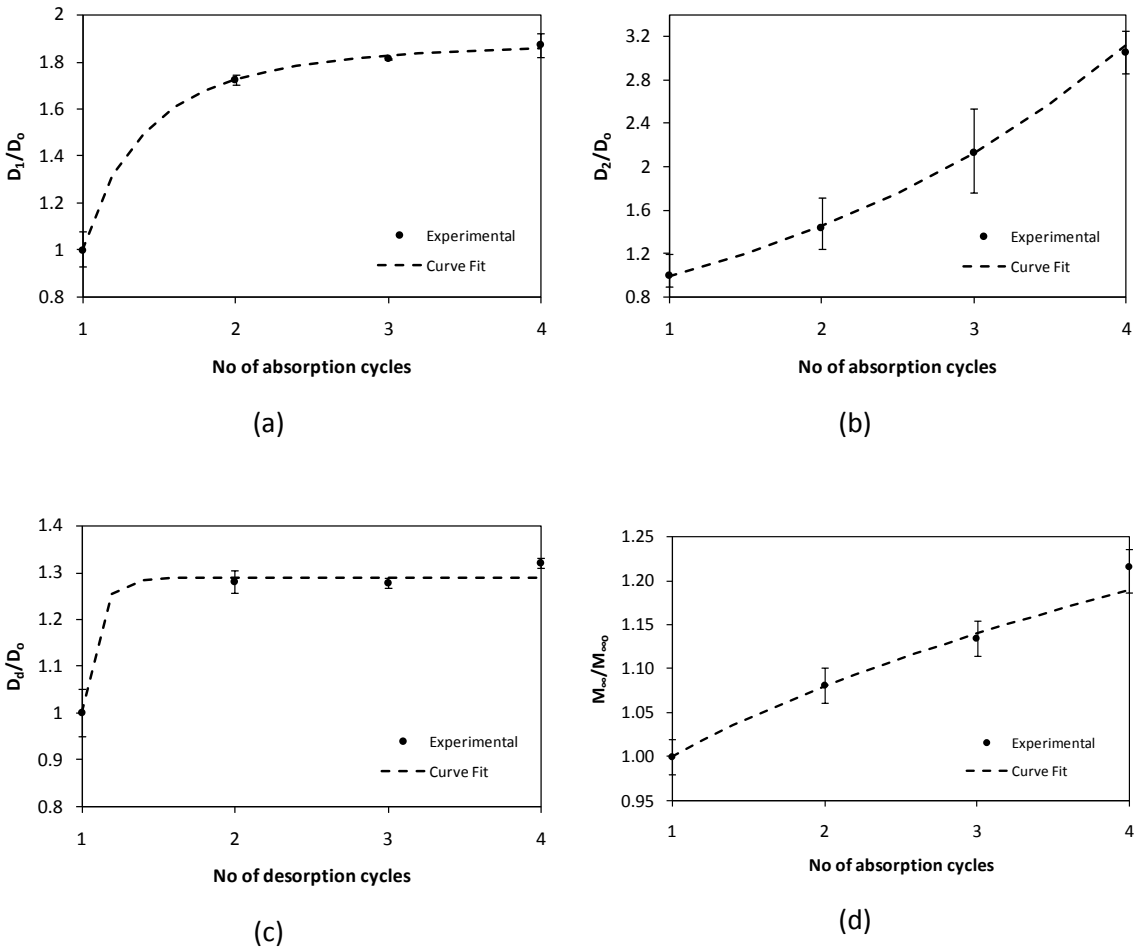

Figure 6.6: Moisture diffusion characteristics of 1 mm thick samples over multiple absorption-desorption cycles when conditioned at 50°C (a) D_1 (b) D_2 (c) D_d (d) M_∞.

Table 6.1: Constants obtained by curve fitting for empirical diffusion characteristic functions when conditioned at 50°C.

Diffusion variable	u	v	w
D_1	-0.8885	-2.432	1.889
D_d	-0.2884	-11.7	1.288
M_∞	0.2144	0.4574	0.7856
	p	q	
D_2	0.677	0.3814	

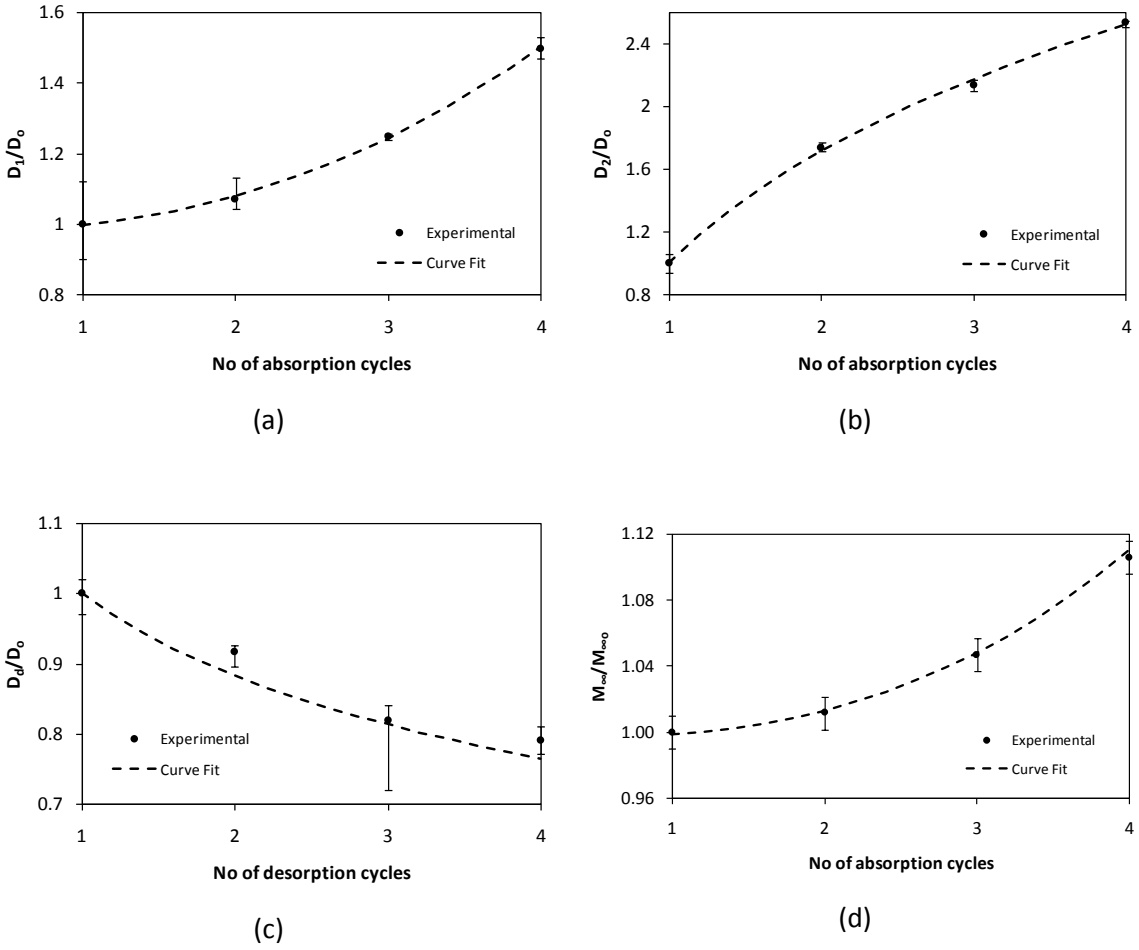

Figure 6.7: Moisture diffusion characteristics of 1 mm thick samples over multiple absorption-desorption cycles when conditioned at 70°C (a) D_1 **(b)** D_2 **(c)** D_d **(d)** M_∞**.**

Table 6.2: Constants obtained by curve fitting for empirical diffusion characteristic functions when conditioned at 70°C.

Diffusion variable	*u*	*v*	*w*
D_1	0.02015	2.353	0.9759
D_d	5.13	0.1871	-4.125
M_∞	-40.67	0.004167	41.67
D_2	0.002541	2.747	0.996

In order to explain the changes in the moisture diffusion characteristics over multiple diffusion cycles, the effects of moisture on the adhesive need to be

considered. Moisture cycling affects polymers in several ways, including; an increased volume due to swelling [59], possible chemical reaction of water with the polymer, leaching of material, micro-cracking and other progressive damage mechanisms. Carter and Kibler [27] suggested that water in a polymer can exist in free or bound states. If there are chemical reactions between the polymer and the water, the water becomes attached to the polymer and is not free to move, whereas, the water present in the free volume of the polymer is free to move. The free volume exists in a polymer due to the gaps between the polymer chains and depends on the density and physical state of the polymer. The diffusion of water in a polymer depends on the available free volume within the polymer, a higher free volume results in a higher capacity for the absorption of water. A Langmuir type model was suggested by Carter and Kibler to predict the moisture concentration, which has additional parameters to those used in a Fickian diffusion; the probability that bound water may be released and the probability that free water may become bound. It has also been suggested that during initial moisture uptake, the moisture enters the free volume of the polymer, which does not cause swelling of the polymer [24]. During later stages, when most of the free volume is filled, the absorbed moisture distorts the polymer network and causes swelling. As the polymer swells, additional free volume may become available for diffused water.

It may be seen from Figure 6.6 and Figure 6.7 that the absorption and desorption cycles affect D and M_∞ in a different manner at 50°C and 70°C. At 50°C, in the rapid initial uptake of water by the adhesive value of D_1 is higher than that of D_2. This may be when the water is primarily diffused into the free volume of the adhesive. However, in the later stages, as the free volume decreases, swelling of the adhesive takes place and a lower value of D_1 is observed. As a consequence of swelling, the induced strain may cause micro-cracking. The increased volume may also mean that more sites for the reaction of water and the adhesive will become available. During the desorption, a Fickian diffusion curve indicates that free water diffusion is the predominant process as any bound water is not able to detach due to chemical attachment.

Diffusion is a thermally activated process and an increase in temperature causes an increase in diffusion rate, as can be seen in Figure 6.8a, b and c, where the diffusion coefficients are higher at 70°C than 50°C for all cases except the D_2 for the fourth cycle. However, as D_1 is significantly higher at 70°C than 50°C except this cycle, the overall diffusion rate is still greater at the higher temperature. A small increase in M_∞ over multiple cycle for both 50°C and 70°C samples can be seen. A significantly higher value of M_∞ was observed at 70°C than 50°C, as shown in Figure 6.7d, which may be because of the greater swelling of the adhesive at 70°C.

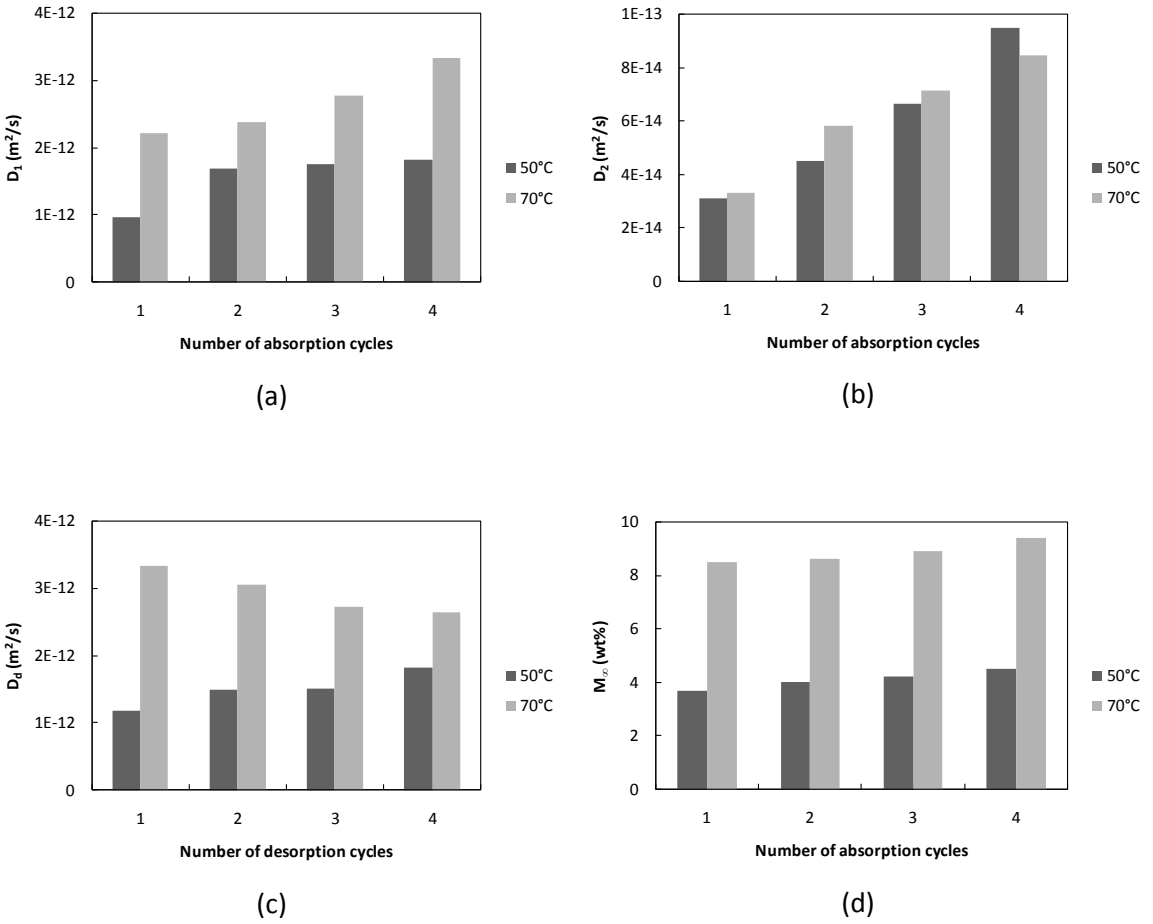

Figure 6.8: Effect of temperature on moisture diffusion characteristics over multiple absorption and desorption cycles (a) D_1 (b) D_2 (c) D_d (d) M_∞ for 1 mm thick samples.

6.4 Methodology for Prediction of Cyclic Moisture Diffusion

The overall methodology for predicting cyclic moisture diffusion is illustrated in Figure 6.9.

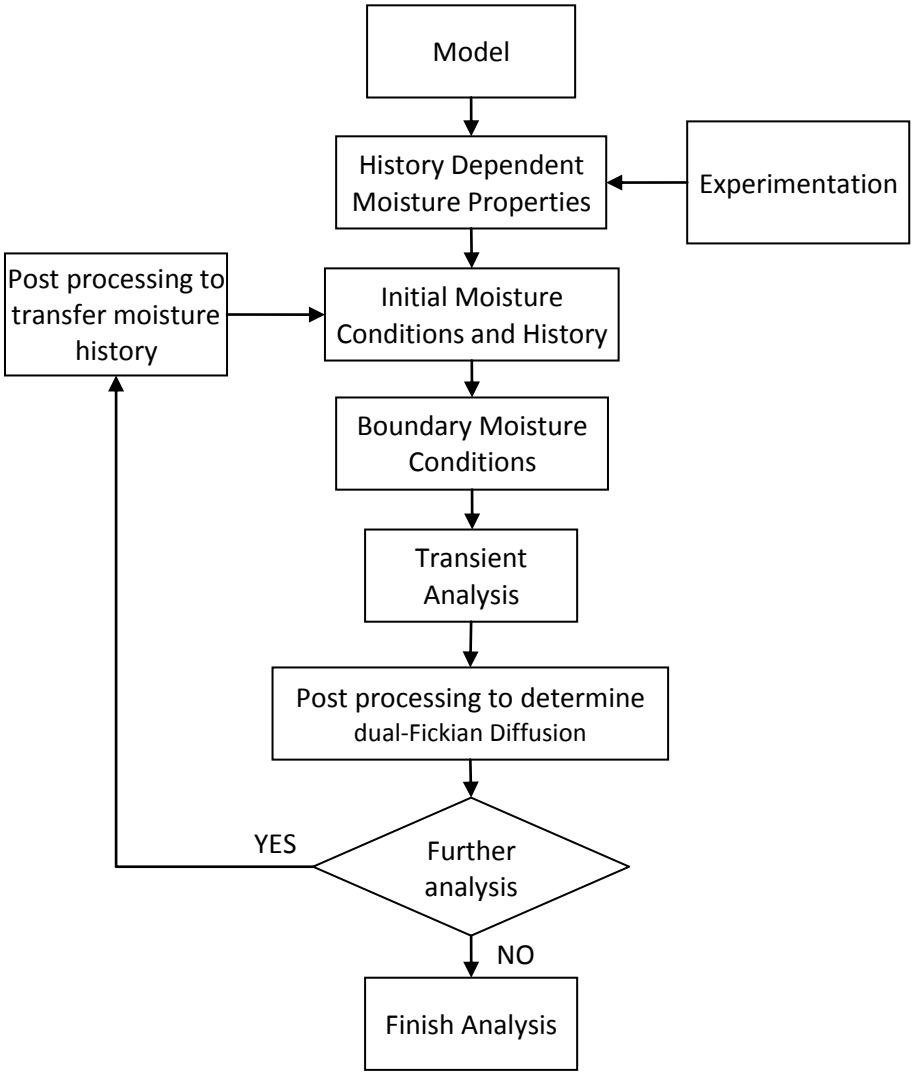

Figure 6.9: Methodology for modelling cyclic moisture diffusion.

The FE model is assigned history dependent diffusion properties determined by experimentation. The in-built material models in Abaqus were not adequate for this purpose and the proposed methodology was implemented by introducing a user subroutine. The dual Fickian model based moisture concentration may be determined by post processing the results of two Fickian diffusion models, as

described in Section 6.2. In the case of multiple cycles, the moisture history and the state of material, from one analysis, is transferred to the next analysis by post processing routines and the analysis may continue for any number of cycles. The detailed implementation of the user subroutine is discussed in the next section.

6.5 Implementation of Cyclic Moisture Dependent Predictive Model

The cyclic moisture dependent model was implemented in the commercial finite element code ABAQUS. Subroutine, UMATHT, is available in ABAQUS for introducing a user defined heat transfer material model and was used to implement the moisture history dependence. The structure of the subroutine is illustrated by the flow chart in Figure 6.10. The moisture history of the adhesive was maintained during the analysis by the use of scalar internal state variables, denoted by SV. Three state variables were used; the first state variable stores the moisture history in the form of absorption-desorption cycles. The second variable stores the nature of the diffusion process, i.e. absorption or desorption, while the third state variable records the amount of moisture diffused during a single absorption or desorption. The internal state variables were implemented as solution dependent variables.

The moisture cycling is based on a minimum amount of moisture absorbed in the adhesive that would change the diffusion characteristics of the adhesive. The critical concentration is an input parameter to the user subroutine, which is used to avoid minute fluctuations in moisture concentration when determining completion of a diffusion cycle. As the boundary conditions are changed, small changes in concentration may occur causing the user subroutine to determine many diffusion cycles. Thus an absorption-desorption cycle is established when the moisture concentration at a point in the adhesive exceeds a critical concentration upon change of boundary conditions.

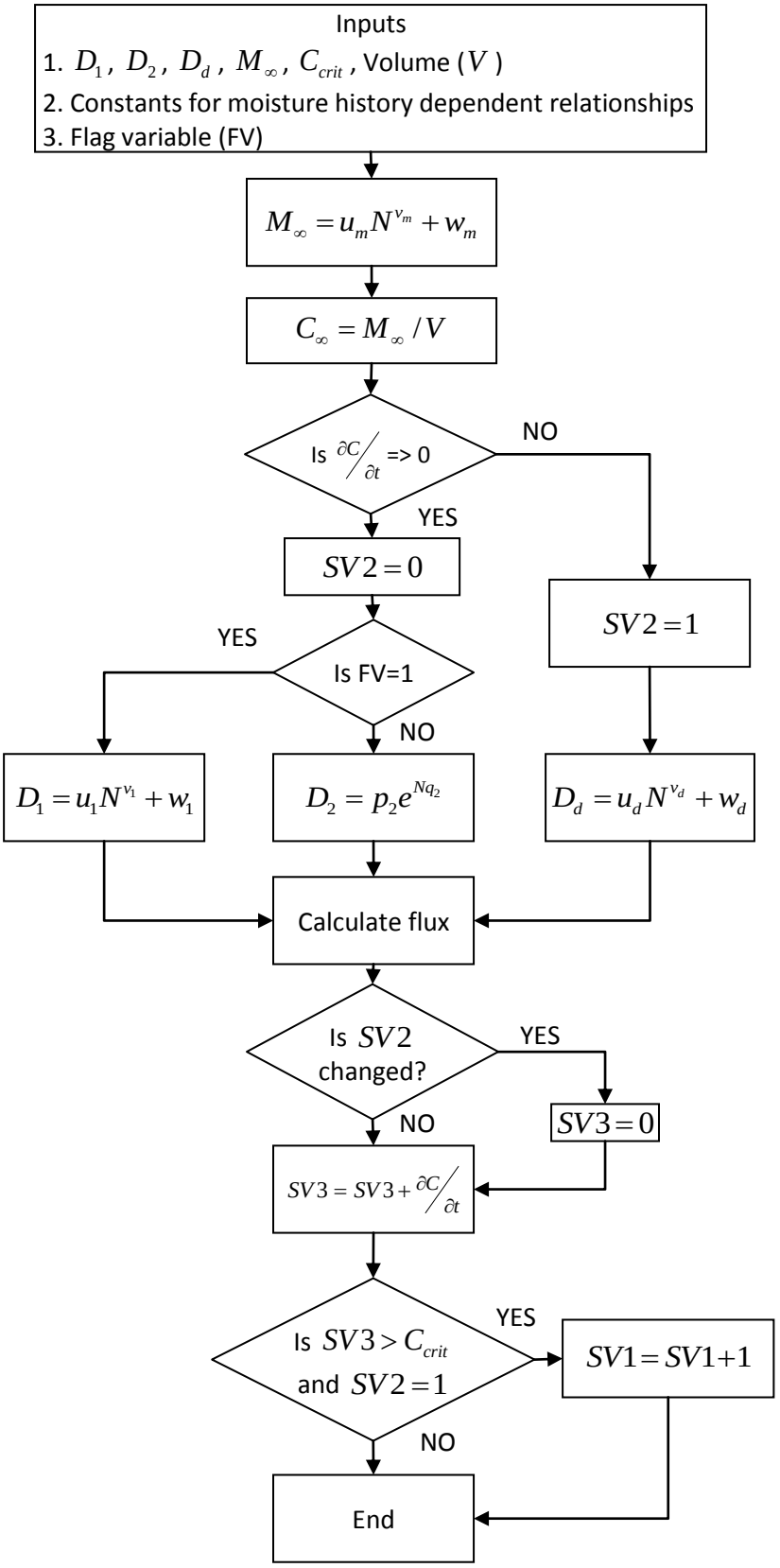

Figure 6.10: Structure of user defined material subroutine UMATHT.

The history dependence of diffusion characteristics was incorporated by using the relationships developed in Section 6.3. The user subroutine uses a flag variable (FV) to determine the appropriate diffusion coefficients in the case of dual Fickian diffusion, where two parallel Fickian models were used to obtain the total moisture diffusion. The moisture history is transferred between sequential analyses by using a Python script and the SDVINI subroutine. SDVINI is an ABAQUS subroutine for initiating state variables.

6.6 Comparison of Moisture Prediction Methodologies

In this section, numerical experiments were carried out to observe the moisture diffusion under various cyclic moisture conditions by applying the developed moisture prediction methodology. This provides an insight in moisture distribution when cycles of different time durations are used and shows the applicability of the developed methodology to varied environmental conditions. In addition to using the developed methodology, moisture diffusion was also predicted using a methodology that does not include the moisture history effects and a comparison with the results of the proposed methodology is presented to highlight the differences between the two methods. Two cases of multiple absorption and desorption in a single lap adhesive joint are considered in order to illustrate the effect of including the cyclic moisture absorption on the prediction of moisture concentration. In the first case, the diffusion parameters are based on a single absorption curve while diffusion parameters determined from multiple absorption-desorption cycles are used in the second case, which incorporates the effects of the changes in D and M_∞ during cyclic diffusion. The history dependence of diffusion parameters is implemented via the developed user subroutines.

A single lap joint was modelled with aluminium adherends bonded by the adhesive FM73-M. Diffusion was assumed to be taking place through the bulk adhesive only i.e. no interfacial diffusion was considered. However, interfacial diffusion can be easily modelled by introducing a layer with higher diffusion coefficient at the interface. Using symmetry, only one quarter of the adhesive layer was modelled.

The adherends, as non-absorbing, did not need to be explicitly included in the model and are represented only by insolubility boundary condition. Fillets were also not included in the model as they would not affect the comparative study. The boundary conditions were applied in the form of normalised moisture concentration and specific boundary conditions for each case are discussed later. A refined mesh with 0.3 x 0.3 mm four node, linear 2D quadrilateral heat transfer field elements was used. Figure 6.11 illustrates the geometry of the single lap joint and the meshing of the adhesive layer.

Four cyclic conditioning environments, with absorption and desorption times of 1200, 2400, 4800 and 9600 hrs, were considered and each conditioning environment consisted of three absorption-desorption cycles. The durations of the cycles were selected to achieve different moisture concentrations at the middle of the adhesive layer. Similar conditions may be observed where diffusion path and moisture cycles are shorter in duration. A typical multi-cycle conditioning environment is shown in Figure 6.12, in this case with absorption and desorption times of 2400 hrs each.

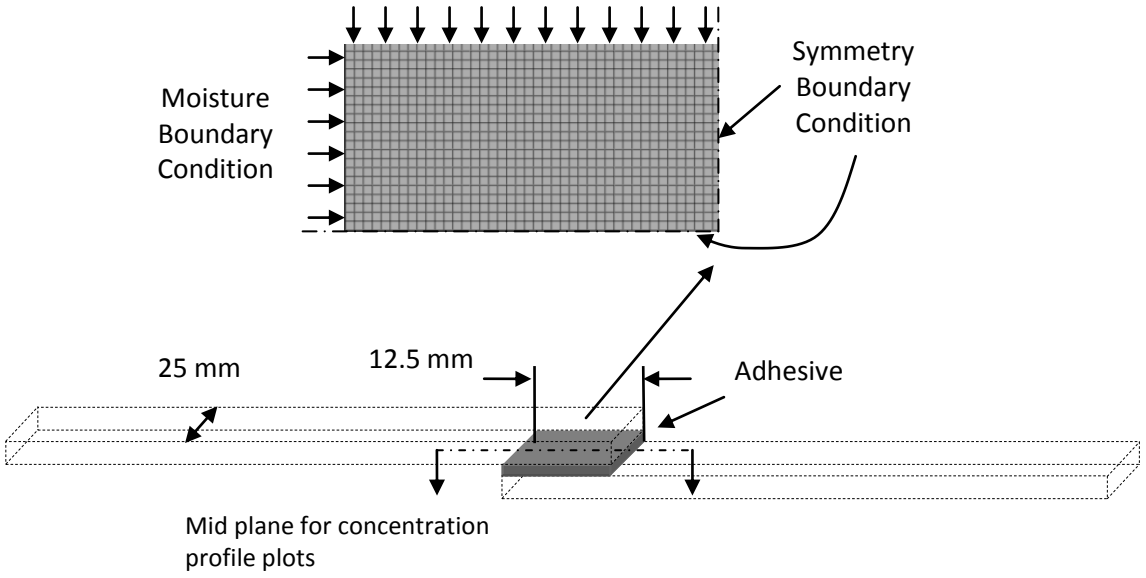

Figure 6.11: Single lap joint geometry with finite element mesh of the adhesive layer used for modelling the cyclic moisture diffusion.

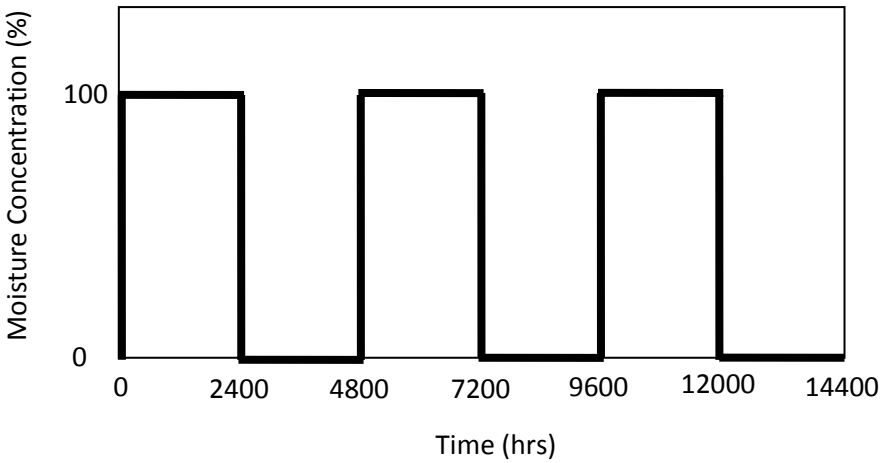

Figure 6.12: Cyclic moisture conditioning environment for finite element modelling.

6.6.1 Case I: Predictive Modelling Using Diffusion Parameters Based on a Single Moisture Uptake Curve

The diffusion coefficients determined by curve fitting a dual Fickian diffusion model to the first experimental absorption data, were used to predict concentration in the adhesive layer after multiple absorption cycles. The boundary conditions were applied in the form of normalised moisture concentration (C / C_{∞}). The dual Fickian model was implemented by running two sequential analyses with $D = D_1$ and $D = D_2$ and a script was used to add the concentration at each integration point, providing the dual Fickian moisture uptake. The absorption cycles were followed by desorption cycles, which were based on a Fickian diffusion model. The first diffusion coefficient obtained for the dual Fickian model, D_1, was used to predict the desorption. The concentration predicted in the first step was used as the initial concentration for the next analysis step. The analysis continued until the completion of the required environmental cycling.

Figure 6.13 compares concentration profiles after the first absorption for the four conditioning environments, the plots showing concentration at the centre of the adhesive layer, as illustrated in Figure 6.11. It can be seen that the amount of absorbed moisture increases with absorption time, however, saturation is still not reached even after 9600 hrs of absorption. Figure 6.14 plots the moisture

concentration in the adhesive layer after the first desorption cycle and shows that some moisture remains in the adhesive layer at the end of the desorption for all cycle times. The amount of moisture is maximum at the centre of the overlap except for the desorption cycle of 1200 hrs. The diffusion process is governed by the moisture activity in the adhesive layer.

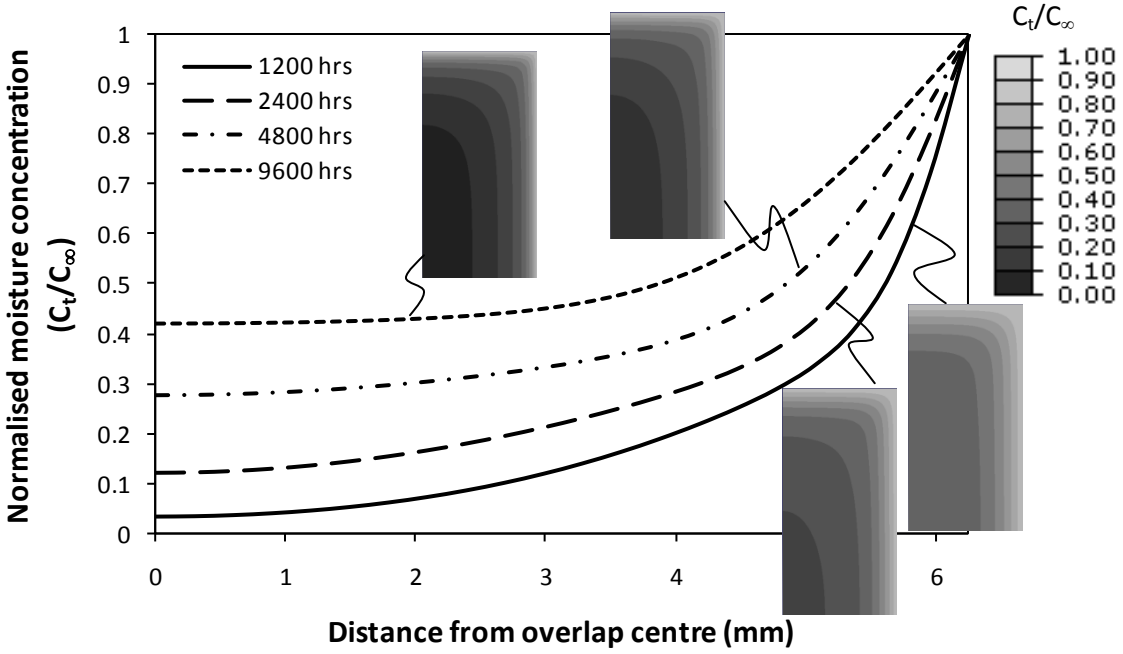

Figure 6.13: Moisture concentration in the adhesive layer after first absorption cycle.

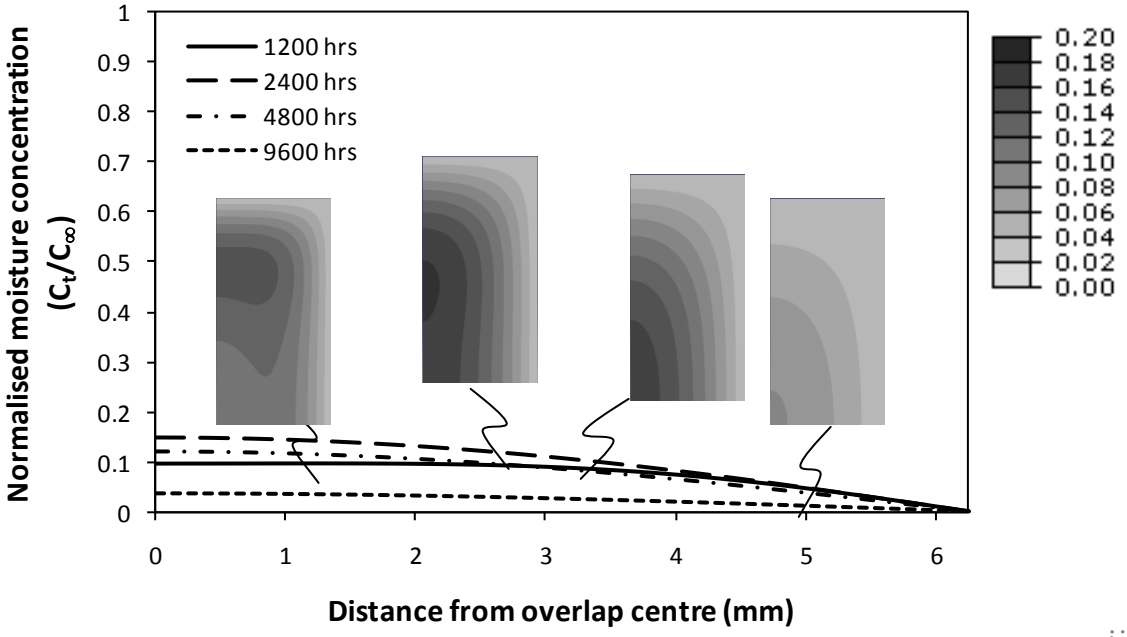

Figure 6.14: Moisture concentration in the adhesive layer after first desorption cycle.

At the start of the desorption, there is a high concentration gradient in areas close to the edges of the joint because saturation was not achieved during the previous absorption. This drives diffusion towards the centre of the overlap, in addition to the drive for diffusion towards the edges of the adhesive caused by the introduction of the "dry" boundary condition. Thus during the initial stages of the desorption, both absorption and desorption processes are occurring simultaneously in different areas of the adhesive layer. Desorption from the overlap centre starts only after a higher concentration in the surrounding material is achieved. Owing to this simultaneous absorption and desorption different parts of the adhesive may be subjected to different diffusion rates. Figure 6.15 shows a typical desorption process where the adhesive layer is not fully saturated at the start of the desorption. As desorption cycle starts, diffusion to the middle of the adhesive layer continues from the surrounding high concentration areas. This continues until the centre of the adhesive layer achieves a higher concentration than the surrounding material because of moisture transport towards both the edges and centre from this region.

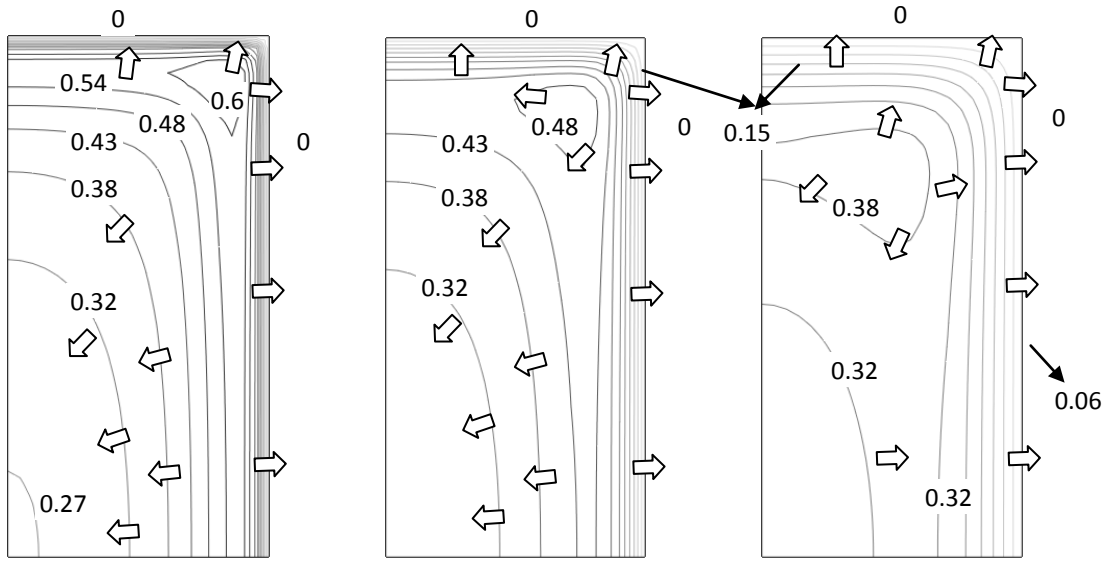

Figure 6.15: Contour plots of normalised moisture concentration in the adhesive layer during a typical desorption process. Localised concentration gradients result in simultaneous absorption and desorption in different areas of the adhesive layer. Arrows indicate direction of moisture transport.

The experimental results, as shown in Figure 4.2, showed that desorption was faster than absorption and thus the residual moisture predicted in the adhesive layer using an absorption based diffusion coefficient will tend to result in an over-prediction of the moisture concentration. Figure 6.16 compares the moisture concentration in the adhesive layer after repeated cycles of 4800 hrs and it can be seen that the moisture concentration increases with each absorption cycle. As the D and M_∞ remain constant between diffusion cycles, the increase in moisture concentration can be attributed to the residual moisture left in the adhesive after each desorption process. The amount of residual moisture also increased after each desorption as the moisture accumulated over desorption cycles, however, the increase in residual moisture becomes less with increasing number of cycles. The increase in residual moisture can be attributed to the fact that the adhesive layer did not achieve saturation during absorption and moisture flowed towards the centre of the adhesive layer from surrounding areas during subsequent cycles. The residual moisture in the adhesive layer is reduced when the cycle time is increased to 9600 hrs, as shown in Figure 6.17. Owing to the increased absorption time, less residual moisture is predicted in the adhesive layer during each desorption of 9600 hrs. As water distribution in the adhesive layer is more homogeneous than with the 4800 hrs cycles, the difference between residual moisture at the centre of adhesive layer after repeated cycles is greatly reduced.

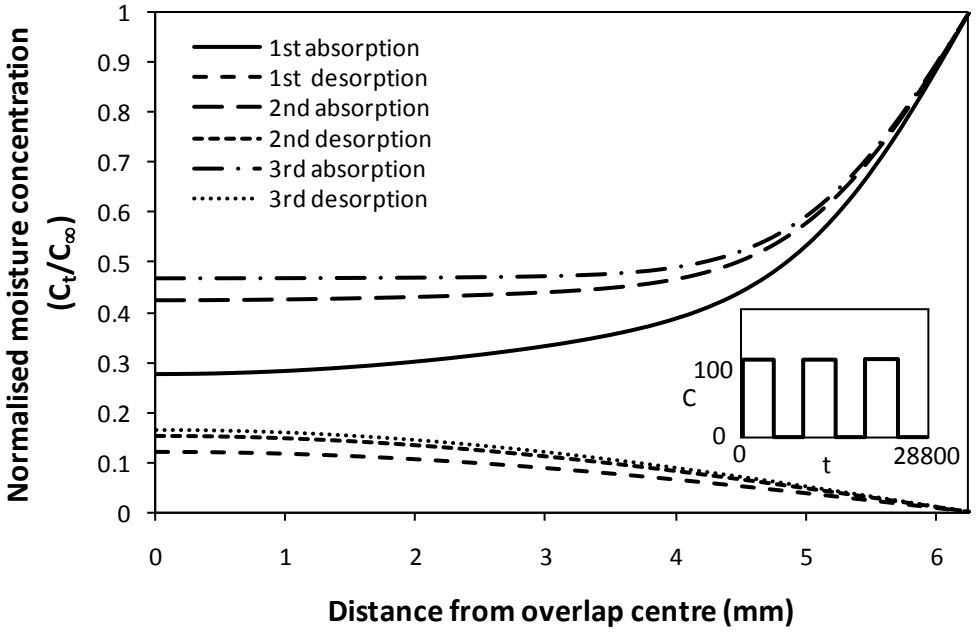

Figure 6.16: Moisture concentration in the adhesive layer after absorption-desorption cycles of 1200 hrs each.

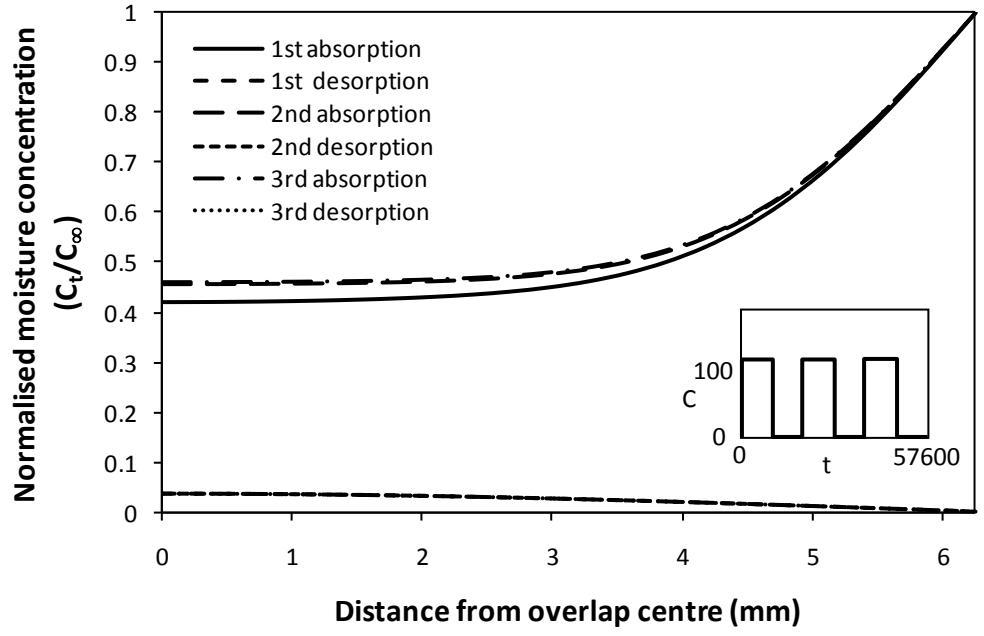

Figure 6.17: Moisture concentration in the adhesive layer after absorption-desorption cycles of 2400 hrs each.

6.6.2 Case II: Predictive Modelling Using Diffusion Parameters Based on Multiple Diffusion Cycles

To demonstrate the effects of history dependent diffusion characteristics on moisture concentration prediction, the modelling methodology described in Section 6.4 was applied to a single lap joint subjected to the same environmental conditions as that for Case I in Section 6.6.1. Figure 6.18 compares the concentration profiles at the middle of the adhesive layer for the 4800 hrs cyclic conditioning environment. The predicted concentration after the first absorption processes is similar for both Case I and II, as seen by comparing Figure 6.16 and Figure 6.18, since the diffusion coefficients are the same for the first absorption. However, because of the faster desorption, the amount of residual moisture after the first desorption is less in Case II than in Case I. The moisture concentration after the second absorption was higher in Case II even though the amount of the residual moisture was less at the start of the absorption than in Case I. This was because of the effect of using moisture dependent absorption coefficients. The third absorption, in Case II, also predicted a higher moisture concentration than in the Case I.

In the case of 9600 hr cycles, the moisture concentration in the first absorption is the same in both cases, as may be seen in Figure 6.17 and Figure 6.19. In the second absorption, higher moisture concentration is predicted in Case II than in Case I and the moisture absorption predicted after the third absorption is also higher in Case II than in Case I, which is consistent with the predictions with the 4800 hr cycles. The residual moisture after each desorption is also lower in Case II than Case I. The longer cycles also result in lower residual moisture at the end of the desorption cycles.

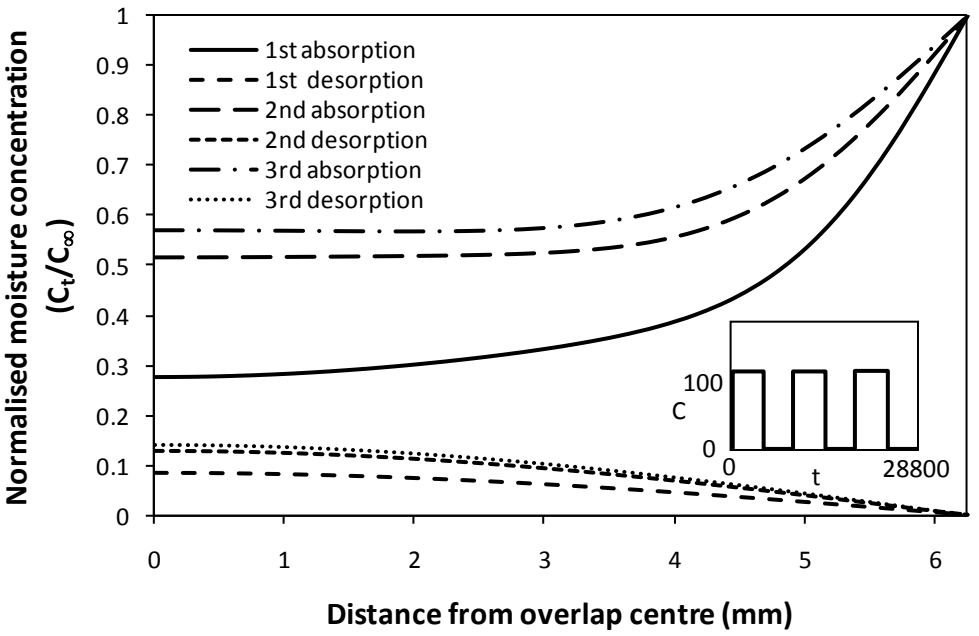

Figure 6.18: Moisture concentration in the adhesive layer, using multi-cycle model, after absorption-desorption cycles of 1200 hrs each.

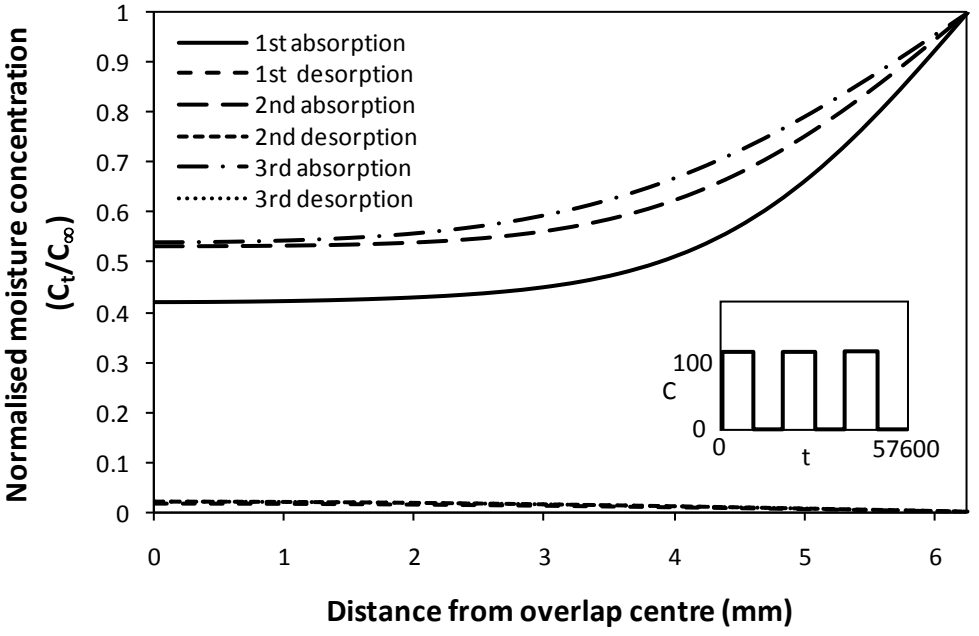

Figure 6.19: Moisture concentration in the adhesive layer, using multi-cycle model, after absorption-desorption cycles of 2400 hrs each

6.6.3 Discussion

Comparison of the modelling methodologies where the effect of hygroscopic history is ignored (Case I) and included (Case II) show that the predicted moisture concentrations were different in the two cases. This is true for both absorption and desorption cycles. The predicted concentration after absorption in Case II either increases or stays the same between cycles and has no clear trend under different absorption times, as shown in Figure 6.20(a) and (b). Thus the amount of moisture in the adhesive layer, along with history dependent diffusion coefficients, presents a unique diffusion situation in each absorption cycle, which is difficult to predict based on a general pattern.

In general, the desorption cycles in Case II predicted a lower residual moisture at the end of each cycle than Case I, as can be seen in Figure 6.21(a) and (b). This is the result of the use of moisture dependent diffusion coefficients, which increase with each desorption cycle. The lower predicted moisture when using history dependent moisture uptake may mean that higher strength is retained by the adhesive after desorption.

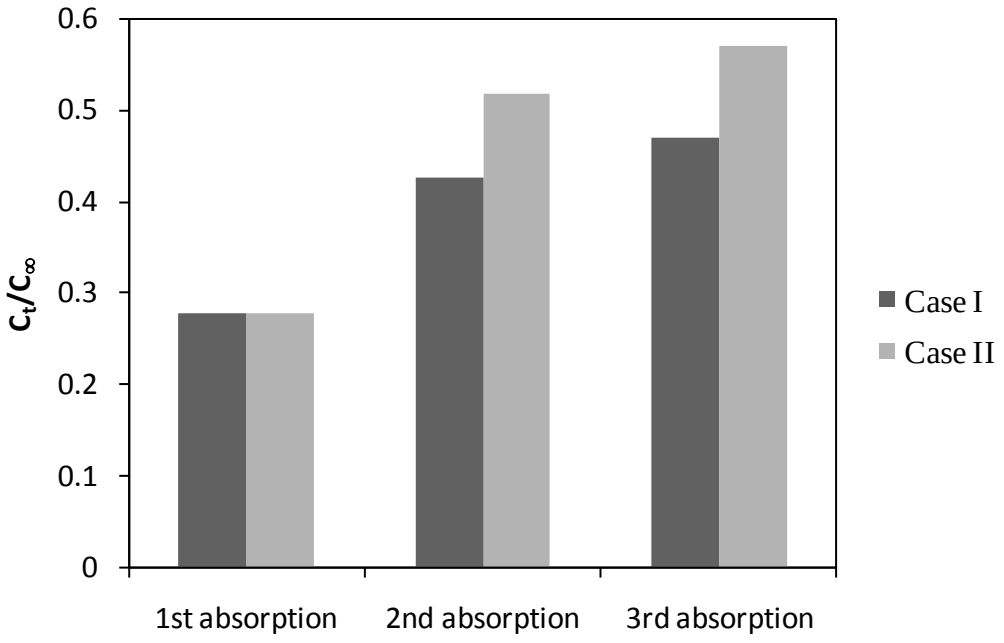

(a)

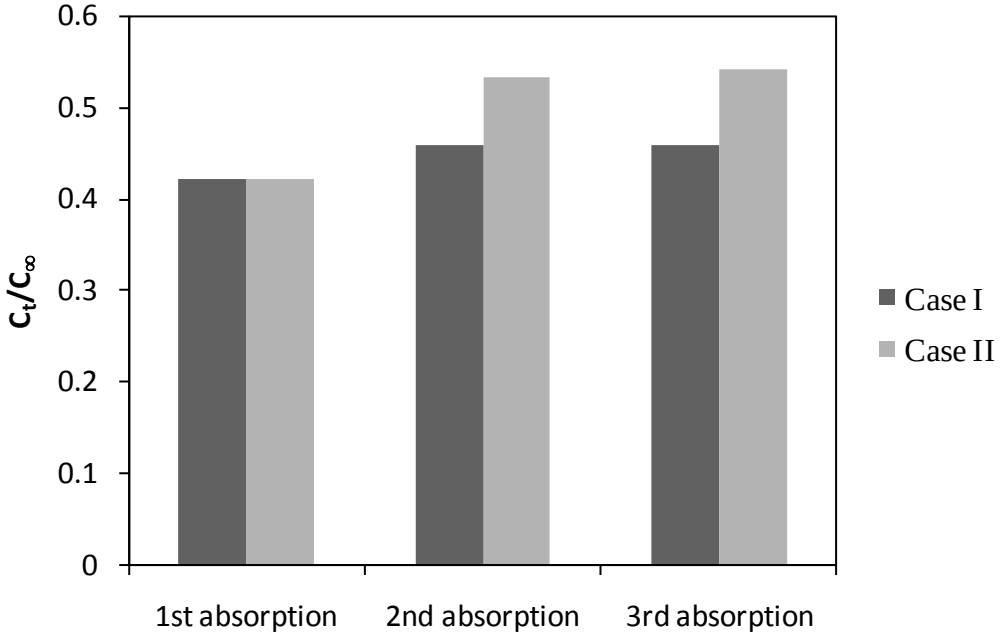

(b)

Figure 6.20: Normalised moisture concentration at the overlap centre after absorption for (a) 1200 hrs (b) 2400 hrs conditioning.

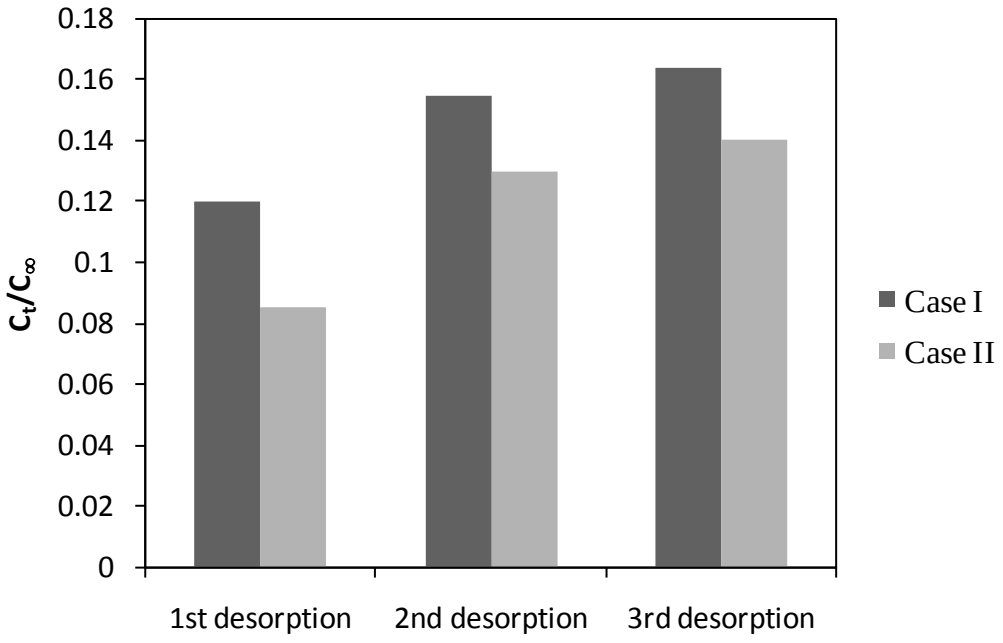

(a)

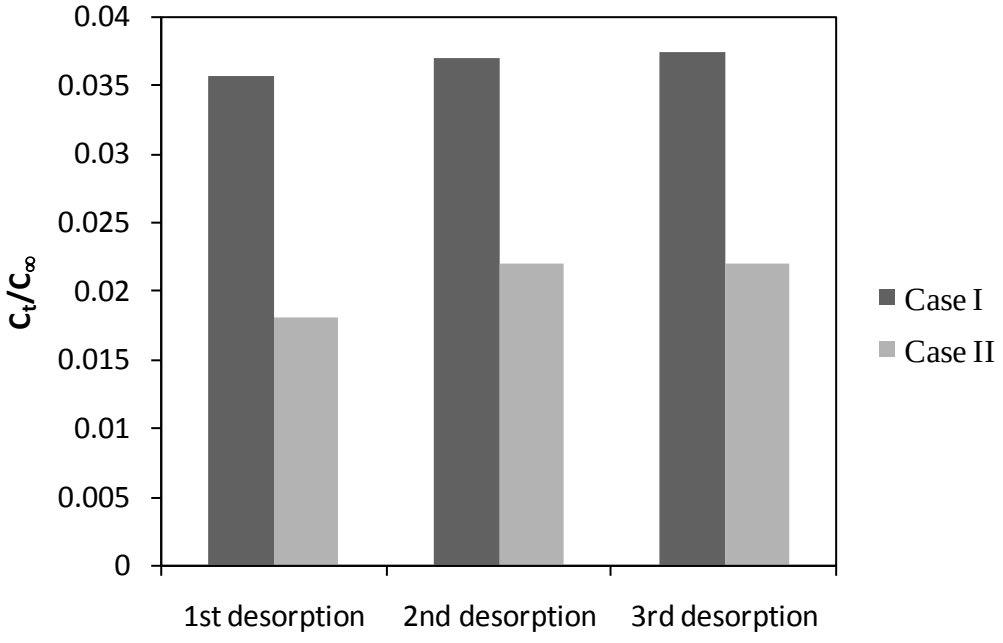

(b)

Figure 6.21: Normalised moisture concentration at the overlap centre after desorption for (a) 1200 hrs (b) 2400 hrs conditioning.

6.7 Cyclic Moisture Diffusion in Single Lap Joints

The moisture diffusion in the single lap joints that were conditioned for single and multiple absorption and desorption cycles, at 50°C and 70°C, was determined by using the cyclic moisture dependent methodology. A quarter of the adhesive layer, in a single lap joint was modelled, utilising the geometric and loading symmetry, as discussed in Section 5.2. A three dimensional model was required to apply the correct moisture boundary conditions. Fillets were included at the ends of the adhesive layer based on average dimensions measured from manufactured joints. Since the adherends were prepared by using ACDC pretreatment detailed in Section 3.3.2, which promoted good wetting of the adherends, the potential of enhanced moisture diffusion along the interface is reduced and, hence the main moisture path was considered to be through the adhesive. Three dimensional, linear continuum field elements with eight nodes were used. Normalised moisture concentration was applied as a boundary condition and moisture concentrations were obtained for diffusion time intervals of 7, 14, 28, 56 and 182 days, as used in the experimental testing. The predicted moisture concentrations were later used to determine the hygroscopic stresses, as discussed in Chapter 7.

6.7.1 Single Absorption-Desorption Cycle at 50 ℃

Figure 6.22 shows the predicted normalised moisture concentrations in the adhesive layer, at different time intervals, after moisture absorption and desorption at 50°C. The moisture concentration in the adhesive layer increase progressively with the increasing conditioning time; however, the adhesive layer did not achieve saturation even after 182 days of moisture absorption. Residual moisture was present in the adhesive layer at all desorption time intervals. As the adhesive layer was not fully saturated under all conditioning times, the moisture front moved in two different directions, during desorption, to achieve equilibrium, as discussed in Section 6.6.1. The pockets of high residual moisture changed location and shape in the adhesive layer, based on the conditioning time. The highest amount of residual

moisture in the adhesive layer was after 182 days of moisture absorption-desorption cycles.

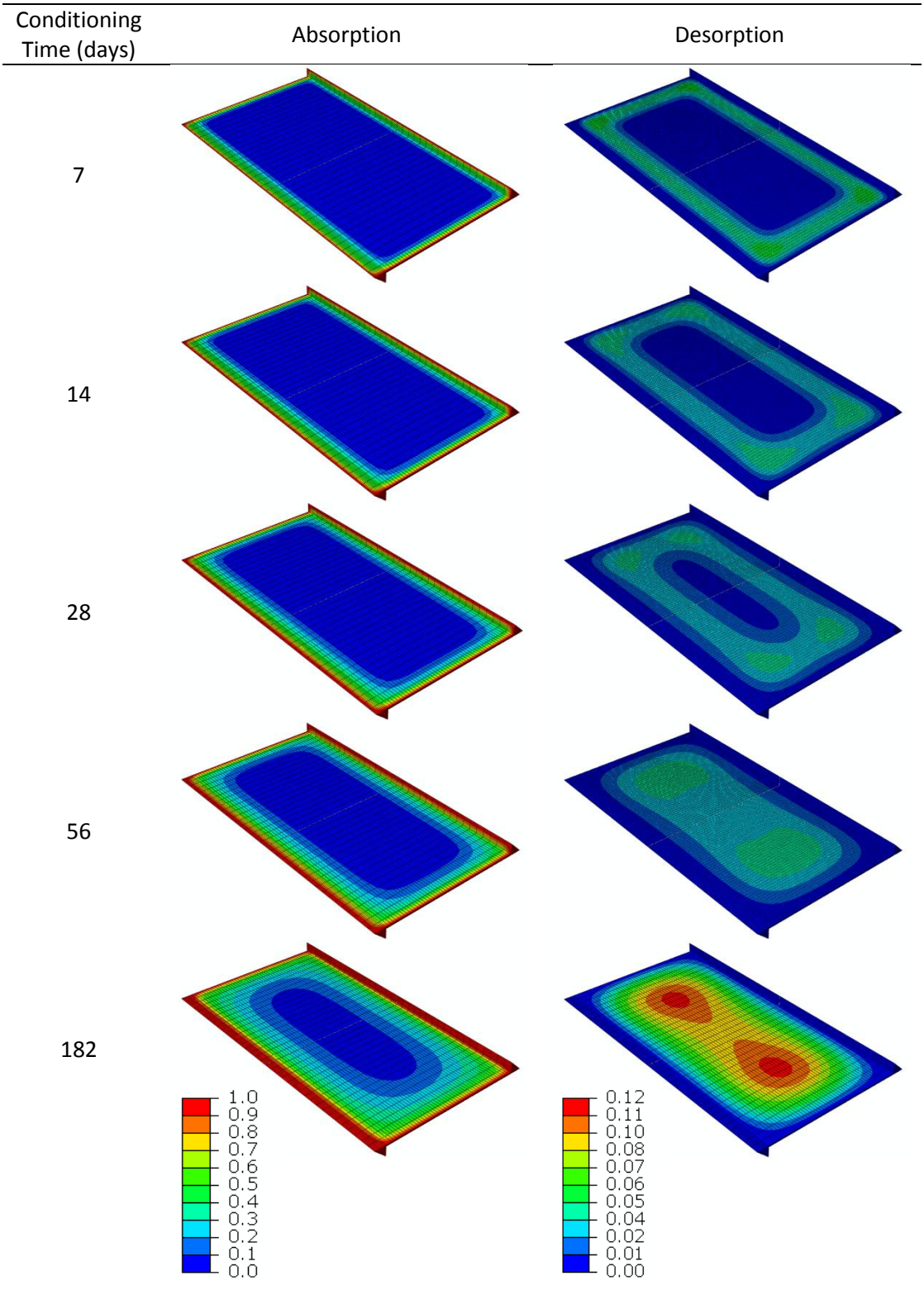

Figure 6.22: Normalised moisture concentration profiles in the adhesive layer of single lap joint after absorption and desorption cycles, conditioned at 50°C.

6.7.2 Single Absorption-Desorption Cycle at 70℃

The prescribed normalised moisture concentrations in the adhesive layer, at different time intervals, are shown in Figure 6.23 for absorption and desorption cycles when conditioned at 70°C. The amount of moisture in the adhesive layer increased with increasing conditioning time, as was observed in the single lap joints conditioned at 50°C. Residual moisture was present in the adhesive layer after all desorption time intervals. A comparison of normalised residual moisture in the adhesive layer at 50°C and 70°C shows that less residual moisture was retained at 50°C than at 70°C. For the 56 and 182 days desorption, the centre of the adhesive layer achieved equilibrium with its surrounding adhesive and the moisture diffusion front only progressed towards the outer boundaries. This resulted in lower residual moisture after 182 days of desorption than 56 days of desorption. In contrast, the highest amount of residual moisture at 50°C was predicted after 182 days of desorption. This shows that a state of moisture concentration in the adhesive layer may be achieved after which the residual moisture starts to decrease.

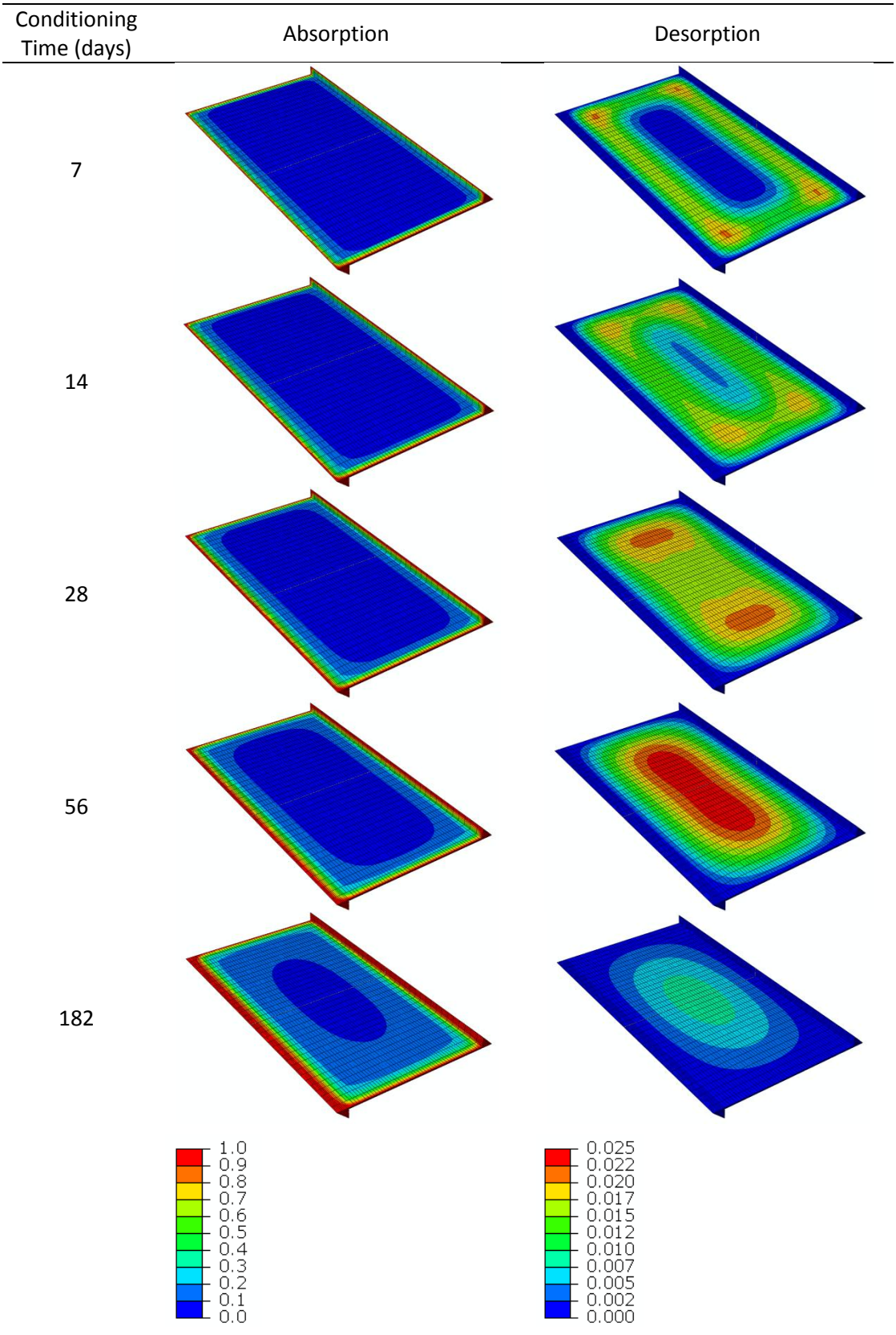

Figure 6.23: Normalised moisture concentration profiles in the adhesive layer of single lap joint after absorption and desorption cycles, conditioned at 70°C.

6.7.3 Multiple Absorption-Desorption Cycles at 70℃

The normalised moisture concentration profiles of single lap joints conditioned at 70°C for five absorption-desorption cycles are shown in Figure 6.24. It can be seen from the moisture absorption plots that the amount of moisture is progressively increasing, in the centre of the adhesive layer, with each absorption cycle. The desorption concentration plots show residual moisture in the adhesive layer at the end of each desorption cycle. The adhesive layer did not achieve saturation during any absorption cycle, thus moisture absorption from areas of high moisture concentration continued towards the centre of adhesive, even during desorption cycles. Thus the moisture concentration in the centre of the adhesive may be seen as progressively increasing in the desorption concentration plots. When the subsequent absorption cycle occurred, the moisture absorbed in the adhesive layer increased owing to the presence of residual moisture. This indicates that the amount of moisture would continue increasing until a state of equilibrium was achieved in the adhesive layer. Hence, the moisture cycling will increase the total amount of absorbed moisture, thus degrading the adhesive properties.

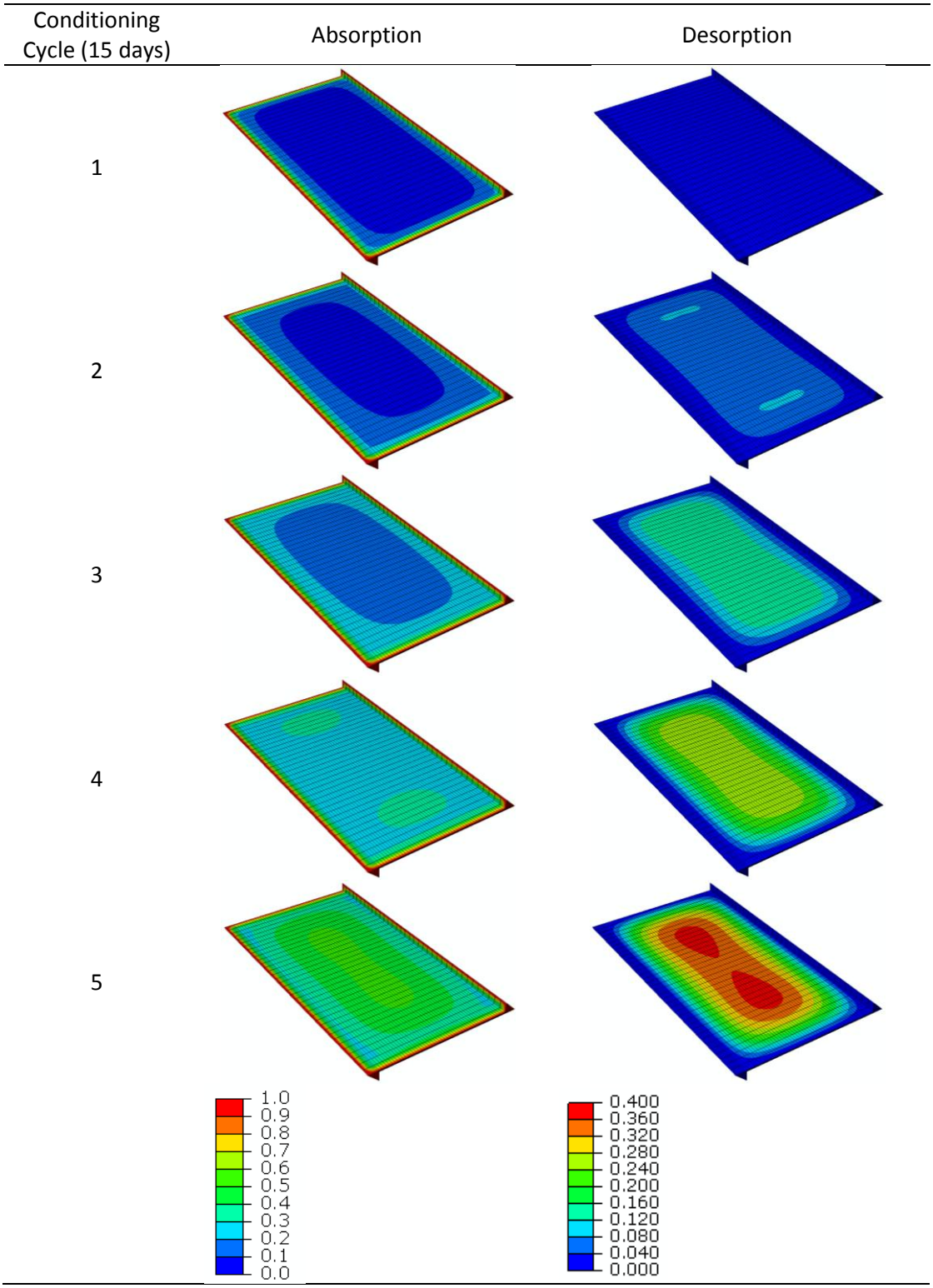

Figure 6.24: Normalised moisture concentration profiles in the adhesive layer of single lap joint after absorption and desorption cycles, conditioned at 70°C.

6.8 Summary

An experimental investigation of cyclic moisture diffusion showed that the absorption of moisture in the adhesive is a non-Fickian process and desorption is a Fickian process. The rate of diffusion is dependent on the moisture history of the adhesive and increase in D and M_∞ were observed with moisture cycling. The observed change in the nature of the absorption and desorption processes with cycling indicates that the structure of the adhesive is altered by moisture absorption.

A comparison of moisture predictions based on diffusion parameters from a single absorption curve (Case I) and history dependent diffusion parameters (Case II) revealed that the amount of residual moisture predicted in Case I is always greater than Case II. If equilibrium is not reached during a cyclic situation, localised desorption and absorption processes occur in the adhesive layer and the use of the corresponding diffusion coefficients is necessary for a correct moisture prediction. Neglecting the moisture history dependent diffusion coefficient can result in over or under prediction of moisture during absorption. Since the diffusion rates in absorption and desorption are different and also have different dependencies on moisture history, it is necessary to use a methodology including moisture history for the accurate prediction of degradation and residual joint strength of environmentally cycled adhesive joints. This can be seen by the prediction of moisture concentration in the adhesive joints, conditioned at 50°C and 70°C for single and multiple absorption and desorption cycles.

Chapter 7
Stress Prediction in Cyclic Environmental Conditions

7.1 Introduction

A methodology for the prediction of the transient moisture concentration under cyclic moisture diffusion conditions was presented in Chapter 6. This chapter extends the cyclic moisture diffusion methodology by coupling with a stress analysis method. Predictions of stress using this methodology were verified by comparing the model results with bulk adhesive experimental data. The method was then used to study the stresses in single lap joints, conditioned for different time intervals at 50°C and 70°C in water. Stresses arising from thermal, hygroscopic and mechanical loading were included in the analysis. The strength of adhesive joints may be predicted by combining predicted stresses with a failure criterion and is discussed in the next chapter.

7.2 Stress Prediction under Cyclic Moisture Conditions

The framework for cyclic stress prediction is given in Figure 7.1. The cyclic moisture diffusion prediction coupled with a cyclic stress prediction method will be referred to as the *variable moisture and stress prediction methodology.* The moisture history dependence of mechanical properties was introduced in the model by using field variables. The elastic and plastic properties of the adhesive were considered functions of; (i) the normalised moisture concentration, (ii) the moisture history in the form of the number of diffusion cycles and (iii) the diffusion process i.e. either

absorption or desorption. This dependency is illustrated by Equations (7.1) and (7.2)

.

$$E(C_t, FV1, FV2) \tag{7.1}$$

$$\varepsilon^{pl}(C_t, FV1, FV2) \tag{7.2}$$

where ε^{pl} is the plastic strain of the adhesive, C_t is the normalised moisture concentration at time t and $FV1$ and $FV2$ are two field variables. $FV1$ represents the moisture history in the form of the number of absorption and desorption cycles and $FV2$ represents the nature of the diffusion process i.e. absorption or desorption. The moisture history and moisture process are stored in state variables in the form of a spatially resolved field for the adhesive layer. The ABAQUS user subroutine USDFLD was used to define the coupling between the field variables and the state variables. USDFLD allows the definition of field variables at a material point as a function of time or any available material point quantity [193]. The moisture history, normalised concentration and moisture process definitions required for the predictive stress model were obtained from a cyclic moisture diffusion analysis.

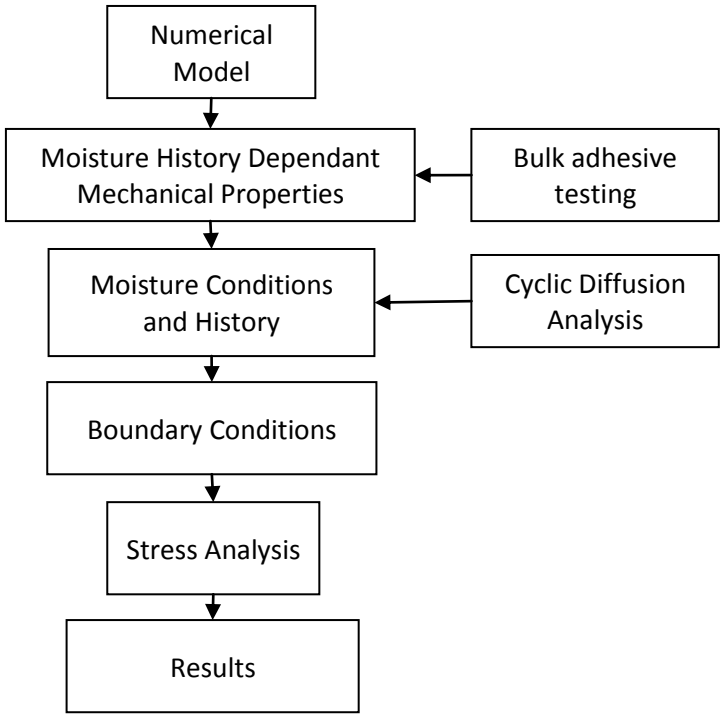

Figure 7.1: Framework for the cyclic stress prediction method.

7.3 Comparison of Cyclic Stress Predictions with Experimental Results

To verify the cyclic stress prediction methodology, a tensile specimen of the adhesive was modelled to predict the stress after cyclic moisture diffusion and the results were compared with experimental data. The geometry of the tensile specimen, along with the finite element model is shown in Figure 7.2. A three dimensional model of the sample gauge length was used for the analysis. Symmetry enabled this to be represented by a quarter of the geometry, as shown in Figure 7.2b. The three dimensional model was necessary for the correct application of moisture boundary conditions. The model was meshed with eight node, continuum brick elements, which provide a good response under large displacements [191]. In order to represent the experimentally observed deformation of the tensile samples, a small geometric imperfection was introduced along line Y-Y and a biased mesh, with higher number of elements in the middle of the specimen was used.

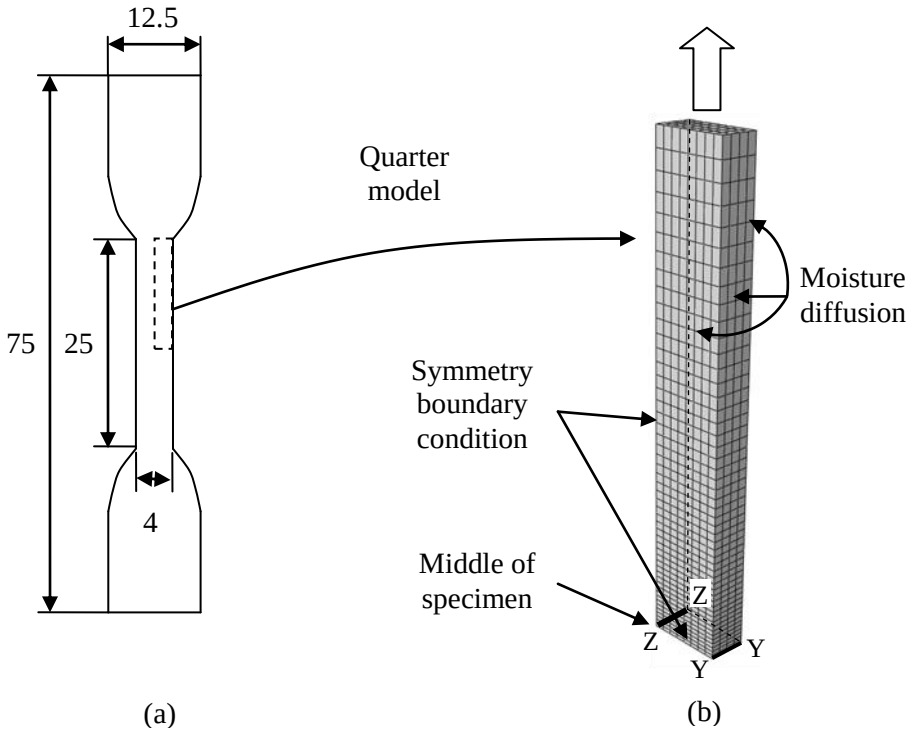

Figure 7.2: Tensile test specimen. (a) Sample geometry and (b) finite element model with boundary conditions. All dimensions are in mm (not to scale).

The stress-strain response of the model was determined for four different moisture conditions; (i) unconditioned, (ii) first absorption for 1400 hrs, (iii) dried for 1400 hrs after first absorption and (iv) second absorption for 2000 hrs. These moisture conditions were selected based on the available experimental data. Moisture concentration in the tensile specimen at the selected moisture conditions was determined using the cyclic moisture diffusion methodology detailed in Chapter 6. A dual Fickian model [65] was used for the prediction of moisture concentrations after both the first and the second absorption whilst a Fickian diffusion model was used for the desorption. The normalised moisture concentrations, at the middle of the tensile specimen are plotted in Figure 7.3.

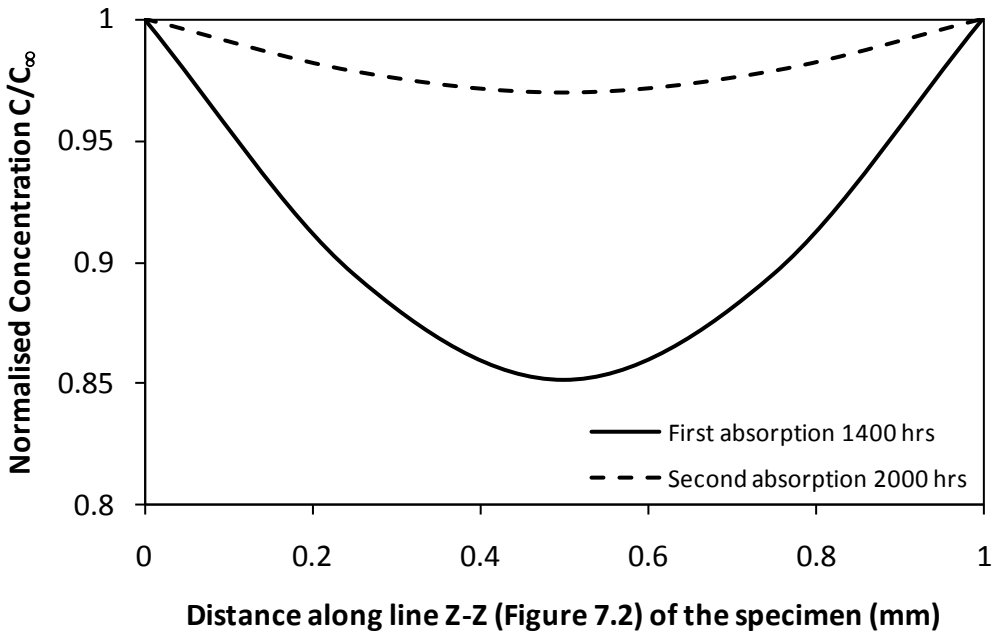

Figure 7.3: Normalised moisture concentration profiles in the tensile test specimen.

The predicted moisture concentration and history were used as initial conditions in the stress analysis of the tensile specimen. Moisture history dependant elastic-plastic properties were used for the adhesive, based on the experimental stress-strain curves described in Section 4.2.3. The yield surface of the adhesive has hydrostatic stress dependence and, hence, a linear Drucker Prager model was used to define the yield surface, where the yield function, F_y, is given by [119]:

$$F_y = t^* - p^* \tan(\beta) - d^* = 0 \tag{7.3}$$

where

$$t^* = \frac{\bar{\sigma}}{2}\left[1 + \frac{1}{K^*} - \left(1 - \frac{1}{K^*}\right)\left(\frac{r^*}{\bar{\sigma}}\right)^3\right] \tag{7.4}$$

$$\bar{\sigma} = \sqrt{3J_2} \tag{7.5}$$

$$d^* = \left(1 - \frac{1}{3}\tan(\beta)\right)\sigma_c \tag{7.6}$$

where β is the material angle of friction, K^* is the flow stress ratio, $\bar{\sigma}$ is von Mises equivalent stress, r^* is the third stress invariant, p^* is hydrostatic stress, J_2 is the second stress invariant and σ_c is the uniaxial compressive yield stress. The Drucker Prager model constants for FM73 have been defined to be β = 27.8° and K^* = 0.85 [119]. The tensile specimen was loaded using displacement control. Comparisons of the stress-strain curves obtained from the finite element model and the experimental tensile tests are shown in Figure 7.4. Excellent correlation between the predicted and experimental results can be seen for all the selected moisture conditions.

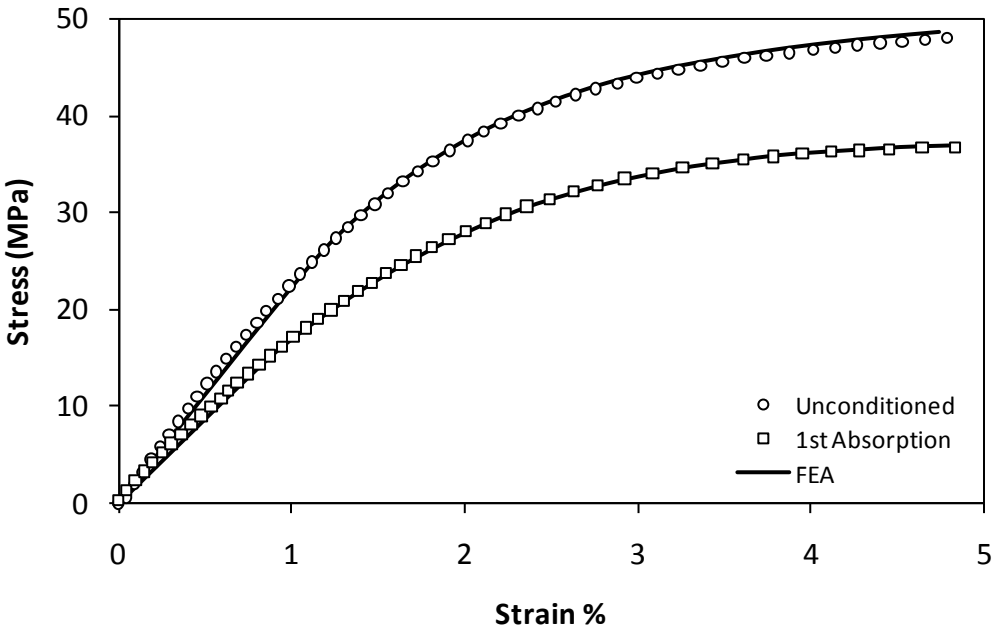

(a)

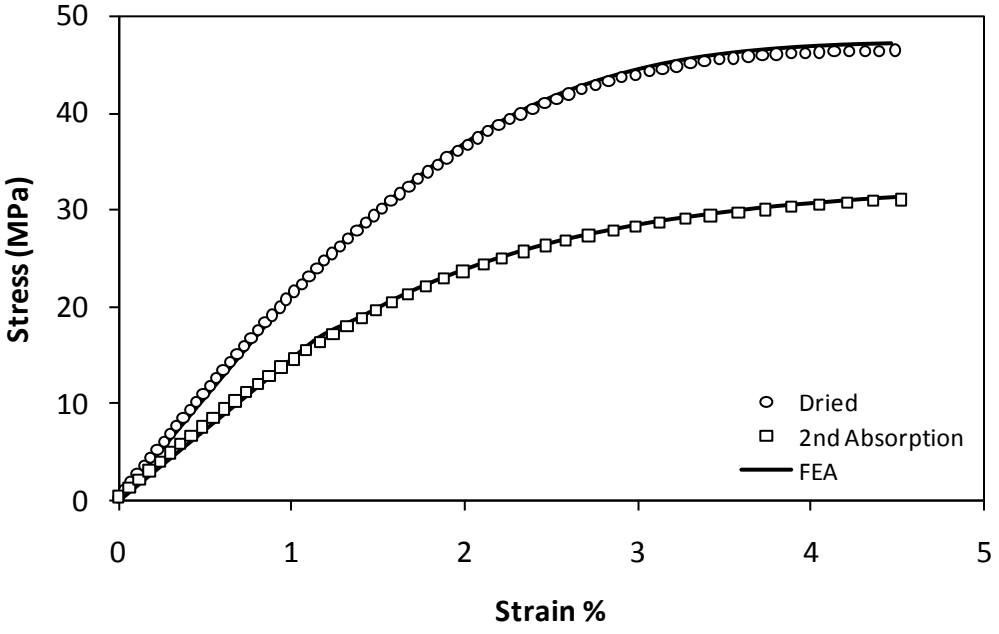

(b)

Figure 7.4: Comparison of experimental and finite element analysis determined stress-strain curves under cyclic moisture diffusion. (a) Unconditioned and first absorption. (b) Dried and second absorption.

7.4 Single Lap Joints under Cyclic Moisture Conditions

The cyclic stress prediction methodology was used to predict the stress in single lap joints conditioned for various moisture absorption and desorption cycles, as discussed in Chapter 3. Geometric and loading symmetry allowed modelling of one half of the single lap joint, as shown in Figure 7.5. Fillets were included at the end of the adhesive layer based on the average dimensions measured from manufactured joints. A three dimensional model, meshed with linear eight node, continuum brick elements, was used for the analyses. A minimum element size of 0.12 x 0.06 x 0.12 mm was used in the adhesive layer, as shown in Figure 7.6. During the joint manufacture, conditioning and testing; thermal, hygroscopic and mechanical stresses are generated in single lap joints and a multi-step analysis was carried out to determine the stresses after each of these stages. Each step was modelled using a corresponding numerical procedure, as shown in Figure 7.7.

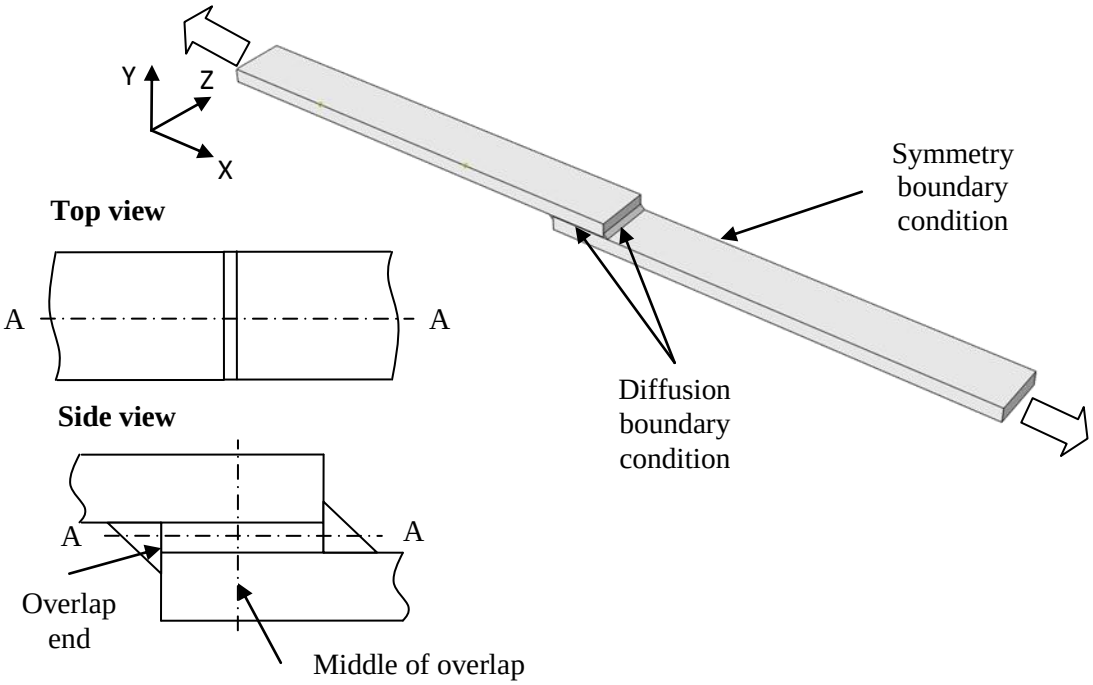

Figure 7.5: Half model of the single lap joint with boundary conditions.

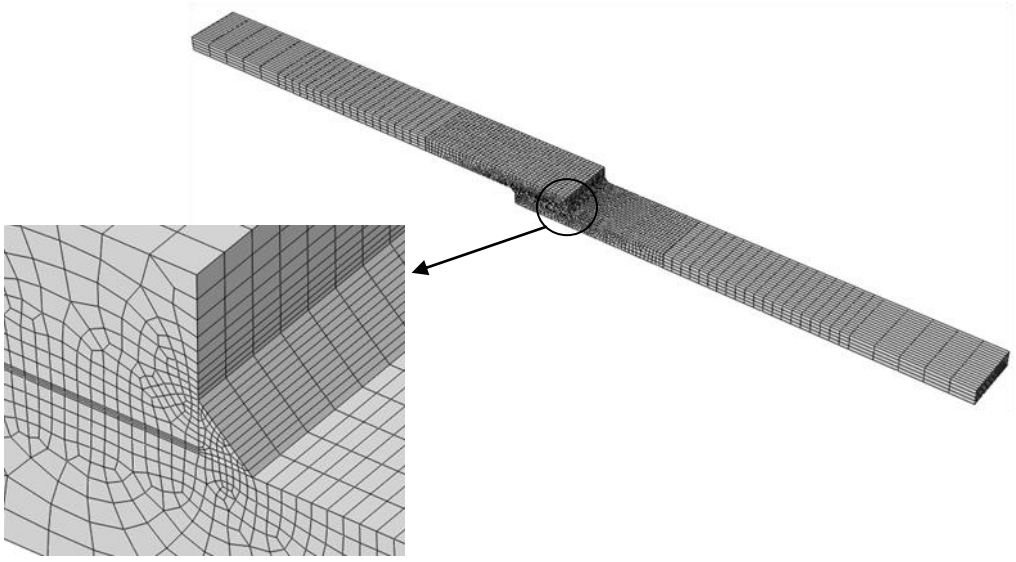

Figure 7.6: Finite element mesh with detail in the adhesive layer and fillet.

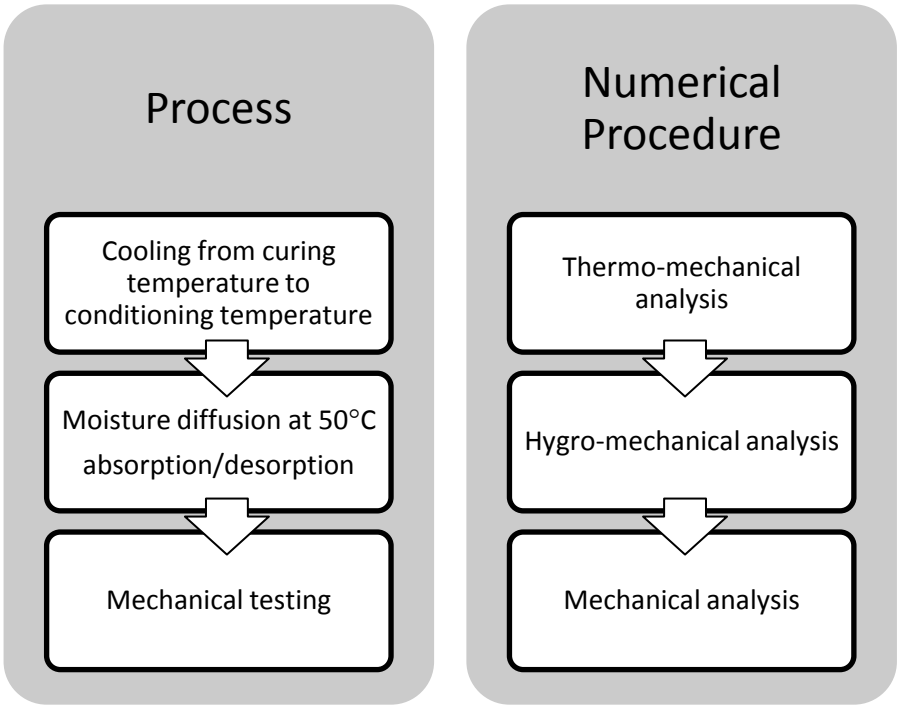

Figure 7.7: Process history of the single lap joint and corresponding numerical analysis procedure.

In the first step, a thermo-mechanical analysis was used to determine the thermal residual stresses in the adhesive and adherends after curing. Coefficients of thermal expansion for the Al2024 adherend material and the FM73 adhesive are given in Table 7.1. The analysis started by heating the joint to 120°C from room temperature, as occurs at the start of the curing process. At the curing temperature, the adhesive was considered stress free [194]. Cooling of the joints to the conditioning temperature was carried out, which resulted in thermal stresses in the joints.

Table 7.1: Thermal properties of aluminium alloy 2024 [195] and FM73 adhesive [176].

Coefficient of thermal expansion (K^{-1})	Value
Al2024	23.2×10^{-6}
FM73	7.7×10^{-5}

In the second step, the thermal stresses were used as an initial condition and a hygro-mechanical analysis was carried out to determine the moisture concentrations and hygrothermal stresses in the joints. As with the bulk adhesive specimens, the moisture concentrations in the adhesive layer were determined using the cyclic moisture diffusion methodology detailed in Chapter 6, with a dual Fickian model for moisture absorption and a Fickian model for moisture desorption. The moisture boundary conditions were applied in the form of normalised moisture concentrations, as shown in Figure 7.5 and the diffusion analysis was carried out for durations of 7, 14, 28, 56 and 182 days. Each absorption analysis was followed by a desorption analysis of the same duration to determine the moisture distribution after drying. As the adherends were prepared by degreasing and the ACDC pretreatment, which promoted good wetting of the adherends, the potential for enhanced moisture diffusion along the interface was reduced and, hence the only moisture path considered in this case was through the adhesive. However, it should be noted that interfacial diffusion may be readily included in the proposed methodology by using a faster diffusion rate in an interfacial layer, if required.

In the final step, a stress analysis was performed and a load of 5 kN was applied to determine the stresses under tensile loading, as experienced during tensile testing of the joints. The moisture history, normalised moisture concentration and stresses from the hygroscopic analysis were used as initial conditions for the stress prediction. A load of 5 kN was selected as it was below the failure load of unconditioned and conditioned joints whilst causing plastic deformation in the joints.

7.5 Stresses in Single Lap Joints Conditioned at 50°C

Before discussing the development of stresses in the joint, the moisture concentration in the joints is considered, which is the source of the hygroscopic stresses. Moisture concentration predictions for the joints conditioned at 50°C in water were presented in Section 6.7.1 and only the results along the path of the stress plots are discussed here. Figure 7.8 plots the normalised moisture concentration in the adhesive layer, along line A-A in Figure 7.5, after different periods of moisture absorption at 50°C in water. The moisture concentration in the adhesive layer increases with conditioning time; however, saturation is not achieved, even after 182 days of exposure. Figure 7.9 shows the normalised moisture concentration after the desorption of moisture for 182 days. Although the desorption rate was higher than the absorption rate, as was discussed in Section 4.2.1, moisture was still present in the adhesive layer after all desorption time periods. This may appear surprising, however, since the adhesive layer had low moisture concentration in the middle of the overlap after absorption, the desorption boundary condition only caused the moisture to desorb from the outer regions of the adhesive layer while moisture absorption continued towards the inner regions of the adhesive. Thus two simultaneous processes of absorption and desorption occurred in the adhesive layer during the desorption cycle. The joints conditioned and dried for 7, 14 and 28 days showed peaks in the residual moisture between the end and the middle of the overlap region, these can be seen as localised highs in the normalised concentrations in Figure 7.9.

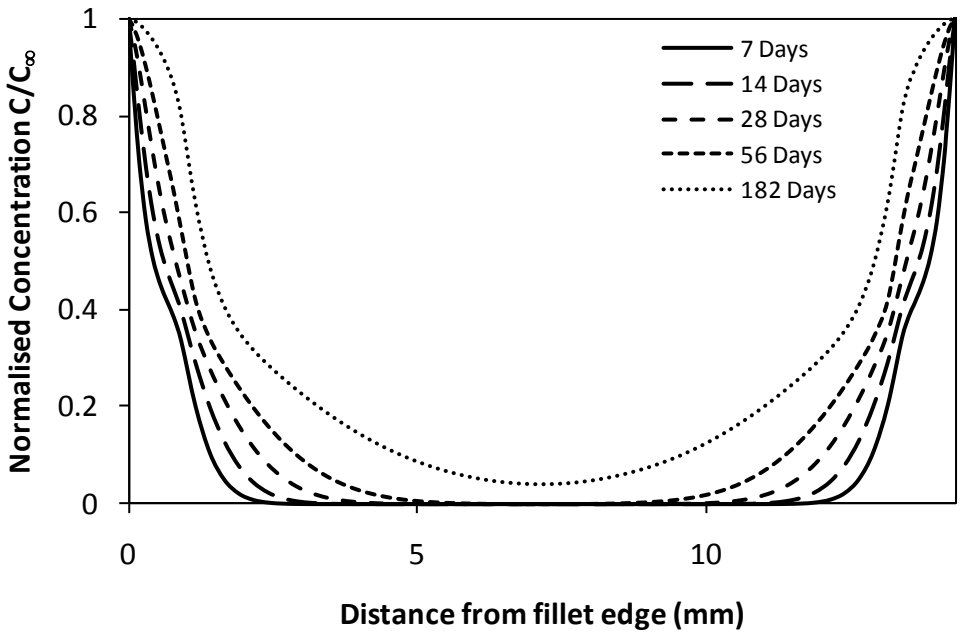

Figure 7.8: Normalised moisture concentration in the adhesive layer along line A-A (from Figure 7.6), when conditioned at 50°C.

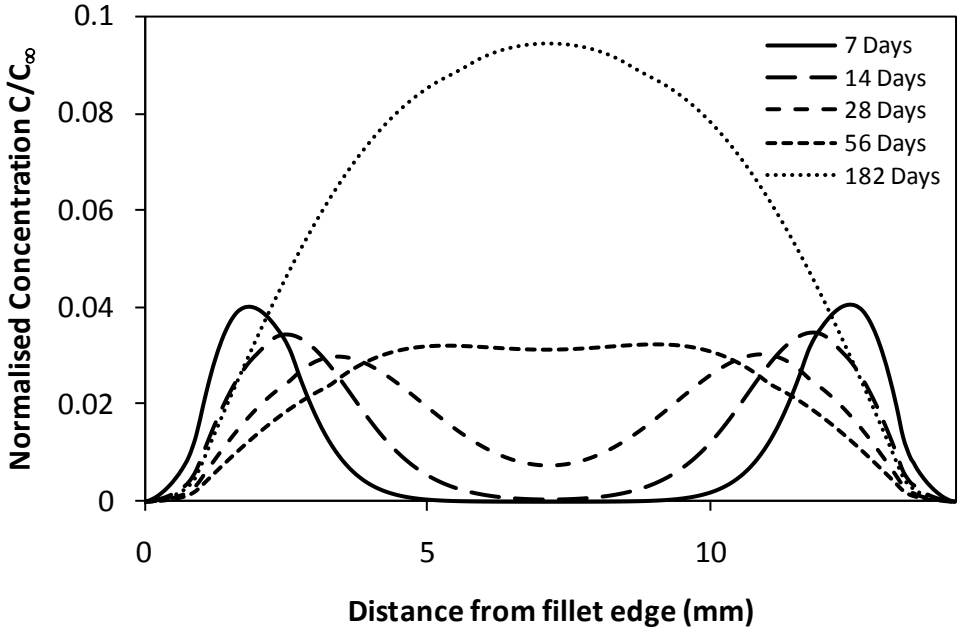

Figure 7.9: Normalised moisture concentration in the adhesive layer along line A-A (from Figure 7.6), when conditioned at 50°C and dried for the same period of time.

In contrast, the maximum amount of residual moisture was seen in the middle of the overlap in the joint conditioned and dried for 182 days. The amount of residual moisture is relatively high in this case but it should be noted that this residual moisture is after 182 days of absorption and desorption and the joint will continue to desorb moisture if the desorption is continued.

7.5.1 Single Lap Joints with Al2024 T3 Adherends

The development of stresses, during the manufacture, conditioning and mechanical loading of a single lap joint with Al2024 T3 adherends, conditioned for 7 days, is shown in Figure 7.10. The stresses were plotted along line A-A, as shown in Figure 7.5. The stresses are divided in two components; (i) stresses along the X-direction (Figure 7.5) are called longitudinal stresses and stresses along Y-direction (Figure 7.5) are referred to as peel stresses. The vertical dashed lines in the figures represent the ends of the overlap. The difference in thermal expansion coefficients of the adhesive and adherends caused significant thermal longitudinal stresses in the adhesive layer. Both the longitudinal and the peel thermal stresses are fairly uniform over the central region of the overlap, varying at the ends and in the fillets. The highest longitudinal stresses were in areas closer to the middle of the overlap while the highest peel stresses were at the overlap edges.

When the joints were exposed to moisture, the diffusing moisture caused plasticisation and swelling of the adhesive. After conditioning for 7 days, the moisture had diffused into the fillets and areas close to the overlap ends and a drop in residual longitudinal stress in these areas was observed. The residual peel stress close to the fillet edges also decreased with moisture ingress and the maximum peel stress moved from the edges of the fillet to inside the fillet. This may be attributed to the relief of the thermal stress by hygroscopic swelling of the adhesive. Application of a tensile load of 5 kN resulted in high longitudinal and peel stresses in the adhesive layer. The highest peel stresses after conditioning and tensile load application was at the overlap ends. When the tensile load was applied after drying of the joints, the highest peel stress was in the same region as it was in

the conditioned joints, which indicates that failure in both the conditioned and dried joints will be initiated close to the overlap end.

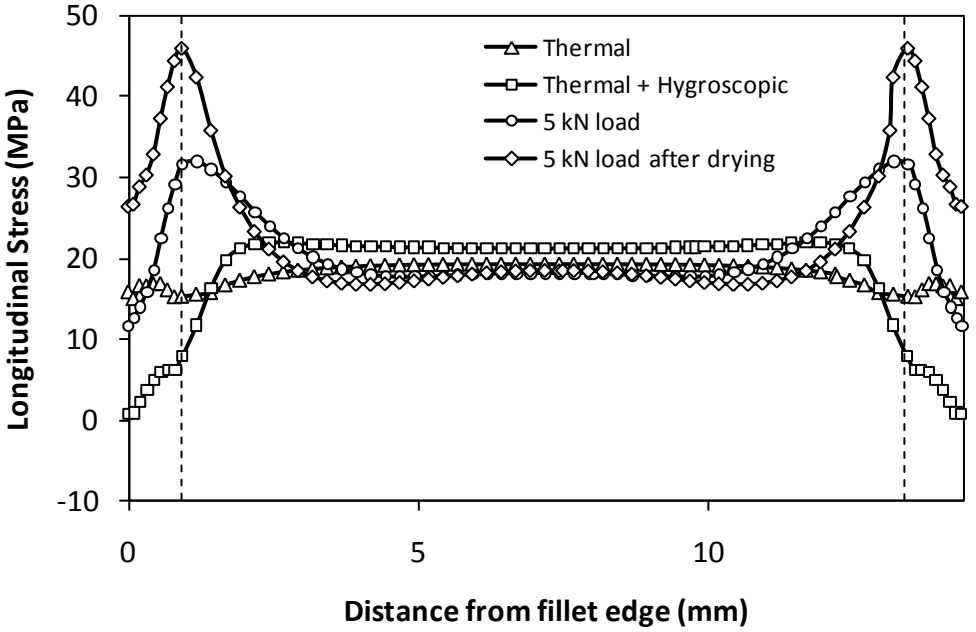

(a)

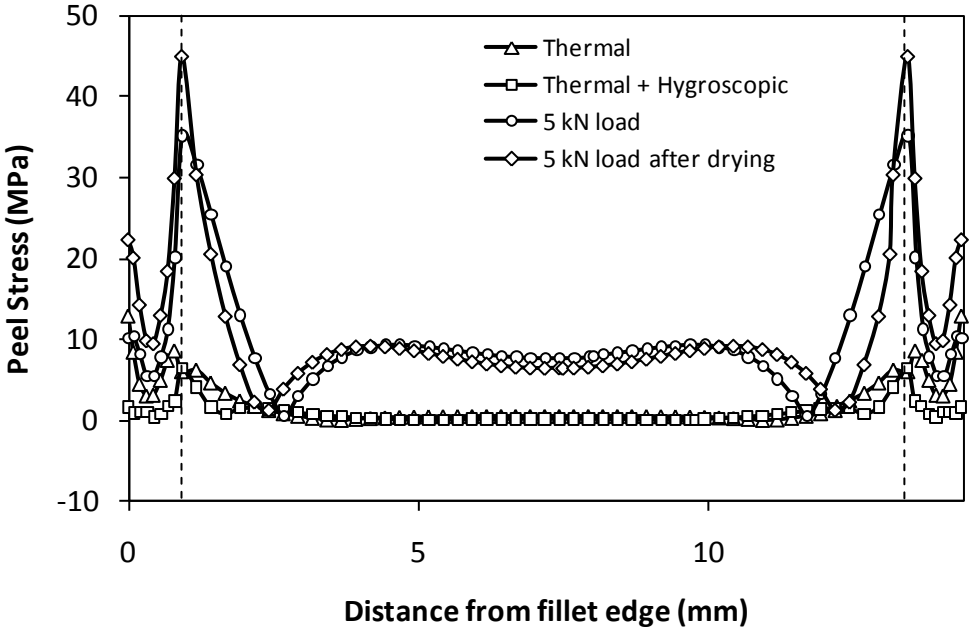

(b)

Figure 7.10: Development of (a) longitudinal stresses and (b) peel stresses in a single lap joint with Al2024 T3 adherends, conditioned for 7 days at 50°C.

The development of longitudinal and peel stresses for joints conditioned for 182 days is plotted in Figure 7.11. The predicted thermal residual stresses were the same for all the joints as they were cured under the same conditions.

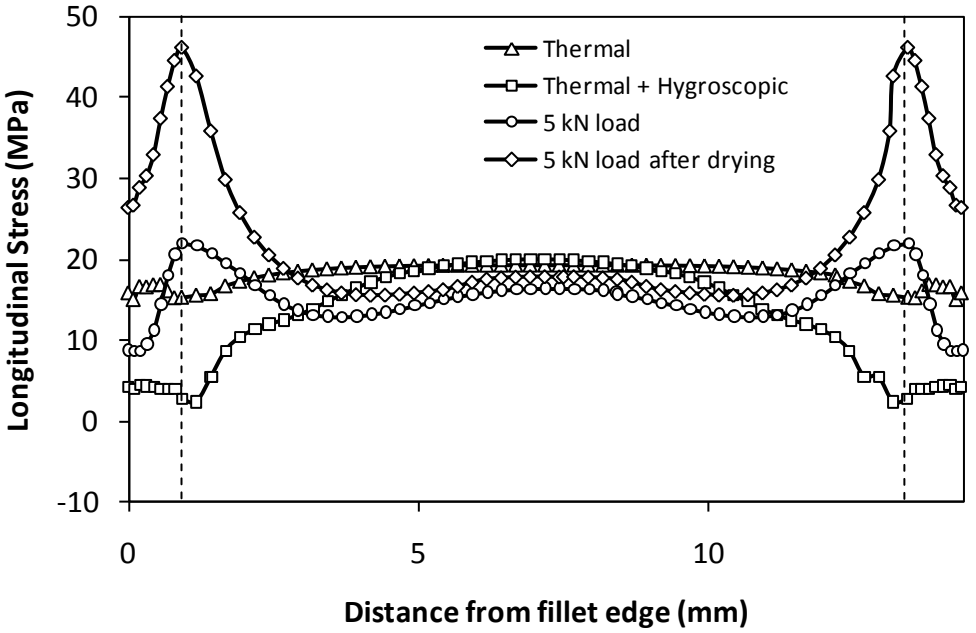

(a)

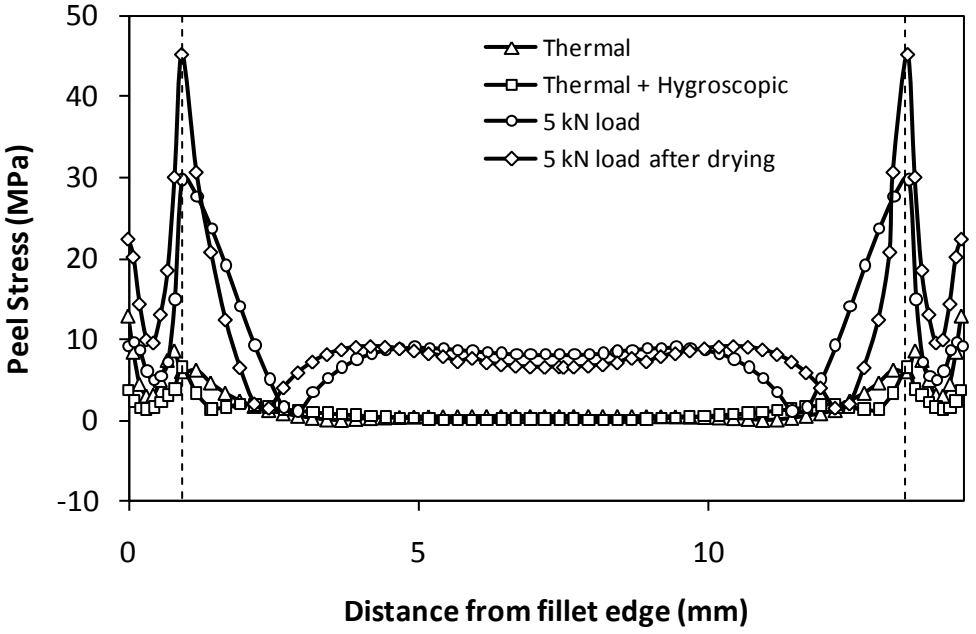

(b)

Figure 7.11: Development of (a) longitudinal stresses and (b) peel stresses in a single lap joint with Al2024 T3 adherends, conditioned for 182 days at 50°C.

It can be seen that the moisture had diffused through the entire overlap length after 182 days and the highest peel stress had moved from the fillet edge to the end of the overlap. When a tensile load of 5 kN was applied to the joints, the highest longitudinal and peel stresses remained at the overlap ends. As discussed above, moisture absorption provides some relief from thermal residual stresses, whilst the highest peel stress moves from the fillet edges to the overlap end with increasing amount of moisture in the adhesive layer. The joints conditioned for 14, 28 and 56 days showed stress development patterns with similar trends.

7.5.2 Single Lap Joints with Al2024 O Adherends

The longitudinal and peel stress development in the single lap joints with Al2024 O adherends, conditioned for 7 days, is shown in Figure 7.12. The thermal and hygrothermal stresses in the T3 and O joints were the same as both types of joint were manufactured and aged under the same conditions. The maximum longitudinal stresses occurred at the end of the overlap after the application of a 5 kN load. When the joints were dried and a tensile load of 5 kN was applied, the location of the maximum stress remained the same as in the conditioned joints, however, a significant increase in the stresses was observed. The maximum peel stress was located close to the end of the overlap, in both conditioned and dried joints. In the joints conditioned for 182 days, the location of the maximum longitudinal and peel stresses was the same as observed in the joints conditioned for 7 days, as seen in Figure 7.13. However, after conditioning and application of the tensile load, the maximum longitudinal and peel stresses were lower in the joints conditioned for 182 days than the joints conditioned for 7 days. A comparison of the stresses in T3 and O joints showed lower longitudinal and peel stresses in T3 than O joints under the same moisture absorption and tensile loading conditions.

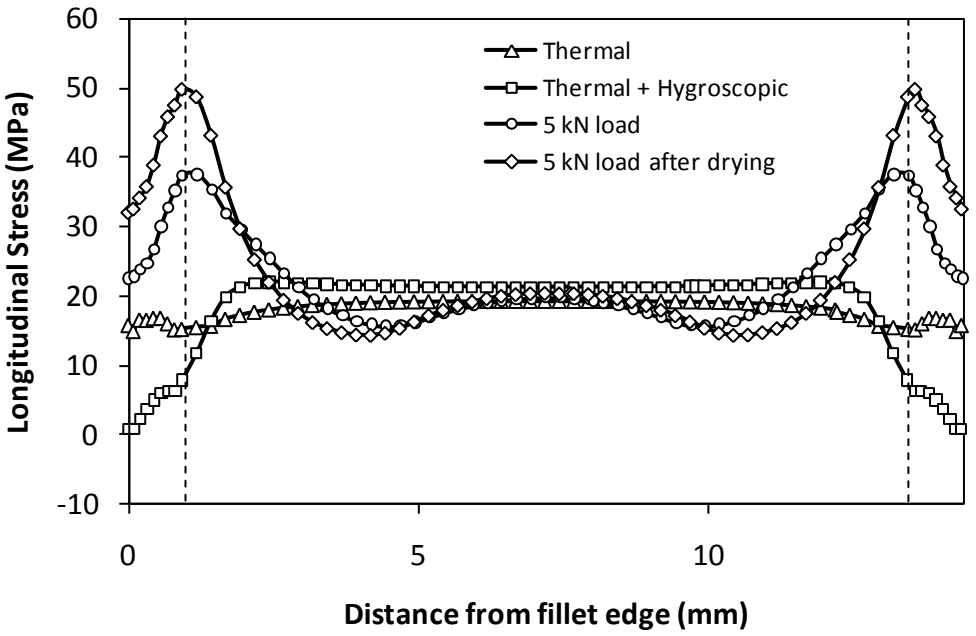

(a)

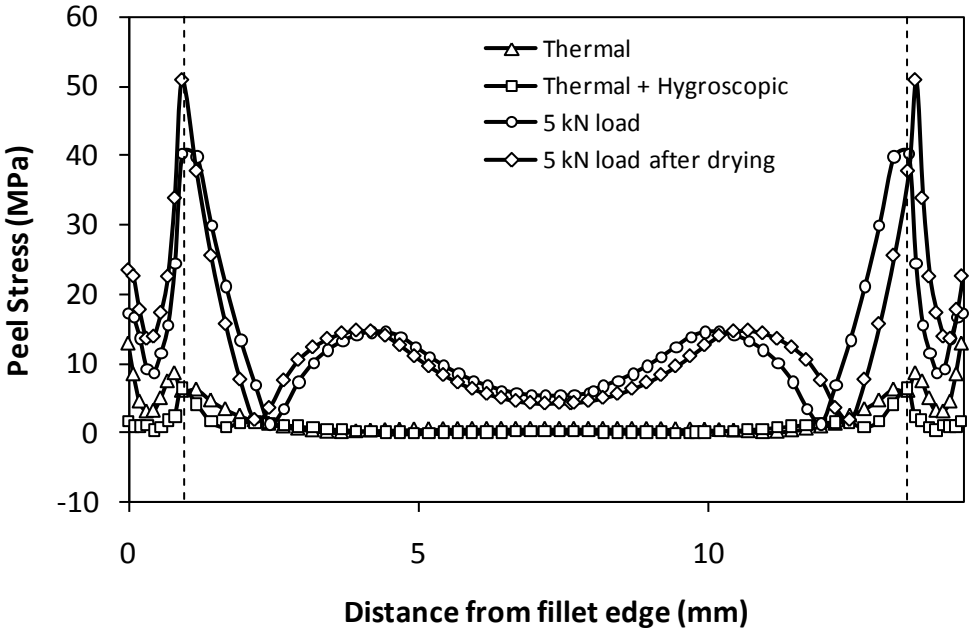

(b)

Figure 7.12: Development of (a) longitudinal stresses and (b) peel stresses in a single lap joint with Al2024 O adherends, conditioned for 7 days at 50°C.

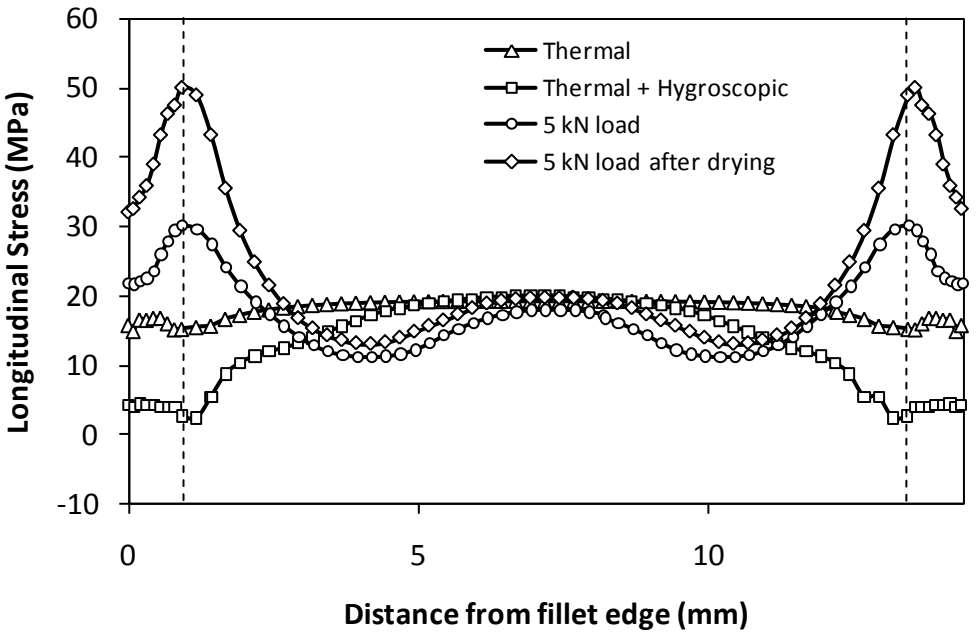

(a)

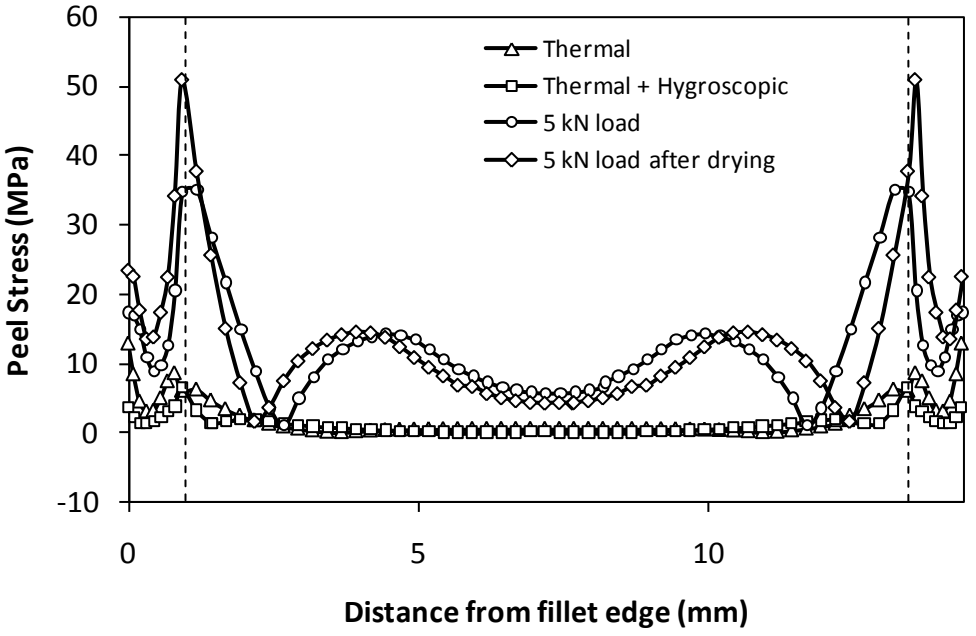

(b)

Figure 7.13: Development of (a) longitudinal stresses and (b) peel stresses in a single lap joint with Al2024 O adherends, conditioned for 182 days at 50°C.

Plastic deformation of the adherends was observed during the tensile testing of the O joints. This may explain the differences in the stress levels under different

moisture conditions and in different types of joints. The lower longitudinal and peel stresses in the O joints, after 182 days than 7 days of conditioning and tensile loading, were due to the increased plastic deformation of the adhesive as the strength of the adhesive degraded with the increasing moisture content. The differences in the stresses of T3 and O joints may be attributed to the plastic deformation of the adherends during tensile loading where the increased rotation of the adherends resulted in higher stresses in O joints than in T3 joints.

7.6 Stresses in Single Lap Joints Conditioned at 70°C

The moisture concentration predictions in the single lap joints, conditioned at 70°C in water, were discussed in Section 6.7.2. The normalised moisture concentration profiles along line A-A (from Figure 7.5) for joints conditioned at 70°C are plotted in Figure 7.14 and the stresses in the joints are plotted along the same line. The middle of the adhesive layer had an insignificant amount of moisture even after 56 days of moisture diffusion and moisture had diffused completely through the adhesive layer only after 182 days of diffusion. The normalised moisture desorption profiles along the line A-A (from Figure 7.5) for joints conditioned and dried at 70°C are plotted in Figure 7.15. In joints conditioned for 7 and 14 days and dried, the maximum residual moisture was present in the form of pockets of moisture between the end and the middle of the overlap. Maximum residual moisture was present in the middle of the joints conditioned for 56 days and dried. This is in contrast to the joints conditioned at 50°C where the maximum residual moisture was found in the joints conditioned for 182 days and dried. This may be attributed to the faster moisture absorption and desorption rates at 70°C than 50°C.

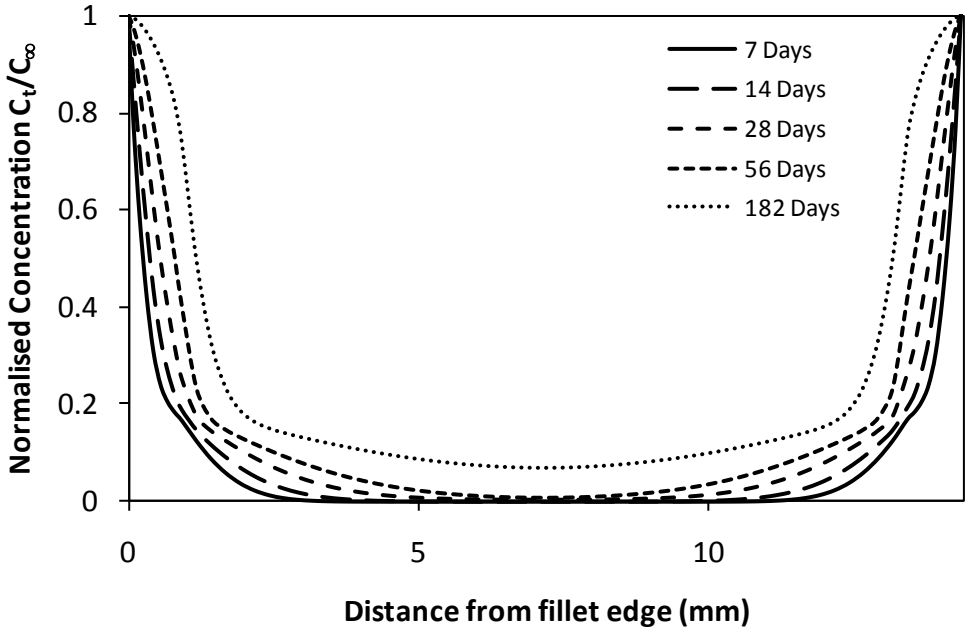

Figure 7.14: Normalised moisture concentration in the adhesive layer along line A-A (from Figure 7.6), when conditioned at 70°C.

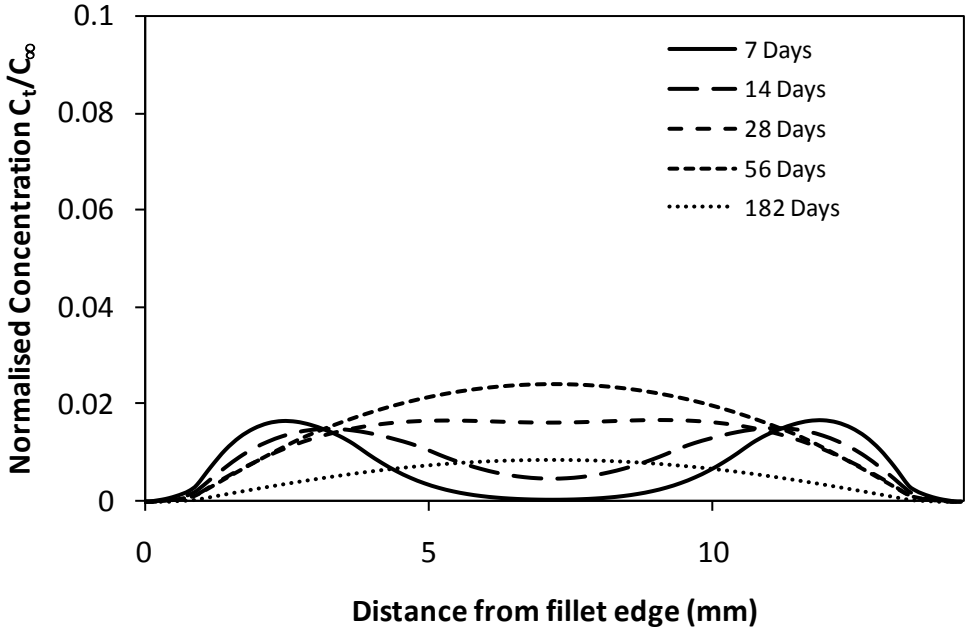

Figure 7.15: Normalised moisture concentration in the adhesive layer along line A-A (from Figure 7.6), when conditioned at 70°C and dried for the same period of time.

7.6.1 Single Lap Joints with Al2024 T3 Adherends

The progression of stresses during the manufacture, conditioning and testing of T3 joints, conditioned at 70°C for 7 days, is shown in Figure 7.16.

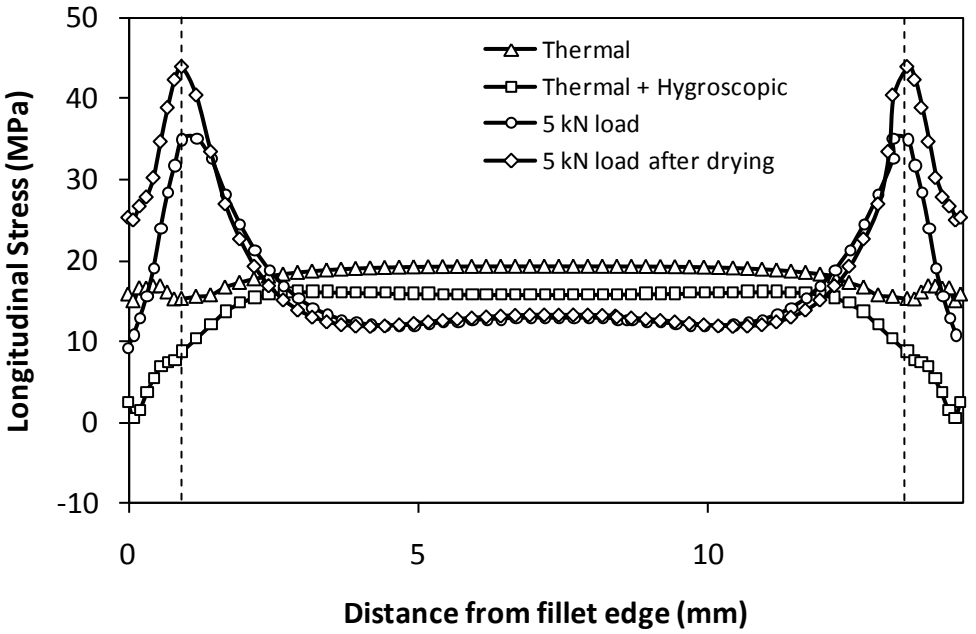

(a)

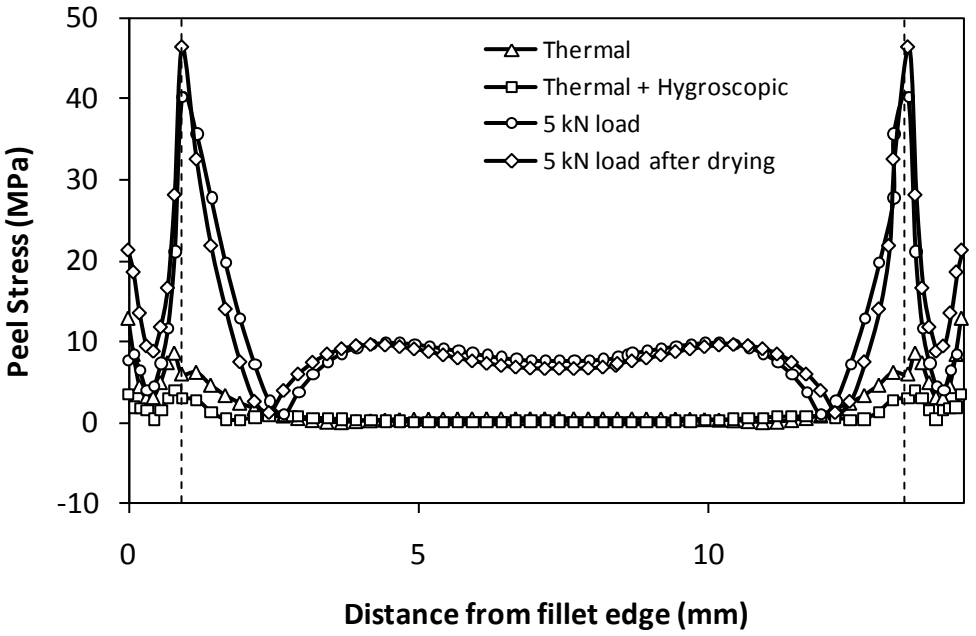

(b)

Figure 7.16: Development of (a) longitudinal stresses and (b) peel stresses in a single lap joint with Al2024 T3 adherends, conditioned for 7 days at 70°C.

The hygroscopic stresses resulting from the moisture absorption can be seen to provide some relief from the longitudinal thermal stresses. The longitudinal hygrothermal stresses were uniform in the overlap middle and decreased near the overlap ends. Peel thermal stresses in the fillet region were also reduced by the hygroscopic stresses. The maximum longitudinal and peel stresses in the conditioned and the dried joints under tensile loading were at the end of the overlap. The location of maximum stresses after mechanical loading is similar to that seen in joints conditioned at 50°C.

The longitudinal hygroscopic stresses, in the middle of the overlap, provided greater relief from the thermal stresses after 182 days than after 7 days of conditioning, as shown in Figure 7.17. However, the stresses increased in the fillet regions after moisture absorption. When 5 kN load was applied to the conditioned joints, the maximum longitudinal and peel stresses moved from the overlap end to inside the overlap and were lower in magnitude than the stresses after 7 days of conditioning. The maximum longitudinal and peel stresses returned to the overlap end when the joints were dried and a tensile load was applied.

The changes in the stresses may be explained by considering the moisture concentration and its effects on the mechanical properties of the adhesive. As the moisture diffusion had extended through the adhesive layer after 182 days of conditioning, greater relief of thermal stresses was observed in the overlap than after 7 days of conditioning. The increased amount of moisture in the fillet region resulted in expansion of the adhesive, relieving the shrinkage owing to curing. This resulted in an increase in the longitudinal hygrothermal stresses in the fillet region. The plastic deformation of the adhesive provided relief of stresses at the overlap end and since the degradation in the stiffness of the adhesive is greater at 70°C than 50°C, the maximum longitudinal and peel stresses were observed inside the overlap. Similar patterns of stress development were observed in the joints conditioned for 14, 28 and 56 days.

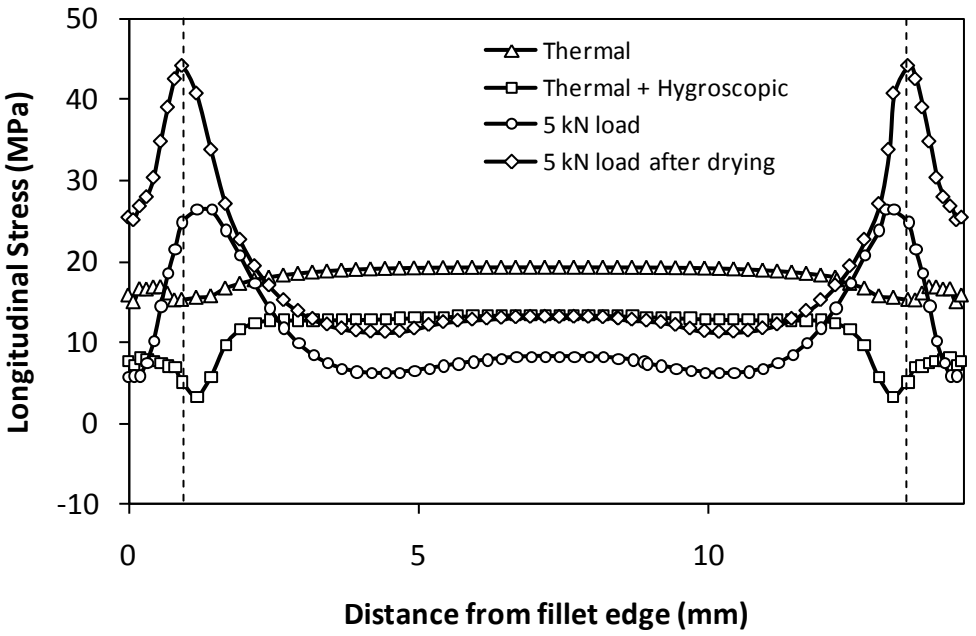

(a)

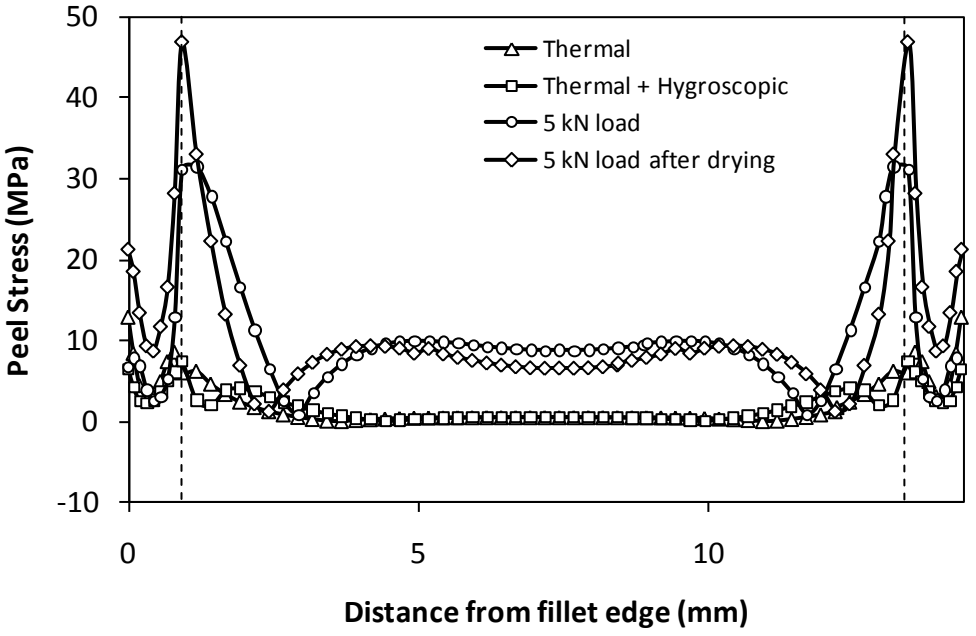

(b)

Figure 7.17: Development of (a) longitudinal stresses and (b) peel stresses in a single lap joint with Al2024 T3 adherends, conditioned for 182 days at 70°C.

7.6.2 Single Lap Joints with Al2024 O Adherends

Stresses in the joints with Al2024 O adherends and conditioned for 7 and 182 days, are plotted in Figure 7.18 and Figure 7.19, respectively.

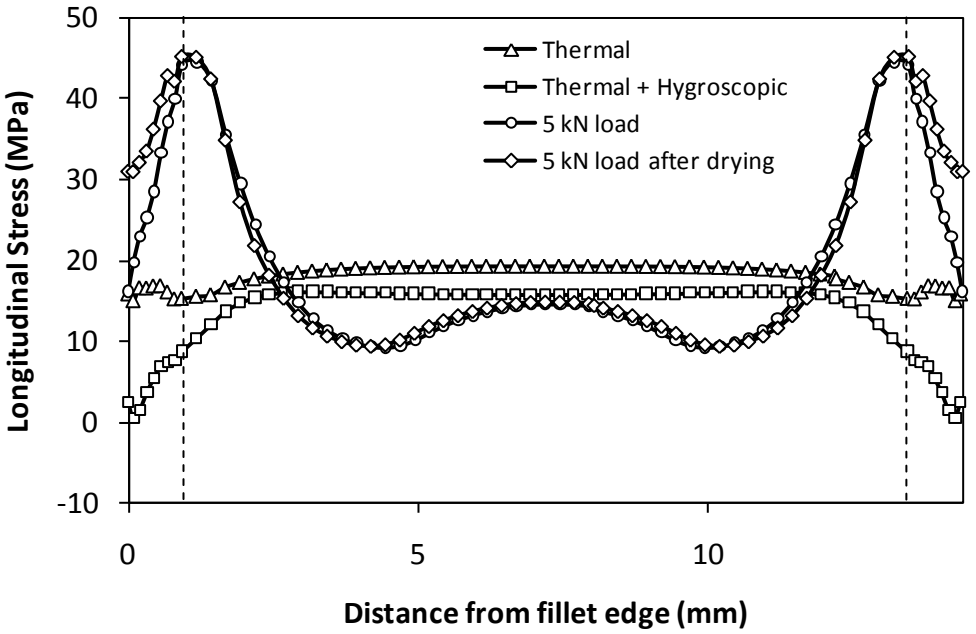

(a)

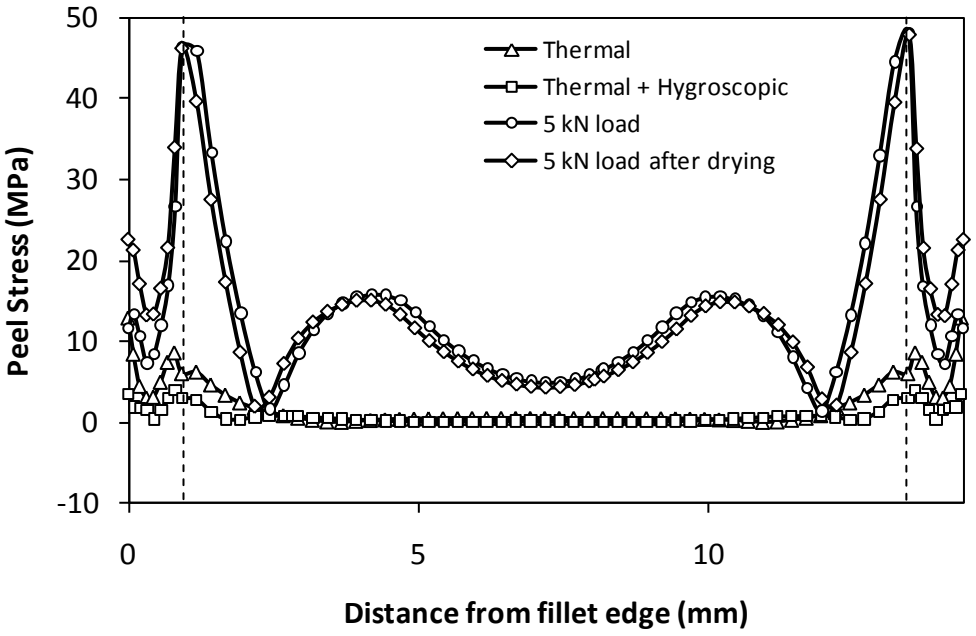

(b)

Figure 7.18: Development of (a) longitudinal stresses and (b) peel stresses in a single lap joint with Al2024 O adherends, conditioned for 7 days at 70°C.

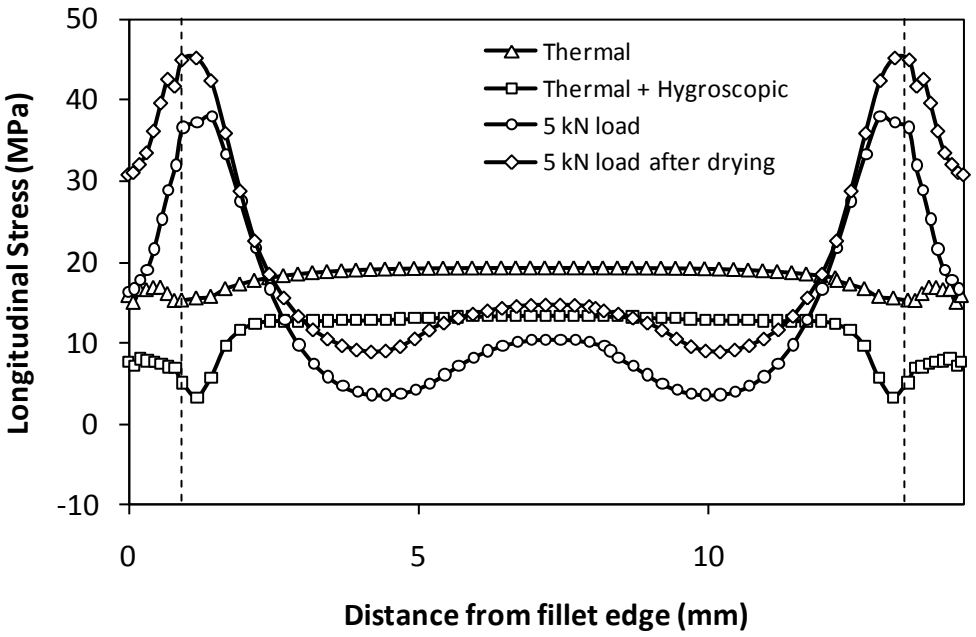

(a)

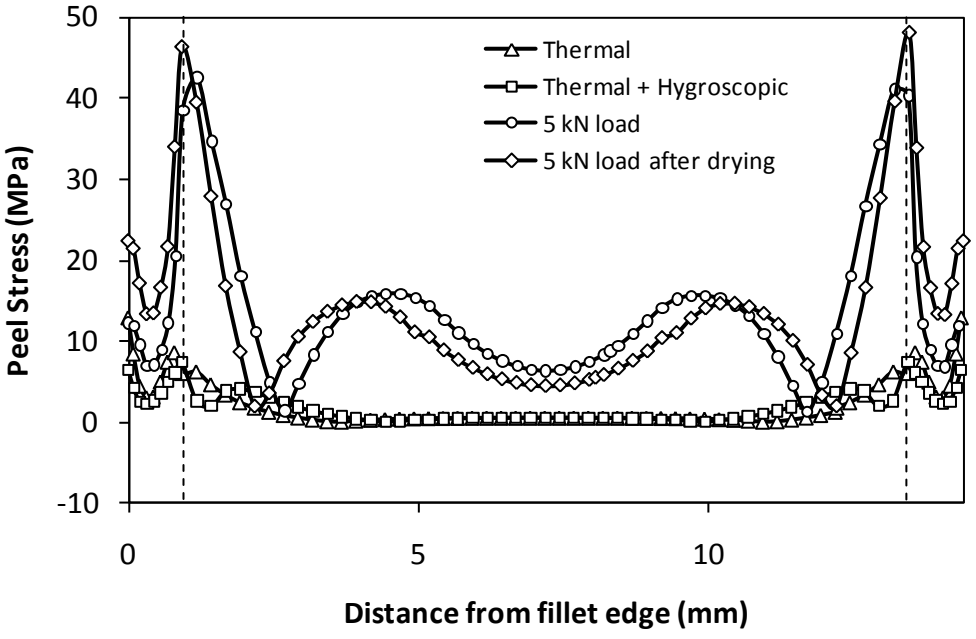

(b)

Figure 7.19: Development of (a) longitudinal stresses and (b) peel stresses in a single lap joint with Al2024 O adherends, conditioned for 182 days at 70°C.

As the O and T3 joints were cured and aged under the same conditions, similar thermal and hygrothermal stresses were observed in both types of joint. The maximum longitudinal stresses after application of the 5 kN load were of similar magnitude in the conditioned and the dried joints. This was also true for peel stresses. In the joints conditioned for 182 days and loaded in tension, the maximum longitudinal and peel stresses were within the overlap, as was observed in the T3 joints conditioned for the same duration. Also, the magnitude of the highest longitudinal and peel stresses was lower after 182 days than after 7 days conditioning. However, the dried joints had similar maximum longitudinal and peel stresses after 7 and 182 days of conditioning. In comparison to the T3 joints, the conditioned O joints with 5 kN of load had higher longitudinal and peel stresses. This agrees with the stress development in the joints conditioned at 50°C.

7.7 Stresses in Single Lap Joints Conditioned for Multiple Cycles

The variable moisture and stress prediction methodology was used to predict the stresses in single lap joints conditioned for multiple cycles of absorption and desorption at 70°C in water, as discussed in Section 3.3.5. The experimentally determined moisture dependent stress-strain response of the bulk adhesive was available for two moisture absorption cycles. In order to predict the moisture diffusion of five absorption and desorption cycles, the experimental results were extrapolated to obtain stress-strain curves for third, fourth and fifth absorption cycles as shown in Figure 7.20.

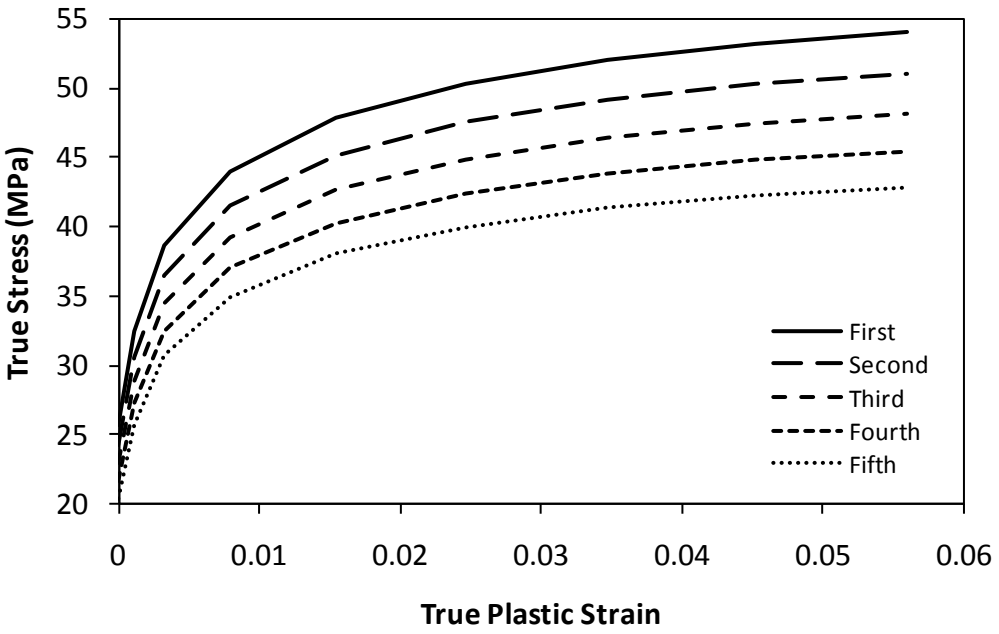

Figure 7.20: True stress vs true plastic strain of FM73 at start of five moisture absorption cycles after conditioning in water at 70°C.

Detailed moisture concentration predictions for the joints were presented in Section 6.7.3 and only the moisture concentration in the middle of the adhesive layer is discussed here. Figure 7.21 plots the moisture concentration along line A-A, from Figure 7.5. It can be seen that moisture concentration in the middle of the overlap was negligible after the first moisture absorption but this increased progressively with each absorption cycle. After the fourth absorption cycle, the moisture concentration was at a similar level across the overlap length. The moisture concentration in the middle of the overlap became higher than at the overlap edges after the fifth absorption cycle. The increase in moisture concentration in the overlap middle with each absorption cycle is because of the continued absorption of moisture to the overlap middle even during the desorption cycle, as explained in Chapter 6. The outer fillet regions did not observe significant changes in moisture concentration over absorption and desorption cycles.

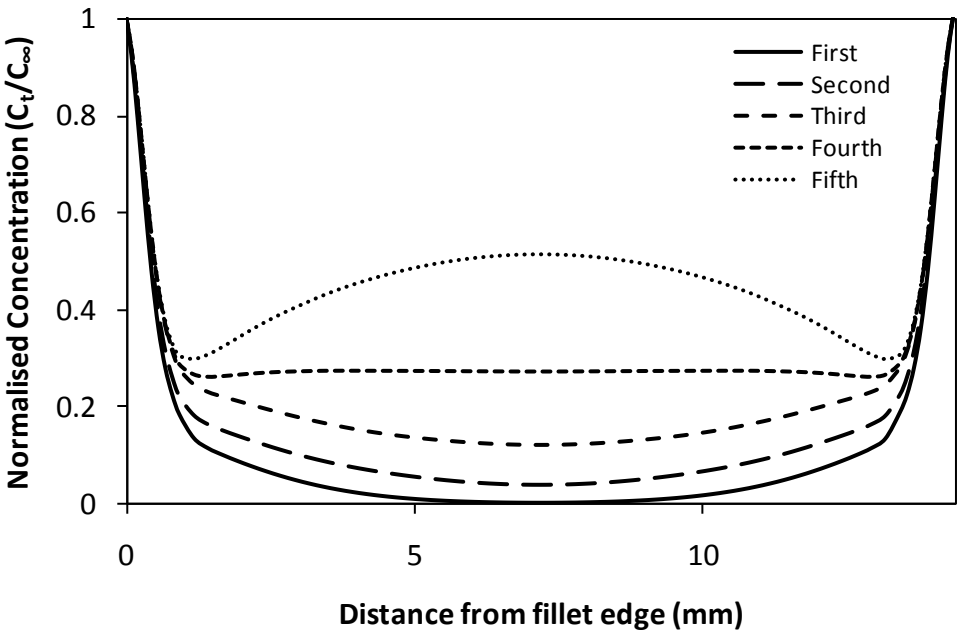

Figure 7.21: Normalised moisture concentration in the adhesive layer after multiple cycles of moisture absorption at 70°C.

A tensile load of 5 kN was applied to the conditioned joints after conditioning and the longitudinal and peel stresses are plotted in Figure 7.22. The highest longitudinal stresses occurred at the overlap end and progressively decreased from the first moisture absorption cycle to the fifth absorption cycle. The longitudinal stress in the middle of the overlap also decreased progressively from the first moisture absorption cycle to the fourth absorption cycle. However, the longitudinal stresses in the middle of the overlap increased after the fifth absorption. The highest peel stresses were seen in the overlap end region. A progressive decrease in the highest peel stress was observed from the first absorption cycle to the fifth absorption cycle. The peel stresses in the middle of the overlap had no significant change over multiple absorption cycles.

The decrease in the highest longitudinal and the peel stresses was owing to the increased plastic deformation of the adhesive as the adhesive stiffness decreased with each absorption cycle. The longitudinal stresses in the middle of the overlap decreased with each absorption cycle as the moisture concentration in the middle of the overlap increased and provided relief from the residual thermal stresses.

However, as the hygrothermal stresses increased with increasing moisture concentration, the hygroscopic expansion of the adhesive resulted in increased longitudinal stresses in the middle of the overlap.

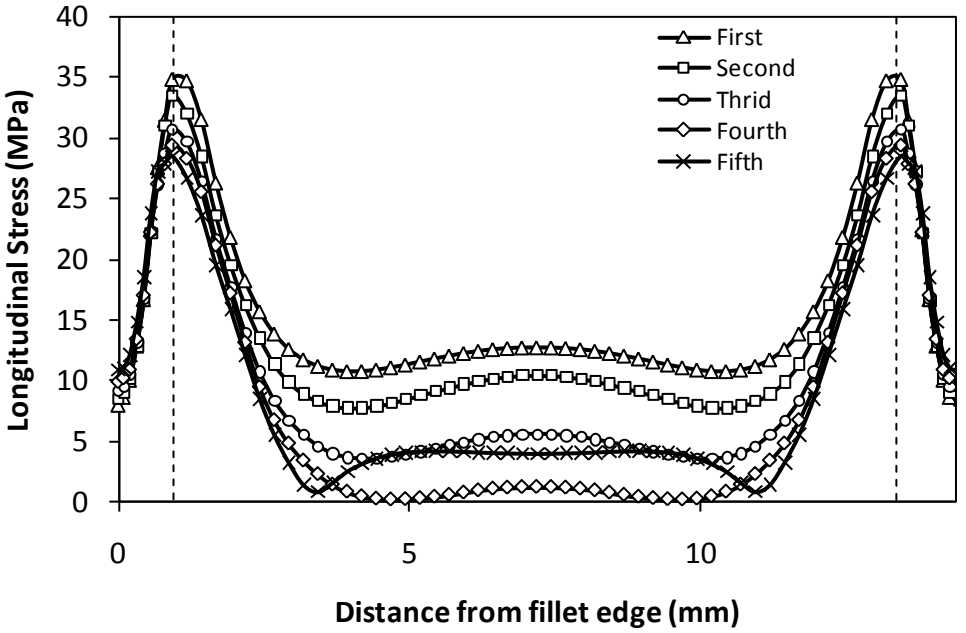

(a)

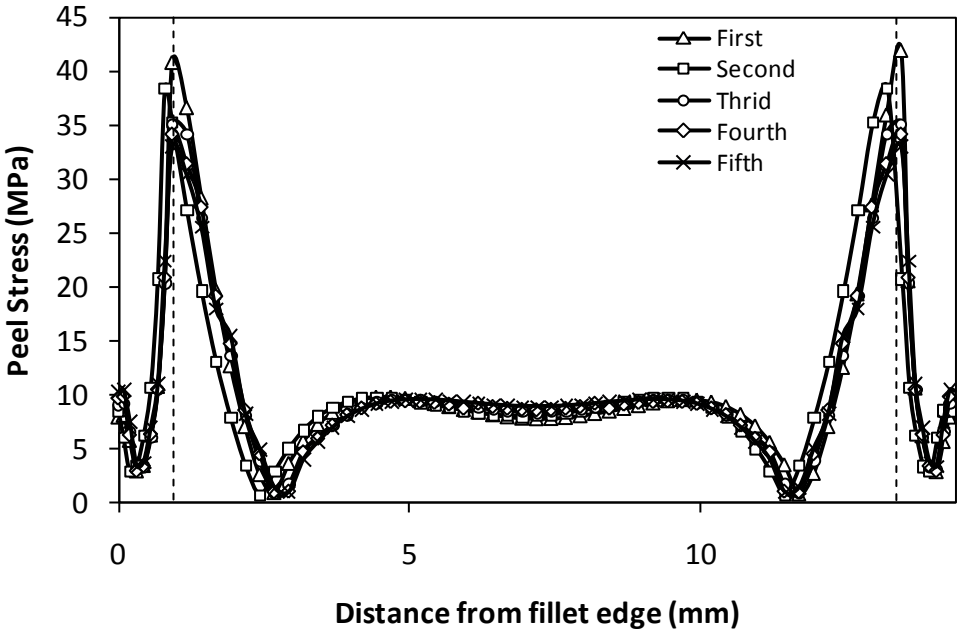

(b)

Figure 7.22: Longitudinal and peel stresses, after conditioning and 5 kN load, in single lap joint with Al2024 T3 adherends, conditioned for multiple cycles at 70°C.

7.8 Summary

A variable moisture and stress prediction methodology is presented, which is able to predict joint stress under variable moisture conditions. The methodology provides a coupling between the cyclic stress prediction method and stress based methods. Verification of the proposed methodology was carried out by comparing the experimental and predicted stress-strain plots for bulk adhesive samples, conditioned for multiple cycles. Excellent correlation between the experimental and predicted results was observed. The methodology was then applied to single lap joints conditioned in deionised water at 50°C and 70°C for multiple absorption and desorption cycles. Residual stresses, originating from curing and moisture conditioning, were included in the analysis. The results showed that a significant amount of stress was present in the adhesive layer after curing of the joints. The hygroscopic stresses provided some relief from the curing stresses, but as the moisture concentration increased, the increased hygroscopic expansion overcame the shrinkage of the adhesive and resulted in stress increase. When a tensile load was applied to the joints, maximum stresses were observed in the overlap end region. Study of the stresses revealed that the degradation in the strength of the adhesive was the major contributor in the strength loss of the adhesive joints. In joints conditioned for multiples absorption and desorption cycles, the maximum stresses decreased with each absorption cycle as the stiffness of the adhesive decreased.

Chapter 8
Damage and Failure Predictions in Adhesive Joints

8.1 Introduction

In Chapter 6, a methodology for predicting the transient moisture distribution in adhesive joints under cyclic moisture conditions was introduced and in Chapter 7, this was coupled with a stress analysis. In this chapter the coupled stress analysis is used in combination with cohesive zone modelling (CZM) to determine the progressive damage and failure in single lap joints subjected to cyclic environmental ageing. The cohesive zone model was calibrated using a combination of experimental and numerical methods. The calibrated model was used to predict the failure load of single lap joints under different moisture and temperature conditions. Three dimensional single lap joint models were used during the prediction of damage and failure.

8.2 Cohesive Zone Model (CZM)

The use of cohesive zone modelling for moisture durability prediction was reviewed in Chapter 2 and its application for damage and failure prediction of single lap joints is discussed in this section. The cohesive zone model is a phenomenological model, which may be used to represent a crack in an adhesive layer or at an interface. The cohesive zone method was selected because of a number of advantages it offers over other methods. The cohesive zone method does not require an initial crack to model failure, as is the requirement in fracture mechanics based methods. However, the path of the crack propagation needs to be defined. In bonded joints,

where failure may occur at various locations, several possible crack propagation paths may need to be defined. The cohesive zone model requires fewer parameters compared to continuum damage models for example the Gurson model, and is capable of predicting both damage and failure.

A built-in cohesive zone modelling capability is available in ABAQUS, which was employed in this research to predict the failure load of single lap joints in both conditioned and unconditioned states. The cohesive zone model is implemented in FEA through the use of cohesive elements. A cohesive element is a continuum element that may be considered as two faces separated by a distance and the relative movement of the two faces is used to determine damage and failure. A cohesive element has a thickness direction, which should be normal to the crack faces during meshing. In two dimensional cohesive elements, displacements normal and parallel to the crack face are considered. In three dimensional cohesive elements, one normal displacement and two parallel displacements to the crack face are considered. A three dimensional continuum cohesive element is shown in Figure 8.1.

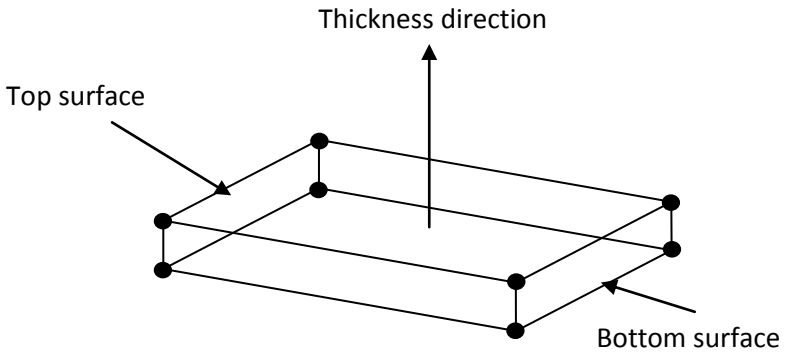

Figure 8.1: Schematic representation of an eight node continuum cohesive zone element.

The general framework for damage and failure of the cohesive zone elements is based on a damage initiation criterion, a damage evolution law and choice of element removal after achieving the fully damaged state. In this case, a bilinear constitutive cohesive zone law was selected for modelling the single lap joints as this has been successfully used to model failure in bonded joints in previous work

[23, 138, 146, 196, 197]. A bilinear cohesive zone law provides a good compromise between computational cost and the number of elements required to represent the damage zone and failure [148]. The bilinear cohesive zone law is shown in Figure 8.2 in the form of a traction-separation response. The material behaviour is linear elastic before the damage initiation. The area under the traction-separation curve is the cohesive fracture energy, G_{coh}. The stiffness before damage initiation, K, is given by the slope of the linear curve. τ_c is the critical value of traction, τ, known as tripping traction, after which the damage initiates. δ_m^o is the displacement at damage initiation and δ_m^f is the displacement at failure. Once damage initiation occurs, softening of the material is governed in this model by a linear decrease in material stiffness.

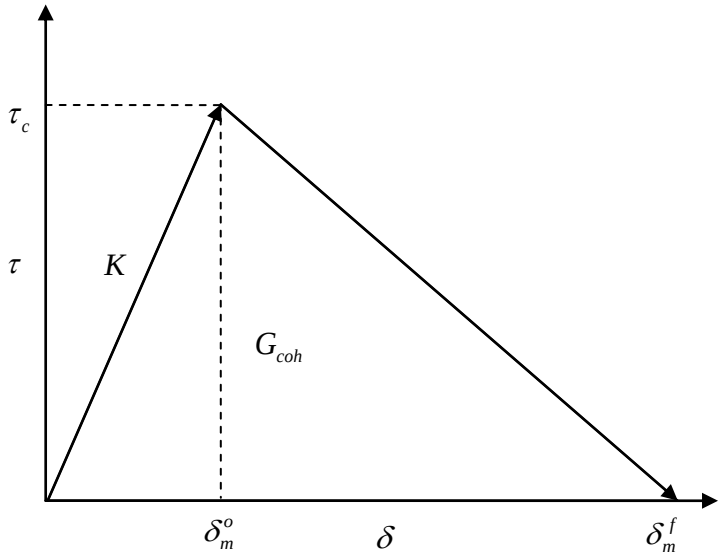

Figure 8.2: Bilinear cohesive zone law.

A stress criterion was used for damage initiation where the damage was assumed to initiate when the ratio of stress at any time increment to the maximum stress reached a value of one as given by Equation (8.1).

$$\max\left(\frac{\langle t_n \rangle}{t_n^o}, \frac{t_s}{t_s^o}, \frac{t_t}{t_t^o}\right) = 1 \tag{8.1}$$

where t_n^o is the maximum stress in normal direction, t_s^o and t_t^o are the maximum stresses in shear directions. t_n, t_s and t_t are the corresponding stresses at any time increment. "$\langle\rangle$" is a Macaulay bracket, showing that no damage occurs under pure compression.

Once the damage initiation criterion is met, damage will occur according to the defined damage evolution law, which describes the rate at which the material stiffness degrades. A scalar damage variable, D_c, with an initial value of zero, was used to represent the damage. The value of D_c increased from zero to one as damage increased in an element. The stress components of the traction-separation law are affected by damage as follows;

$$t_n = \begin{cases} (1-D_c)\bar{t}_n, & \bar{t}_n \geq 0 \\ \bar{t}_n, & otherwise \end{cases} \tag{8.2}$$

$$t_s = (1-D_c)\bar{t}_s \tag{8.3}$$

$$t_t = (1-D_c)\bar{t}_t \tag{8.4}$$

where $\bar{t}_n$, $\bar{t}_s$ and $\bar{t}_t$ are the stress components calculated without damage.

The evolution of damage occurred according to a cohesive energy based crack propagation criterion and the value of the damage variable, D_c, was determined as follows:

$$D_c = \frac{\delta_m^f(\delta_m^{\max} - \delta_m^o)}{\delta_m^{\max}(\delta_m^f - \delta_m^o)} \tag{8.5}$$

where δ_m^o is the displacement at damage initiation, δ_m^f is the displacement at failure and $\delta_m^{\max}$ is the maximum displacement during the loading history. The elements were removed from the mesh when D_c reached a value of one at all the integration points of the element.

8.3 Calibration of the Cohesive Zone Model (CZM)

The bilinear cohesive zone model may be completely defined by the parameters G_{coh}, K and τ_c. The moisture dependent fracture energy of the adhesive FM73 was determined by Liljedahl et al [23] by using a mixed mode flexure (MMF) specimen. MMF specimens were tested under dry, 80% RH and 96% RH conditions. The specimens were conditioned as open faced specimens and a second adherend was bonded after the required moisture concentrations were achieved. The specimens were tested under three-point bending conditions until debonding started. The failure load was used to determine the fracture energies at different conditions and the determined fracture energy as a function of moisture content is given in Figure 8.3. The moisture dependent fracture energy is later used in the cohesive zone model where linear interpolation is carried out to determine values between experimental data points.

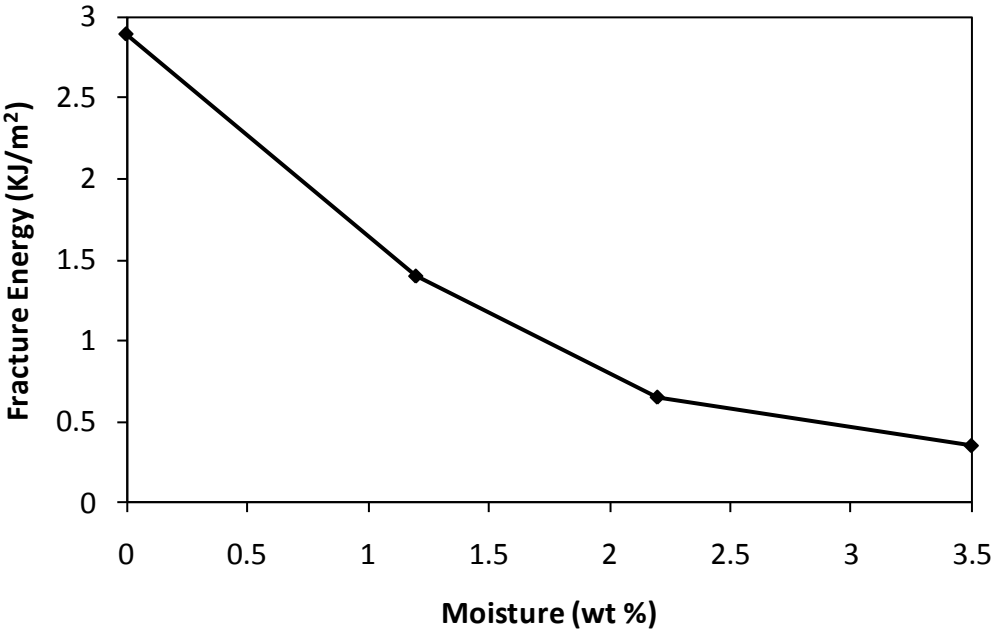

Figure 8.3: Moisture dependent fracture energy of the adhesive [23].

Cohesive zone elements are used either to represent a material of some finite thickness or to represent an interface or crack. Representation of a finite material thickness with cohesive zone elements treats the continuum material as a crack

instead of representing the crack. Thus use of zero or a very small thickness as compared to overall structure dimensions for cohesive zone elements provides better representation of a crack or interface. In the present work, cohesive elements with a small thickness were used and discussed further in Section 8.5. As the cohesive zone elements represent a crack or an interface, the stiffness of the elements should be infinity prior to damage so that the compliance of the structure is not affected by this inclusion. However, in the FEM model, a large value, of the order of 10^4 or higher [157] may be used satisfactorily. Use of very large stiffness values result in severe convergence difficulties in the finite element analysis and thus a suitable value must be chosen that provides good convergence as well as correct structural representation. Turon et al [157] provided a relationship for determining the value of stiffness based on the properties of the surrounding material, which for an isotropic material is given by:

$$K = \frac{\alpha E}{t} \tag{8.6}$$

where E is the elastic modulus, t is the thickness of surrounding material and α is a parameter whose value should be much larger than 1 $(\alpha >> 1)$. A value of 50 or greater was recommended for α [157]. Based on Equation (8.6), the value of stiffness was calculated to be 8.3 x 10^5 N/mm^3, however, convergence difficulties were observed during modelling and a lower value of 1 x 10^5 was used for the cohesive zone model.

For a bilinear traction-separation law, tripping traction, τ_c, may be related to G_{coh} and δ_m^f by:

$$\tau_c = \frac{2G_{coh}}{\delta_m^f} \tag{8.7}$$

Since the fracture energy was known, the δ_m^f was varied parametrically to obtain the τ_c that would provide the experimentally observed failure load. This approach has been defined as the penalty based cohesive zone finite element approach by Diehl [197, 198]. A two dimensional single lap joint model was used to determine the τ_c. The joint adherends were of Al2024 T3. A layer of cohesive elements was

embedded in the mesh based on the experimental observations. Two dimensional, continuum four node, plane strain elements were used for the adhesive and the adherends. The mesh for the two dimensional model is shown in Figure 8.4. The boundary conditions for a rotational symmetric model were described in Section 5.2.

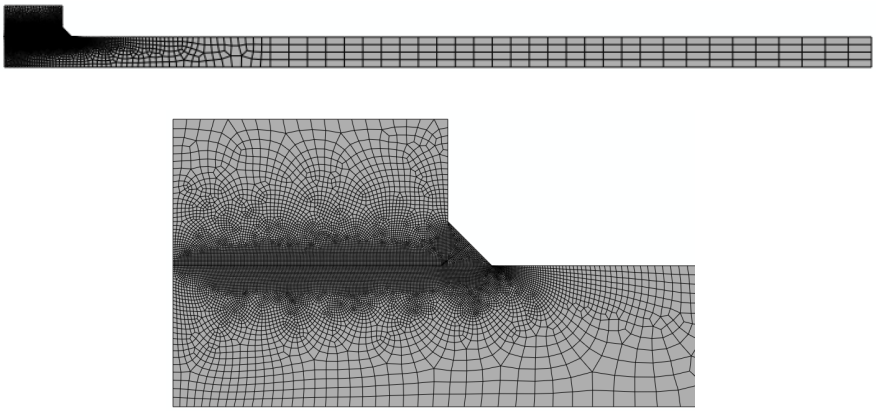

Figure 8.4: Mesh of two dimensional single lap joint model.

The joint was loaded in displacement control and the predicted failure load was calibrated to the experimental failure load to determine the value of τ_c. The force vs. displacement response of the calibrated single lap joint model is show in Figure 8.5.

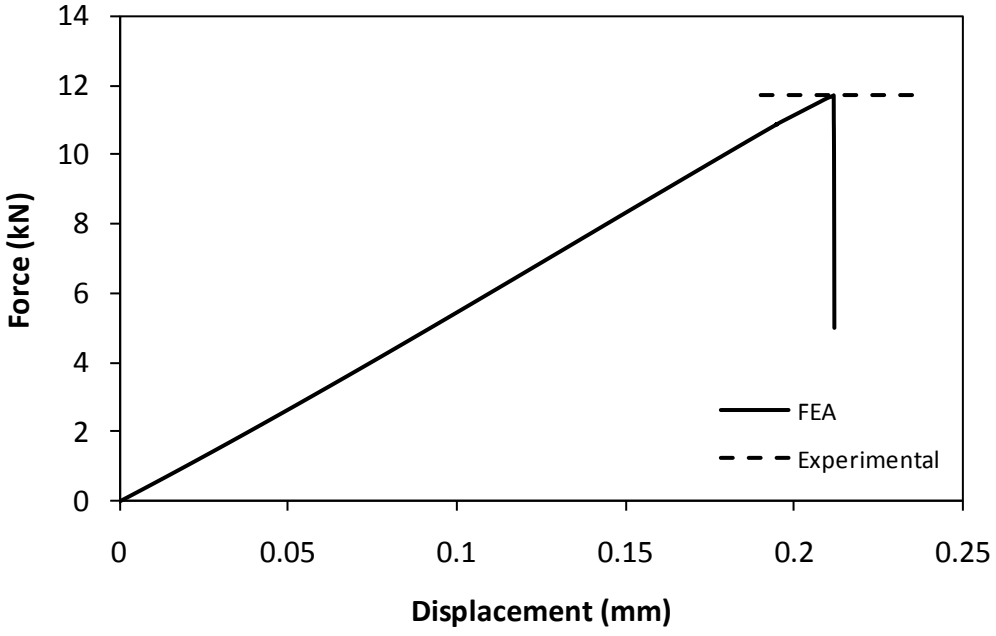

Figure 8.5: Force vs. displacement response of the two dimensional single lap joint.

The finalised parameters for the bilinear cohesive zone law are given in Table 8.1.

Table 8.1: The cohesive zone model parameters for dry single lap joint.

Tripping traction τ_c (MPa)	Stiffness K (N/mm^3)	Cohesive energy G_{coh} (kJ/mm^2)
39	1 x 10^5	2.9

8.4 Coupling between hygrothermal analysis and CZM

In order to predict the durability of the single lap joints under cyclic moisture conditions, the moisture concentration and mechanical strength under cyclic conditions has to be determined. A methodology for the prediction of moisture concentration under cyclic moisture conditions was presented in Chapter 6 and the hygro-mechanical coupling was established in Chapter 7. The general framework of hygro-mechanical coupling detailed in Section 7.2 was used to couple the cyclic moisture diffusion with the CZM based analysis. The moisture dependence in the CZM was introduced by using a moisture dependent G_{coh}. The moisture concentration and moisture history, which were stored in the form of state variables in the hygroscopic model, were used as initial conditions in the CZM analysis. The G_{coh} was defined as:

$$G_{coh}(C_t, FV1, FV2) \tag{8.8}$$

where $FV1$ and $FV2$ are field variables and C_t is the normalised moisture content at any point in the adhesive layer. The field variables were related to state variables using an ABAQUS USDFLD user subroutine. The change in the cohesive zone law based on the moisture dependent cohesive energy is shown in Figure 8.6.

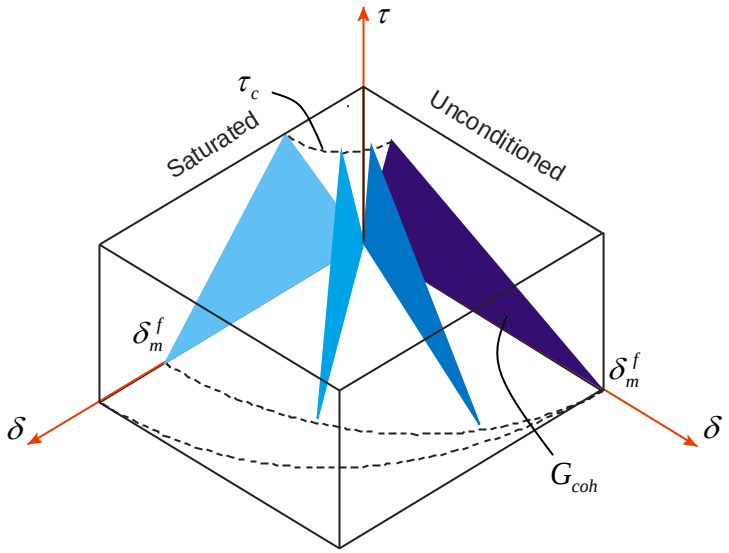

Figure 8.6: Change in bilinear cohesive zone law with increasing moisture concentration.

8.5 Predictive Modelling of Single Lap Joints

Singe lap joints with Al2024 T3 and O adherends, conditioned in deionised water at 50°C and 70°C, were modelled using the proposed methodology. A 3D model of the single lap joint was used, owing to the moisture and structural boundary condition requirements. A quarter model, based on symmetry in the geometry and the loading, as discussed in Chapter 5, was used. Continuum, eight node, linear elements (C3D8I) were used for meshing of the adhesive layer. The adherends were meshed using a combination of continuum and continuum shell elements, as shown in Figure 8.7. The continuum elements were eight node, linear elements (C3D8I) and the continuum shell elements were eight node, quadrilateral, reduced integration elements (SC8R).

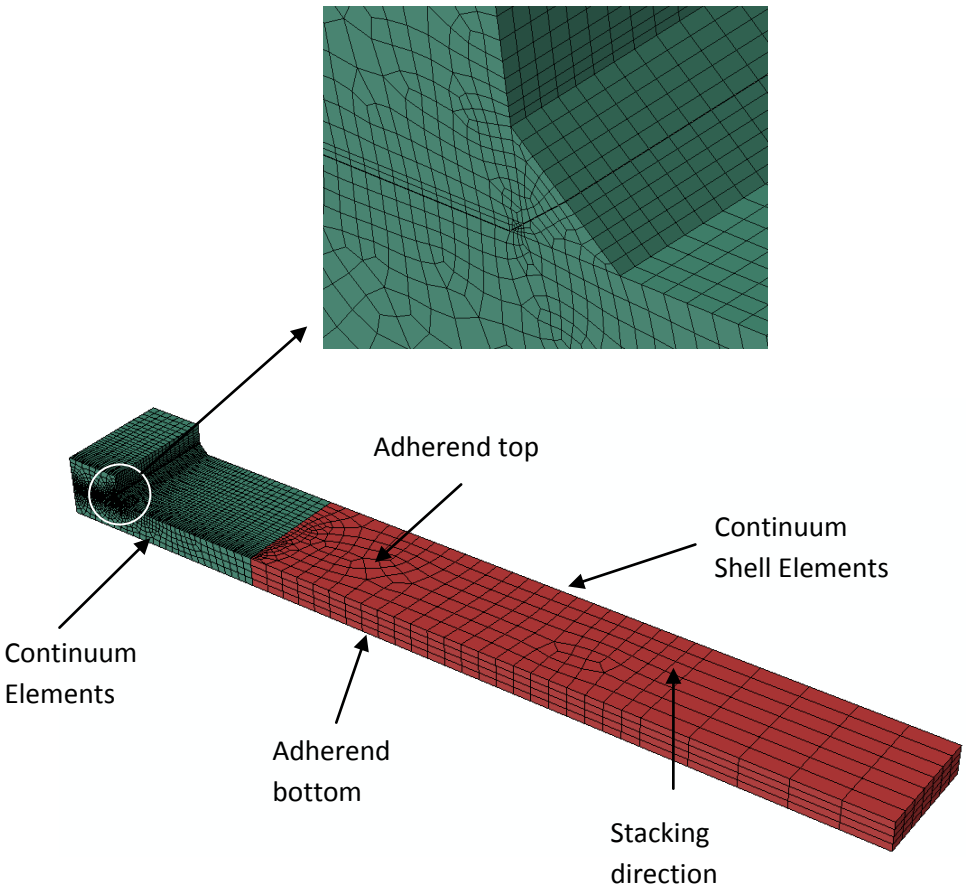

Figure 8.7: The 3D mesh used for CZM based analysis of single lap joints.

The stacking direction of the continuum shell elements was from the bottom of the adherend to the top of the adherend is shown in Figure 8.7. A layer of the cohesive zone elements was embedded between the continuum elements of the adhesive and the adherends. Although, the cohesive zone elements may have zero thickness, a thickness of 0.005 mm was used, which is very small as compared to the overall dimensions of the single lap joint. A finite thickness was necessary as the analysis was carried out in two steps. In the first step, moisture diffusion analysis was carried out and the normalised moisture concentrations were determined. During moisture diffusion analysis, continuum, 8 node, linear heat transfer elements (DC3D8) were used for meshing. The zero thickness elements were not allowed during the moisture diffusion analysis. Since the same mesh was used in second step to predict the damage and failure based on the CZM, the elements of very

small thickness were used during moisture diffusion analysis, which were later converted to cohesive zone elements in the structural analysis. The thickness direction of the cohesive zone elements was from the base of the adherend to the top of the adherend.

The single lap joints were loaded in displacement control where a fixed displacement was applied to a reference node. The nodes at the end of the adherend were coupled with the reference node using kinematic constraint equations. This allowed for easy extraction of reaction forces during the post processing of the model. As already mentioned, a sequential hygro-mechancial analysis was carried out and the results of the diffusion analysis were used as initial conditions in the structural analysis. The experimental failure load of the single lap joints, as given in Chapter 4, was used to validate the predicted strength. The results of predictive modelling of different types of joints are discussed in the following sections.

8.5.1 Al2024 T3 Single Lap Joints Conditioned at 50°C

For Al2024 T3 joints, an elastic material definition was used for the adherends and moisture and moisture history dependent elastic properties were used for the adhesive. The bilinear cohesive law with moisture and moisture history dependent cohesive energy was used for the cohesive elements. The predicted normalised moisture concentration in the adhesive layer is given in Section 6.7.1. The load-displacement response of the unconditioned and 182 days conditioned T3 joints is shown in Figure 8.8. It can be seen the initial load-displacement curve for both unconditioned and 182 days conditioned T3 joints is linear. In unconditioned T3 joints, the load-displacement response becomes nonlinear after 8.21 kN of load is applied and is represented by dotted lines in Figure 8.8. At this point, 20% of the overlap and 91.7% of the fillet area was damaged, as determined from the finite element model. In 182 days conditioned T3 joints, a nonlinear load-displacement response was observed when 15.5% of the overlap and 65.9% of the fillet area was damaged. This shows that the load carrying capacity of the joints start to decrease

with the damage appearing in the adhesive layer and fillet, at loads lower than the failure of the joint.

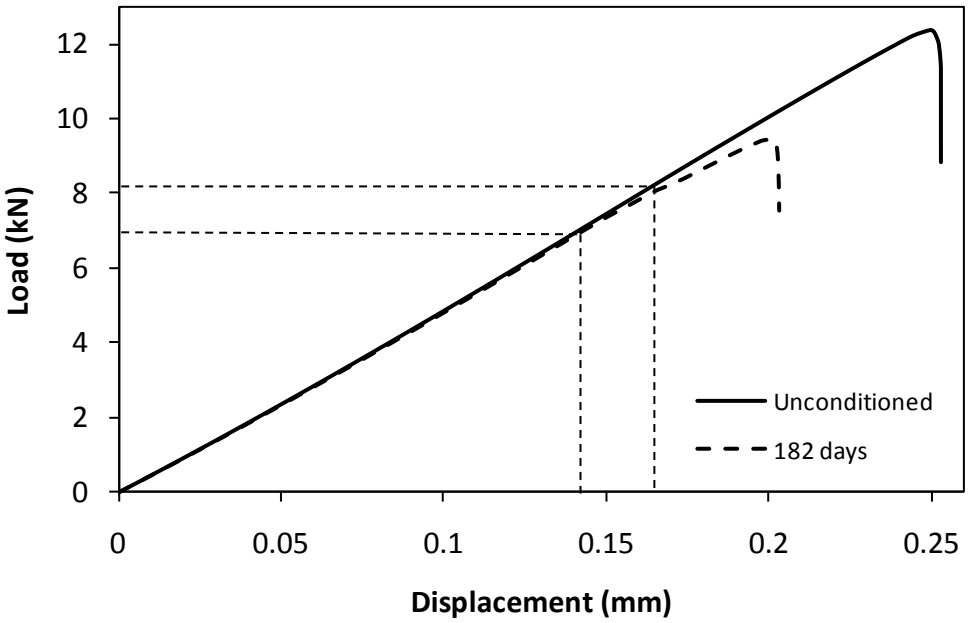

Figure 8.8: Force-displacement response of Al2024 T3 unconditioned and 182 days conditioned joints.

The predicted and experimental failure loads for the Al2024 T3 joints are plotted in Figure 8.9. The predicted failure load is the maximum load sustained by the single lap joint during the finite element simulations, as obtained from load-displacement curve. The predicted unconditioned failure load was 5.3% higher than the experimental unconditioned failure load. For conditioned T3 joints, the predicted failure load is in good agreement with the experimental failure load for all the conditioning time intervals. When the T3 joints were dried after moisture conditioning, they regained most of their unconditioned strength and the same was also observed after the predictive modelling. The predicted failure load under all dried conditions was higher than the experimental failure load and was within 7% of the experimental results. The difference between the failure load of the experimental and predicted unconditioned T3 joints may be attributed to the differences of meshing, element type and element formulation between the 2D and

3D models, since the cohesive zone model parameters for unconditioned joint were calibrated using a 2D model.

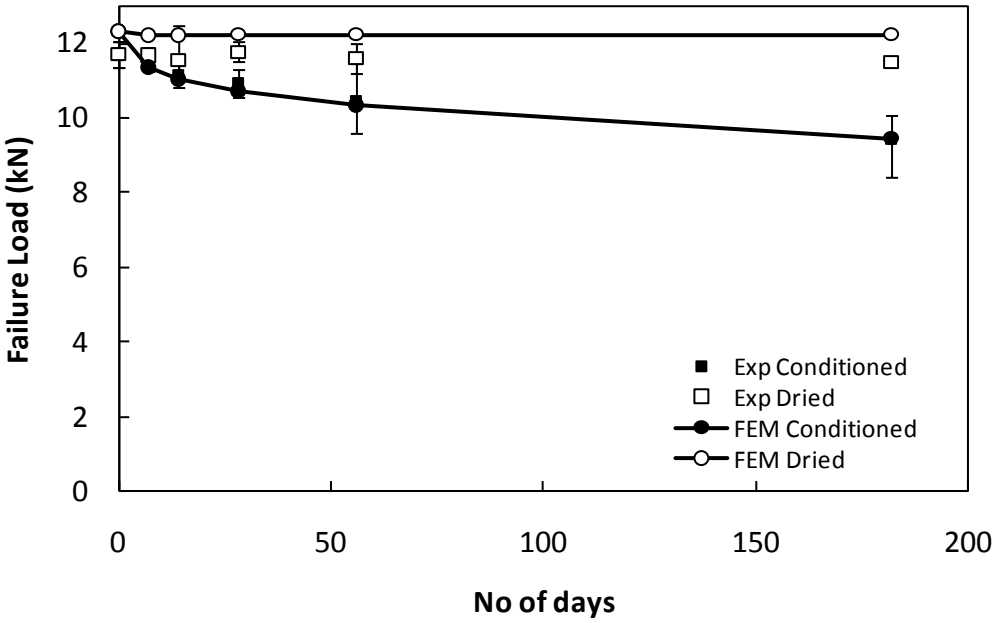

Figure 8.9: Predicted and experimental failure load of the Al2024 T3 joints when conditioned at 50°C.

Damage and crack development in the unconditioned T3 joints, as predicted by the finite element modelling, is shown in Figure 8.10. The contour plots show the damage, represented by a scalar damage variable SDEG, in the adhesive layer and it can be seen that most of the overlap region was damaged before rupture occurred. The crack initiated in the fillet region, marked as 1 in Figure 8.10a, and major crack growth occurred towards the edges, as shown in Figure 8.10b. Once the crack reached the edges, it propagated towards the middle of the overlap in X direction as may be seen from Figure 8.10d.

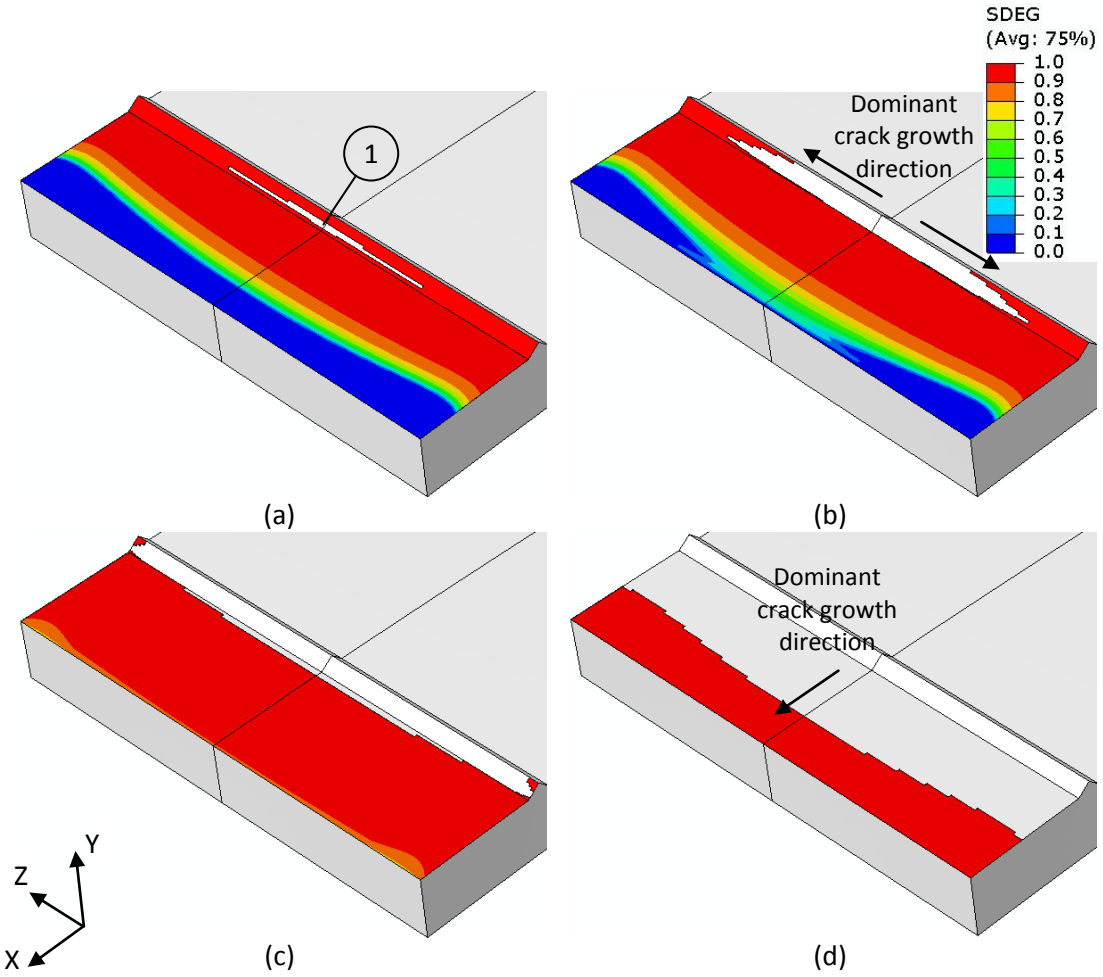

Figure 8.10: Damage and crack propagation in unconditioned Al2024 T3 single lap joint.

Crack initiation in the T3 joints conditioned for 182 days was in the fillet region, marked as 2 in Figure 8.11a, which was similar to the unconditioned joints. However, at the time of the crack initiation, the damage zone in the conditioned T3 joints was much smaller than in the unconditioned T3 joints. After crack initiation, the major crack growth occurred from region 2 towards edges, as given in Figure 8.11b. Cracks also initiated from the edges of the adherends, as shown in Figure 8.11c eventually joining the crack growing from region 2. The crack then progressed towards the middle of the overlap in direction X.

The crack propagation rate in the unconditioned and conditioned T3 joints may be compared by plotting the change in crack length with applied displacement. The crack lengths of the unconditioned and 182 days conditioned T3 joints, as a function of applied displacement, are plotted in Figure 8.12. After crack initiation, a region of

stable crack growth exists for both unconditioned and 182 days conditioned T3 joints. The stable crack growth is followed by a period of rapid growth leading to failure. The stable crack growth in the unconditioned T3 joints occurred for a shorter duration than in the 182 days conditioned T3 joints. This may be owing to the more ductile response of the adhesive after moisture absorption. Once a major portion of the adhesive layer was damaged, failure occurred instantaneously in both unconditioned and conditioned T3 joints.

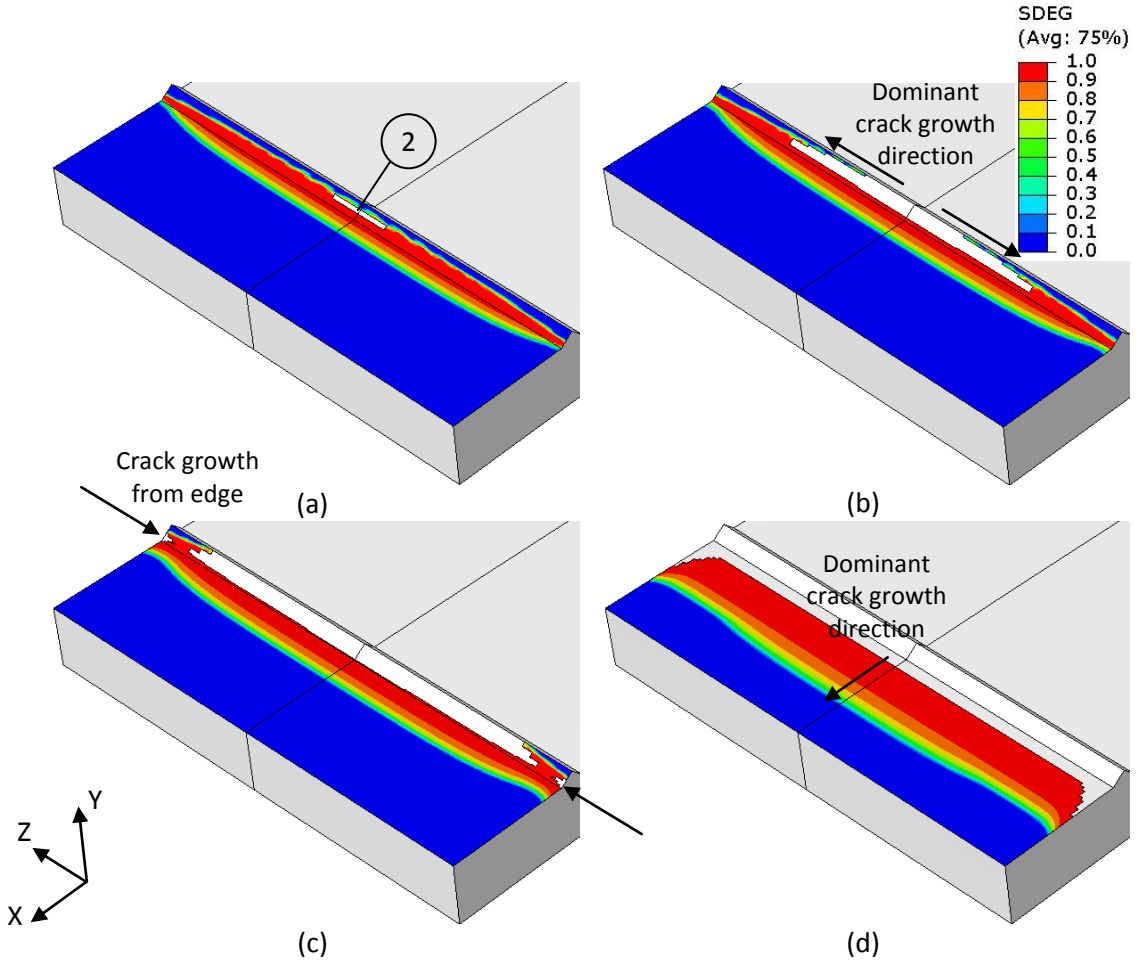

Figure 8.11: Damage and crack propagation Al2024 T3 joints, conditioned at 50°C for 182 days.

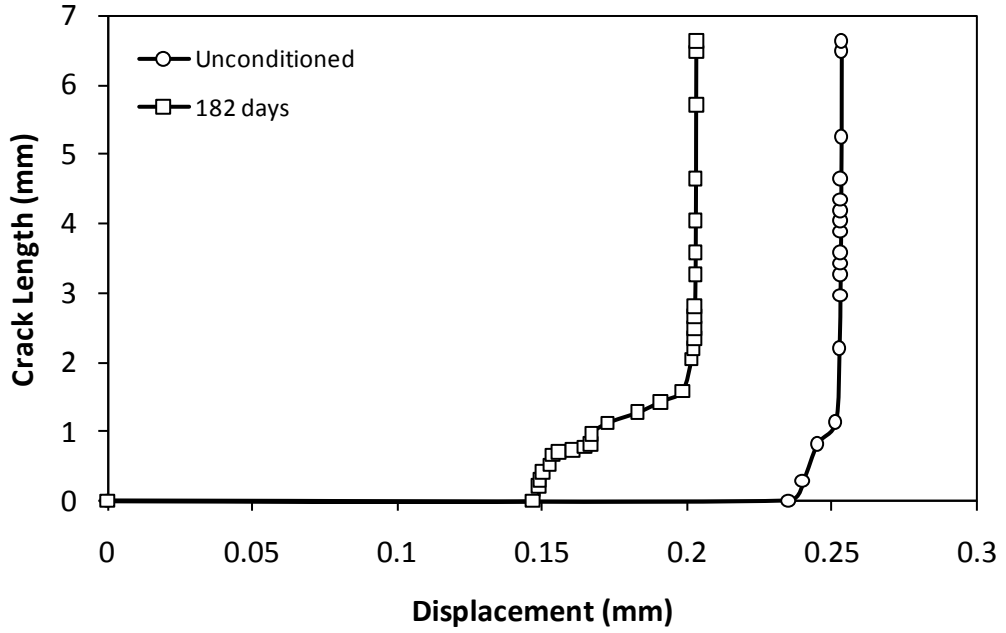

Figure 8.12: Crack length of Al2024 T3 joints, conditioned at 50°C, as a function of displacement.

8.5.2 Al2024 O Single Lap Joints Conditioned at 50°C

The adherends of the O joints were modelled using an elasto-plastic material model whilst moisture history dependent elastic properties were used for the adhesive. The cohesive zone model parameters used were the same as those used for the T3 joints. The force vs. displacement response of the O joints may be seen in Figure 8.13 where a nonlinear relationship between force and displacement was observed after load of 1.84 kN. This can be attributed to the plastic deformation of the adherends as damage was not visible in the adhesive at this load in both unconditioned and 182 days conditioned joints.

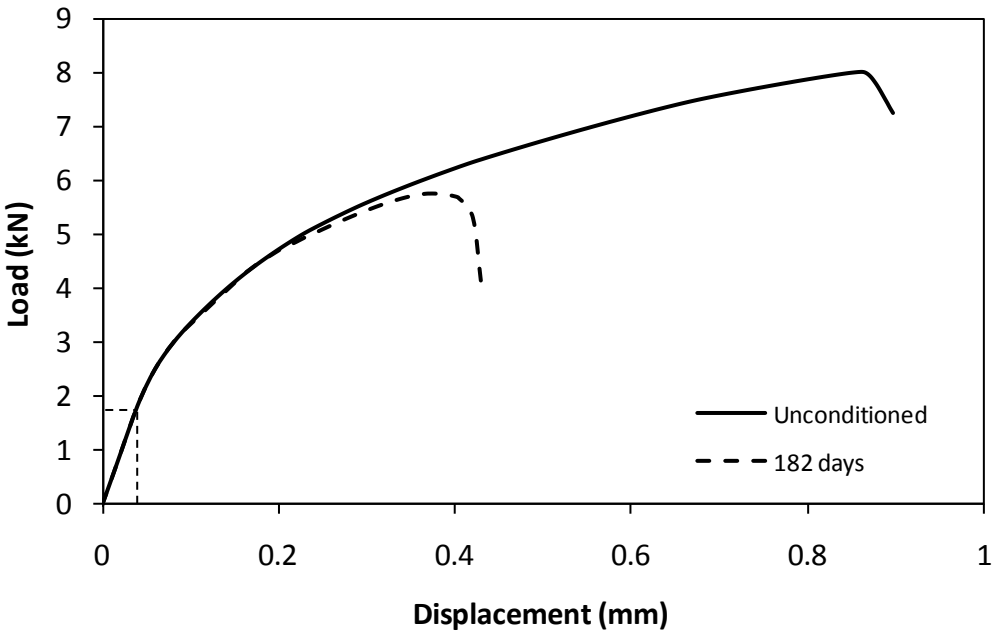

Figure 8.13: Force-displacement response of Al2024 O unconditioned and 182 days conditioned joint.

A comparison between the experimental and finite element predicted deformation of the adherends of the unconditioned O joints is shown in Figure 8.14. A good correlation between the shape of the experimentally deformed adherends and the finite element model exists.

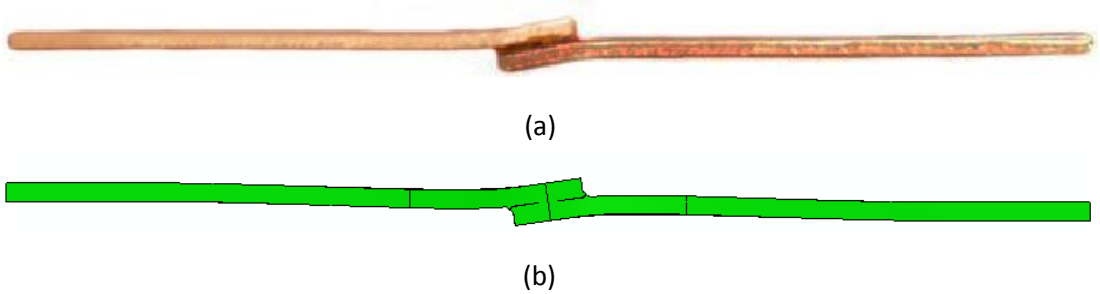

Figure 8.14: Plastic deformation in Al2024 O adherends after tensile testing (a) experimental (b) FEM.

The experimental and predicted failure loads of the O joints, conditioned for various time intervals, are shown in Figure 8.15. The failure load of the unconditioned O

joint was under predicted by 9% by the model. The predicted failure loads at conditioning times of 7, 14 and 28 days were higher than the average experimental failure loads and were within 11.5% of the average failure loads. The experimental strength of the O joints recovered somewhat after 56 and 182 days of moisture conditioning, however, the finite element model predicted a progressive decrease in the failure load under these conditions. The strength of the dried O joints was under predicted at all moisture conditions except for 7 days of moisture conditioning, however, the predicted strength was within 6% of the average experimental results.

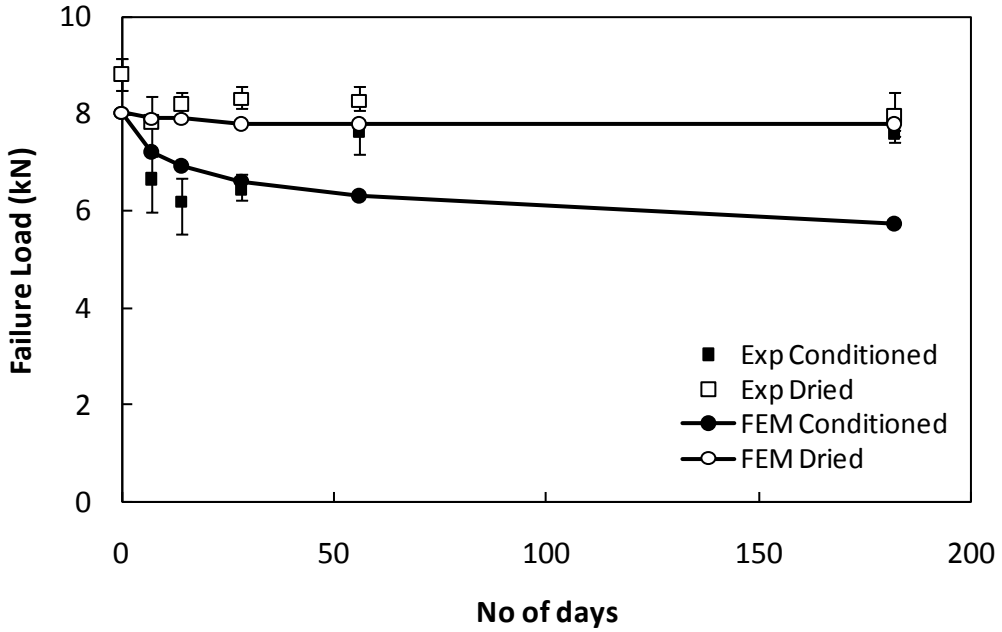

Figure 8.15: Predicted and experimental failure load of the Al2024 O joints when conditioned at 50°C.

Crack initiation in the O joints occurred at the outer fillet edge in region 3, as can be seen in Figure 8.16a, which was different from the T3 joints where crack initiated in the middle of the fillet. After the crack initiation, major crack growth occurred towards the edges in ±Z directions and once the crack reached the edges, the crack propagated towards the middle of the overlap in X direction. The damage zone was smaller in the unconditioned O joints than the unconditioned T3 joints during crack

propagation. The difference in crack initiation region between O and T3 joints may be owing to the increased peel stresses in O joints, resulting from the adherend rotation.

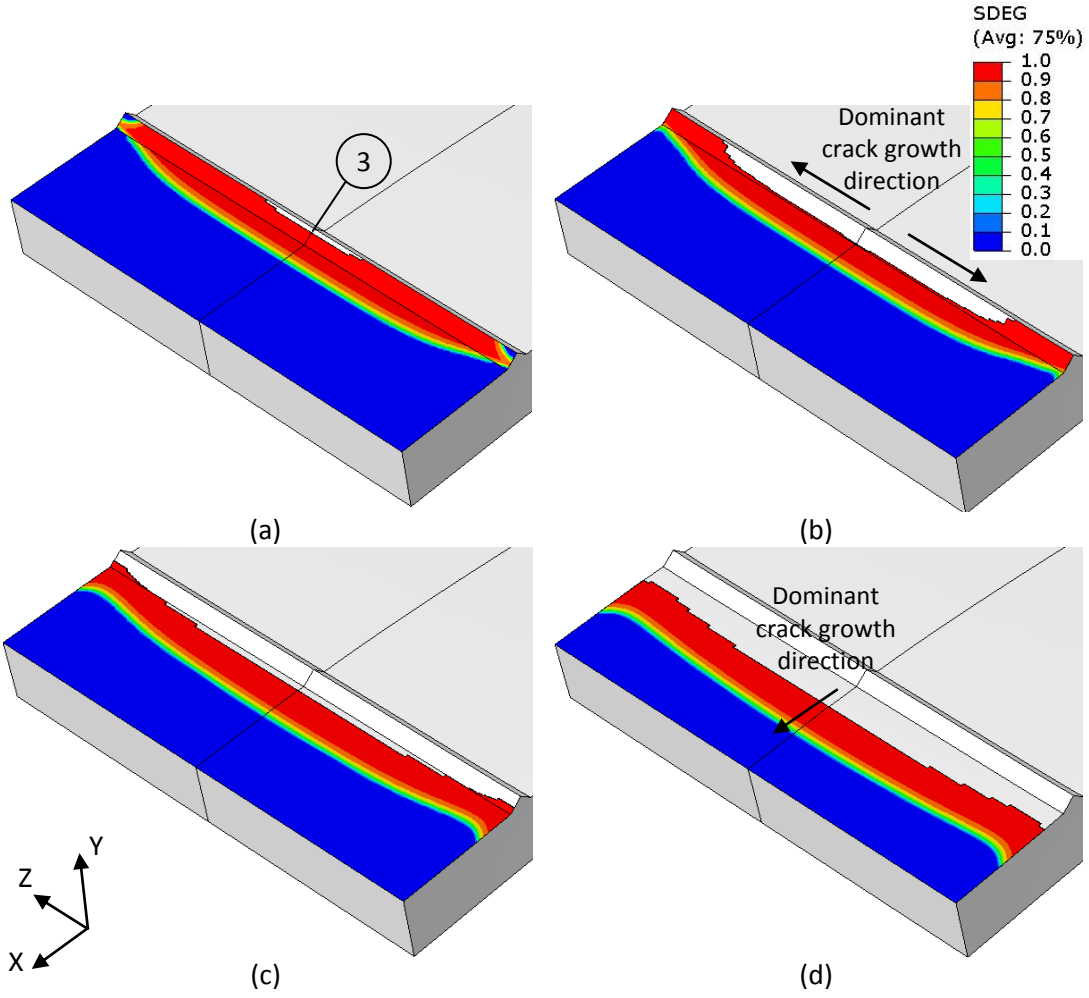

Figure 8.16: Damage and crack propagation in unconditioned Al2024 O single lap joint.

In the O joints conditioned for 182 days, the crack initiation location was similar to the 182 days conditioned T3 joints, as shown in Figure 8.17. The crack propagated towards the middle of the overlap in X direction after reaching the joint edges.

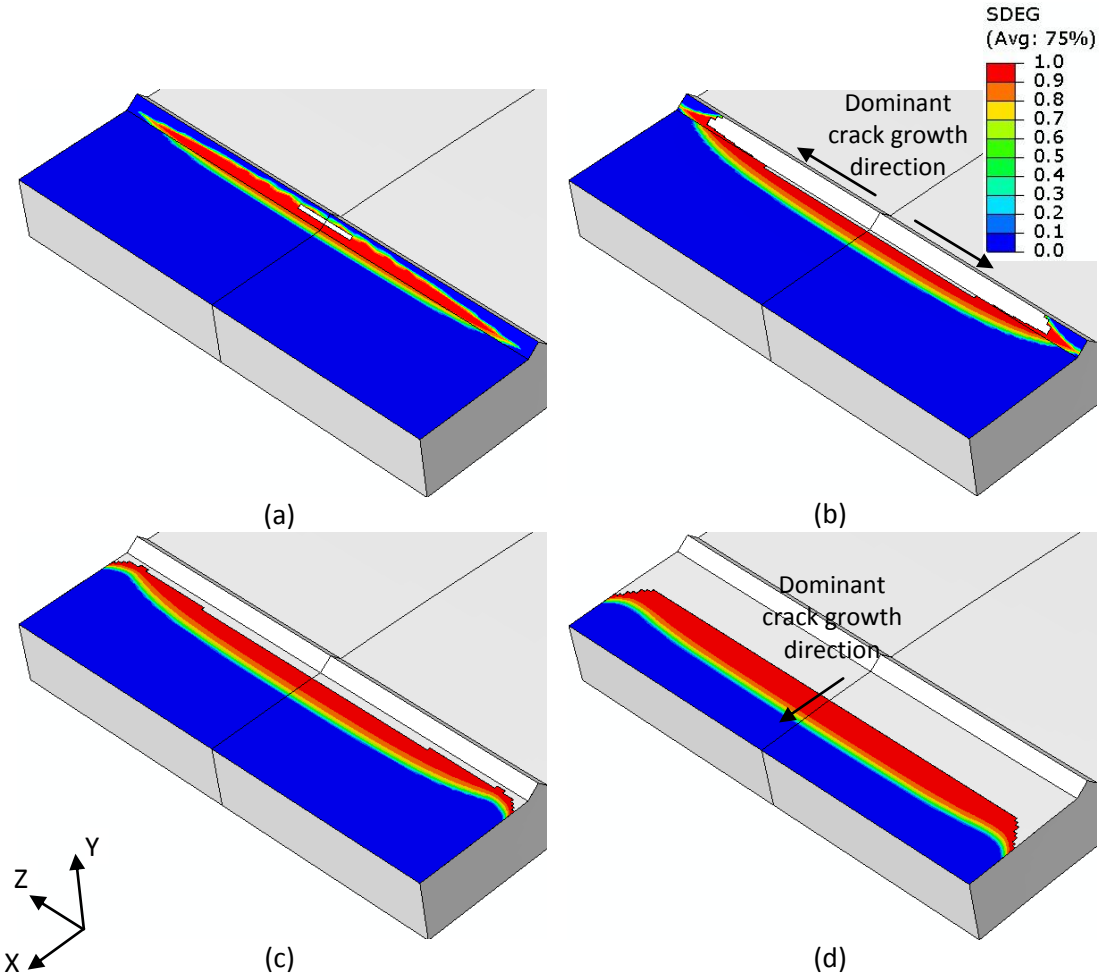

Figure 8.17: Damage and crack propagation Al2024 O single lap joint, conditioned at 50°C for 182 days.

There are three regions of crack propagation after crack initiation in unconditioned O joints, as may be seen in Figure 8.18. A relatively fast crack growth region is followed by a period of slow, more stable crack growth. This is then followed by another period of rapid crack growth, this time leading to failure of the joint. In the 182 days conditioned O joints, the region of slow crack growth is smaller than in the unconditioned O joints. Comparison of Figure 8.12 and Figure 8.18 shows that the crack propagation was more gradual in the O joints than the T3 joints.

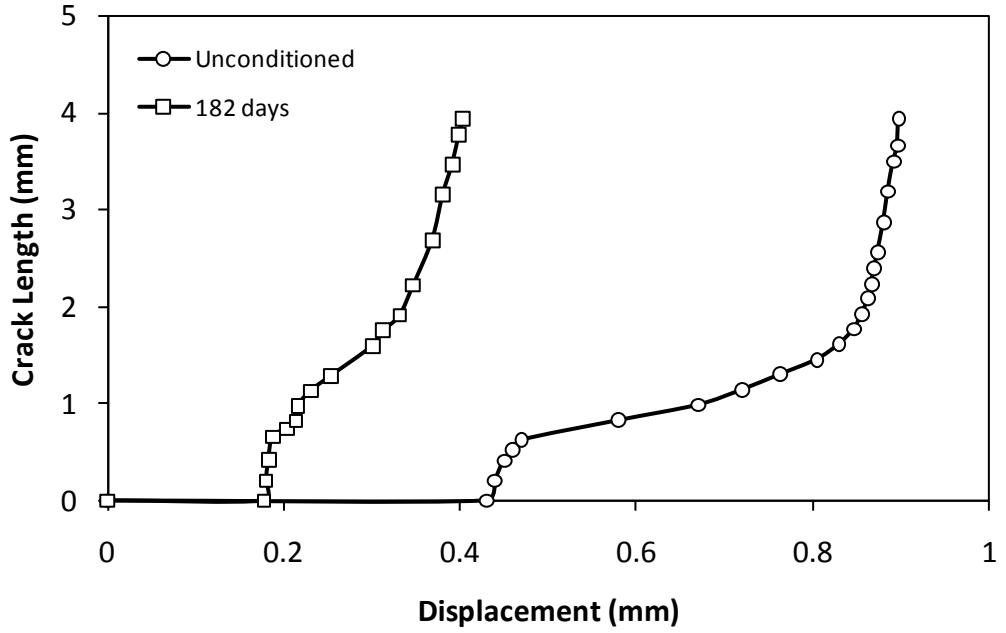

Figure 8.18: Crack length as a function of displacement in Al2024 O joints conditioned at 50°C.

8.5.3 Al2024 T3 Single Lap Joints Conditioned at 70°C

The cohesive zone parameters for the T3 and O joints, conditioned at 70°C, were derived based on the experimental data for the T3 and O joints conditioned at 50°C. The change in the fracture energy and the tripping traction with moisture content, at 70°C, was considered to be similar to the change in the elastic modulus of the adhesive with moisture content at 50°C.

Comparison of the experimental and the predicted failure loads of the T3 joints conditioned at 70°C is given in Figure 8.19. The predicted failure load after moisture conditioning for 7, 14 and 28 days is in good agreement with the experimental results. Higher failure loads were predicted after 56 and 182 days moisture conditioning than the experimental results, however, the predicted results were within 8% of the experimental results. Under dried conditions, the predicted failure load was higher than the experimental failure loads where the predicted results were within 9% of the experimental results. The crack initiation and propagation in the T3 joints conditioned at 70°C was similar to the T3 joints conditioned at 50°C.

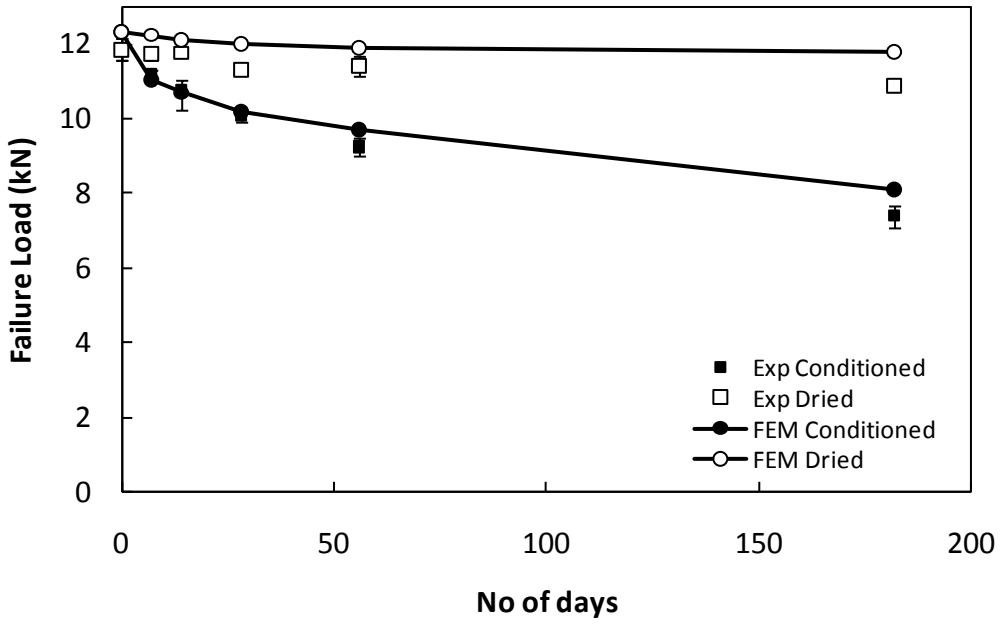

Figure 8.19: Predicted and experimental failure load of the Al2024 T3 joints conditioned at 70°C.

8.5.4 Al2024 O Single Lap Joints Conditioned at 70°C

Comparison of the experimental and predicted failure loads for the O joints conditioned at 70°C is given in Figure 8.20. For conditioned O joints, the failure load at 7, 14 and 28 days of conditioning is predicted well by the finite element model while higher failure loads were predicted at 56 and 182 moisture conditioning. In dried O joints, higher failure loads were predicted at all moisture conditions. The maximum difference between the experimental and the predicted failure loads was observed at 182 days for both conditioned and dried joints. This may be owing to the lack of availability of direct experimental data for modelling as the moisture dependent cohesive zone model parameters were extrapolated from the experimental data available for 50°C. The crack initiation and propagation was similar to the O joints conditioned at 50°C.

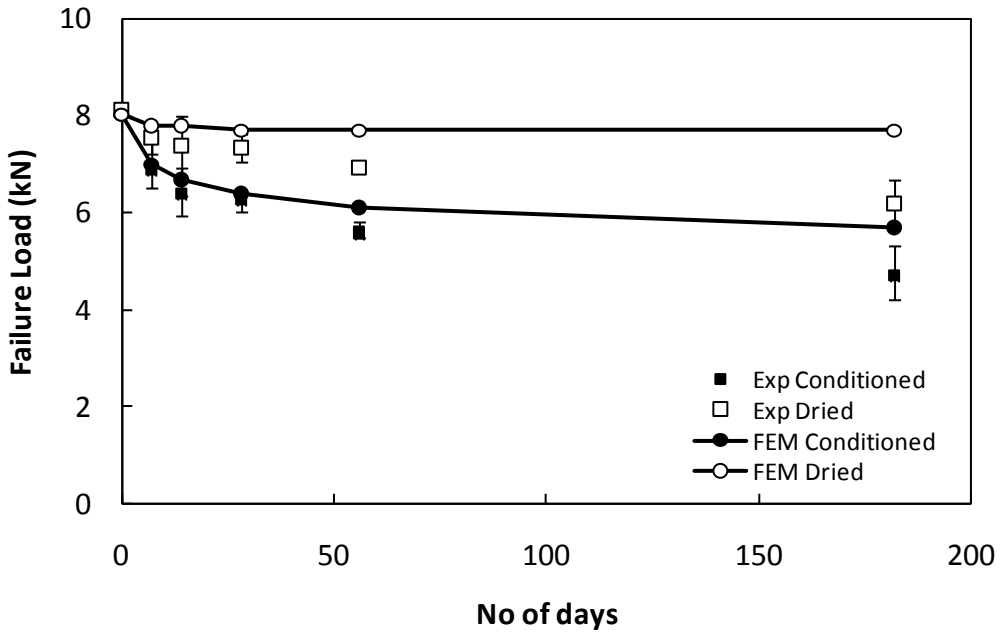

Figure 8.20: Predicted and experimental failure load of the Al2024 O joints conditioned at 70°C.

8.6 Summary

The "variable moisture and strength prediction methodology" was used in combination with a cohesive zone model to predict the damage and failure in single lap joints under different moisture and temperature conditions. A bilinear cohesive zone model was coupled with hygroscopic model using concentration and history dependent cohesive energy. The cohesive zone model parameters were calibrated using a 2D single lap joint model.

The methodology was used to determine the damage and failure in T3 and O single lap joints, conditioned at 50°C and 70°C. For T3 joints conditioned at 50°C, good predictions of failure load were observed while higher failure load was predicted in dried T3 joints. The failure load at low moisture conditions of up to 28 days was successfully predicted for O joints conditioned at 50°C, however, the observed strength recovery at higher moisture conditions was not predicted by the model. The dried O joints had failure load predictions within 6% of the experimental results except for 7 days of conditioning and drying.

At 70°C, the failure load of T3 conditioned joints was well predicted except for the T3 joints conditioned for 182 days. The failure load of the dried T3 joints was predicted within 9% of experimental results at all moisture conditions. The predicted failure load of conditioned and dried O joints, at 70°C, was in good agreement with the experimental failure load for moisture conditioning up to 28 days. However, after 56 and 182 days of moisture conditionings, the predicted and experimental failure loads were not in agreement.

Chapter 9
Discussion

9.1 Introduction

A discussion of the experimental results and the numerical modelling carried out using the proposed variable moisture and strength prediction methodology is presented in this chapter. The effects of moisture on joint durability and possible mechanisms to explain changes in the joint strength are discussed, along with the nature of the failure surfaces observed after tensile testing. The predicted stresses in the joints are analysed to explain the degradation and recovery in joint strength with moisture diffusion. The results of the damage and failure modelling are discussed at the end of the chapter. This provides an insight into crack development and propagation in the conditioned and dried joints.

9.2 Durability of Adhesive Joints

Degradation in the joint strength was observed with increasing moisture concentration, except for Al2024 O joints conditioned at 50°C, as shown in Section 4.4. The degradation of joint strength may be due to deterioration of the adhesive system i.e. FM73-M and BR127, the interface or a combination of the two. Moisture affects the adhesive in the form of plasticisation and swelling. A combination of both chemical and mechanical adhesion mechanisms may explain the nature of adhesion in the aluminium/epoxy joint system used in this work. The chemical theories attribute adhesion to London dispersion forces, acid base interactions or metal organic complex formation [199-201]. The metal organic complex is also thought to introduce a needle like structure at the interface giving a “fibre

reinforced" interphase. The mechanical interlocking theory is based on a "lock and key" effect, achieved through wetting of the surface porosity of the adherends.

In the single lap joints, the interface between the primer and the oxide layer forms a non-planar path as the primer penetrates the oxide layer, as shown in Figure 9.1. Also, there is no distinct interface between the primer and the adhesive but an interphase is present [202, 203]. This is because primer BR127 is an epoxy phenolic and forms bonds with the epoxy adhesive FM73-M. In the case of a cohesive failure, the crack travels through the adhesive (or primer) layer and the failure may be attributed to the breakage of primary bonds. This suggests that the interface has strong adhesion forces in an unconditioned joint. In the case of conditioned joints, the adhesive and interface, or interphase, may be affected by the moisture uptake. The adhesive plasticises and swells, which decreases it's strength and the oxide layer may become hydrated. When cohesive failure was observed, it is suggested that the degradation of the interface was not significant, whilst the adhesive had degraded and caused the failure.

In the case of apparent interfacial failure, it is important to consider that the primer and oxide layer are not only joined by interatomic forces, but a strong mechanical interlocking is also present, which would make complete separation of the primer from the oxide layer very difficult. Thus, where apparent interfacial failure was observed, the FEGSEM analysis showed that failure was actually within the primer layer, but very close to the oxide layer. This allows for the explanation of strength recovery when the joint was dried. If it is considered that the diffused water caused disruption of inter-atomic forces at the interface, the re-establishment of strong secondary forces would be unlikely, as this requires very close contact between the primer and adherend surfaces. This was possible during joint manufacture because of the low viscosity of the uncured primer but cannot occur easily after the primer has cured. However, if the adhesive or primer layer fails cohesively, as is the case in this study, the removal of moisture by drying would recover the strength of the adhesive and primer and recovery of joint strength would be observed.

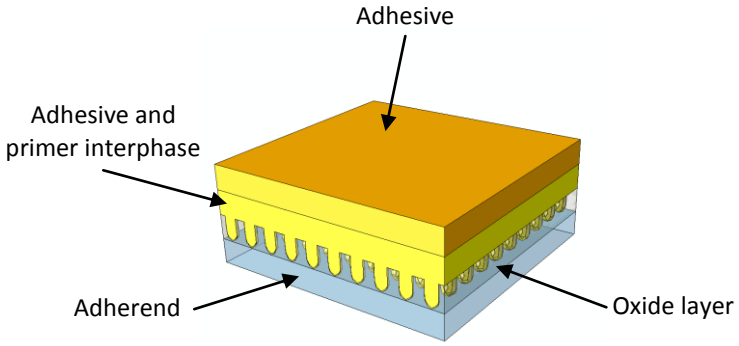

Figure 9.1: A schematic representation of the adhesive-adherend interface.

Approximately 90% of unconditioned strength recovery was observed in Al2024 O joints after conditioning for greater than 56 days, while no such phenomenon was observed in other joints. The differentiating characteristic of the non heat treated alloy joints is the lower strength of the adherends compared with the T3 heat treated alloy joints. When tested in the unconditioned state, the Al2024 O joints undergo large deformations, in the form of rotations, and adherend yielding occurs before joint failure. After moisture absorption for 7 and 14 days, most of the adhesive layer still has a low moisture concentration, but the adhesive may have become significantly weaker in the critical fracture initiation sites. Hence a combination of yielding in the adherends and a decrease in the strength of the adhesive and the primer in the failure initiation region may be responsible for the observed decrease in failure strength. After 56 or 182 days of moisture absorption, larger areas of the adhesive become plasticised, which results in reduced yielding and rotation of the adherends whilst there is little change in the moisture content, and hence strength, of the adhesive and primer in the areas of failure initiation.

It can be seen that moisture concentration in the failure initiation area reaches almost complete saturation in 56 days and that this corresponds to a fall in adhesive strength in this area. Hence the combination of high interfacial strains through yielding and rotation of the adherends and the weakness of the adhesive in the area of failure initiation results in a decrease in strength, that recovers when plasticisation of the adhesive layer reduce the yielding and hence interfacial strains. As expected, this effect is much reduced when a high yield adherend is used.

9.3 Stresses in Adhesive Joints

Plastic deformation of the adhesive may be the major contributing factor in the joint strength and recovery. The stresses predicted by the variable moisture and strength prediction methodology may contribute to the understanding of these phenomena. The thermal and hygroscopic stresses did not produce any plastic deformation in the adhesive layer in any of the joints. In the T3 unconditioned joints, plastic deformation occurred after the application of a 5 kN tensile load, as shown in Figure 9.2a. The plastic deformation starts in the centre of the adhesive layer and spans across the width of the joint, in the Z direction. As the load increases during tensile testing, the plastic deformation zone increases in size and grows towards the middle of the overlap i.e. in the X direction. The plastic zone is larger at the centre of the adhesive layer than at the edges. The maximum plastic strain occurs at the ends of the overlap. The plastic deformation in the unconditioned Al2024 O joints also starts at the centre of the adhesive layer, as shown in Figure 9.2b. However, a large plastic deformation zone is present at the edges as well as in the centre of the adhesive layer.

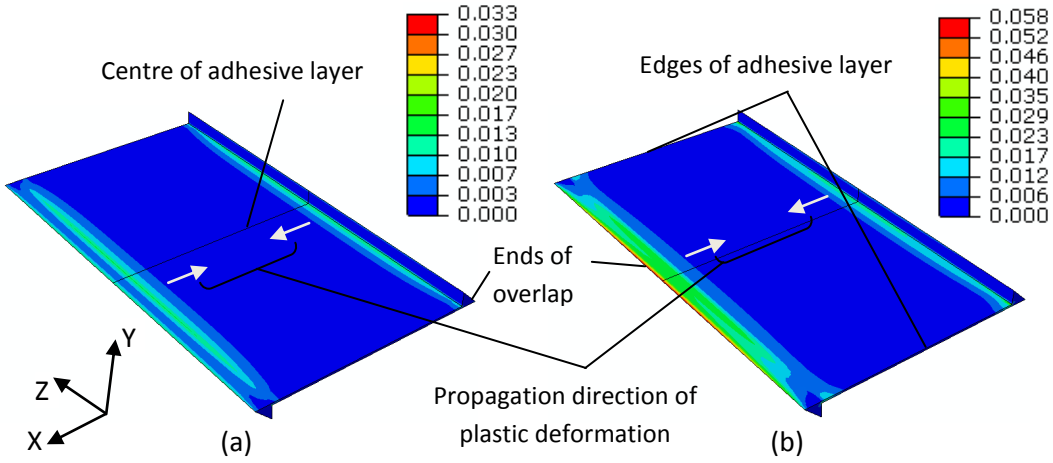

Figure 9.2: Equivalent plastic strain distribution in the adhesive layer of unconditioned (a) T3 and (b) O joints after application of 5 kN of load.

The adhesive plastic deformation in T3 and O joints, conditioned at 50°C, is similar to the unconditioned T3 joints. The maximum plastic strain was greater in the T3 and O joints conditioned for 182 days than in those conditioned for 7 days. This is because of the degradation of adhesive stiffness with increasing moisture absorption. Higher plastic deformation of the adhesive layer was observed in O joints as compared to T3 joints. This can be seen in Figure 9.3 for joints conditioned for 182 days at 50°C. As described earlier, the adherends of the O joints exhibited rotation and plastic deformation during the tensile tests. This results in higher stresses in O joints than T3 joints and decreases the strength of the O joints, as was observed experimentally in Section 4.4.

Residual moisture was present in the joints dried after conditioning, which affected the adhesive strength and thus the plastic deformation of the adhesive layer under tensile loading. In T3 joints conditioned for 182 days and dried, a larger plastic deformation zone is present and the maximum plastic strain is lower than the unconditioned T3 joints. This decrease in the maximum plastic strain may be attributed to the spread of plastic deformation over a larger area in the T3 dried joints. This was not observed in O joints dried after 182 days of conditioning, which may be owing to the higher magnitude of plastic deformation in unconditioned O joints than T3 joints.

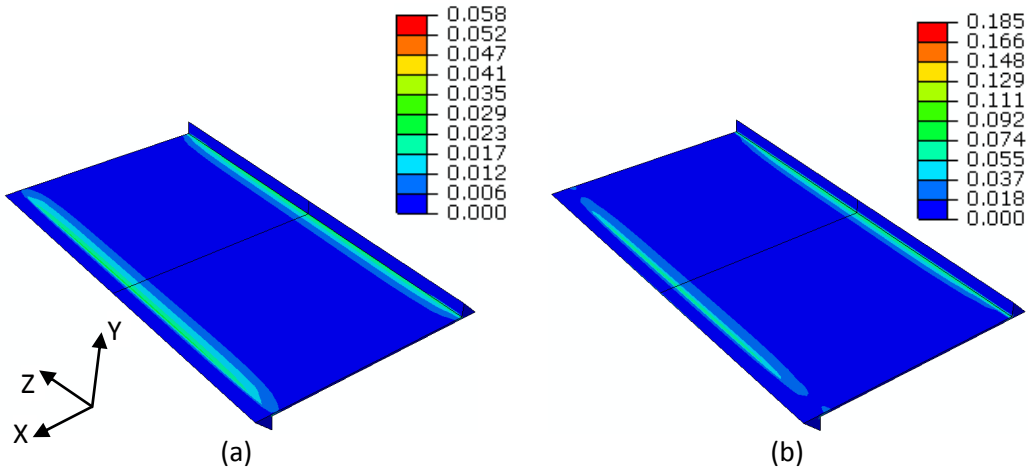

Figure 9.3: Equivalent plastic strain distribution in the adhesive layer of (a) T3 and (b) O, joints conditioned at 50°C for 182 days, after application of 5 kN of load.

Plastic strain was greater in T3 and O joints conditioned for 182 days at 50°C compared with 70°C, as shown in Figure 9.4. The zone of plastic deformation was also larger in the joints conditioned at 70°C than those at 50°C. The amount of plastic deformation decreased after drying the adhesive due to the reversible effects of plasticisation.

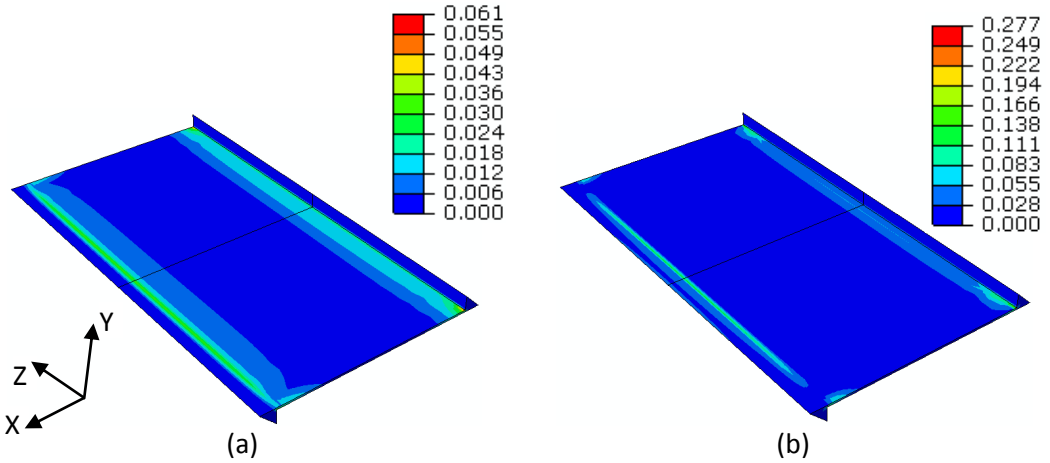

Figure 9.4: Equivalent plastic strain distribution in the adhesive layer of (a) T3 and (b) O, joints conditioned at 70°C for 182 days, after application of 5 kN of load.

The adhesive stresses provide a basis for the implementation of damage and failure criteria, which are discussed in the next section.

9.4 Damage and Failure in Adhesive Joints

Coupling of the variable moisture and strength prediction methodology with a cohesive zone model provided the ability to predict damage and failure in the joints. In both T3 and O joints, the crack initiation region was in the centre of the adhesive layer in the Z-plane, as shown in Figure 9.5. This is in agreement with the stress model predictions, discussed in Section 9.3, where the highest plastic strains were present in the centre of the adhesive layer. This was the case for all conditioned joints. However, the difference in adherend strength affected the crack initiation region in the unconditioned O joints. The greater rotations of the Al2024 O adherends during tensile loading resulted in higher peel stresses and crack initiation

occurred at the outer fillet edge, as shown in Figure 9.5. Failure of the T3 unconditioned joints is faster after crack initiation than the O unconditioned joints. This may be owing to most of the adhesive layer being damaged before crack initiation in the T3 unconditioned joints.

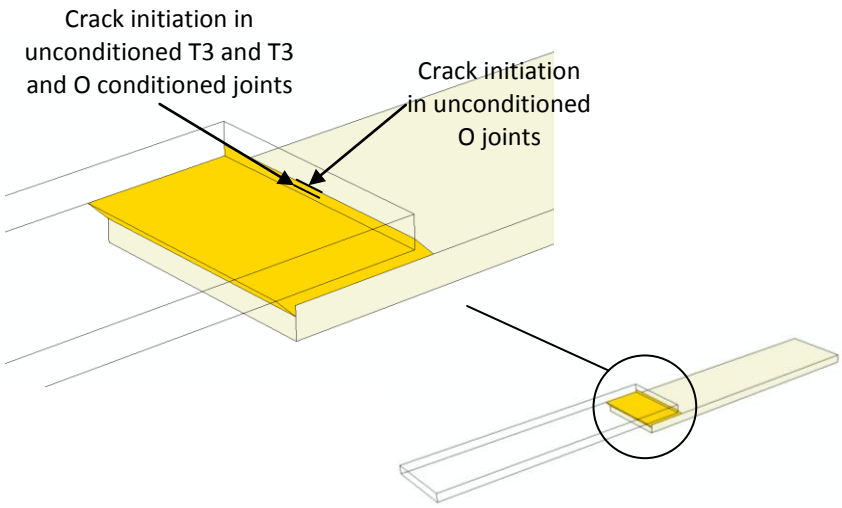

Figure 9.5: Failure initiation in T3 and O single lap adhesive joints.

The conditioned joints showed similar crack initiation and propagation in O and T3 joints and at both 50°C and 70°C conditioning temperatures, as is shown in Chapter 8. In T3 joints conditioned for 182 days, small cracks also initiated from the adhesive layer edges. The similarities in crack propagation in conditioned joints may be attributed to the moisture concentration in the critical areas and adhesive strength degradation.

9.5 Summary

Degradation in the strength of the adhesive joints was observed after moisture diffusion. Cohesive failure generally occurred in the adhesive layer of the unconditioned adhesive joints whereas the apparent interfacial failure occurred in the adhesive and primer layers, close to the interface, of the conditioned adhesive joints. More than 90% of the unconditioned strength of the joints recovered after drying and may be attributed to the recovery of adhesive (and primer) strength.

Hygrothermal stresses arising from curing and moisture conditioning may result in significant residual stresses in single lap joints. The residual stresses, combined with mechanical loading produce plastic deformation in the adhesive layer. The plastic deformation initiates at the centre of the adhesive layer and crack initiation occurs as the rupture stress of the adhesive is reached.

This research presents a significant step in durability modelling of adhesive joints by characterising moisture dependent material properties and presenting a methodology to predict adhesive joint strength under varying environmental conditions. A flowchart outlining the overall variable moisture diffusion and strength prediction methodology is shown in Figure 9.6. The ability to predict moisture concentration under varying environmental conditions provides increased confidence in the use of adhesive joints in structural applications. The methodology may be adapted to develop “black box” applications for use during the design and development of products. The predictive methodology may also be used to inform maintenance and repair methods and schedules.

Due to the ability of the finite element method to deal with complex geometries, most types of the adhesive joint configurations may be used with the proposed methodology. By changing the material diffusion properties, the variable moisture diffusion model may also be used to predict moisture concentration of not only adhesives, but also for other moisture sensitive polymers and polymer matrix composites. A change in the moisture dependent mechanical properties allows for stress predictions in joint configurations made up of various types of materials. Finally, cohesive zone elements may be used to predict the damage and failure based on the moisture dependent fracture energy.

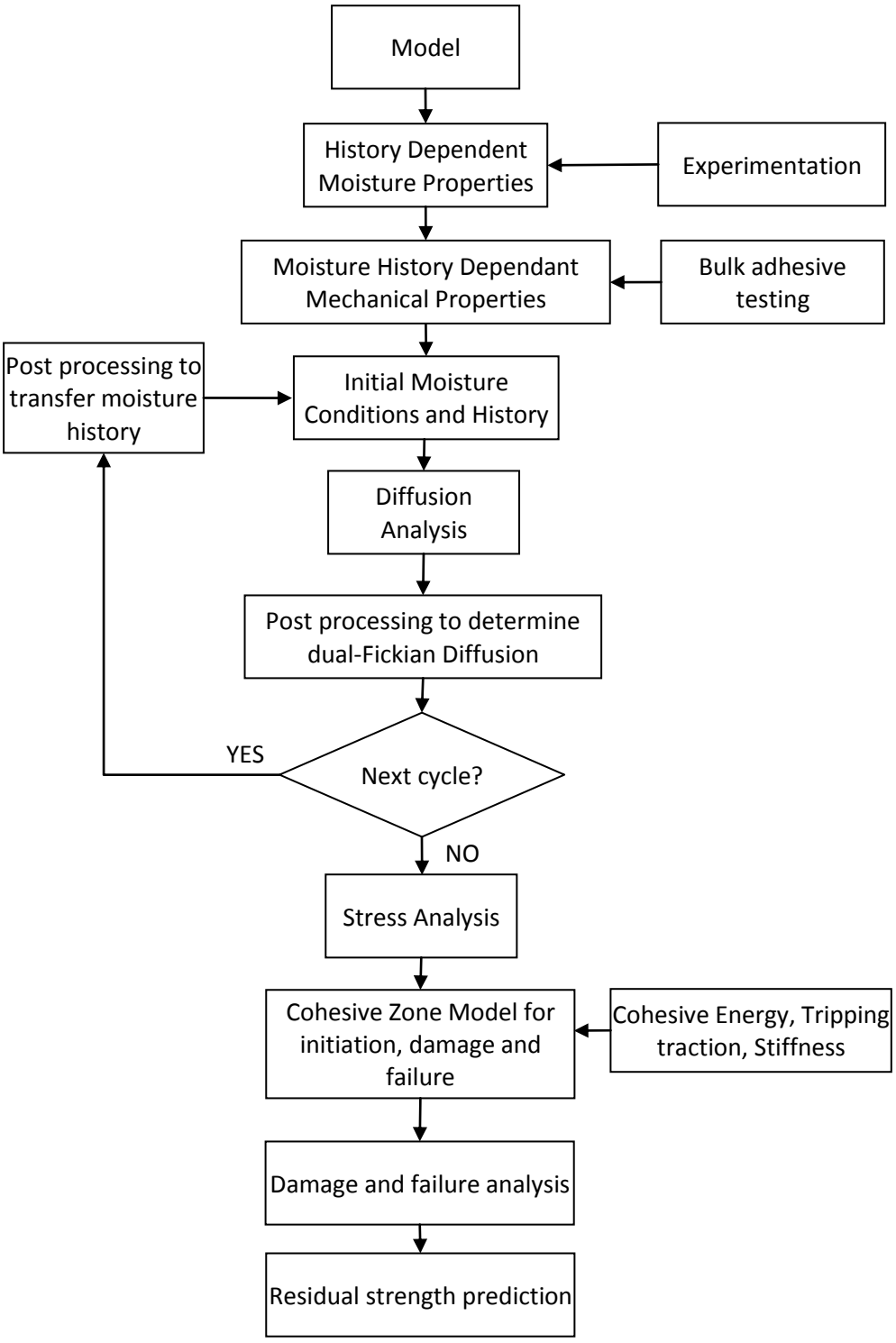

Figure 9.6: Overall flowchart of variable moisture diffusion and strength prediction methodology.

Chapter 10
Conclusions and Future Work

10.1 Introduction

The aim and objectives of the research, as laid down in Section 1.2, have been successfully achieved by; (i) the experimental characterisation of moisture dependent material properties and (ii) the development of a methodology that is able to predict moisture diffusion and joint strength under variable environmental conditions. The conclusions of the research work and suggestions for future work are presented in this chapter.

10.2 Conclusions

The main conclusions of this research are as follows;

1. Moisture absorption of the adhesive is non-Fickian, whereas moisture desorption is a Fickian process.
2. The moisture diffusion coefficient, saturated moisture content and the strength of the adhesive are moisture history dependent.
3. Failure of well-prepared unconditioned adhesive joints is mainly through cohesive failure of the adhesive.
4. The failure path changes from cohesive to apparent interfacial failure with moisture conditioning.
5. Conditioned adhesive joints may recover a large amount of their unconditioned strength after drying.

6. Strength recovery mainly occurs because of the recovery of the cohesive strength of the adhesive and primer.
7. The proposed cyclic moisture diffusion prediction methodology can successfully predict the moisture concentration in an adhesive after exposure to varying environmental conditions.
8. In cases when equilibrium is not reached during a cyclic situation, localised absorption and desorption processes occur simultaneously in the adhesive layer.
9. Neglecting the moisture history dependence of moisture diffusion may result in over or under prediction of diffused moisture in the adhesive layer.
10. Significant hygrothermal residual stresses may be present in adhesive joints after curing and moisture conditioning.
11. The failure initiation region in an adhesive joint may change based on the strength of the adherends.
12. Crack growth before sudden failure, in a conditioned single lap joint, is more stable than in an unconditioned joint.
13. The proposed variable moisture and strength prediction methodology can successfully predict the strength of adhesive joints under cyclic environmental conditions.

10.3 Future Work

The proposed variable moisture and strength prediction methodology may be expanded by including the effects of stress on moisture diffusion in an adhesive. This would improve the predictions of moisture concentration and durability of adhesive joints under different loading conditions.

The effects of viscoelasticity of the adhesive may be included in the strength predictions. The inclusion of viscoelasticity would provide more realistic predictions of the joint stresses when conditioned for long durations.

Continuum damage models may be coupled with the proposed methodology to predict damage and failure in adhesive joints. Calibration of such models under unconditioned and conditioned state would be required. The use of continuum damage models would allow the study of complex joint structures with multiple cracks.

Further experimental validation of the proposed methodology may be carried out by using experimental data obtained under variable moisture conditions. Variable moisture experiments may be designed based on “real world” data. This would provide more confidence in the use of the methodology for industrial applications.

Experimental methods may be investigated and developed to obtain mapped moisture concentrations experimentally for direct comparison with numerically determined moisture predictions to improve confidence in the proposed methods.

References

1. Adams, R.D., J. Comyn, and W.C. Wake, *Structural adhesive joints in engineering*. 2nd ed. 1997, London: Chapman and Hall.

2. Dixon, D.G., *Aerospace applications of adhesives*, in *Handbook of Adhesion*, D.E. Packham, Editor. 2005, John Wiley & Sons, Ltd. p. 40-42.

3. Watson, C., *Engineering design with adhesives*, in *Handbook of Adhesion*, D.E. Packham, Editor. 2005, John Wiley & Sons, Ltd. p. 138-141.

4. Minford, J.D., *Handbook of Aluminum Bonding Technology and Data*. 1993, New York: Marcel Dekker, Inc.

5. da Silva, L.F.M., P.J.C. das Neves, R.D. Adams, and J.K. Spelt, *Analytical models of adhesively bonded joints - Part I: Lieterature survey.* Int. J. Adhesion and Adhesives, 2009. **29**: p. 319-330.

6. Grant, L.D.R., R.D. Adams, and L.F.M. da Silva, *Experimental and numerical analysis of single-lap joints for the automotive industry.* International Journal of Adhesion and Adhesives, 2009. **29**(4): p. 405-413.

7. Hua, Y., A.D. Crocombe, M.A. Wahab, and I.A. Ashcroft, *Continuum damage modelling of environmental degradation in joints bonded with EA9321 epoxy adhesive.* International Journal of Adhesion and Adhesives, 2008. **28**(6): p. 302-313.

8. Hua, Y., 2006. *Modelling environmental degradation in adhesively bonded joints*, PhD Thesis, University of Surrey.

9. Jumbo, F.S., 2007. *Modelling residual stresses and environmental degradation in adhesively bonded joints*, PhD Thesis, Loughborough University.

10. Keat, L.W., 2002. *Modelling interfacial degradation in adhesively bonded structures*, PhD Thesis, University of Surrey.

11. Critchlow, G.W. and D.M. Brewis, *Review of surface treatments for aluminium.* Int. J. Adhesion and Adhesives, 1996. **16**: p. 255-275.

12. Packham, D.E., ed. *Handbook of adhesion*. 2005, John Wiley & Sons: Chichester.

13. Bowditch, M.R., *The durability of adhesive joints in the presence of water.* Int. J. Adhesion and Adhesives, 1996. **16**: p. 73-79.

14. Brewis, D.M., J. Comyn, A.K. Raval, and A.J. Kinloch, *The effect of humidity on the durability of aluminium-epoxide joints.* Int. J. Adhesion and Adhesives, 1990. **10**(4): p. 247-253.

15. Brewis, D.M., J. Comyn, R.J.A. Shalash, and J.L. Tegg, *Interaction of water with some epoxide adhesives.* Polymer, 1980. **21**: p. 357-360.

16. Brewis, D.M., J. Comyn, and S.T. Tredwell, *Diffusion of water in some modified phenolic adhesives.* Int. J. Adhesion and Adhesives, 1987. **7**(1): p. 30-32.

17. Brewis, D.M. and G.W. Critchlow, *Influence of surface treatment on the durability of aluminum-epoxide lap joints.* Transactions of the Institute of Metal Finishing, 1976. **74**(6): p. 198-201.

18. Briskham, P. and G. Smith, *Cyclic stress durability testing of lap shear joints exposed to hot-wet conditions.* Int. J. Adhesion and Adhesives, 2000. **20**: p. 33-38.

19. Broad, R., J. French, and J. Sauer, *New, effective, ecological surface pretreatment for highly durable adhesively bonded metal joints.* Int. J. Adhesion and Adhesives, 1999. **19**: p. 193-198.

20. De Neve, B. and M.E.R. Shanahan, *Effects of humidity on an epoxy adhesive.* Int. J. Adhesion and Adhesives, 1992. **12**(3): p. 191-196.

21. Dickie, R.A., L.P. Haack, J.K. Jethwa, A.J. Kinloch, and F.J. Watts, *The fatigue and durability behaviour of automotive adhesives. Part II: Failure mechanisms.* J. Adhesion, 1998. **66**: p. 1-37.

22. Grant, L.D.R., R.D. Adams, and L.F.M. Da Silva, *Effect of temperature on the strength of the adhesively bonded single lap and T joints for the automotive industry.* Int. J. Adhesion and Adhesives, 2009. **29**: p. 535-542.

23. Liljedahl, C.D.M., A.D. Crocombe, M.A. Wahab, and I.A. Ashcroft, *Modelling the environmental degradation of adhesively bonded aluminium and composite joints using a CZM approach.* Int. J. Adhesion and Adhesives, 2007. **27**: p. 505-518.

24. Adamson, M.J., *Thermal expansion and swelling of cured epoxy resin used in graphite/epoxy composite materials.* J. Mat. Sci., 1980. **15**: p. 1736-1745.

25. Masaro, L. and X.X. Zhu, *Physical models of diffusion for polymer solutions, gels and solids.* Prog. Polym. Sci., 1999. **24**: p. 731-775.

26. Drozdov, A.D., J.d. Christiansen, R.K. Gupta, and A.P. Shah, *Model for anomalous moisture diffusion through a polymer clay nanocomposite.* J. Poly. Sci. Part B: Poly. Phys., 2003. **41**: p. 476-492.

27. Carter, F.G. and K.G. Kibler, *Langmuir-Type Model for Anomalous Moisture Diffusion In Composite Resins.* J. Comp. Mater., 1978. **12**(2): p. 118-131.

28. Doyle, G. and R.A. Pethrick, *Environmental effects on the ageing of epoxy adhesive joints.* International Journal of Adhesion and Adhesives, 2009. **29**(1): p. 77-90.

29. Popineau, S. and M.E.R. Shanahan, *Simple model to estimate adhesion of structural bonding during humid ageing.* Int. J. Adhesion and Adhesives, 2006. **2006**: p. 363-370.

30. Popineau, S., C. Rondeau-Mouro, C. Sulpice-Gaillet, and M.E.R. Shahnahan, *Free/bound water absorption in an epoxy adhesive.* Polymer, 2005. **46**: p. 10733-10740.

31. Lindqvist, S.A., *Theory of dielectric properties of heterogeneous substances applied to water in a paint film.* Corrosion, 1985. **41**(2): p. 69-75.

32. Zanni-Deffarges, M.P. and M.E.R. Shahnahan, *Diffusion of water into an epoxy adhesive: comparision between bulk behaviour and adhesive joints.* Int. J. Adhesion and Adhesives, 1995. **15**: p. 137-142.

33. Wahab, M.A., A.D. Crocombe, A. Beevers, and K. Ebtehaj, *Coupled stress diffusion analysis for durability study in adhesively bonded joints.* Int. J. Adhesion and Adhesives, 2002. **22**: p. 61-73.

34. Nakamura, K., T. Maruno, and S. Sasaki, *Theory of the decay of the wet shear strength of adhesion and its application to metal/epoxy/metal joints.* Int. J. Adhesion and Adhesives, 1987. **7**(2): p. 97-102.

35. Hua, Y., A.D. Crocombe, M.A. Wahab, and I.A. Ashcroft, *Modelling Environmental Degradation in EA9321-Bonded Joints using a Progressive Damage Failure Model.* The Journal of Adhesion, 2006. **82**: p. 135-160.

36. Baker, A., F. Rose, and R. Jones, eds. *Advances in the bonded composite repair of metallic aircraft structure*. First ed. Vol. 1. 2002, Elsevier Science Ltd.: Oxford.

37. *BS EN ISO 62:1999 Plastics - Determination of water absorption*. 1999, London: British Standards Institution.

38. Westing, E.P.M.V., *The determination of coating performance with impedance measurements - II. Water uptake of coatings.* Corrosion, 1994. **36**: p. 957-977.

39. McKnight, S.H. and J.W.J. Gillespie, *In situ examination of water diffusion to the polypropylene-silane interface using FTIR-ATR.* J. Appl Polym Sci, 1997. **64**: p. 1971-1985.

40. Katya, I.I., A.P. Richard, and S. Affrossman, *Hygrothermal aging of rubber modified and mineral filled dicyandiamide cured DGEBA epoxy resin. III. Dielectric spectroscopy investigation.* J. Appl Polym Sci, 2002. **84**: p. 1011-1024.

41. O'Briena, E.P., P.F. Reboab, M. Fieldb, D. Pullenb, D. Markelb, and T.C. Ward, *A novel impedance sensor design for measuring the distribution and transport of fluids at the interface.* Int. J. Adhesion and Adhesives, 2003. **23**: p. 335-338.

42. Wapner, K. and G. Grundmeier, *Spatially resolved measurements of the diffusion of water in a model adhesive / silicon lap joint using FTIR transmission microscopy.* Int. J. Adhesion and Adhesives, 2004. **24**: p. 193-200.

43. Hamerton, I., H. Herman, K.T. Rees, A. Chaplin, and S.J. Shaw, *Water uptake effects in resins based on alkenyl-modified cyanate ester-bismaleimide blends.* Polym Int, 2001. **50**: p. 475-483.

44. Sahlin, J.J. and N.A. Peppas, *An investigation of polymer diffusion in hydrogel laminates using near field FTIR microscopy.* Macromolecules, 1996. **29**: p. 7124-7129.

45. Li-Ping, S., D. Yu-Min, X.-W. Shi, X. Chen, J.-H. Yang, and Y.-M. Xu, *A new approach to chemically modified carboxymethyl chitosan and study of its moisture-absorption and moisture retention abilities.* J. Appl Polym Sci, 2006. **102**: p. 1303-1309.

46. Jain, A., V. Gupta, and S.N. Basu, *A quantitative study of moisture adsorption in polyimide and its effect on the strength of the polyimide/silicon nitride interface.* Acta Materialia, 2005. **53**: p. 3147-3153.

47. Liljedahl, C.D.M., A.D. Crocombe, F.E. Gauntlett, M.S. Rihawy, and A.S. Clough, *Characterising moisture ingress in adhesively bonded joints using nuclear reaction analysis.* Int. J. Adhesion and Adhesives, 2009. **29**: p. 356-360.

48. De Rosa, L., T. Monetta, and F. Bellucci, *Moisture uptake in organic coatings monitored with EIS.* Materials Science Forum, 1998. **289-292**: p. 315-326.

49. Wright, W.W., *The effect of diffusion of water into epoxy resins and their carbon fibre reinforced composites.* Composites, 1981. **12**: p. 201-205.

50. Gledhill, R.A., A.J. Kinloch, and S.J. Shaw, *Model for predicting joint durability.* J. Adhesion, 1980. **11**: p. 3-15.

51. Bao, L.R. and A.F. Yee, *Moisture diffusion and hygrothermal aging in bismaleimide matrix carbon fibre composites - Part I: uni-weave composites.* Composites Science and Technology, 2002. **62**: p. 2099-2110.

52. Duncan, B.C., J. Pilkington, S. Nottay, C.R.G. Allen, K. Lawrence, J.M. Urquhart, and S.J. Roberts, *Diffusion of moisture in adhesive bonds*. 2007, National Physical Laboratory (NPL).

53. Vanlandingham, M.R., R.F. Eduljee, and J.R. Gillespie, *Moisture diffusion in epoxy systems.* J Appli Polym Sci, 1999. **71**: p. 787-798.

54. Lin, Y.C. and X. Chen, *Investigation of moisture diffusion in epoxy system: Experiments and molecular dynamics simulations.* Chemical Physics Letters, 2005. **412**(4-6): p. 322-326.

55. Duncan, B., J. Urquhart, and S. Roberts, *Review of measurement and modelling of permeation and diffusion in polymers*. 2005, National Physical Laboratory (NPL).

56. Brewis, D.M., J. Comyn, and J.L. Tegg, *The uptake of water vapour by an epoxide adhesive formed from teh diglycidyl ether of bisphenol-A and di(1-aminopropyl-3-ethoxy) ether.* Polymer, 1980. **21**: p. 134-138.

57. El-Sa'ad, L., M.I. Darby, and B. Yates, *Moisture absorption characteristics of rubber particulate filled epoxy adhesives.* J. Mat. Sci., 1989. **24**: p. 1653-1659.

58. Brewis, D.M., J. Comyn, B.C. Cope, and A.C. Moloney, *Effect of carriers on the performance of aluminum alloy joints bonded with a structural film adhesive.* Poly. Engg. Sci., 2004. **21**(12): p. 797-803.

59. Lin, Y.C. and X. Chen, *Moisture sorption-desorption-resorption characteristics and its effects on the mechanical behaviour of the epoxy system.* Polymer, 2005. **46**: p. 11994-12003.

60. Apicella, A., L. Nicolais, G. Astarita, and E. Drioli, *Effect of thermal history on water sorption, elastic properties and the glass transition of epoxy resins.* Polymer, 1979. **20**: p. 1143-1148.

61. De'Nève, B. and M.E.R. Shanahan, *Water absorption by an epoxy resin and its effect on the mechanical properties and infra-red spectra.* Polymer, 1993. **34**(24): p. 5099-5105.

62. Comyn, J., *Humidity*, in *Handbook of Adhesion*, D.E. Packham, Editor. 2005, John Wiley & Sons, Ltd.

63. Wylde, J.W. and J.K. Spelt, *Measurement of adhesive joint fracture properties as a function of environmental degradation.* Int. J. Adhesion and Adhesives, 1998. **18**: p. 237-246.

64. Shuangyan Xu, D.A. Dillard, and J.G. Dillard, *Environmental aging effects on the durability of electrically conductive adhesive joints.* Int. J. Adhesion and Adhesives, 2003. **23**: p. 235-250.

65. Loh, W.K., A.D. Crocombe, M.A. Wahab, and I.A. Ashcroft, *Modelling anomalous moisture uptake, swelling and thermal characteristics of a rubber toughened epoxy adhesive.* Int. J. Adhesion and Adhesives, 2005. **25**: p. 1-12.

66. Hand, H.M., C.O. Arah, D.K. McNamara, and M.F. Mecklenburg, *Effects of environmental exposure on adhesively bonded joints.* Int. J. Adhesion and Adhesives, 1991. **11**(1): p. 15-23.

67. Ward, I.M. and J. Sweeney, *Mechanical Properties of Solid Polymers*. 2nd ed. 2004, Chichester: John Wiley & Sons Ltd.

68. Bao, L.R., A.F. Yee, and C.Y.C. Lee, *Moisture absorption and hygrothermal aging in a bismaleimide resin.* Polymer, 2001. **42**: p. 7327-7333.

69. Bond, D.A., *Moisture Diffusion in a Fiber-reinforced Composite: Part I – Non-Fickian Transport and the Effect of Fiber Spatial Distribution.* Journal of Composite Materials, 2005. **39**(23): p. 2113-2141.

70. Apalak, Z.G., M.K. Apalak, and M.S. Genc, *Progressive damage modeling of an adhesively bonded unidirectional composite single-lap joint in tension at the mesoscale level.* Journal of Thermoplastic Composite Materials, 2006. **19**: p. 671-702.

71. You, M., Z.-M. Yan, X.-L. Zheng, H.-Z. Yu, and Z. Li, *A numerical and experimental study of adhesively bonded aluminium single lap joints with an inner chamfer on the adherends.* Int. J. Adhesion and Adhesives, 2008. **28**: p. 71-76.

72. Harris, J.A. and R.D. Adams, *Strength prediction of bonded single lap joints by non-linear finite element methods.* Int. J. Adhesion and Adhesives, 1984. **4**(2): p. 65-78.

73. Fessel, G., J.G. Broughton, N.A. Fellows, J.F. Durodola, and A.R. Hutchinson, *Evaluation of different lap-shear joint geometries for automotive applications.* International Journal of Adhesion and Adhesives, 2007. **27**(7): p. 574-583.

74. *BS ISO 4587:2003 Adhesives - Determination of tensile lap-shear strength of rigid-to-rigid bonded assemblies*, British Standards Institution.

75. Da Silva, L.F.M. and A. Ochsner, eds. *Modeling of Adhesively Bonded Joints*. 2008, Springer: Berlin.

76. *BS 5350-C13: 1990 Adhesives - Part C13: Climbing drum peel test*, British Standards Institution.

77. *BS EN 1464:1995 Adhesives - Determination of peel resistance of high-strength adhesive bonds - Floating roller method*, British Standards Institution.

78. *BS EN 28510-1: 1993 Adhesives - Peel test for a flexible-bonded-to-rigid test specimen assembly - Part 1: 90 peel*, British Standards Institution.

79. *BS EN 28510-2: 1993 Adhesives - Peel test for a flexible-bonded-to-rigid test specimen assembly - Part 2: 180 peel*, British Standards Institution.

80. Comyn, J., *Adhesion Science*. 1997: The Royal Society of Chemistry.

81. *BS 7991:2001 Determination of the mode I adhesive fracture energy G of structure adhesives using double cantilever and tapered double cantilever beam specimens*, British Standards Institution.

82. Kinloch, A.J., ed. *Durability of Structural Adhesives*. 1983, Applied Science London: London.

83. Orman, S. and C. Kerr. *Aspects of Adhesion*. in *Aspects of Adhesion*. 1971. London: University of London Press.

84. Dillard, D.A. and A.V. Pocius, eds. *The mechanics of adhesion*. Adhesion science and engineering - I, ed. A.V. Pocius. 2002, Elsevier science: Amsterdam.

85. Comrie, R., S. Affrossman, D. Hayward, R.A. Pethrick, X. Zhou, and G.E. Thompson, *Ageing of Adhesive Bonds with Various Surface Treatments, Part 3: Aluminium–Dicyandiamide Cured Aluminium Filled Epoxy Joints.* J. Adhesion, 2005. **81**: p. 1199-1215.

86. Gledhill, R.A. and A.J. Kinloch, *Environmental failure of structural adhesive joints.* J. Adhesion, 1974. **6**(4): p. 315-330.

87. Crank, J., *The Mathematics of Diffusion*. 2nd ed. 1975, Oxford: Clarendon Press.

88. Vieth, W.R. and K.J. Sladek, *A model for diffusion in a glassy polymer.* Journal of Colloid Science, 1965. **20**(9): p. 1014-1033.

89. Gurtin, M.E. and C. Yatomi, *On a model for two-phase diffusion in composite materials.* J. Comp. Mater., 1979. **13**: p. 126-130.

90. Bonniau, P. and A.R. Bunsell, *A comparative study of water absorption theories applied to glass epoxy composites.* J. Comp. Mater., 1981. **15**(3): p. 272-293.

91. Dewimille, B. and A.R. Bunsell, *The modelling of hydrothermal aging in glass fibre reinforced epoxy composites.* J. Phys. D: Appl. Phys., 1982. **15**: p. 2079-2091.

92. Saleh, N., 2005. *Effects of humidity and ageing on epoxy based stereolithography materials*, PhD Thesis, Loughborough University.

93. Berens, A.R. and H.B. Hopfenberg, *Induction and measurement of glassy-state relaxations by vapor sorption techniques.* J. Poly. Sci., 1979. **17**(10): p. 1757-1770.

94. Joshi, S. and G. Astarita, *Diffusion-relaxation coupling in polymers which show two-stage sorption phenomena.* Polymer, 1979. **20**(4): p. 455-458.

95. Frisch, H.L., *Sorption and transport in glassy polymers - A review.* Poly. Engg. Sci., 1980. **20**(1): p. 2-13.

96. Mensitieri, G., M.A. Del Nobile, A. Apicella, and L. Nicolais, *Moisture-matrix interactions in polymer based composite materials.* Revue De L'Institut Francais Du Petrole, 1995. **50**(4): p. 551-571.

97. Berens, A.R. and H.B. Hopfenberg, *Diffusion and relaxation in glassy polymer powders: 2. Separation of diffusion and relaxation parameters.* Polymer, 1978. **19**(5): p. 489-496.

98. Wilde, W.P.D. and P.J. Shopov, *A simple model for moisture sorption in epoxies with sigmoidal and two stage sorption effects.* Composite Structures, 1994. **27**: p. 243-252.

99. Roy, S., W.X. Xu, S.J. Park, and K.M. Liechti, *Anomalous moisture diffusion in viscoelastic polymers: Modelling and testing.* J Appl Mech, 2000. **67**: p. 391-396.

100. Gupta, K.M. and S.J. Pawar, *A nonlinear diffusion model incorporating edge and surface texture effects to predict absorption behaviour of composites.* Materials Science and Engineering A, 2005. **412**: p. 78-82.

101. Tsai, C.L., M.C. Cheng, and S.L. Chang, *Gradient dependent model for moisture diffusion in a polymer matrix composite laminate.* Journal of Composite Materials, 2007. **41**(4): p. 419-434.

102. Apalak, M.K., R. Günes, and L. Fídanci, *Geometrically non-linear thermal stress analysis of an adhesively bonded tubular single lap joint.* Finite elements in analysis and design, 2003. **39**(3): p. 155-174.

103. Dean, G.D. and L.E. Crocker, *Comparison of the measured and predicted deformation of an adhesively bonded lap-joint specimen*. 2000, National Physical Laboratory.

104. Clarke, M., M. Buckley, J.G. Broughton, and A.R. Hutchinson, *Characterisation and simulation of structural adhesives*, in *7th European LS-DYNA Conference*. 2009: Salzburg, Austria.

105. Cui, J., R. Wang, A.N. Sinclair, and J.K. Spelt, *A calibrated finite element model of adhesive peeling.* International Journal of Adhesion and Adhesives, 2003. **23**(3): p. 199-206.

106. Feih, S. and H.R. Shercliff, *Adhesive and composite failure prediction of single-L joint structures under tensile loading.* International Journal of Adhesion and Adhesives, 2005. **25**(1): p. 47-59.

107. Dean, G., L. Crocker, B. Read, and L. Wright, *Prediction of deformation and failure of rubber-toughened adhesive joints.* International Journal of Adhesion and Adhesives, 2004. **24**(4): p. 295-306.

108. Broughton, W.R., L.E. Crocker, and J.M. Urquhart, *Strength of adhesive joints: A parametric study*. 2001, National Physical Laboratory (NPL).

109. Hart-Smith, L.J., *Adhesive bonded single lap joints*. 1973, NASA.

110. Hart-Smith, L.J., *Analysis and design of advanced composite bonded joints*. 1974, NASA.

111. Adams, R.D., R.W. Atkins, J.A. Harris, and A.J. Kinloch, *Stress analysis and failure properties of carbon-fibre-reinforced-plastic/steel double lap joints.* J. Adhesion, 1986. **20**(1): p. 29-53.

112. Adams, R.D., *Strength predictions for lap joints, especially with composite adherends. A Review.* J. Adhesion, 1989. **30**: p. 219-242.

113. Lee, S.J. and D.G. Lee, *Development of a failure model for the adhesively bonded tubular single lap joint.* J. Adhesion, 1992. **40**(1): p. 1-14.

114. Hollaway, L., A. Romhi, and M. Gunn, *Optimisation of adhesive bonded composite tubular sections.* Composite Structures, 1990. **16**(1-3): p. 125-170.

115. Adams, R.D. and J.A. Harris, *The influence of local geometry on the strength of adhesive joints.* Int. J. Adhesion and Adhesives, 1987. **7**(2): p. 69-80.

116. Wang, C.H. and L.R.F. Rose, *Determination of triaxial stresses in bonded joints.* International Journal of Adhesion and Adhesives, 1997. **17**(1): p. 17-25.

117. Duncan, B.C., L.E. Crocker, J.M. Urquhart, E. Arranz, R.D. Mera, and B. Broughton, *Flailure of flexible adhesive joints*. 2001, National Physical Laboratory.

118. Dean, G.D. and W.R. Broughton, *Models for predicting deformation and failure in adhesives and polymer matrix composites*. 2002, National Physical Laboratory (NPL).

119. Wang, C.H. and P. Chalkley, *Plastic yielding of a film adhesive under multiaxial stresses.* International Journal of Adhesion and Adhesives, 2000. **20**(2): p. 155-164.

120. Crocombe, A.D., *Global yeilding as a failure criterion for bonded joints.* Int. J. Adhesion and Adhesives, 1989. **9**(3): p. 145-153.

121. Kim, K.-S., Y.-M. Yi, G.-R. Cho, and C.-G. Kim, *Failure prediction and strength improvement of uni-directional composite single lap bonded joints.* Composite Structures, 2008. **82**(4): p. 513-520.

122. Dorn, L. and W. Liu, *The stress state and failure properties of adhesive bonded plastic metal joints.* Int. J. Adhesion and Adhesives, 1993. **13**(1): p. 21-31.

123. Towse, A., K.D. Potter, M.R. Wisnom, and R.D. Adams, *The sensitivity of a Weibull failure criterion to singularity strength and local geometry variations.* International Journal of Adhesion and Adhesives, 1999. **19**(1): p. 71-82.

124. Griffith, A.A., *The phenomenon of rupture and flow in solids.* Philosophical Transactions of the Royal Society, 1920. **A221**: p. 163-198.

125. Irwin, G.R., *Analysis of stresses and strains near the end of a crack traversing a plate.* J Appl Mech, 1957. **24**: p. 361-364.

126. Ashcroft, I.A., D.J. Hughes, and S.J. Shaw, *Mode I fracture of epoxy bonded composite joints: 1. Quasi-static loading.* Int. J. Adhesion and Adhesives, 2001. **21**: p. 87-99.

127. Imanaka, M., Y. Nakamura, A. Nishimura, and T. Iida, *Fracture toughness of rubber-modified epoxy adhesives: effect of plastic deformability of the matrix phase.* Composites Science and Technology, 2003. **63**(1): p. 41-51.

128. Chai, H. and M.Y.M. Chiang, *A crack propagation criterion based on local shear strain in adhesive bonds subjected to shear.* Journal of the Mechanics and Physics of Solids, 1996. **44**(10): p. 1669-1689.

129. Chai, H. and M.Y.M. Chiang, *Finite element analysis of interfacial crack propagation based on local shear, part II--Fracture.* International Journal of Solids and Structures, 1998. **35**(9-10): p. 815-819.

130. Daghyani, H.R., L. Ye, and Y.W. Mai, *Effect of thermal residual stress on the crack path in adhesively bonded joints.* J. Mat. Sci., 1996. **31**(10): p. 2523-2529.

131. Ashcroft, I.A., *A simple model to predict crack growth in bonded joints and laminates under variable-amplitude fatigue.* J. Strain Analysis, 2004. **39**(6): p. 707-716.

132. Hamoush, S.A. and S.H. Ahmad, *Fracture energy release rate of adhesive joints.* Int. J. Adhesion and Adhesives, 1989. **9**(3): p. 171-178.

133. Akisanya, A.R. and C.S. Meng, *Initiation of fracture at the interface corner of bi-material joints.* Journal of the Mechanics and Physics of Solids, 2003. **51**(1): p. 27-46.

134. Marannano, G.V., L. Mistretta, A. Cirello, and S. Pasta, *Crack growth analyis at adhesive-adherent interface in bonded joints under mixed mode I/II.* Engineering Fracture Mechanics, 2008. **75**: p. 5122-5133.

135. Shahin, K. and F. Taheri, *The strain energy release rates in adhesively bonded balanced and unbalanced specimens and lap joints.* Int. J. Adhesion and Adhesives, 2008. **45**: p. 6248-6300.

136. Wahab, M.M.A. and G. de Roeck, *3D finite element computation of strain energy release rate using different displacement and stress fields.* Engineering Fracture Mechanics, 1994. **49**(5): p. 659-665.

137. Wahab, M.A., *On the use of fracture mechanics in designing a single lap adhesive joint.* Journal of Adhesion Science and Technology, 2000. **14**(6): p. 851-865.

138. Zhang, L. and J. Wang, *A generalized cohesive zone model of the peel test for pressure-sensitive adhesives.* Int. J. Adhesion and Adhesives, 2009. **29**: p. 217-224.

139. Ural, A., V.R. Krishnan, and K.D. Papoulia, *A cohesive zone model for fatigue crack growth allowing for crack retardation.* Int. J. Solids Struct., 2009. **46**: p. 2453-2462.

140. Zavattieri, P.D., L.G. Hector Jr, and A.F. Bower, *Cohesive zone simulations of crack growth along a rough interface between two elastic-plastic solids.* Engineering Fracture Mechanics, 2008. **75**(15): p. 4309-4332.

141. Freed, Y. and L. Banks-Sills, *A new cohesive zone model for mixed mode interface fracture in bimaterials.* Engineering Fracture Mechanics, 2008. **75**(15): p. 4583-4593.

142. Carlberger, T. and U. Stigh, *An explicit FE model of impact fracture in an adhesive joint.* Engineering Fracture Mechanics, 2007. **74**: p. 2247-2262.

143. Elices, M., G.V. Guinea, J. Gomez, and J. Planas, *The cohesive zone model: advantages, limitations and challanges.* Engineering Fracture Mechanics, 2002. **69**: p. 137-163.

144. Sun, C., M.D. Thouless, A.M. Waas, J.A. Schroeder, and P.D. Zavattieri, *Ductile-brittle transitions in the fracture of plastically deforming, adhesively*

bonded structures. Part II: Numerical studies. International Journal of Solids and Structures, 2008. **45**(17): p. 4725-4738.

145. Meo, M. and E. Thieulot, *Delamination modelling in a double cantilever beam.* Composite Structures, 2005. **71**(3-4): p. 429-434.

146. Fan, C., P.Y.B. Jar, and J.J.R. Cheng, *Cohesive zone with continuum damage properties for simulation of delamination development in fibre composites and failure of adhesive joints.* Engineering Fracture Mechanics, 2008. **75**(13): p. 3866-3880.

147. Chandra, N., H. Li, C. Shet, and H. Ghonem, *Some issues in the application of cohesive zone models for metal-ceramic interfaces.* Int. J. Solids Struct., 2002. **39**(10): p. 2827-2855.

148. Alfano, G., *On the influence of the shape of the interface law on the application of cohesive-zone models.* Composites Science and Technology, 2006. **66**: p. 723-730.

149. Volokh, K.Y., *Comparison between cohesive zone models.* Commun. Numer. Meth. Engng, 2004. **20**: p. 845-856.

150. de Borst, R., *Numerical aspects of cohesive-zone models.* Engineering Fracture Mechanics, 2003. **70**(14): p. 1743-1757.

151. Valoroso, N. and L. Champaney, *A damage-mechanics-based approach for modelling decohesion in adhesively bonded assemblies.* Engineering Fracture Mechanics, 2006. **73**(18): p. 2774-2801.

152. Gustafson, P.A. and A.M. Waas, *The influence of adhesive constitutive parameters in cohesive zone finite element models of adhesively bonded joints.* Int. J. Solids Struct., 2009. **46**: p. 2201-2215.

153. Goyal, V.K., E.R. Johnson, and V.K. Goyal, *Predictive strength-fracture model for composite bonded joints.* Composite Structures, 2008. **82**(3): p. 434-446.

154. Li, V.C. and R.J. Ward, *A novel testing technique for post-peak tensile behaviour of cementitious materials*, in *Fracture toughness and fracture energy - testing methods for concrete and rocks*, H. Mihashi, H. Takahashi, and F.H. Wittmann, Editors. 1989, Balkema Publishers: Rotterdam. p. 183-195.

155. Sorensen, B.F. and T.K. Jacobsen, *Determination of cohesive laws by the J integral approach.* Engineering Fracture Mechanics, 2003. **70**: p. 1841-1858.

156. Ferracin, T., C.M. Landis, F. Delannay, and T. Pardoen, *On the determination of the cohesive zone properties of an adhesive layer from the analysis of the wedge-peel test.* Int. J. Solids Struct., 2004. **40**: p. 2889-2904.

157. Turon, A., C.G. Davila, P.P. Camanho, and J. Costa, *An engineering solution for mesh size effects in the simulation of delamination using cohesive zone models.* Engineering Fracture Mechanics, 2007. **74**: p. 1665-1682.

158. Harper, P.W. and S.R. Hallett, *Cohesive zone length in numerical simulations of composite delamination.* Engineering Fracture Mechanics, 2008. **75**: p. 4774-4792.

159. Allix, O. and F. Hild, *Continuum damage mechanics of materials and structures*. 2002, Oxford: Elsevier.

160. Voyidadjis, G.Z. and P.I. Kattan, *Damage mechanics*. 2005, New York: Taylor & Francis.

161. Lemaitre, J. and R. Desmorat, *Engineering damage mechanics*. 2005, New York: Spring - Verlag Berlin Heidelberg.

162. Lemaitre, J., *Local approach of fracture.* Engineering Fracture Mechanics, 1986. **25**(5-6): p. 523-537.

163. Zairi, F., M. Nait-Abdelaziz, K. Woznica, and J.-M. Gloaguen, *Constitutive equations for the viscoplastic-damage behaviour of a rubber-modified polymer.* European Journal of Mechanics - A/Solids, 2005. **24**(1): p. 169-182.

164. Gurson, A.L., *Continuum theory of ductile rupture by void nucleation and growth.* J. Eng. Mater. Technol., Trans ASME, 1977. **99**: p. 2-15.

165. Tvergaard, V., *Influence of voids on shear band instabilities under plane strain conditions.* Int. J. Fracture, 1981. **17**(4): p. 389-407.

166. Chu, C.C. and A. Needleman, *Void nucleation effects in biaxially stretched sheets.* J. Eng. Mater. Technol., 1980. **102**: p. 249-256.

167. Lemaitre, J., ed. *Handbook of Materials Behavior Models*. Vol. II. 2001, Academic Press.

168. Springmann, M. and M. Kuna, *Identification of material parameters of the Gurson-Tvergaard-Needleman model by combined experimental and numerical techniques.* Computational Materials Science, 2005. **33**(4): p. 501-509.

169. Klamser, H., D. Malcher, and P.A.G. Weissach, *Damage modelling of automobile components of aluminium materials under crash loading*, in *Material II - Metalle. LS-DYNA Anwenderforum, Ulm 2006*. 2006.

170. Lemaitre, J. and J. Dufailly, *Damage measurements.* Engineering Fracture Mechanics, 1987. **28**(5-6): p. 643-661.

171. Xue, L., *Constitutive modeling of void shearing effect in ductile fracture of porous materials.* Engineering Fracture Mechanics, 2008. **75**: p. 3343-3366.

172. Crocombe, A.D., Y. Hua, W.K. Loh, M.A. Wahab, and I.A. Ashcroft, *Predicting the residual strength for environmentally degraded adhesive lap joints.* Int. J. Adhesion and Adhesives, 2006. **26**: p. 325-336.

173. Liljedahl, C.D.M., A.D. Crocombe, M.A. Wahab, and I.A. Ashcroft, *The effect of residual strains on the progressive damage modelling of environmentally degraded adhesive joints.* J. Adhesion Sci. Technol., 2005. **19**(7): p. 525-547.

174. Crocombe, A.D., *Durability modelling concepts and tools for the cohesive environmental degradation of bonded structures.* Int. J. Adhesion and Adhesives, 1997. **17**: p. 229-238.

175. Broughton, W.R. and G. Hinopoulos, *Evaluation of the single lap joint using finite element analysis*. 1999, National Physical Laboratory (NPL).

176. Liljedahl, C.D.M., A.D. Crocombe, M.A. Wahab, and I.A. Ashcroft, *Modelling the Environmental Degradation of the Interface in Adhesively Bonded Joints using a Cohesive Zone Approach.* The Journal of Adhesion, 2006. **82**: p. 1061-1089.

177. Cytec Engineered Materials, *Datasheet - FM73 Toughened Epoxy Film*. 1998.

178. *Datasheet - BR127 Corrosion Inhibiting Primer*. 1996, Havre de Grace: Cytec Engineered Materials.

179. *BS EN ISO 527-2:1996 Plastics - Determination of tensile properties - Part 2: Test conditions for moulding and extrusion plastics*, British Standards Institution.

180. *BS ISO 11003-2:2001 Adhesives - Determination of shear behaviour of structural adhesives - Tensile test method using thick adherends*, British Standards Institute.

181. Critchlow, G.W., I.A. Ashcroft, T. Cartwright, and D. Bahrani, *Anodising aluminium alloy,* Patent No 2006, United Kingdom.

182. Abel, M.L., A.N.N. Adams, A.J. Kinloch, S.J. Shaw, and F.J. Watts, *The effects of surface pretreatment on the cyclic fatigue characteristics of bonded aluminium alloy joints.* Int. J. Adhesion and Adhesives, 2006. **26**: p. 50-61.

183. Briggs, D. and M.P. Seah, *Practical surface analysis: Auger and X-Ray photoelectron spectroscopy*. 1996: John Wiley & Son Ltd.

184. *Mathcad 14 Online Help*. 2007, Needham, MA: Parametric Technology Corporation.

185. Kutz, M., ed. *Handbook of Materials Selection*. 2002, John Wiley & Sons, Inc.: New York.

186. Bishopp, J., *Primers for adhesive bonding*, in *Handbook of adhesion*, D.E. Packham, Editor. 2005, John Wiley & Sons Ltd. p. 389-393.

187. Panigrahi, S.K. and B. Pradhan, *Through-the-width delamination damage propagation chracteristics in single-lap laminated FRP composite joints.* Int. J. Adhesion and Adhesives, 2009. **29**: p. 114-124.

188. Wu, Z., *Stress concentration analyses of bi-material bonded joints without in-plane stress singularities.* Int. J. Mech. Sci., 2008. **50**: p. 641-648.

189. Wahab, M.A., I.A. Ashcroft, A.D. Crocombe, and L. Joussot, *Lifetime prediction for fatigue damage in bonded joints.* Key Engineering Materials, 2003. **245-246**: p. 43-50.

190. Yu, X.X., A.D. Crocombe, and G. Richardson, *Material modelling for rate-dependent adhesives.* International Journal of Adhesion and Adhesives, 2001. **21**(3): p. 197-210.

191. *Abaqus Analysis User's Manual*. 2008, Dassault Systemes Simulia Corp. Providence, RI, USA.

192. Carslaw, H.S. and J.C. Jaeger, *Conduction of heat in solids*. 2nd ed. 1959, Oxford: Oxford University Press.

193. *Abaqus User Subroutines Reference Manual*. 2008, Dassault Systemes Simulia Corp. Providence, RI, USA.

194. Yu, Y., I.A. Ashcroft, and G. Swallowe, *An experimental investigation of residual stresses in an epoxy–steel laminate.* Int. J. Adhesion and Adhesives, 2006. **26**: p. 511-519.

195. Cardarelli, F., *Materials Handbook - A Concise Desktop Reference*. 2nd ed. 2008, London: Springer-Verlag London Limited.

196. de Moura, M.F.S.F. and J.A.G. Chousal, *Cohesive and continuum damage models applied to fracture characterization of bonded joints.* Int. J. Mech. Sci., 2006. **48**: p. 493-503.

197. Diehl, T., *On using a penalty-based cohesive-zone finite element approach, Part II: Inelastic peeling of an epoxy-bonded aluminum strip.* International Journal of Adhesion and Adhesives, 2008. **28**(4-5): p. 256-265.

198. Diehl, T., *On using a penalty-based cohesive-zone finite element approach, Part I: Elastic solution benchmarks.* International Journal of Adhesion and Adhesives, 2008. **28**(4-5): p. 237-255.

199. Aufray, M. and A.A. Roche, *Epoxy-amine/metal interphases: Influences from sharp needle-like crystal formation.* Int. J. Adhesion and Adhesives, 2007. **27**: p. 387-393.

200. Barthes-Labrousse, M.G., *Adhesion mechanisms at amine-cured epoxy/aluminium interfaces.* J. Adhesion, 1996. **57**(1): p. 65-75.

201. Kobozeva, I.A. and I.A. Petrova, *IR Spectroscopic study of curing mechanism of epoxy oligomers by aluminium chelates.* Zhurnal Prikladnoi Spektroskopii, 1990. **52**(4): p. 607-611.

202. Possart, G., M. Presser, S. Passlack, P.L. GeiB, M. Kopnarski, A. Bronyanski, and P. Steinmann, *Micro-marco characterisation of DGEBA-based epoxies as a priliminary to polymer interphase modelling.* Int. J. Adhesion and Adhesives, 2009. **29**: p. 478-487.

203. Bengu, B. and F.J. Boerio, *Interaction of Epoxy/Dicyandiamide Adhesives with Metal Substrates.* The Journal of Adhesion, 2006. **82**: p. 1133-1155.